AD NUMBER

AD865062

NEW LIMITATION CHANGE

TO

Approved for public release, distribution unlimited

FROM

Distribution authorized to U.S. Gov't. agencies only; Administrative/Operational Use; NOV 1969. Other requests shall be referred to Commanding officer, US Army Tank-Automotive Command, Warren, MI 48090.,.

AUTHORITY

USATAC ltr, 10 Apr 1974

TECHNICAL REPORT NO. 10733
(LL 136)

AD 865062

THE THEORY OF PENETRATION FAILURE
IN COMPACT SOILS

November 1969

D D C

FEB 17 1970

C

*by* Brian D. Witney

Land Locomotion Division

# TACOM

## MOBILITY SYSTEMS LABORATORY

### U.S. ARMY TANK AUTOMOTIVE COMMAND  Warren, Michigan

CLEARINGHOUSE

The findings in this report are
not to be construed as an official
Department of the Army position.

---

The citation of commercial products
in this report does not constitute
an official indorsement or approval
of such products.

---

Citation of equipment in this report does
not constitute an official indorsement or
approval of the use of such commercial
hardware.

---

TECHNICAL REPORT NO. 10733 (LL 136)

THE THEORY OF PENETRATION FAILURE
IN COMPACT SOILS

November 1969

by
Brian D. Witney

AMCMS 5011.11.861

Land Locomotion Division
Mobility Systems Laboratory

# ABSTRACT

A unified procedure is employed in the determination of the penetration resistance of continuous strip footings and foundations buried up to ten times their width in compact soil. The quasi-static analysis is based on the soil failure theory of classical soil mechanics.

The theoretical data is presented by means of a two part additive equation, two dimensionless factors describing the effect of weight and cohesion. These factors are functions not only of the angle of internal friction and the penetration ratio but also of the shaft parameters and the dimensionless group dependent on the density, the cohesion and the breadth of the footing. The factors are calculated for the same figure of rupture and the practice of treating a portion of weight within the failure boundary as a surcharge has been eliminated. The inherent approximations and resultant errors in the computation are fully stated.

Experimental verification is given both of the penetration resistance and of the failure geometry by model testing in a glass sided soil tank. The penetration resistance data in compact soil support the quantitative theoretical values. The measured failure patterns are shown to be in agreement with the predicted shapes only when the effect of changing soil properties and constraints are carefully evaluated throughout the duration of the test.

# CONTENTS

# ACKNOWLEDGEMENT

# OBJECT

This programme of research is concerned with the development of theory of penetration failure which may be used as the basis of a more complex theory of slip-sinkage.

## NOTATION

| | | |
|---|---|---|
| $a_\theta$ | Exponential function | dimensionless |
| $A_1 - A_9$ | Functions | various |
| $B$ | Breadth of footing | in |
| $c$ | Cohesion | lb in$^{-2}$ |
| $c_a$ | Adhesion | lb in$^{-2}$ |
| $C_s$ | Adhesive force on the shaft | lb in$^{-1}$ |
| $C_1, C_2, C_3$ | Cohesive forces | lb in$^{-1}$ |
| $d_c, d_q, d_\gamma$ | Empirical depth factors | dimensionless |
| $d, d_1 - d_{11}$ | Dimensions | in |
| $e$ | Base of natural logarithm | dimensionless |
| $f$ | Rupture distance | in |
| $f_1, f_2$ | Functions | dimensionless |
| $F$ | Total force | lb in$^{-1}$ |
| $F_c$ | Resultant cohesive-frictional force | lb in$^{-1}$ |
| $F_\gamma$ | Resultant weight-frictional force | lb in$^{-1}$ |
| $F_{c1}, F_{c2}$ | Cohesive-frictional boundary forces | lb in$^{-1}$ |
| $F_{\gamma 1}, F_{\gamma 2}$ | Weight-frictional boundary forces | lb in$^{-1}$ |
| $F_{cs}$ | Cohesive-frictional force on the shaft | lb in$^{-1}$ |
| $F_{\gamma s}$ | Weight-frictional force on the shaft | lb in$^{-1}$ |
| $g$ | Acceleration due to gravity | in sec$^{-2}$ |
| $H_c$ | Critical height of vertical bank | in |
| $i_c, i_q, i_\gamma$ | Empirical inclination factors | dimensionless |
| $k$ | Sinkage modulus<br>Radius of gyration | dimensionless<br>in |
| $k_c$ | Cohesive sinkage modulus | lb in$^{-1-n}$ |

| | | |
|---|---|---|
| $k_\phi$ | Frictional sinkage modulus | lb in$^{-2-n}$ |
| $k'_c$ | Cohesive sinkage modulus | dimensionless |
| $k'_\phi$ | Frictional sinkage modulus | dimensionless |
| $k_{cs}$ | Shaft coefficient of earth pressure due to cohesion and friction | dimensionless |
| $k_{\gamma s}$ | Shaft coefficient of earth pressure due to weight and friction | dimensionless |
| $k_a$ | Shaft coefficient of active earth pressure | dimensionless |
| $k_p$ | Shaft coefficient of passive earth pressure | dimensionless |
| $k_{\phi c}$ | Boundary coefficient of earth pressure due to cohesion and friction | dimensionless |
| $k_{\phi \gamma}$ | Boundary coefficient of earth pressure due to weight and friction | dimensionless |
| $l$ | Characteristic length | in |
| $L$ | Dimension | in |
| | Length of footing | in |
| $m$ | Mobilisation of shear stress on equivalent free surface | dimensionless |
| $M_c$ | Moment of cohesion | lb in$^{-1}$ |
| $M_\xi, M_\eta$ | Moments of area | in$^3$ |
| $n$ | Sinkage exponent | dimensionless |
| | Boundary exponent | dimensionless |
| $N_c, N_q, N_\gamma,$ $N_a$ | General factors for cohesion, surcharge weight and adhesion | dimensionless |
| | Bearing capacity factors | dimensionless |
| $N_{cq}, N_{\gamma q}$ | Composite bearing capacity factors | dimensionless |
| $N_{q\infty}$ | Surcharge factor for a weightless soil | dimensionless |
| $N_{\gamma o}$ | Weight factor for zero surcharge | dimensionless |
| | Weight factor for zero interface friction | dimensionless |
| $N_{\gamma \delta}, N_{\gamma \phi}$ | Weight factors for intermediate and maximum interface friction | dimensionless |
| $N_{\gamma a}, N_{\gamma s},$ $N_{\gamma p}$ | Weight factors for various shaft coefficients | dimensionless |

| Symbol | Description | Units |
|---|---|---|
| $p$ | Bearing pressure | lb in$^{-2}$ |
| | Penetration resistance | lb in$^{-2}$ |
| | Cartesian co-ordinate | in |
| $p_0$ | Normal equivalent free surface stress | lb in$^{-2}$ |
| $q$ | Surcharge pressure | lb in$^{-2}$ |
| $r$ | Radius | in |
| $r_0, r_1$ | Initial and final spiral radii | in |
| $R_1 - R_6$ | Functions | various |
| $s_c, s_q, s_\gamma$ | Empirical shape factors | dimensionless |
| $u$ | Constant | dimensionless |
| $v$ | Velocity of penetration | in sec$^{-1}$ |
| | Constant | dimensionless |
| $V_1 - V_8$ | Functions | various |
| $W, W_1$ | Weight forces | lb in$^{-1}$ |
| $x_0$ | Centroid distance | in |
| $z, z_0, z_1 - z_3$ | Sinkage | in |
| $\alpha$ | Angle of average inclination of the major plane | degree |
| $\gamma$ | Soil density | lb in$^{-3}$ |
| $\delta$ | Angle of interface friction | degree |
| $\Delta_0$ | Area of the logarithmic spiral sector | in$^2$ |
| $\epsilon$ | Angle of the slip planes to the horizontal in a passive Rankine zone | degree |
| $\zeta$ | Slope angle of the radial boundary of the zone of shearing flow | degree |
| | Cartesian co-ordinate | in |
| $\eta$ | Cartesian co-ordinate | in |
| $\theta, \theta'$ | Angle of orientation of the slip planes | degree |

| $\theta_a$, $\theta_p$ | Angle of rotation of principle stresses from the vertical and horizontal | degree |
| $\lambda$ | Polar co-ordinate of the spiral pole | in |
| $\lambda_{min}$ | Polar co-ordinate defining the spiral pole for which the force is a minimum | in |
| $\mu$ | Correction factor | dimensionless |
| $\rho$ | Coefficient | lb in$^{-2}$ |
| $\sigma$ | Normal Stress | lb in$^{-2}$ |
| $\tau$ | Shear stress | lb in$^{-2}$ |
| $\phi$ | Angle of internal shearing resistance | degree |
| $\psi$ | Base angle of the fixed soil wedge | degree |
| $\omega$ | Angle subtended by the spiral | degree |

# LIST OF FIGURES

(xii)

# 1. INTRODUCTION

The evaluation of the stress deformation characteristics of soil not only forms the basis of foundation engineering but also represent one of the major problems hindering progress in soil-vehicle relationships. In the past, this common interest in one and the same problem has not generated viable co-operation between the two fields. In fact, rather the reverse is true, partly due to the divergence in practical requirements.

For the design of foundations, complete soil failure at its ultimate bearing capacity must be avoided with an adequate margin of safety, and the total and relative settlements must be less than the limits tolerated by the superstructure. The point of complete failure is determined by the maximum stress in soil, whereas the settlement is due to soil consolidation under the weight of the structure, and depends on smaller stresses which can be described by elastic analysis. Thus, bearing capacity theories are based on mathematical analyses for ideal soils, and minor deviations from realistic conditions are adequately safeguarded by the adoption of a factor of safety of three.

In mobility investigations, the theories of penetration resistance must be more precise for application in the more complex theories of motion resistance, slip sinkage and the ultimate immobilisation of the vehicle. Greater emphasis has been placed on empirical relations and similarity techniques to overcome the problems of describing accurately the influence of stress strain characteristics, compressibility and layered conditions in the disturbed top soil. Although it is doubtful whether these factors will ever be predicted accurately in a rigorous analysis, any empirical analysis must be firmly based on soil mechanics theory. The solution must be capable of modification and extension to include the influence of combined loading and vehicle attitude on the mode of failure and the load bearing of the soil.

## 1.1    Analytical Techniques

The diverse approaches employed to determine the stress deformation characteristics of the soil may be divided into the following five categories:-

(1)    Static analysis, a rigorous mathematical analysis based on the stress conditions at failure in a rigid heavy Coulomb material.

(2)    Plasticity theory, the association of static analysis with suitable stress strain relationships.

(3)    Soil mechanics theory, an approach based on 1 or 2 above, but involving simplifying assumptions in order to obtain reasonably economical solutions to real problems.

(4)    A semi-empirical analysis employing measured soil stress deformation characteristics.

.(5)    Model experiments guided by dimensional analysis.

The main difficulty with the various types of rigorous analysis—for example static analysis, plasticity theory and limit analysis—is that they are not relevant to real soils. In order to

1

obtain immediate solutions to practical problems, soil mechanics theory has incorporated much of this more fundamental work without fully defining all the assumptions and approximations. The result is that particular problems have numerous solutions which have little point of contact with each other. Both rigorous and theoretical analysis are combined with empiricism and dimensional theory to yield a wealth of possibilities. The potential and limitations of these evaluation techniques are illustrated in this review of previous work.

## 1.2 Static Analysis

Perhaps the most relevant approach to soil mechanics is through the method of static analysis, particularly associated with the work of Sokolovski[1]. It is based on the properties of a rigid Coulomb material and combines the known relationships between the stresses at failure with the partial differential equations of equilibrium.

The simplest way of describing stress conditions at failure is by the Coulomb equation[2],

$$\tau = c + \sigma \tan \emptyset \qquad \qquad ..... 1.2.1.$$

where $\tau$ represents the maximum shear stress along any plane of incipient failure, c the cohesion, $\sigma$ the normal stress on the plane and $\emptyset$ the angle of internal shearing resistance. A more general version of this yield condition showing the relation between the normal and shear stresses on any two mutually perpendicular planes at a point of incipient failure is:-

$$\frac{\sigma_x + \sigma_y}{2} \sin \emptyset + \left[ \left( \frac{\sigma_x + \sigma_y}{4} \right)^2 + \tau_{xy} \right]^{1/2} - c \cos \emptyset = 0 \qquad ..... 1.2.2.$$

The equations of static equilibrium are:-

$$\left. \begin{array}{l} \dfrac{\delta \sigma_x}{\delta x} + \dfrac{\delta \tau_{xy}}{\delta y} = 0 \\[2em] \dfrac{\delta \tau_{xy}}{\delta x} + \dfrac{\delta \sigma_y}{\delta y} = 0 \end{array} \right\} \qquad ..... 1.2.3.$$

The total distribution of stress throughout a mass of failing soil can be obtained by integration of these equations starting from known boundary stresses. This can be done by a step by step numerical method using more convenient versions of equations 1.2.2. and 1.2.3. Sokolovski has published an account of the applications of this method to many rather simple problems. Prager[3] developed an alternative graphical technique called the Pole Trail method which was used by Josselin de Jong[4] to obtain the bearing capacity of a surface footing on a frictional material with weight and surcharge.

The most fundamental proposition that emerges from this analysis is that slip planes occur in pairs inclined at an angle of $\pi/2 + \emptyset$ to each other at all points in a mass of soil at failure. This can be seen immediately from the Mohr diagram in Fig 1.2.1.

2

In general, the slip line field will consist of two sets of curved lines intersecting at the correct angle of $\pi/2 + \emptyset$. Where a discontinuity occurs in the boundary stress conditions (as at the corner of a footing) two different slip line fields meet each other. In order to obtain a continuous slip line field, a third fan shaped zone is introduced with one set of slip lines emanating from the point of discontinuity or singular point (Fig 1.2.2.)

When a uniform loading is applied parallel or at right angles to the gravitional force, the curved slip lines are straightened to form stress fields in the well known active and passive Rankine states, respectively. In addition, if a singular point occurs between two straight slip line fields, then all the lines emanating from that point are straight radii, and the other family are inclined at an angle $\emptyset$ to the circumferential direction to satisfy the condition of equilibrium so that the slip lines are at an angle of $\pi/2 + \emptyset$. The increment of length of the curved slip line is:-

$$r \, d\theta \, \sec\emptyset = dr \, \csc\emptyset \qquad \dots \dots 1.2.4.$$

and after integration

$$r_1 = r_o \, e^{\theta \tan\emptyset} \qquad \dots \dots 1.2.5.$$

where $r_o$ is the radius for $\theta = 0$ (Fig 1.2.3.). Thus the circular failure plane is replaced by a logarithmic spiral when friction is present in the radial fan.

Static analysis can only be applied to problems where the soil mass at a state of failure is completely isolated by boundaries of known stresses and known failure surfaces within the soil. Examples are the surface foundation and retaining wall problems illustrated in Figs 1.2.4a. and 1.2.4b. Note that, in these cases, all the soil within the boundaries ABCDE and ABCDEFGH is definitely failed.

Unfortunately, the techniques cannot yield a complete solution to the deep foundation problem shown in Fig 1.2.5. This is because a large part of the zone BDEG consists of soil which is definitely not in a state of failure. It is possible to obtain the zone ABC by static analysis and to see that there must be a fan with initially straight radii emanating from B. The other limits of the fan BCD would normally be obtained from the slip line field in the region BDEG by integration inwards from known boundary stresses along BG and GE. This cannot be done because the soil is not in a state of failure along these boundaries.

A rigorous solution to this problem would require a knowledge of the stress strain relation for the soil extending over the whole elastic plastic range. This would provide a separate set of kinematic constraints from which extra equations could be established. Such a system of static and kinematic requirements constitutes a theory of plasticity.

## 1.3.    Theories of Plasticity

The combination of static requirements based on force equilibrium and a failure criterion, and kinematic requirements based on stress strain relations is the basic feature of any plastic theory. The most successful solutions have been developed for incompressible, frictionless materials failing according to the Tresca criterion:-

$$\tau_{max} = k \qquad \dots \dots 1.3.1.$$

3

Normally (e.g. for metals) K is far greater than the gravitional stresses which may then be neglected, resulting in the assumption of a weightless material. The way in which stress strain relation can be described in a plastic material is highly complex. Let it suffice to say that it is derived from the concept of a yield function which, for a stable material, requires that the strain rate vector is always normal to the yield surface when axes of plastic strain are superimposed on the axes of stress in Mohr's circle construction. The ratio of plastic extension to plastic shear rate is uniquely determined by the shape of the yield surface.

This theory of plasticity has been used with limited success for certain simple problems concerning the working of metals or of relatively strong clays. When more complex boundary conditions are introduced, the complicated mathematical expressions for the curvature of the slip lines are not always capable of yielding a general solution.

Even in a perfectly plastic weightless material with $\emptyset$ = O, few problems have been solved. Prandtl[5] achieved an exact solution for the identation of a flat surface by a long flat punch (Fig 1.3.1a.). The regions ABC and BDE are regions of constant stress whilst BCD is a zone of radial shear. However, Hill[6] proposed an alternative stress distribution for the same problem which gives the same bearing capacity (Fig 1.3.1b.). The velocity fields for the two solutions were added by Shield[7]. In Prandtl's solution, the rupture distance BE is twice that in Hill's solution, but the velocities are halved so that the volume of material raised above the undisturbed surface after the punch has penetrated a small distance is the same in both cases. It has been proposed that the double wedge is applicable to a smooth base and the single wedge to a rough base when friction is present. This distinction is later used in soil mechanics.

Considering the penetration of the load into an ideally plastic material, the surface bearing capacity is not the maximum base penetration resistance, and it increases with depth to some steady value. At this ultimate bearing state, Jaky[8] has postulated the slip line field for the case of plain strain (Fig 1.3.2.). In the zone of radial shear BCD, the slip lines turn through an angle of $\pi$ radians instead of $\pi/2$ radians in Prandtl's solution. The two regions of constant stress ABC and BDE remain intact, but the rupture surface CDE breaks out at the vertical free surface as opposed to the horizontal free surface in the surface case.

In view of the difficulty of obtaining a precise solution, an approximate method known as limit analysis has been developed within this theory of plasticity. The collapse or limit design theorems were first introduced by Drucker and Prager[9] and refer to the constant loads if the accompanying changes in geometry are disregarded. In other words, the equilibrium conditions may be set up in the undeformed body and represent a great simplification because the deformation constitutes one of the unknowns in the collapse problem.

The two theorems are:-

(a)   Collapse will not occur if any state of stress can be found which satisfies the equations of equilibrium and stress boundary conditions.

(b) . Collapse must occur if, for any compatible flow pattern considered as plastic only, the rate at which the external forces do work on the body equals or exceeds the rate of internal dissipation.

Based on the first theorem, a perfectly plastic material will adjust itself to carry the load if there is a possible way. This statically admissible state of stress gives a lower bound solution for the equilibrium stress conditions at every point of a plastic zone. From the second theorem, the soil will fail if a path of failure exists. This kinematically admissable velocity field gives an upper bound solution which is only valid for perfectly elastic materials. Thus a lower bound solution is maximised whilst an upper bound solution is minimised. The actual solution lies at the point where these two approaches have the same value for the applied force. The use of these theorems is tedious and there is no guarantee that the upper and lower bound solution will converge accurately on the same mean value.

Attempts have been made to develop a theory of plasticity for a material with weight and internal friction, which would be appropriate to real soils. The Tresca yield criterion has been replaced by the Von Mises - Coulomb criterion and the material assumed to be non-work hardening. This activity is well represented by the recent work of Drucker[10], Haythornthwaite[11] and Shield[12]. This attempt has failed, however; the resulting material has the property of enormous dilation with shearing strain and is, therefore, quite unlike soil[13]. One negative outcome of the work is the realization that the limit analysis theorems need extensive modification before they can be applied to frictional materials[14].

Frequent reference to the theory of plasticity is made in published work in soil mechanics. Terzaghi's work[15] on bearing capacity is based on Prandtl's solution and Meyerhof's[16] on Jaky's. In the particular case of strong frictionless clays, there is some justification for this, due allowance being made for the controversial nature of the plasticity solutions themselves. However, the minimisation procedure which are often used in soil mechanics and justified by vague references to limit analysis do not appear to be correct.

## 1.4     Shallow Foundation Theory

Soil mechanics commenced as a serious theoretical study with the publication of 'Theoretical Soil Mechanics' by Terzaghi in 1943[15]. The basis for the theories, developed therein, is clearly the theory of plasticity for frictionless weightless materials. Modifications to suit heavy frictional soils have been attempted by numerous workers, each applying different assumptions and simplifications. No major effort is made to explain why rigorous solutions of real problems are not possible, nor to develop suitable principles for non-rigorous methods. This unsatisfactory position in current soil mechanics can best be appreciated by a critical examination of the existing theories of bearing capacity.

The failure geometry assumed by Terzaghi for a surface foundation is shown in Fig 1.4.1a. From the conditions of stress beneath the base of the footing, he postulated the existence of a wedge shaped body of soil ABC, which remains permanently in a state of elastic equilibrium and behaves as part of the sinking footing. Furthermore, the shape of the wedge has dependent on the base roughness such that the base angle $\psi$ could take any value between $\pi/4 + \emptyset/2$ for a perfectly smooth base and $\emptyset$ for a rough base. The latter value was adopted for two reasons, first because he found that the angle of base friction was always less than the angle of shearing resistance, and secondly because he assumed that the footing could sink only if the soil immediately below the wedge tip C moved vertically downwards. For this condition, the stress trajectories must emanate from a vertical tangent. This gives rise to an impossible stress condition at point C, where four failure planes intersect in a Coulomb material at angles of other than the correct values of $\pi/2 + \emptyset$ and $\pi/2 - \emptyset$ radians.

For a surface foundation, the region BDE is uninfluenced by the structure, and is dependent only on the weight of the soil below the horizontal soil surface plus any uniform surcharge layer. These known stress conditions yield a plane shear zone in the passive Rankine state. The maximum extent of this region is determined by the outer boundary of the fan shaped zone which emanates from the tip of the wedge beneath the footing.

The calculation of the resultant bearing pressure was derived from a two part calculation and presented in terms of an additive equation:-

$$p = cN_c + qN_q + \tfrac{1}{2}\gamma BN_\gamma \qquad \qquad \dots\dots 1.4.1.$$

where $N_c$, $N_q$ and $N\gamma$ are dimensionless factors depending only on $\phi$. The effect of weight was obtained for a purely frictional material and that of cohesion and surcharge for a weightless material with friction. The former is reasonable since it is the condition for dry sand, but the second is completely unrealistic and was chosen only because it greatly simplified the computation of the bearing capacity.

Based on an extension of Prandtl's analysis[5], Terzaghi assumed that the pole of the logarithmic spiral is at point A for the calculation of the cohesion and surcharge factors. This is entirely satisfactory since it gives the correct orientation of stress along face AC, and D'E' is tangential to the spiral CD'. For calculating the weight factor, Terzaghi adopted a semi-graphical treatment based on the work of Ohde[17]. The pole of the spiral is restrained to move anywhere along BD or that line produced. The actual point is chosen such that the resultant bearing capacity is a minimum. Unless the pole of the spiral is at the corner of the footing, the stress directions are incorrect where they intersect the wedge boundary BC and the failure surfaces CD'E' are dissimilar.

In a weightless media, the fixed soil body and the passive Rankine zone are separated by a zone of radial shear, comprising radii and logarithmic spirals whole pole lies at the corner of the footing. Ohde proposed that these constraints were excessive for a heavy Coulomb material when existence of a doubly curved slip line field was known. For mathematical convenience, he retained the concept of a zone of radial shear, but relaxed the requirement that the region must radiate from the corner of the footing. By restraining the pole to the boundary of the passive Rankine zone, only one stress discontinuity occurred. This discontinuity was present along the retaining wall in his theory and was ignored because the obliquity of the slip planes was influenced by the friction on the interface. Thus, both sources of error were collected at one point and their effect minimised by the adoption of a minimum value postulate. Since the minimising procedure was not carried out for a series of failure surfaces which all satisfy the conditions of equilibrium, the boundary conditions and the idealised soil properties, there seems little logical justification for using it. There is even less reason for its application in the case of bearing capacity where the stress conditions along the soil to soil boundary of the fixed soil wedge have already been positively assumed. If it is initially assumed that the fan shaped zone is enclosed by two straight boundaries (the sides of the wedge and the passive Rankine zone) meeting at a singular point, then it follows implicitly that the intermediate slip line field comprises radii and logarithmic spirals with their pole at the singular point i.e. at the corner of the footing.

The weak link in this reasoning lies in the initial assumption of the stress conditions which exist beneath the footing. A study of the effect of weight and surcharge on the ultimate bearing capacity of a cohesionless material was first conducted by Lundgren and Mortensen[18].

6

This analysis was based on plasticity theory. The failure patterns which result from the three combinations of weight and surcharge are shown in Fig 1.4.2. The upper diagram illustrates the traditional Prandtl failure pattern for a weightless soil with surcharge. The inclusion of soil weight in the analysis results in a curved wedge boundary and a doubly curved slip line field in the fan. When both weight and surcharge are considered, the failure surface is unique and it has been postulated that the ultimate bearing pressure in a cohesionless soil can be expressed more correctly by the formula:-

$$p = \mu \ (qN_{q\infty} \ + \ \tfrac{1}{2}\gamma BN_{\gamma 0})$$

..... 1.4.2.

where $N_{q\infty}$ is the surcharge factor for a weightless soil, $N_{\gamma 0}$ is the weight factor for zero surcharge and $\mu$ is a function of $\emptyset$ and the surcharge to weight ratio. For $\emptyset = 30^\circ$ the correcting factor $\mu$ is given in Fig 1.4.3. As its maximum value is only 1.17, the error made when neglecting $\mu$ is thus not excessive.

It is also interesting to note that the value of $\mu$ remains positive for quite large surcharges. In Terzaghi's theory where shallow sinkage is considered in terms of a surcharge soil layer, the maximum value of the correcting factor when $\emptyset = 30^\circ$ occurs for a penetration ratio of 0.4 and the correcting factor is greater than zero provided the penetration ratio is less than ten. This lends proof to Terzaghi's original argument that by neglecting the shear strength of the overburden and discarding a correcting factor, the computation is simplified and any error is located on the safe side. Unfortunately, Lundgren's value of $N_{\gamma 0}$ corresponds to a solution which is statically correct but kinematically i. possible and is now thought to be over conservative.

An alternative solution was developed by Gorbunov-Passadov[19] who based his analysis on the assumption that the velocities in the plastic zones have the same direction as the active slip surfaces. Although this assumption is open to criticism, he did provide some experimental substantiation from a photographic analysis of the particle paths at failure. From his calculations, there results a two part wedge (Fig 1.4.4.). The inner elastic zone ABC is almost the same shape as that found by Lundgren. From the outer boundary of the compacted core ABD, the slip lines curve to make vertical contact with the boundary of the inner elastic core. With this type of failure mechanism, the value of $N\gamma$ is much larger than those given by the classical method (Fig 2.10.1.). It is, however, a valuable attempt to find a statically correct solution based on the kinematic evidence obtained from test data.

The two preceding theories [18, 19] suffer from this disadvantage that cohesion is not considered. A less vigorous but more general analysis has been proposed by Hu[20] in his 'Variable Factor-Theory'. The slip surface comprises a logarithmic spiral with its pole constrained at the corner of the footing and a straight sided wedge under the foundation whose variable base angle $\psi$ is determined by the condition for which the ultimate bearing capacity is a minimum (Fig 1.4.5.). Hence, the minimum value postulate depending on the position of the spiral pole is replaced by one depending on the base angle of the wedge using the same moment equation as the basis of the analysis. It therefore suffers from the same criticism as Terzaghi's small wedge, namely, that the failure planes at the wedge tip do not meet and the correct angles in a Coulomb material. It will later be shown that the minimum value postulate wholly depends on the mathematical constraints of the problem when dissociated from the correct stress conditions and not on the mechanism of failure (c.f. Section 5).

Rowe's solution[21] combines the procedure of slices as described by Bishop [22] and Janbu[23] with the stress dilatancy relations. In the failure geometry, the slip line is replaced

7

by the α -line where α is the average inclination of the major plane at which the particles are interlocked (Fig 1.4.6.). The angle of rotation of the principle stresses when measured from the vertical is denoted by $\theta_a$ in the figure and when measured from the horizontal by $\theta_p$. This analysis has several advantages. The stress boundaries are nowhere violated, the analysis can be simplified by approximate methods without involving errors of practical importance, and the solutions are identical with those based on the Mohr-Coulomb criterion when the dilatancy is zero.

The solution seems to provide a suitable compromise or correlation between the two conflicting groups adopting the straight and curved wedge boundaries.

## 1.5    Deep Foundation Theory

Terzaghi applied the term 'deep foundation' to one whose sinkage is greater than the width. The first comprehensive study was conducted by Meyerhof[16]. He extended Terzaghi's bearing capacity theory to deal with deep foundations, and made a major contribution in that the failure geometry was not only dependent on $\emptyset$ but also on the sinkage. A failure pattern was proposed with a smooth transition from the surface case to that of a deep foundation (Fig 1.5.1.). The zone of mobilised soil is again divided into three regions - the wedge, the plane shear zone and the zone of radial shear. As sinkage increases the segment if the spiral is extended, and the plane shear zone is reduced in size.

Meyerhof assumed that the wedge angle must always have a base angle of $\pi/4$ + $\emptyset/2$ regardless of the roughness of the footing, but in accordance with placticity theory, stated that beneath a perfectly smooth base, two wedges were formed instead of one which effectively halves the total bearing capacity (c.f. Figs 1.3.1a. and 1.3.1b.). In practice, however. a smooth base is never found, and may be discounted.

For the determination of the failure geometry and the calculation of the bearing capacity factors, Meyerhof was obliged to assume a certain pressure distribution along BC, ED and DB (Fig 1.5.1a.). Along the wedge boundary BC, he assumed that the weight-frictional component of pressure would always have its centre of pressure two thirds of the way from B to C. From the analogy of hydrostatic pressure, this would be correct for a surface foundation, but as the sinkage increased, the centre of pressure would move towards the centre of BC.

The resultant forces acting on the foundation shaft BG, and the weight of the adjacent soil wedge BEG are replaced by 'equivalent stresses' normal and tangential to the plane BE, which may then be treated as an 'equivalent free surface'. It is not stated however that these stresses are uniformly distributed along BE, nor is it made clear that the pressure due to both cohesion and weight are equally di... .buted on all sides of the triangle BDE. The startling assumption comes from using Mohr's circle to determine the equilibrium of the triangle BDE upon which the geometry depends. The Mohr circle, however, is a construction that is correct for the stresses at a point where uniform distribution of stress is a reasonable assumption.

The bearing pressure was represented by the equation:-

$$p = cN_c + p_0N_q + \tfrac{1}{2}\gamma BN_\gamma \qquad\qquad ..... 1.5.1.$$

where $p_0$ is the normal equivalent free surface stress along BE. The calculation of the cohesion and surcharge factors is again based on an extension of Prandtl's work in a weightless material, and the pole of the radial shear zone lies at the corner of the footing. For the

8

calculation of the weight factor, Meyerhof minimised with even greater abandonment than Terzaghi and has attempted to justify this in published work[24] on surface foundations. Even further discontinuities are introduced by the complete relaxation of the restraints on the spiral centre (Fig 1.5.1.). Unfortunately the unrestrained pole necessitates discontinuous slip planes along the boundaries of the wedge BC, and the passive Ranking zone, BD. It is also unacceptable on the grounds that the failure surface CDE has a sharp corner in it at point D which is unlikely where soil movement is occurring. Unless these discrepancies are small, there remains little support for describing the shape of the curve by the equation of the logarithmic spiral, apart from the advantage that of the frictional forces pass through the pole. Compared with Terzaghi's $N\gamma$ factor for the same wedge angle of $\pi/4 + \emptyset/2$ he did obtain values of up to 10% lower at the larger values of $\emptyset$, but only by sacrificing the more acceptable stress field. With the inclusion of the sinkage parameter, the freedom of movement of the pole is much more considerable and impossible stress field can be derived. In the presence of the surcharge, zone BEG is also neglected so that the geometry reduces to that of a footing on a slope. Meyerhof also shows that there is little difference in the value of $N\gamma$ if the plane shear zone is replaced by an extension of the radial shear zone, but rotational equilibrium of the forces was not examined in either case. It is hardly surprising, therefore, that the failure geometry for the $N\gamma$ calculation is much smaller than that for the weightless material; when the plane shear zone is absent, the former may be half the other.

In the generalisation procedure, Meyerhof confuses the concept of a surcharge with that of a force due to soil weight and cohesion. He considers triangle BEG as a surcharge. There seems no justification for this and it is perfectly possible to include the effect of this triangle in the weight term. This leaves open the possibility of considering any surcharge applied to the surface EG.

In fact, Meyerhof did attempt to express the resultant bearing capacity by the equation:-

$$p = cN_{cq} + \tfrac{1}{2}\gamma BN_{\gamma q} \qquad\qquad \dots\dots 1.5.2.$$

where one term represents the influence of cohesion and the other the influence of weight. The factors $N_{cq}$ (depending on $N_c$ and $N_q$) and $N_q$ (depending on $N\gamma$ and $N_q$) are functions of $\emptyset$, the penetration ratio and the soil-structure properties along the shaft. Equation 1.5.2. gives the base resistance of the foundation and any skin friction along the shaft must be added to obtain the total bearing capacity. The equation may be used for only two special cases. The composite factors both depend on $N_q$ which in turn is governed by the interaction of cohesion and weight. For a general solution, it is only possible to determine $N_{cq}$ and $N_{\gamma q}$ when one or other is zero or may be neglected; $N_{cq}$ can be found for a purely cohesive material when $\emptyset = 0$, and $N_{\gamma q}$ for a purely frictional soil. No solution is possible for a frictional soil with cohesion unless some arbitrary division of $N_q$ is assumed. In other words, the dependence of the bearing capacity factors on the cohesion to weight ratio is hidden in the calculation.

Balla[25] considered the same problem of a deep foundation but recognised that the bearing factors depended on the cohesion to weight ratio in addition to $\emptyset$ and the penetration ratio. The same sliding surface was used to calculate all the $N$ factors and is shown in Fig 1.5.2. He observed that Terzaghi's proposal for two curved failure surfaces to be parallel and coincident with each other at point C is impossible, and opens them out to the correct angle. Unfortunately he retains Terzaghi's small wedge which still leave angle ABC incorrect, and an intersection of four failure planes at point C which is not possible for a rigid Coulomb Material.

9

According to Balla, the failure surface CDE is made up of a circle CD and a straight line DE. It is not possible for a rigid body bounded by a circle and a straight line to move without opening up large cavities along the boundary CDE. Neither is it possible for the circular segment OCD to rotate pushing the triangle ODE upwards without cavities appearing along the line OD.

Another serious criticism is that the theory has been restricted to a maximum penetration ratio of 1.5, without any possibility of an extension to greater depths. This limitation has arisen from the assumption that the plane boundary DE must always make an angle of $\pi/4 - \phi/2$ with the horizontal free surface. This is a valid statement in itself but it has two repercussions: first, that the increasing effect with depth of the foundation side thrust on the base resistance cannot be evaluated and secondly, that it allows for no minor re-orientation of the failure surface. For example, an inflexion in the curved boundary, or a slight angular displacement of the plane shear zone boundary suggested by Meyerhof[16] would satisfy this condition without giving additional complexity to the basic theory. On Balla's rigid interpretation of this condition, the rupture distance must increase rapidly with depth and ultimately tend to infinity.

The analysis is based on Kotter's equations of static equilibrium and the moment referring to the centre of the circular arc is also zero. Even though a surcharge zone is not delineated, it is noted that the final solution is presented in the usual form of a three part additive equation, instead of combining all the forces due to weight in a single N factor (Eqn 1.4.1.).

The N factors according to this theory are markedly different from all previous values. The $N\gamma$ factor is much greater and therefore the breadth of the foundation has more influence on the value of the bearing capacity (Fig 2.10.1). The increase due to depth, however, is much less than in Meyerhof's theory, but the latter is hardly a proper basis for comparison because of the anomalies previously reviewed. Balla also stated that the theory is best applied to granular soils or to those with little cohesion, so that $N_c$ is not of great significance.

## 1.6    Empirical Factors in the Basic Equation

The theoretical analysis may be applied only to the idealised situation of a centrally loaded continuous footing in an idealised material. For more practical problems in real soils, many other effects must be considered by empirical changes to the basic equation.

The influence of soil compressibility and the state of drainage presents an added complication to in-situ testing. In a compressible material, the practical application of any theory calculated for soils at their minimum density will lead to sources of error. Terzaghi[15] overcame this problem by suggesting an empirical reduction in $\tan\phi$ to two thirds of its maximum value, whereas Meyerhof[16] introduced a compressibility factor which varied from $\tan\phi$ for shallow footings to $0.85\tan\phi$ for deep footings. Similar factors were evolved for the influence of ground water conditions but are not of relevance to the present study.

This practice was extended to evaluate other modifying influences such as shape and depth of the foundation and inclination or eccentricity of the load. Denoting the shape factor s, the depth factor by d, and the inclination factor by i, Brinch Hansen[26] generalised Terzaghi's formula by multiplying each term with a set of factors:-

$$p = cN_c s_c d_c i_c + qN_q s_q d_q i_q + \tfrac{1}{2}\gamma BN_\gamma s_\gamma d_\gamma i_\gamma \qquad \ldots\ldots 1.6.1.$$

10

Using the known relationship between Terzaghi's $N_c$ and $N_q$ factors, the number of parameters may be reduced by rearranging equation 1.6.1. in the form:-

$$p = (c + q \tan \emptyset) \; N_c s_c d_c i_c \quad + \quad \tfrac{1}{2}\gamma B N_\gamma s_\gamma d_\gamma i_\gamma \qquad \text{..... 1.6.2.}$$

However, this method of overcoming the limitations of a basic theory, which itself contains many simplifications, can yield some anomalous results. For example, $d_\gamma$ must always be equal to unity because $N_\gamma$ is calculated for $c = O$ in the basic equation, and the inclinations of the load would tend to cause assymmetrical failure instead of the symmetrical failure assumed in the original theory. Thus, both depth and inclination factors must bear no relation to the original theory to be of practical significance.

On the other hand, it is realistic to adopt an empirical shape factor to modify the bearing capacity of a continuous strip footing to that of a rectangle on the basis of similarity of the soil movement. The factor is then only accounting for the end effect; the technique becomes increasingly suspect however, as the strip approaches a square or circle. Conversely, the aspect ratio L/B is important in the selection of the length of footing to represent two dimensional failure in model studies. Skempton[27] investigated the influence of shape for the special case of clay and proposed that:-

$$N_c \; (\text{rectangle}) = \left[1 + 0.2 \frac{B}{L}\right] \; N_c \; (\text{strip})$$

Meyerhof[16] presented his experimental data in the form of a graph and suggested that the combined shape factor is a function of density, $\emptyset$ and the penetration ratio. Brinch Hansen[26] combined these results with Terzaghi's and formulated further shape factors independent of depth. For small aspect ratios, cohesion and surcharge become increasingly more important than the weight of the material:-

$$N_c \; (\text{rectangle}) = \left[1 + (0.2 + \tan^6 \emptyset)\frac{B}{L}\right] N_c \; (\text{strip})$$

$$N_\gamma \; (\text{rectangle}) = \left[1 - 0.5 \; (0.2 + \tan^6 \emptyset)\frac{B}{L}\right] N_\gamma \; (\text{strip}) \qquad \text{..... 1.6.4.}$$

There is ample experimental evidence to corroborate these empirical relations for shape and they are later used to determine the aspect ratio of the footings used in the current tests.

## 1.7     Semi Empirical Analysis

The problems involved in soil failure beneath vehicles are similar in nature to those of civil engineering earthworks but are generally more complex. All the early attempts to solve them have been based on describing the soil by measuring its response to certain simple loading tests. Empirical curve fitting equations were used to describe the experimental results, and these used as a basis of mathematical analysis of the more complicated vehicle situations.

The general pressure sinkage equation, which forms the basis of the current empirical approach is attributed to Bernstein[28] and Letoshnev[29] and is of the form:-

$$p = kz^n \qquad \text{..... 1.7.1.}$$

where p is the pressure beneath the footing. The values of the sinkage modulus k and the exponent n were obtained by plotting experimental pressure sinkage results on logarithmic axes. The exponent was found to be fairly independent of the soil properties, but it was later found that the sinkage modulus was a function of the size and shape of the footing.

In an attempt to improve Bernstein's equation to cover the complete soil range, Bekker[30] proposed that the relationship may be expressed by:-

$$ p = \left\{ \frac{k_c}{B} + k_\emptyset \right\} z^n \qquad \ldots\ldots 1.7.2. $$

where $k_c$ and $k_\emptyset$ are soil constants which may be determined from tests for two different plate sizes. Although $k_c$ is predominant in cohesive soils and $k_\emptyset$ in frictional soils, they are not true soil constants and were still found to vary considerably with plate size and shape.

A more recent change to the pressure sinkage relationship has been suggested by Reece[31]. Influenced by Meyerhof's bearing capacity theory, he proposed the equation in the form:-

$$ p = (c\, k'_c + \tfrac{1}{2}\gamma B\, k'_\emptyset) \left\{ \frac{z}{B} \right\}^n \qquad \ldots\ldots 1.7.3. $$

which is dimensionally more attractive and introduces the various parameters in a more acceptable way. The relationships between Meyerhof's bearing capacity factors (equation 1.5.2.) and the constants in the equation above are given by:-

$$ \left. \begin{array}{l} N_{cq} = k'_c \left\{ \dfrac{z}{B} \right\}^n \\[2ex] N_{\gamma q} = k'_\emptyset \left\{ \dfrac{z}{B} \right\}^n \end{array} \right\} \qquad \ldots\ldots 1.7.4. $$

Equation 1.7.4. links the empirical approach with theoretical soil mechanics and it should be possible to calculate the values of $k'_\emptyset$ and $k'_c$ for compact soils. This is, in fact, the way in which this project originated. Even for loose soils, an equation like 1.7.4. which is based on some theoretical reasoning should be superior to others and a comprehensive series of measurements made by Wills[32] has endorsed this.

1.8    Dimensional Analysis

Dimensional Analysis has also been used to describe the phenomenon of penetration failure by means of a dimensionally correct equation containing selected variables. Although a number of variables in the problem may be reduced by dimensional reasoning, neither the complete solution nor the inner mechanism is revealed.

The most important variables in the problem of penetration failure may be summarised by the following equation:-

$$ p = f\ (\emptyset, \gamma, c, v, d, z) \qquad \ldots\ldots 1.8.1. $$

where v denotes the velocity of penetration and d the characteristic dimension of the probe. With the exception of velocity which may be neglected[33], these parameters have been combined

12

to form almost-every conceivable dimensional group and inverse function, some of which bear little relation to the parallel work in soil mechanics.

In a more realistic study of model analysis for earthmoving equipment Emori and Schuring[34] employed the following functional equation to describe soil deforming processes in general:-

$$p/\gamma d^2 = f(\emptyset, c/\gamma d, v^2/gd) \qquad \dots 1.8.2.$$

For the specific case of penetration failure in a composite soil with both cohesion and friction, it was tentatively suggested that equation 1.8.2. could be written in the form:-

$$p/\gamma B^2 = c/\gamma B. \; f_1(\emptyset) + f_2(\emptyset) \qquad \dots 1.8.3.$$

where the characteristic dimension B denotes the breadth of the footing and $f_1$, and $f_2$ are functions of $\emptyset$. As the comparison of various footing sizes is possible only when there is both geometric similarity and a consistent penetration ratio, it follows that the functions $f_1$ and $f_2$ are also dependent on the aspect ratio, L/B, and the penetration ratio.

The final form of equation 1.8.3. is identical to the current civil engineering approach, but it is no nearer the ultimate solution: the main contribution of the technique lies in its ability to present the complexities of the problem in an organised manner.

## 1.9    Experimental Measurements

The experimental verification of any failure theory in real soils is extremely difficult. The measurement of the soil parameters requires a high degree of accuracy and considerable skill. The soil structure variables, and the variation of the soil parameters with bulk density must also be determined. Osman[35] summarised the results obtained by translational, compressive and torsional methods showing that identical values of cohesion and $\emptyset$ can be measured independently by different methods of testing.

In an attempt to verify the actual shape of the failure zone beneath a foundation, many workers [19, 36-39] have employed a photographic technique through a glass sided tank. No reference in published literature has been found on the effect of soil interface frction and the validity of any photographic analysis is open to question. This problem may be overcome by testing the model in the centre of a tank full of sand mixed with metallic particles. An X-ray technique can then be adopted, but the complexity is a very real deterrent. Alternatively, the sand may be replaced by cylindrical metal or wooden rollers of varying diameters[37]. This, however, diverges from the physical reality of a natural soil. The over-simplified two dimensional mechanism of failure exhibited by the roller model can not yield sufficient corroborative evidence on its own merits alone but it does provide a simple tool for demonstration purposes during the development of the theory. For the additional tests, the most convenient solution is to carefully investigate and minimise the effect of interface friction prior to analysing the experimental data[40].

Both the force measurements and the failure geometry depend on plate size and shape. The influence of aspect ratio in the study of two dimensional failure has already been stressed. Not only is aspect ratio important, but also the breadth of the footing. Dimensional

13

reasoning can no longer be applied, especially in compressible soils, when the plate breadth is small in relation to particle size because lateral compression occurs rather than general shear failure. It has been suggested that the minimum breadth lies between 1 and 1½ in and will increase with compressibility[31]. As this estimate of the minimum breadth was obtained in a soil which was below the maximum bulk density, it is probably on the safe side. Nevertheless, any results obtained for footings of less than 1 inch wide must remain suspect.

The available pressure penetration test data for high aspect ratio footings are surprisingly limited compared with the vast fund of theoretical work. The major part of the available experimental work has been carried out in a dry sand which is a convenient material to use, or in soils with little cohesion. In his paper, Balla[25] has summarised the experimental data for the surface bearing capacity of foundations and presented a comparison between theoretical and test results in the form of a graph. Selig and McKee[41] conducted static loading tests on small footings resting on the soil surface. Meyerhof[16] also presented detailed experimental verification of this theory for deep sinkage over the complete soil range. More recently, test results have been published by Muhs[42], Lebeque[39] and Biarez[37], the latter including skin friction data. However, in many deep loading trials with strip foundations, the effect of skin friction along the shaft is not considered separately. Although much more research on skin resistance is available for piles, the effect of the small aspect ratio is unknown. Unless the exact nature of all the test conditions are fully described, it is not always possible to apply the results.

A similar situation exists in the field of soil vehicle mechanics, and test data for footings of reasonable size and shape in uniform constant soil conditions are not readily available. Only one test in compact sand by Wills[32] may be compared with the present theory for incompressible soils.

Finally, the prediction of the penetration resistance by means of a quasi-static analysis depends on negligible velocity effect. In a study of this phenomenon, Vesic, Banks and Woodward[43] have demonstrated that the minimum bearing capacity of a surface footing in both dry and saturated sand occurs at a penetration velocity of 0.25 in min and is approximately 30% less than that for static loading. Thereafter, the bearing capacity increases again at a slower rate with speed. Haley and Hegedus[33], found that the bearing capacity in saturated sand at a penetration speed of 1750 in min was up to 30% higher than that at 0.6 in min. The apparent drop in bearing capacity at low speed is attributed to an increase in compressibility when particles have insufficient time to reorientate after each new load increment. As speed increases the loading is too rapid for shear failure to occur along the paths of least resistance and punching shear replaces general shear failure. At very high loading rates in saturated sand, apparent cohesion is also developed by the negative pore water pressures. Similar velocity effects were obtained by Goodman[44] from small scale footing tests on clay. It may be concluded, therefore, that the effect of velocity is not insignificant. However, in the vehicle situation where high rates of loading occur, it is justifiable to assume that the penetration resistance is equivalent to the static bearing capacity by neglecting the trough in the curve of load versus speed.

14

# 2. THEORY

Soil Mechanics cannot be a rigid discipline and cannot be treated as an exercise in mathematics because the mathematical properties of soil are so complex. An adequate solution to any problem can be achieved only by a scientific combination of theory and experiment. It has been proposed that nothing less than the following constitutes an adequate basis for a solution.

First, the properties of the idealised soil for the theoretical analysis must be fully stated. This must be followed by a careful description of both the behaviour of such soil and the simplifying assumptions which are necessary to overcome mathematical difficulties. These soil properties and simplifying assumptions must be combined with the normal conditions of equilibrium to determine the shape of the failure surface within the soil. Ideally every part of the soil involved in the failure should be in equilibrium. This may prove impossible, but the departure from the correct equilibrium conditions must be small and must be described quantitatively. Furthermore, the correct stress conditions must exist at every point on the boundaries. Once again, this may not be possible, but divergencies from the ideal must be small, they must be shown to cause only small changes in the final answers and, ideally, they should be shown to represent an approximation to a more accurate but more complex failure pattern. The failure pattern so developed must be verified by carefully controlled experiments on a limited number of soils which cover a large part of the possible soil range. Once the failure pattern has been established, the forces involved can be calculated and a suitable computer programme developed. The results of these force calculations must be experimentally verified over the same wide range of soil types. Finally, generalising equations must be developed to enable the communication of the results of the computer programme in a simple way. The errors involved in this generalisation must also be stated.

The whole of this process of interlocking theoretical and experimental methods is necessary because any single part is subject to such large possibilities of error. It is difficult even to measure the basic soil parameters as they exist in the problem under investigation, far less to apply them in a theoretical analysis, and it is difficult to repeat experiments maintaining the same soil conditions. The process described above would require such a total corroboration of theory and experiment that it would leave little room for doubt that not only were the right answers achieved, but that they were achieved for the right reasons.

## 2.1.  The Basis of Soil Failure Theory

The soil is heavy, and it is assumed to be homogeneous, rigid and incompressible and not to dilate when shearing. It fails according to Coulomb's equation from which it results that lines of incipient failure occur in pairs making an angle of $\pi/2 + \emptyset$ to one another in a plane strain problem. This is an idealisation in that real soil is not quite incompressible or rigid and does dilate slightly as it shears. It will be shown later than an initially homogeneous soil can become completely non-uniform during loading.

When the soil slides along the surface of the loading structure, the stresses at the soil structure interface are assumed to be described by a modification of Coulomb's equation. In this, the cohesion, $c$, is replaced by the adhesion, $c_a$, and the angle of internal shearing resistance, $\emptyset$, by the angle of soil-structure friction, $\varepsilon$. Under these conditions, the soil-structure interface is not a failure plane, and if an interface exists, the correct orientation of the slip planes must be determined from Mohr's circle.

15

The above failure criterion together with known boundary stress conditions are sufficient to make certain rather simple problems statically determinate, and a rigorous solution may be obtained by Static Analysis. Frequently, this technique can be employed in special cases which form the basis of a more general theory, but when the stress boundary conditions cannot be rigorously determined over the entire failure surface, the complete solution of many practical problems requires the adoption of further kinematic assumptions.

In most soil structure problems, the point of failure is represented by the loading at which flow begins. There are certain characteristics of soil flow which are common to the flow of any other incompressible material. The motion will arrange itself so that the energy, lost in the friction generated by the soil flow, is minimised. This requires that the paths of individual particles are as straight as possible and only deviate from straight lines by making the smallest angles of deflection on the largest radii. Soil will not flow along paths with sharp corners except on a plane of symmetry.

The kinematics of soil flow in response to a small movement of the structure can be simplified by defining only two possible types of flow. In the first, large masses of soil move as rigid bodies. It is not possible for soil flow to result in the appearance of large cavities within the soil; this is a common observation which depends on the low strength to weight properties of soil. If the soil does not move as a rigid body, then it is convenient to describe the other type of movement as shearing flow. Zones of shearing flow will generally be bounded by non-circular curves and when the soil exhibits high strength to weight properties, these boundaries need not be sharply defined. A given displacement can be achieved with a minimum energy input by rigid body motion. This is therefore the preferred mode of movement, but may not be possible due to the boundary conditions of the problem.

The static analysis of rigid Coulomb materials leads to the concept of continuous slip line fields. In practice, these are only continuous in zones of shearing flow. The slip line fields are non-existent over the main area in which rigid body motion taken place. The absence of com      lip line fields and the occurrence of rigid body motion is made possible because the s         tly compressible. Definite deformations along the slip surfaces are necessary in ord         lop slip lines and soil failure.

The forces involved in the shearing of soil have two components, one due to the cohesion and internal friction of the soil, and the other due to the weight and the internal friction. In practice, these forces are generated together simultaneously along the same failure plane whose path is dependent on the angle of internal shearing resistance. The relative magnitude of these two components can vary, and the solution should be correct when either is zero. It seems logically justifiable, therefore, to divide the force on the structure into two parts, one part due to the cohesive-frictional soil forces, and the other due to the weight-frictional forces. This simplifies the analysis.

The equilibrium of the soil masses at failure depends on the distribution of the normal and shearing stresses on the straight and circular failure surfaces of the rigid body zones. (This does not include the zones of shearing flow). This distribution is difficult to obtain by rigorous methods. It was originally proposed to assume that the stresses due to cohesive-frictional forces were distributed uniformly along the straight or circular failure surfaces and further to assume that the stresses due to the weight-frict on l forces were distributed in a

16

hydrostatic manner, namely, that they were proportional to the depth, $z_0$, from the nearest part of the free soil surface vertically above the failure plane. These two assumptions are described by the following relationship:

$$\left. \begin{array}{l} \sigma_{\phi c} , \ \tau_{\phi c} \propto k_{\phi c} \\[2ex] \sigma_{\phi \gamma} \propto \tau_{\phi \gamma} \propto k_{\phi \gamma} \quad z_0 \end{array} \right\} \qquad \dots\dots 2.1.1.$$

Along both the failure surface boundaries of any single rigid body zone, the two co-efficients $k_{\phi c}$ and $k_{\phi \gamma}$ were assumed to have constant values which satisfied the condition that the values must be identical at the intersection of the two boundaries. The determination of the two coefficients from the horizontal and vertical equilibrium of the plane shear zone gave the correct relationships for the active and passive Rankine zones. With the introduction of sinkage, an unbalanced couple yielded a source of error.

In the following analysis the relationships are modified by considering rotational equilibrium of the plane shear zone and include a dimensionless exponential term such that:

$$\left. \begin{array}{l} \sigma_{\phi c} \ \propto \ \tau_{\phi c} \ \propto \ k_{\phi c} \propto \left( \dfrac{z_0}{B} \right)^n \\[3ex] \sigma_{\phi \gamma} \ \propto \ \tau_{\phi \gamma} \ \propto \ k_{\phi \gamma} \propto \left( \dfrac{z_0}{B} \right)^n \quad z_0 \end{array} \right\} \qquad \dots\dots 2.1.2.$$

where $-1 < n < 3$. This effectively permits a variable pressure distribution to be used along the failure planes to obtain complete equilibrium. This does not affect the limiting case of the passive Rankine zone or the condition that the values of the coefficients for the two planes must be identical at the point of intersection. It should be noted that these relationships are purely empirical. The basis for their selection is further discussed in Section 2.9. in relation to the overall theory of penetration failure, and the merits of the system may be assessed from the analytical results.

The final solution to a soil structure problem is most valuable if the results can be extended over the full range of soil and structural parameters and presented in a readily usable manner. This is particularly true in the case of soil-machine mechanics where a general picture of performance over a wide range of soil types is required. There are three groups of variables involved in a soil mechan. s problem—the soil and soil to structure properties, the structural shape described by angle. and other ratios of its dimensions and, finally, the size of the structure and the associated soil masses. The complete solution has to be such that an actual problem can be solved by means of a set of graphs or tables and a slide rule.

By considering the cohesive, weight and surcharge terms separately, the complete solution may be presented in the form of an additive equation. Reece[47] has proposed that the most complete form of this equation is:

$$F \ (lb) \ = \ d^2 c N_c \ + \ d^3 \gamma N_\gamma \ + \ d^2 q N_q \ + \ d^2 c_a N_a \qquad \dots\dots 2.1.3.$$

where d represents the characteristic dimension of the structure. This equation may be used to describe the force required to fail soil by any kind of structure whatsoever. The fourth term takes into account the adhesion between the soil and the structure. The N factors are functions

17

not only of $\emptyset$ but also of the soil structure friction and the shape of the structure. It should also be noted that the surcharge term must not be confused with the weight of the soil involved in the soil flow. It will generally refer to some loading on the soil which does not contribute any shearing, for example the loading applied by a smooth surface foundation of some adjacent building.

The additive nature of this equation follows from the addition of the various components of the soil force, and the dimensionless parts are necessary in order to provide dimensional homogeneity. The weakness of this equation is that the N factors are not independent of the values of the dimensionless terms in the equation. The use of the equation will, therefore, involve an error, which can be computed and must be presented in a complete analysis of the problem. Another possibility is to compute the N factors for different proportions of the four sources of force on the structure and it is shown later that this approach is applicable to the case of the penetration resistance for a deep footing.

In a recent analysis of the retaining wall problem[48], which includes surface bearing capacity, the following scheme was adopted:

$$N_\gamma \text{ calculated with } c/\gamma z = q/\gamma z = c_a/\gamma z = 0$$

$$N_c \text{ calculated with } c/\gamma z = 1, q/\gamma z = c_a/\gamma z = 0$$

$$N_a \text{ calculated with } c/\gamma z = c_a/\gamma z = 1, q/\gamma z = 0$$

$$N_q \text{ calculated with } c/\gamma z = 1, c/\gamma z = c_a/\gamma z = 0$$

The $N_\gamma$ and $N_q$ factors are, therefore, correct for a dry sand, whilst the $N_c$ factor is computed for a soil with weight but no adhesion or surcharge. The $N_a$ factor is calculated for a soil with weight and cohesion, which is reasonable since it is not possible to have adhesion without cohesion. The actual value of $c/\gamma z$, $c_a/\gamma z$ and $q/\gamma z = 1$ was chosen for computational simplicity and it was later shown that the errors would not exceed 5% over the complete range of likely combinations of these properties.

Recent work has cast doubt on the necessity for the minimum value postulate in soil mechanics although, initially, tremendous effort was expended in obtaining it for the computation of Terzaghi's and Meyerhof's bearing capacity factors in this programme of research and in the analysis of the retaining wall problem[48]. These minimising methods would seem better based upon the following simple common sense proposition:

If a family of failure surfaces can be found which everywhere satisfy the conditions of equilibrium, the boundary conditions and the idealised soil properties, then the soil will fail on that surface which requires the minimum force.

In fact, such a family of failure surfaces do not exist and, by establishing the only possible failure surface which satisfies these conditions, the minimising procedures are not applicable.

For example, in the retaining wall problem, the correct failure surface may be selected by considering the stress conditions at the interface. For a purely frictional soil with known interface friction, the correct stress conditions for an element of soil adjacent the structure may be determined from Mohr's circle (Fig. 2.1.1.). The orientation of the slip planes at the structure, angles $\theta$ and $\theta'$, may then be deduced. By this means, the correct

18

position of the spiral pole which gives the correct stress conditions on the element at the soil-structure interface and at the passive Rankine zone may be located. It is recognised that the location of the pole by this technique does not eliminate stress discontinuities along the full length of the interface, but by the selection of an element at some point other than at the tip of the wedge, the discontinuities can be minimised. Alternatively, the correct stresses along the full length of the interface may be obtained by interposing a zone of plane shear between the interface and the zone of radial shear (Fig 2.1.2.). This is more applicable to the case of a wedge shaped foundation. In Mintskovsky's analysis[49], for example, this modification does not result in serious deviations from the original criteria assumed for a sliding surface.

A further problem arises with the addition of cohesion and adhesion because the stresses become indeterminate unless a value for the normal stress is assumed (Fig 2.1.3.). Variation of the normal stress in the range, $0.5\gamma z$ to $3\gamma z$, makes little difference to the angle between the soil structure interface and the slip plane. For this reason, an arbitrary value of $\gamma z$ was applied to Mohr's circle in the investigation. The positions of the spiral centre derived from the analysis were compared with those obtained for the minimising procedure in reference 48. The correlation was very good indicating that the minimum value postulate degenerates into a very complicated method of determining the correct stress conditions.

Adopting this technique in the determination of the failure geometry for the surface bearing capacity of a continuous flat footing, the correct stress conditions are satisfied only by locating the pole of the spiral at the corner of the footing. Furthermore, it will be shown in a more detailed investigation of the unrestrained pole (Section 5) that the nature of the bearing capacity calculation is such that it cannot tolerate unrestraint and always tends to adopt a pole close to the corner of the footing regardless of the complexity of the minimising procedures.

## 2.2 Failure Geometry

The soil displaced by a moving structure will always endeavour to minimise the energy lost in flow. It is quite prepared to modify the shape of the structure to make it more streamlined, by arranging a fixed soil body between the structure and the flowing soil. A fixed soil body will form, if the energy losses are reduced by a less angular flow path, by a larger radius of turn or where shearing flow can be replaced by rigid body motion. Its actual shape and size will be determined by the fact that it is made of soil and must satisfy the requirements of the ideal soil properties, the soil structure properties and the conditions of equilibrium. The existence of such a body covering the structure surface will greatly simplify the problem if for no other reason that it eliminates two of the variable (i.e. $\delta = \emptyset$ and $c_a = c$). The determination of the existence and shape of such a body is therefore the starting point for the solution of any problem.

When a continuous footing is forced vertically into a uniform soil under ideal conditions, the flow of the displaced soil must be symmetrical about the vertical axis through the centre of the footing in order to minimise the lateral soil disturbance. As two sharp directional changes in flow are imparted to the soil beneath the structure when it is forced to penetrate, a body of soil attached to the base of the footing could modify the structure shape and reduce the energy losses by providing a less angular flow path if the conditions of equilibrium are fulfilled (Fig 2.2.1.).

The shear stress at any point on the base of a perfectly smooth footing is zero, and the maximum stress must be normal to the base for the footing to penetrate into the soil. Thus, the base of the footing is a major principal plane with lines of incipient failure inclined at angle of $\pi/4 + \emptyset/2$ to the horizontal. As there are no shear stresses on a vertical plane through the axis of the footing due to symmetry, the slip lines are also inclined at angles of $\pi/4 + \emptyset/2$ at this point. Assuming that the body of trapped soil is bounded by straight failure planes, a wedge with sides inclined at angles of $\pi/4 + \emptyset/2$ to the horizontal is formed beneath the footing (Fig 2.2.1b.). Due to lateral constraint of the soil forces, it remains permanently in a state of elastic equilibrium and is unaltered by sinkage. There is no reason to suppose that curved flow lines, requiring at least one point of inflexion to join the points of known stress, could replace the straight lines. This would not only yield more abrupt changes in flow but also impart a rather peculiar slip line field to the adjoining soil mass (Fig. 2.1.1c.). On the same grounds, two wedges, moving laterally, are also inferior because the flow path must then revert to one with sharply angular changes in direction (Fig 2.2.1d.).

If the base of the footing is rough, shear stresses of unknown magnitude and distribution could be mobilised. However, if the wedge is generated and is in equilibrium beneath a perfectly smooth footing without the development of any shear stresses, it is not conceivable that base roughness would in any way influence the shape of the fixed soil body. There is no need for shear stresses to be developed along the base, and there is no way of mobilising them with symmetrical loading under ideal conditions. The base of the structure is no longer important and is replaced by the two soil boundaries of the wedge both of which are failure planes. The directions of the other families of slip lines are known from the conditions of stress at the wedge tip and must emanate at angles of $\pi/2 + \emptyset$ to the wedge boundaries. As the geometry is symmetrical about the central axis of the footing, the failure surface on only one side is subsequently considered.

The particular case when sinkage in zero and the footing smooth is capable of rigorous solution by the method of Static Analysis, and this can be used as the starting point in the development of the failure pattern. Fig 1.2.4a. shows Sokolovski's[1] solution for a foundation obliged to fail on one side only. The zone BDE is always straight sided (Rankine) as long as the surcharge is vertical. The zone ABC is doubly curved but as long as AB is smooth, angles CAB and ABC must always be $\pi/4 + \emptyset/2$. Angle ACB is $\pi/2 - \emptyset$ under any circumstances. Although the case of symmetrical failure was not considered, it is not difficult to see that symmetry requires that C shall lie below the mid point of AB, and the angular requirements, mentioned above, force ABC to become straight sided. The curved fan BCD then becomes a radial shear zone bounded by a logarithmic spiral and the total failure pattern is shown in Fig 2.2.2. This conclusion is confirmed by Josselin de Jong[4]. The wedge is the same shape as had been deduced already.

For the more general case of shallow and deep foundations, there must be a logical transition from the failure geometry of the limiting surface case. There are two possible modifications which can be made to the failure geometry to account for sinkage. First the shape and extent of the radial shear zone may remain unaltered, and the boundary DE of the plane shear zone may be produced to meet the surface at the correct angle of $\pi/4 - \emptyset/2$ (Fig 2.2.3.). This configuration is obviously possible at very small sinkages and has much to commend it. For instance, the correct stresses are attained along the free surface and along the smooth foundation shaft, and the boundary conditions are nowhere violated.

20

It does not apply to a footing because there is no shaft support to cause the passive pressure. It does not even apply to a foundation because it has been shown by experiment that pressing the footing down does not cause the soil to exert full passive pressure against the walls. Also, the rupture distance, GE, does not increase linearly with depth, and consequently this type of failure may be rejected. Alternatively, the zone of shearing flow may be extended in conjunction with a change in the shape of the plane shear zone (Fig 2.2.4a.). The rupture plane, BD, is the last radial slip line of the radial shear zone BCD. The plane shear zone BDEG is delineated on two sides by a pair of failure surfaces, BD snd DE, making an angle of $\pi/2 + \emptyset$ with each other. The boundary, DE, no longer satisfies the stress conditions at the surface but this requirement can be fulfilled without adding complexity to the failure geometry, by a minor re-orientation of the slip plane, DE'.

The failure surface, CDE, in Fig 2.2.4a. is bounded by a logarithmic spiral and a straight line. In a dilating material, it would probably be bounded by curves such as are shown by dotted line CDE. The choice of the dimensions of BCDEG by means of the Coulomb criterion and static equilibrium ensures that the surface is little different from the real one; the approximation being used to simplify the mathematics involved.

The failure geometry can be extended logically to deep foundations by further extension of the radial shear zone. The limiting case depends on the nature of the support and the interface properties along the foundation shaft and on the soil properties. In very strong cohesive soils, where the influence of soil weight may be neglected and the foundation shaft is unsupported, it is assumed that the failure pattern proposed by Jaky[8] occurs (Fig 1.3.2.). For any other cohesive-frictional soil where weight is important, this type of failure is largely discounted. It is more likely that the mode of failure reaches the limit shown in Fig 2.2.4b., then changes to that described by Vesic[51] at deep sinkage when the mass of soil affected by the penetration of the footing becomes sufficiently great to 'absorb' the displaced soil by soil compaction (Fig 2.2.5.). Vesic has suggested the possible upper limit for general shear failure in sand occurs when the skin resistance distribution changes from hydrostatic to uniform. The critical penetration ratio is dependent on density and $\emptyset$. The importance of this change in the mode of failure only becomes significant in the present study of incompressible soils when $\emptyset$ is small. It is important to note, however, that the effect of soil compressibility on the mode of failure even in the highly frictional materials tested is to reduce the penetration ratio at which this changeover occurs.

As the pressure exerted on the foundation shaft constitutes one of the unknown parameters, the problem is simplified by assuming that the vertical wall BG is self-supporting and represents a free surface. From practical observations, this is quite justifiable over most of the soil range to depths in excess of those investigated. It is also particularly relevant to vehicle running gear. One major exception, however, is a dry frictional material. It is proposed therefore, to develop a theory of penetration failure on the following basis:

a.   Dry frictional material—to include the effect of the shaft support or of material falling into the shaft, forming a soil to soil boundary at the central axis of the footing.

b.   Cohesive-frictional material—to assume the shaft is unsupported, but to make provision for further extension to a supported shaft.

The maximum height of the unsupported shaft for a cohesive-frictional soil may be evaluated, approximately, by considering the stability of a vertical bank. It can be shown that the critical height, $H_c$, is given by the equation:

$$H_c = 4(c/\gamma) \tan (45 + \emptyset/2) \qquad \ldots\ldots 2.2.1.$$

and by substituting values for the soil density and $\emptyset$ of 0.06 lb in$^{-3}$ and 40° respectively, a 42 in high bank is stabilised when the cohesion is 0.03 lb in$^{-2}$. This height of bank is equivalent to a penetration ratio of 3 for a 14 in wide vehicle track and represents the upper limit of sinkage; for different values of the parameters the value of $H_c$ is given in Fig 2.2.6.

The zone BDEG will tend to behave as a solid body (Fig 2.2.4a.). Of the two failure boundaries, one must form the last radial slip line of the radial shear zone and therefore must emanate from the corner of the footing; the other must make an angle of $\pi/2 + \emptyset$ to it and be a tangent to the curved slip line, thus forming the continuous outer boundary of the failure surface. These two plane failure surfaces need not be of the same length. From the conditions of equilibrium there is an infinite number of possible configurations for the zone which are a function of the sinkage and the soil parameters. Only one geometrical shape fulfills the condition that the junction of the two failure surfaces must lie on the spiral surface which then determines the failure geometry for the particular parameters which have been selected. As the determination of the failure geometry depends on the equations of equilibrium, it is fully covered in the next sub-section.

Summarising the important aspects of the failure geometry, it is truly symmetrical about the central axis of the footing and consists of only one figure of rupture for a soil with both weight and cohesion. It comprises three different zone types:

a. The fixed soil body is a single wedge with base angle of $\pi/4 + \emptyset/2$ regardless of base roughness.

b. The zone of shearing flow is formed of a family of radii and logarithmic spirals whose pole lies at the corner of the footing.

c. The plane shear zone is bounded by one free surface, the vertical wall of the shaft, and two failure surfaces. These surfaces make an angle of $\pi/2 + \emptyset$ with each other and one determines the extent of the zone of shearing flow. The shape and extent of the plane shear zone is obtained from the conditions of equilibrium.

The outer boundary is a smooth curve to satisfy the flow criterion. The size of the failure geometry is determined by $\emptyset$, the penetration ratio, the cohesion to weight ratio and the shaft parameters.

## 2.3. The Calculation of Penetration Resistance

The calculation of the penetration resistance of a continuous footing may be considered in three parts. First, the figure of rupture is obtained by considering the equilibrium of the straight sided zone. The magnitude and direction of the soil forces due to the weight of the soil mass within the failure zone, and those acting on the boundaries are determined. Finally, knowing the directions of the resultant forces, the penetration resistance is evaluated. The general procedure, assumptions and approximations are discussed in the following sections and the complete theoretical analysis is given in the appendix.

22

It is assumed that, for static equilibrium in a cohesionless soil, the weight, $W_1$, of the plane shear zone BDEG is balanced by two weight-frictional boundary forces $F_{\gamma 1}$ and $F_{\gamma 2}$ on any pair of failure planes, ED and DB respectively and by a shaft force $F_{\gamma s}$, on BG (Fig 2.3.1.). The weight acts vertically downwards the boundary forces act at $\emptyset$ to the normal of the plane and the shaft force acts at an angle $\delta$ to the normal. The two boundary forces are governed by the same boundary coefficient of earth pressure, $k_{\emptyset \gamma}$ modified in accordance with equation 2.1.1. and the normal stresses are distributed in a way which diverges slightly from the hydrostatic manner. The shaft force is governed by the coefficient of earth pressure $k_{\gamma s}$ which is assumed to have a known value and by a hydrostatic stress distribution. Considering any line, BD, sloping at an angle, $\zeta$, to the horizontal, the three equations for horizontal, vertical and rotational equilibrium are respectively:

$$F_{\gamma 1} \cos \zeta - F_{\gamma 2} \sin (\emptyset - \zeta) = F_{\gamma s} \cos \delta \qquad \text{..... 2.3.1.}$$

$$F_{\gamma 2} \cos (\emptyset - \zeta) - F_1 \sin \zeta = W_1 + F_{\gamma s} \sin \delta \qquad \text{..... 2.3.2.}$$

$$W_1 d_1 - F_{\gamma 1} d_3 - F_{\gamma 2} d_4 + F_{\gamma s} d_5 = 0 \qquad \text{..... 2.3.3.}$$

In simple terms, there are three unknowns, the boundary coefficient, the boundary exponent and the slope angle. These are functions of the angles of internal and interface friction, the shaft coefficient of earth pressure and the penetration ratio. However, the relationships are extremely complex because of the exponential terms, and the equations can be solved only be substitution. The equations are written in general terms so that the slope angle can take any value in the range $- (45 - \emptyset/2) < \zeta \leqslant 90$ when the sinkage is greater th than zero. In other words, the extent of the logarithmic spiral zone may vary from the surface condition up to the full extent where it breaks into the foundation shaft. Normally, however, the calculations are terminated when the value of the slope angle reaches $\emptyset$, so that the failure geometry for the limiting case is that shown in Fig 2.2.4b.

When cohesion is added, six further forces must be considered in the equations of equilibrium. First, there are the cohesive forces, $C_1$ and $C_2$, acting along the boundaries DE and BD, respectively, and the adhesive force along the shaft, $C_s$. The magnitude of these forces depend on the length of the relative surfaces and the soil or interface properties. The cohesive-frictional boundary forces, $F_{c1}$ and $F_{c2}$, act at $\emptyset$ to the normal of the planes DE and BD, and the cohesive-frictional shaft force, $F_{cs}$, acts at angle $\delta$ to the normal.

The two cohesive-frictional boundary forces are governed by the same boundary coefficient of earth pressure $k_{\emptyset c}$ (modified in accordance with equation 2.1.2.) and the forces are distributed in a way which diverges slightly from a uniform manner. The cohesive-frictional shaft force is governed by the shaft coefficient of earth pressure, $k_{cs}$ of known value and the force is uniformly distributed. Including these forces in the equations of horizontal, vertical and rotational equilibrium, the complete relationships are:

$$F_{\gamma 1} \cos \zeta - F_{\gamma 2} \sin (\emptyset - \zeta) + F_{c1} \sin (\emptyset - \zeta) =$$
$$F_{\gamma s} \cos \delta + F_{cs} \cos \delta + C_2 \cos \zeta - C_1 \sin (\emptyset - \zeta) \qquad \text{..... 2.3.4.}$$

$$F_{\gamma 2} \cos (\emptyset - \zeta) - F_{\gamma 1} \sin \zeta + F_{c2} \cos (\emptyset - \zeta) - F_{c1} \sin \zeta =$$
$$W_1 + F_{\gamma s} \sin \delta + F_{cs} \sin \delta + C_s + C_1 \cos (\emptyset - \zeta) - C_2 \sin \zeta \qquad \text{..... 2.3.5.}$$

$$W_1 d_1 - F_{\gamma 1} d_3 - F_{\gamma 2} d_4 + F_{\gamma s} d_5 + C_1 d_7 - F_{c1} d_8 - F_{c2} d_9 + F_{cs} d_{10} = 0 \qquad \text{..... 2.3.6.}$$

For this general case, there are four unknowns — the weight-frictional and cohesive-frictional boundary coefficients of earth pressure, the boundary exponent and the slope angle. These depend on three further input parameters, the cohesive-frictional shaft coefficient of earth pressure, the cohesion to weight ratio and the adhesion to weight ratio, in addition to those already listed for a cohesionless material. The parametric complexity may be greatly simplified by considering an unsupported foundation. It avoids the problem of assessing independent coefficients of earth pressure for the weight-frictional and cohesive-frictional shaft forces and it allows the interaction between the remaining variable to be presented more simply in graphical form.

One difficulty remains. In order to determine the four unknowns, a fourth equation must be developed to relate the two boundary coefficients. Alternatively, three of the unknowns may be obtained in terms of the slope angle and the final solution minimised with respect to $\zeta$. The latter course was rejected because of the excessive amount of computation which would be required. The following relationship is adopted to relate the two boundary coefficients:

$$k_{\emptyset c} = (k_{\emptyset \gamma})^{\frac{1}{2}} \qquad\qquad \ldots 2.3.7.$$

This relationship is correct for the surface case and has, therefore, some theoretical basis. When the penetration ratio is greater than zero, the relationship becomes more of an empirical weighting factor because the two coefficients are dependent on the cohesion to weight ratio. It is shown in the appendix that $k_{\emptyset c} = 1$ for a cohesive soil without weight. Hence, the greatest source of error in the value of weight-frictional boundary coefficient occurs in strong cohesive soils where its influence is minimal. Similarly, the greatest source of error in the value of the cohesive-frictional boundary coefficient occurs when the cohesion is small, so that this basis of the analysis does not represent an excessive approximation.

The value of the slope angle, determined from the solution of equation 2.3.4. to 2.3.7. inclusive, fixes the shape of the failure geometry. The soil weight and the soil boundary forces may be determined as shown in the appendix. The weight-frictional, cohesive-frictional and cohesive forces on the plane BD are ignored in the calculation of the resultant forces because they are internal soil forces. Thus the resultant weight-frictional force acting at $\emptyset$ to the normal of the wedge boundary, BC, is dependent on the weight of the soil within the failure zone, BCDEG, and on the weight-frictional forces acting on the boundary, CDE. Similarly the resultant cohesive-frictional force acting at $\emptyset$ to the normal of the wedge boundary, BC, is dependent on the cohesive-frictional forces and the cohesive forces acting along the side of the wedge, BC. The distribution of the resultant forces is in accordance with equation 2.1.1.

The weight-frictional and cohesive-frictional forces along the spiral boundary CD, are difficult to determine. As these forces pass through the pole of the spiral they may be eliminated from the calculation by taking moments about that point. The resultant forces are given by the expressions:

$$F_\gamma = \left( W_1 . d_1 + W . d_2 - F_{\gamma 1} . d_3 \right) / d_6 \qquad\qquad \ldots 2.3.8.$$

$$F_c = \left( C_1 . d_7 - F_{c1} . d_8 + M_c \right) / d_{11} \qquad\qquad \ldots 2.3.9.$$

24

Where the foundation shaft is supported additional terms must be added to the numerators of equations 2.3.8. and 2.3.9. (c.f. Appendix A).

Resolving, vertically, forces $F_\gamma$, $F_c$ and the 'adhesion' force, $C_3$ (all of which act on the two boundaries of the wedge, AB and BC) and considering the weight of the wedge, ABC, the resultant penetration resistance of the foundation is obtained:

$$F \text{ lb in}^{-1} = 2F_\gamma \cos(\psi - \emptyset) - \tfrac{1}{2}\gamma B^2 \tan\psi + 2F_c \cos(\psi - \emptyset) + 2C_3 \sin\psi$$

$$\ldots\ldots 2.3.10.$$

This expression can be written in the form of a two part additive equation:

$$p \text{ lb in}^{-2} = \tfrac{1}{2}\gamma BN_\gamma + cN_c \qquad \ldots\ldots 2.3.11.$$

where:

$$N_\gamma = 2F_\gamma \cos(\psi - \emptyset)/(\tfrac{1}{2}\gamma B^2) - \tan\psi \qquad \ldots\ldots 2.3.12.$$

$$N_c = 2\left[F_c \cos(\psi - \emptyset) + C_3 \sin\psi\right]/(cB) \qquad \ldots\ldots 2.3.13.$$

The dimensionless factors, $N_\gamma$ and $N_c$, are dependent on $\emptyset$, the penetration and cohesion to weight ratios. The implication of the two ratios is derived from the equilibrium of the plane shear zone, and for a buried footing there is no surcharge term. Any real surcharge on the soil surface can be considered separately.

When the foundation shaft is supported, equation 2.3.11. represents the base penetration resistance and the dimensionless factors are further dependent on the shaft parameters. The total penetration resistance is the summation of the base penetration resistance and the surface traction on the foundation shaft.

## 2.4. Computer Programme

The computer programme is divided into three sections, namely for a cohesionless soil, a cohesive soil without weight and a cohesive soil with weight. Additional procedures are required for certain individual cases such as when either $\emptyset$, or the sinkage or the slope angle is zero. The complete block diagram is shown in Fig 2.4.1.

The soil parameters $(\emptyset, \gamma, c)$, the soil structure parameters $(\delta, c_a, k_{\gamma s}, k_{cs})$ and the structure parameters $(B, z)$ are stated on the input data and are thereafter available throughout the programme.

The failure geometry is determined first. The three transcendental equations of equilibrium, which are functions of the boundary coefficient, the boundary exponent and the slope angle are solved by substitution. The range of the slope angle $-(45 - \emptyset/2) < \zeta < \emptyset$ is divided into an arbitrary number of 20 steps. For each value of the slope angle the value of the boundary coefficient, the boundary exponent and the difference or error between the L.H.S. and R.H.S. of the equation of rotational equilibrium are determined. When two values of the slope angle have been selected such that the error is zero within the interval, the

25

correct solution for the slope angle is obtained by an iterative process. The range is bisected and, after each cycle, the section not containing the solution is discarded until the final answer is achieved with a prescribed accuracy of $0.5 \times 10^{-6}$ after about twenty iterations

In the case of a cohesive soil with weight the same procedure is used to determine the value of the boundary exponent by substitution for each value of the slope angle. This additional complexity is not required for the limiting values of the cohesion to weight ratio.

Once the failure geometry has been determined, the final calculation of the soil forces and the penetration resistance is straightforward. No minimising techniques are included in the final form of the programme. However, provision was made in earlier work for investigating the effect of unrestrained spiral pole and of a variable wedge angle on the penetration resistance using simplex[52] (c.f. Section 5.).

## 2.5. Computed Results for a Dry Friction Material with Weight

The dimensionless $N_\gamma$ factors for three values of the shaft coefficient of earth pressure are shown in Figs 2.5.1. - 2.5.3. The $N_\gamma$ factor for each value of the shaft coefficient is completely represented by two families of curves, one for the perfectly smooth shaft interface ($\delta = \emptyset$) and the other for a perfectly rough shaft interface ($\delta = 0$). The data in Fig 2.5.1. is included because the value of unity is commonly selected for the shaft coefficient to provide a rapid solution to practical problems. The additional data in Figs 2.5.2. and 2.5.3. provide the necessary interpolation material for intermediate values of the shaft coefficient.

The presence of interface friction is shown to increase the base penetration resistance of the foundation in proportion to the downward thrust acting on the radial boundary of the zone of shearing flow. The magnitude of this effect is also dependent on the shaft coefficient which may take any value between the coefficient of active earth pressure, $k_a$, and the coefficient of passive earth pressure $k_p$. In practice, however, it is statically impossible to obtain a solution for a perfectly rough interface using the maximum value of the shaft coefficient because soil failure would occur by lateral compression instead of by vertical compression. Hence, the shaft coefficient was restricted in value to two-thirds of that for the coefficient of passive earth pressure. Increasing the value of the shaft coefficient up to this limit increases the base penetration resistance. For the smooth shaft interface, however, increasing the value of the shaft coefficient results in a decrease in the base penetration resistance. This occurs because the horizontal shaft force generates a less than hydrostatic stress distribution on the boundaries of the plane shear zone and effectively increases the anti-clockwise moment of the boundary force, $F_{\gamma 1}$. This condition would not normally be achieved because it is unlikely that the interface friction would be zero except when the shaft coefficient was at its minimum value.

The rupture distance for the three values of the shaft coefficient are shown un Figs 2.5.4. to 2.5.6. As the rupture distance is proportional to the breadth of the footing, the dimensionless ration is f/B where f is the horizontal distance between the edge of the foundation shaft and the point at which the failure plane breaks out at the soil surface. The effect of increasing either the angle of interface friction or the shaft coefficient is to increase the rupture distance because it depresses the slope angle of the radial boundary. When the shaft is smooth, the failure geometry tends towards the statically correct stress field for the limiting condition in which full passive earth pressure is developed on the shaft.

26

## 2.6. Computed Results for a Frictional-Cohesive Material without Weight

The values of $N_c$ for a weightless soil are shown in Fig 2.5.7. In the absence of weight, the shear bulb can be formed around the base of the foundation. Thus, the bearing capacity reaches a constant value which is independent of any further sinkage. This explains why the curves for $N_c$ have a rather unusual form.

The rupture distances fall to zero when the shear bulb is fully formed (Fig 2.5.8.). Thereafter, the rupture distance f is taken as the vertical distance between the base of the footing and the point at which the boundary of the shear bulb breaks into the vertical shaft of the foundation.

## 2.7. Computed Results for a Frictional-Cohesive Material with Weight

The $N_\gamma$ factors, $N_c$ factors and rupture distances for the intermediate $c/\gamma B$ ratios are presented for three different shaft conditions. The relevant data for the unsupported shaft are shown in Figs 2.7.1. to 2.7.3.; those for a perfectly rough shaft $(\delta = c_a = 0)$ are presented in Figs 2.7.4. to 2.7.6. and those for a perfectly rough shaft $(\delta = \emptyset, c_a = c)$ are given in Figs 2.7.7. to 2.7.9. The calculation of the dimensionless groups for the foundation with smooth and rough shafts were based on an arbitrarily chosen value of the shaft coefficients $k_{\gamma s}$ and $k_{cs}$ of unity.

The $N_\gamma$ factors follow the expected pattern. For the smooth shaft, the curves for $c/\gamma B = 0.1$ are very similar to those for $c/\gamma B = 0$, with the curves for the unsupported shaft and the rough shaft lower and higher, respectively. The general effect of increasing the $c/\gamma B$ ratio is to increase the value of the $N_\gamma$ factor until such time as equilibrium can no longer be achieved, and the curves tend very rapidly to zero.

The $N_c$ factors show comparable trends. For the unsupported shaft the curves for $c/\gamma B = 100$ are very similar to those for $c/\gamma B = \infty$. As the $c/\gamma B$ ratio decreases for all shaft conditions, the curves for the $N_c$ factors exhibit either an initial reduction in gradient or a negative gradient with increasing penetration ratio. This becomes more pronounced at the higher values of $\emptyset$. Although this effect may be explained in the case of the unsupported foundation shaft as the negative cohesive force required to replace the lateral support of the shaft, the continued presence of the phenomenon when the shaft is supported would appear to be due to the inflexible coupling between the weight-frictional and cohesive-frictional boundary coefficients.

The variation of the rupture distances for the intermediate $c/\gamma B$ ratios is a reflection of the changes in N factors with a gradual reduction between the limits of those for a cohesionless soil and those for a weightless soil when the shaft is unsupported. More significant changes occur for the different shaft conditions. The influence of shaft support, which is augmented by the presence of shaft traction is to increase the rupture distance by depressing the slope angle of the radial boundary of the zone of shearing flow.

## 2.8. Interpolation

Since $\emptyset$ is represented by a family of curves increasing in steps of $5°$, the main interpolation is required to cover the N factors at intermediate values of $\emptyset$. Interpolation is also required for the influence of the shaft parameters each of which is accounted for at only

27

a few specified values. Interpolation has not been attempted for the data presented in section 2.7. because of the larger number of variables and because of the complexity of the interaction between the various parameters.

For any given penetration ratio, the variation of $N (N_\gamma$ or $Nc)$ with $\emptyset$ can be expressed with considerable accuracy by:

$$N = u \; e^{\; v \tan \emptyset} \qquad \qquad \text{..... 2.8.1.}$$

where $u$ and $v$ are constants dependent on the penetration ratio. For small values of $\emptyset$ radians, $\tan \emptyset = \emptyset$ (the error of such an approximation being only 0.2% for $\emptyset = \pm 5°$). Hence, in the $5°$ intervals it follows that:

$$N = u \; e^{\; v \emptyset} \qquad \qquad \text{.... 2.8.2.}$$

Since the ordinates in the N factor graphs are logarithmic scales, a linear interpolations between the $5°$ curves yields intermediate values of N to a high degree of accuracy. The intermediate values of the rupture distance may be obtained in a similar manner.

For the calculation of the $N_\gamma$ factors at intermediate values of $\delta$, the angle of interface friction is considered as a fraction of the angle of internal friction and this ratio varies from zero for a smooth shaft to unity for a perfectly rough one. The variation of the $N_\gamma$ factor with the $\delta/\emptyset$ ratio is substantially linear (Fig 2.8.1.). The following relationships can thus be established:

$$N_{\gamma\delta} = N_{\gamma o} \left[ \frac{N_{\gamma\emptyset}}{N_{\gamma o}} \right]^{\delta/\emptyset} \qquad \qquad \text{..... 2.8.3.}$$

where $N_{\gamma\delta}$ is the required value of $N_\gamma$ and $N_{\gamma o}$ and $N_{\gamma\emptyset}$ are the corresponding values of $N_\gamma$ at $\delta = \emptyset$, respectively. A similar form of equation 2.9.3. may be derived for the intermediate values of the f/B ratio which exhibit the same trend with respect to the $\delta/\emptyset$ ratio (Fig 2.8.2.).

The $N_\gamma$ factor is also shown to exhibit a linear relationship with variation of the shaft coefficient except at the lower values of $\emptyset$ which are not directly applicable to a cohesionless soil (Fig. 2.8.3.). The form of the interpolation equation is identical to that for the $\delta/\emptyset$ ratio.

$$N_{\gamma s} = N_{\gamma a} \left[ N_{\gamma p}/N_{\gamma a} \right]^{(k_{\gamma s} - k_a)/(k_p - k_a)} \qquad \qquad \text{..... 2.8.4.}$$

where $N_{\gamma s}$ is required value of $N_\gamma$ and $N_{\gamma a}$ and $N_{\gamma p}$ are th    corresponding values of $N_\gamma$ for the minimum and maximum values of the shaft coefficient of earth pressure. This is also applicable to the f/B ratio (Fig 2.8.4.).

28

The application of the interpolation procedures is presented in some detail for the following soil and structural properties.

Soil Properties: $\emptyset$ = 40.5 , $\gamma$ = 0.06 lb in$^{-3}$

Soil-structure interface variables: $\delta$ = 32°, $k_{\gamma s}$ = 1.23

Structural parameters: B = 2 in, z = 6 in

The relevant values of $N_\gamma$ factor may be obtained by three successive interpolation for $k_{\gamma s}$, $\delta$ and lastly for $\emptyset$. Interpolation for the shaft coefficient must be considered first because the limiting values of the shaft coefficient are not the same for the rough and smooth shaft conditions. Improved accuracy can also be achieved by interpolating for a shaft coefficient of 1.23 between the value of unity and the upper limiting value rather than between the value of the coefficient of active earth pressure and the upper limiting value. The eight initial values of $N_\gamma$ are obtained from Figs 2.5.1. and 2.5.3. and listed in Table 1. together with the interpolated $N_\gamma$ values at each successive step.

## TABLE 1

### INTERPOLATED $N_\gamma$ FACTORS

| | Initial Values | | | Interpolated Values | | |
|---|---|---|---|---|---|---|
| $\emptyset$ | $\delta$ | $k_{\gamma s}$ | $N_\gamma$ | $N_\gamma$ ($k_{\gamma s}$ = 1.23) | $N_\gamma$ ($k_{\gamma s}$ = 1.23) ($\delta$ = 32) | $N_\gamma$ ($k_{\gamma s}$ = 1.23) ($\delta$ = 32) ($\emptyset$ = 40.5) |
| 40 | 0 | 1.0 | 630 ) | | | |
| 40 | 0 | 4.598 | 508 ) | 621 ) | | |
| 40 | 40 | 1.0 | 700 ) | | 690 ) | |
| 40 | 40 | 2.2 | 755 ) | 710 ) | | |
| 45 | 0 | 1.0 | 1380 ) | | | 745 |
| 45 | 0 | 5.829 | 1180 ) | 1370 ) | | |
| 45 | 45 | 1.0 | 1530 ) | | 1499 ) | |
| 45 | 45 | 3.0 | 1740 ) | 1552 ) | | |

The difference between the interpolated $N_\gamma$ factor of 745 and the computed $N_\gamma$ factor of 736 represents an error of approximately 1%.

One of the problems encountered in predicting the penetration resistance for a footing is that the shaft parameters are indeterminate. In the absence of any vertical restraint, the sand falls into the shaft and forms a vertical sand to sand barrier along the axis of the footing. As the sand in this region is completely disturbed, it must be at the minimum density. It may be assumed, therefore, that the material is close to the active state. The value of the angle of interface friction probably lies between zero and the value of $\emptyset$ at minimum density. Similarly, the value of the shaft coefficient of earth pressure is probably between the active value and unity.

It is proposed, therefore, that adequate accuracy may be achieved from the $N\gamma$ values for a shaft coefficient of unity interpolated for the value of the angle of interface friction equal to the value of $\emptyset$ at minimum density.

## 2.9.   Inherent Errors

Some penalty must be paid in fulfilling the requirements of rotational equilibrium. This penalty, resulting in some inherent errors in the calculation, may be assessed from the variation of the values of the coefficients of earth pressure and the stress distribution along the sides of the wedge and along the plane shear zone boundaries. For simplicity, the errors for a cohesionless soil and for a cohesive soil are analysed sequentially.

From the initial assumption that the wedge boundary is straight, it is logical to adopt the hydrostatic distribution for the normal stresses dependent on the weight of the displaced material. As sinkage increases, the centre of pressure for the weight-frictional component rapidly moves towards the mid-point of the wedge boundary (Fig 2.9.1.). The effective movement of the centre of pressure is exhibited in the $N\gamma$ curves whose gradient increases with penetration ratio. The assumed stress distribution on the wedge boundary suffers from two known sources of error, particularly at the deeper sinkages. First, the material has inherent frictional properties, whereas hydrostatics is applicable to frictionless media. Secondly, the stress distribution assumed for the wedge boundary differs from that for the pair of failure planes. In both cases, however, the error is minimised because the total length of the wedge boundary is small in relation to the total depth at which the discrepancies between the stress distributions become significant.

The same hydrostatic distribution is used for the weight-frictional stresses on the foundation shaft. This seems adequately justified by the experimental data [37,50] on the variation of skin resistance with foundation depth up to a penetration ratio of 10 in compact soil.

Using a hydrostatic distribution on the shaft makes it impossible to use the same distribution on the two failure boundaries of the plane shear zone unless $\emptyset = 0$. The introduction of an exponent to vary the pressure distribution along these two boundaries satisfies the equations of equilibrium. However, the curved distribution could not occur along a straight failure boundary and it is reasonable to assume that this failure geometry is an approximation to the curved boundaries shown in Fig 2.2.4a.

The rather nebulous errors involved in the determination of the boundary conditions for the plane shear zone are best assessed from a study of the calculated values of the boundary coefficient, the boundary exponent and the slope angle, and an understanding of the complex mechanism for achieving equilibrium. The respective values of these parameters over a range of $\emptyset$ are plotted for an arbitrary value of the shaft coefficient of unity when the shaft is perfectly smooth and perfectly rough (Figs 2.9.2. to 2.9.5.). The equilibrium mechanism may

30

be considered in two parts: first, for a constant slope angle and varying pressure distribution, and secondly for the opposite case. Taking a specific value of the penetration ratio, the shaft force is constant for any given set of shaft parameters. In the first case, the magnitude and and direction of the force due to the internal weight of the soil mass remain constant and the directions of the boundary forces are defined by the slope angle. Under these restraints, the magnitudes and lines of action of the boundary forces are also defined. They may be achieved by either increasing the value of the boundary coefficient and decreasing the value of the exponent or vice versa. The stress distribution for the former case is more uniform and that for the latter increases rapidly with depth. In general terms, the uniform distribution applies to a smooth shaft and other to a rough shaft. In the second case, the slope angle not only controls the direction of the boundary forces but also the internal weight of the plane shear zone and its centre of gravity. Depressing the slope angle causes the boundary forces to move towards the intersection of the planes and alters the relative lengths of the two boundaries. This, in turn, increases the internal weight of the zone and changes the position of the centre of gravity such that the stresses on the outer plane boundary are increased. Basically, depression of the slope angle provides a larger horizontal component of the weight-frictional forces acting on the outer boundary of the plane shear zone and explains why this process is involved when full passive pressure is assumed to act on a perfectly smooth shaft.

In soils with cohesion, the boundary coefficient and exponent additionally control (in modified form) the divergence of the cohesive-frictional stress distribution on the plane shear zone boundaries from that described as uniform along the shaft and wedge boundaries so that equilibrium conditions may be satisfied. The variation of both the boundary coefficient and exponent with the penetration ratio is shown in Figs 2.9.6. and 2.9.7. for various shaft conditions and $c/\gamma B$ ratios. The effect of increasing the $c/\gamma B$ ratio is to reduce the value of the boundary coefficient and to increase the value of the exponent. For both the unsupported shaft and the smooth shaft, the value of the coefficient tends towards unity and that of the exponent towards zero. In the case of the rough shaft, the equilibrium condition is more difficult to achieve because of the shaft traction which is generated by the adhesive forces in addition to the 'vertical' components of the frictional forces on the shaft. The large shift in stress distribution on the boundaries of the plane shear zone may be achieved only by high values of the exponent which in turn governs low values of the coefficient. This explains why equilibrium was not achieved when the $c/\gamma B$ ratio exceeds unity.

There is no rigorous method of evaluating the errors for the approximate boundary conditions. In a negative sense, the variation in the boundary parameters from those accepted for zero sinkage, indicate the undisclosed errors of earlier theories in which the combination of hydrostatic and uniform stress distributions is adopted. Moreover, the variation indicates inconsistencies in the present theory because the equilibrium of the radial shear zone is still not considered. A suitable extension of the existing stress distribution on the plane boundaries to the spiral boundary would enable the only remaining unknown forces in the system to be determined. The equation of equilibrium for the radial shear zone could then be calculated and used to assess the existing errors. These errors could be eliminated by changing the spiral boundary to some form of ellipse whose shape could be determined by the angle of dilation. The adoption of a variable angle of dilation would permit variation in density to be reflected in the shape of the failure boundary. These improvements, however, could be achieved only at the expense of additional theoretical complexity.

## 2.10.  Comparison with Other Theories

The theory of penetration resistance is compared with existing theories of bearing capacity for both a foundation resting on the soil surface and for a buried foundation in cohesionless and in cohesive soils.

The values of the surface bearing factor, $N_\gamma$, are shown in Fig 2.10.1. Terzaghi's and Meyerhof's $N_\gamma$ factors were computed by the author; the former are exactly the same as those published by Lotkin[53] but the latter differ slightly from those published in reference 24, particularly for $\emptyset = 5^\circ$, $10^\circ$, $15^\circ$, and $50^\circ$. Ballas' values[25] are derived with the aid of his graphs for the ratio $\rho$, and Mizuno's values[54] are obtained from his published graphs. Published values are used to construct the curves of Caquot and Kerisel's[55] and Lundgren and Mortensen's[18] $N_\gamma$ factors. As the current theory is based on the maximum size of the wedge with no minimising procedures, it is not surprising that the $N_\gamma$ values tend to be higher than most other theories.

The comparison at shallow depths of penetration is complicated by the fact that none of the bearing capacity theories consider shaft support in a logical way. Terzaghi's theory of surface bearing capacity may not be extrapolated beyond a penetration ratio of 1 because the soil above the base of the foundation is considered as a pure surcharge with no boundary stresses. Ballas' theory is restricted to a penetration ratio of 1.5 because further extension would lead to an impossible figure of rupture when shaft support is ignored. Meyerhof considers shaft support as a surcharge effect for a figure of rupture dissimilar to that for the determination of the bearing capacity due to the internal weight of the mass of soil at failure.

The dimensionless graphs $p/\frac{1}{2}\gamma B$ and $p/c$ are used in Figs 2.10.2. and 2.10.3 to account for the combined effects of $N_\gamma$, $N_q$ and $N_\gamma$, $N_q$, $N_c$, respectively. The excessively small scale of Meyerhof's published graphs[16] of the combined factors in the relevant range precludes a direct comparison with his work. For expediency, Wills results[32], for a restrained version of Meyerhof's theory, are presented for $m = 1$. From a few test computations of Meyerhof's theory, it would appear that the effect of restraint on the pole position is to increase the $N_{\gamma q}$ factor from a value less than the current theory to a value greater than the current theory when the shaft coefficient of earth pressure is unity and the interface friction is zero. (The $N_{\gamma q}$ factor is not affected by restraint).

Although direct equivalence of shaft conditions is not possible in the comparison, the present theoretical curve exhibits a marked similarity to the existing bearing capacities theories adopting some form of spiral failure boundary. The divergence of Ballas' results from the general trend is largely due to the use of a failure boundary which does not appear to have experimental validity.

# 3. APPARATUS, SOIL AND EXPERIMENTAL PROCEDURE

The experimental verification of a pressure penetration theory requires apparatus for the measurement of the forces on a rigid model foundation as it is pushed vertically into the soil. The evaluation of two dimensional soil movement necessitates the use of a glass-sided tank, and in order to cover the complete soil range, tests must be conducted in at least three soils, a cohesionless soil, one with cohesion and friction and a frictionless material. Each soil must be processed to a state which can be readily reproduced for a number of experiments, and the soil parameters must be obtained for these precise conditions. Finally, the interface effects due to model testing in a confined space, the influence of the glass interfaces and sources of error incurred by the photographic analysis of the failure geometry must be investigated.

## 3.1.   The Pressure Penetration Apparatus

Pressure penetration experiments were conducted on a large penetrometer developed by U.S.A.T.A.C. (Fig 3.1.1.). This was used in order to obtain the structural rigidity necessary for the development of symmetrical soil failure. The penetration device is mounted on the base of a vertical shaft running through linear bearings. This prevents any lateral movement of the shaft. Although the shaft is not completely restrained in rotational movement, it did not appear to occur during the tests. The vertical shaft movement of approximately 42 in is controlled by two double acting hydraulic cylinders. The penetration speed may be varied from 12-60 in min$^{-1}$ by means of a variable flow hydraulic control unit.

A glass sided soil tank was mounted on a stand to simplify the photographic procedures. The maximum size of the tank was limited by the weight which could be conveniently man-handled, and by the volume of soil which would be readily processed between experiments. The internal dimensions of the tank were 45 in long, 35 in high and 6 in wide and it contained approximately 500 lb of soil to a total depth of 30 in. As the extent of failure is a function of $\beta$, provision was made for varying the quantity of soil by using two vertical compression plates which could be moved inwards to give any desired tank volume.

The base and ends of the tank were of 6 in x 2 in channel. A ½ in thick 'Plexiglass' sheet was used to form the front of the tank and a ¾ in thick sheet of plywood formed the back. The ends were braced along the length of the tank and the sides across the width of the tank by a series of removable cross bars (Fig 3.1.2.). (It was subsequently found that the 2 in x ½ in crossbars had to be strengthened by a factor of 3 to minimise elastic deformation of the crossbars during tests in very compact materials). On the inside faces of the 'Plexiglass' front and the wooden back were placed two sheets of ⅛ in thick window glass to form the soil glass interfaces. The inner sheets were used to reduce replacement costs; these were expendable when scoring occurred. For a free flowing material such as dry sand, the replacement of the glass was only possible when the box was empty. For self supporting cohesive materials, the glass could be replaced without emptying the soil by gently moving the cross bars after processing.

The penetration device was designed to measure both the base resistance and the shaft forces. The outer shell of the penetration device was a channel section measuring 30 in long, 6 in deep and 1¾ in wide (Fig 3.1.3.). This housed the loading shaft which had a 6000 lb integral ring dynamometer at the lower end to measure the base resistance. The horizontal and vertical side plate loads were transmitted to five cantilevers on the loading shaft through

spherical rod end bearings and small chain links. Any lateral movement of the side plate was constrained by ball bearings recessed in grooves in the strengthening bars on the side plate and impinging on the channel flanges. By measuring the horizontal loads with two pairs of cantilevers, each with a design load of 100 lb, the total thrust and its point of application could be determined. The vertical thrust was measured by a single cantilever with a design load of 300 lb.

The base resistance dynamometer was calibrated against a standard load cell (Fig 3.1.4.). A linear relationship between strain rate and load was obtained with no hysteresis effects.

The side plate cantilevers were calibrated by dead weights. As the individual calibrations of the four cantilevers measuring the horizontal thrust were very uniform, the two signals from the two lower cantilevers, and those from the two upper cantilevers were added electrically to give only two outputs instead of four. On assembling the complete side plate, however, problems were experienced with the calibration of the cantilevers. It was anticipated that some interaction would occur between the horizontal and vertical force measuring units, but unfortunately this was combined with excessive hysteresis. This was attributed to some major misalignments in the assembly of the cantilever linkage. Although some modification did reduce the friction, there was insufficient time to redesign and manufacture a linkage to eliminate the problem and the existing rig had to be used for the current series of experiments. Owing to these factors, a comprehensive series of calibrations were conducted on the side plate. The penetration device was mounted in a Hartford chuck and measurements were made for a series of weights placed at different points along the length of the side plate and three different angles of the side plate— horizontal, 45° and vertical—were also used to assess the interaction of combined loading (Fig 3.1.5.).

The cantilever calibration curves are shown in Figs 3.1.6. to 3.1.8. The results for horizontal loading do not exhibit too much hysteresis, and by combining the upper and lower calibration curves, the resultant calibration curve is identical and independent of the position of the load (Fig 3.1.7.), the interaction obtained in horizontal loading was found to be relatively constant at 9% of the horizontal load (Fig 3.1.8.). This high figure is the result of minimising hysteresis by increasing the linkage clearances which then introduced considerable slack. An angular movement of only ± 4° from the vertical could account for this interaction. This slack also caused 'weight transfer' to occur between the upper and lower cantilevers when when the side plate was tested at an angle to the horizontal. It was therefore decided that the total force calibrations could be used but that the location of the point of application of the total force was subject to an excessive degree of error. The horizontal component of the force applied at 45° was identical to that found for horizontal loading; the vertical component was some 8% higher which agrees well with the interaction figure obtained earlier (Fig 3.1.9.).

The base resistance was recorded against sinkage on an XY plotter and the three force measurements on the side plate were also recorded against sinkage on a multi-pen recorder. The two sinkage measurements were each obtained from half bridge incorporating a rotary potentiometer which was forced to rotate when penetration occurred.

Two further refinements were made to the basic rig. Rough or smooth side plates and base plates could be fitted to investigate the effect of interface friction. The aspect ratio of the penetration device may be increased from 3:1 to 12:1 by attaching a wooden block on each side of the central measuring unit (Fig 3.1.10). This was used to determine the effect of the glass interfaces.

34

Some of the experimental results used in this report were obtained from an earlier series of tests which were conducted on a different apparatus using footings without side-walls. This apparatus is fully described in reference 40 together with the photographic techniques and the methods employed to reduce the effect of the glass interfaces.

## 3.2    Soil Preparation and Properties

Tests were conducted in a roller model soil, two dry sands (Ohio and Leighton Buzzard), damp sand and clay. The rollers were processed manually by rearranging their positions until any visible failure lines from the previous tests had been removed and some degree of compaction had been achieved throughout the mass. Care was also taken to ensure that completely uniform packing did not occur.

The dry sand was first completely cultivated by emptying and refilling the tank, then compacted by an electro-magnetic vibrator until maximum density was achieved and the surface levelled. In the larger tank, a vibrating probe was also used to ensure even compaction.

The loose damp sand was spread evenly in 2 in layers and compacted by means of a falling weight compactor to maximum density. The surface of each successive layer was disturbed before the addition of fresh material and final layer levelled to a set depth by a scraper running along the sides of the tank.

Whereas the tank was completely emptied of sand between each test, the clay was not disturbed. It was processed by filling in the cavity left by the footing and kneading the mass to obliterate any rupture lines. The surface was levelled to a set depth using the same volume of clay as a check for the presence of any air pockets.

The diameters of the wooden rollers were $1/8$ in and $\frac{1}{4}$ in. At a mean density of 0.02 lb/in$^{-3}$ the angle of internal friction was $28^{\circ}$.

The Ohio sand contained rounded particles with a good grain size distribution (Fig 3.2.1.). The angle of internal friction was $40.5^{\circ}$ in a density of 0.065 lb in$^{-3}$. The angle of repose was $32^{\circ}$ at a minimum density of 0.59 lb in$^{-3}$.

The Leighton Buzzard sand was a sieved washed sand again with rounded particles but with a very uniform large grain size laying between 12 mesh (0.0553 in) and 24 mesh (0.0236). At a maximum density of 0.0605 lb in$^{-3}$ the angle of internal friction was $45.5^{\circ}$. At the minimum density of 0.054 lb in$^{-3}$, $\emptyset$ was $32^{\circ}$. Using these two values of the density, the maximum dilation is $10\%$.

The damp sand was a fine, washed 'plastering' sand with sharp grains and had a moisture content of 4.53%. At a maximum density of 0.0672 lb in$^{-3}$ the soil properties were $\emptyset = 43.4^{\circ}$ and c = 0.3 lb in$^{-3}$. At minimum density of 0.047 lb in$^{-3}$, $\emptyset = 33^{\circ}$ and c = 0.2 lb in$^{-2}$.

The clay had a cohesion of 1.8 lb in$^{-2}$ and a negligible friction angle of between $2.5^{\circ}$ and $4^{\circ}$. The moisture content was 32.8% (D.B.) and the density 0.0625 lb in$^{-3}$.

35

# 4. ANALYSIS OF RESULTS

The measured pressures as a function of the penetration ratio gave good agreement with the theory in all materials. The photographs showing the failure boundaries in the roller model were almost identical with the theory and those in dry and damp sand were encouraging in that they were of the same form as the predicted boundaries. Unfortunately, the base wedge was much flattened and the overall width of failure in sand was only about half as big as the theory predicts. In the clay, the failure was markedly different to that predicted.

## 4.1  Penetration Failure in the Roller Model

The theoretical determination of the base resistance and the failure geometry depends on the coefficient of earth pressure and the angle of interface friction on the shaft which were found by experiment to be 0.45 and $12^o$ , respectively. The experimental penetration resistance together with the predicted curve for $k_{\gamma s}$ = 0.45 and $\delta$ = $12^o$ is shown in Fig 4.1.1.

The failure geometry is shown in a series of photographs of a 2 in wide sand coated foundation driven progressively into the roller model from the surface to a penetration ratio of 10 (Figs 4.1.2a. to 4.1.2j.). Mobilisation of the material did not always occur on both sides of the foundation shaft at the same instant even though great care was taken to ensure that the penetration device was vertical. A particularly good example of symmetrical failure is shown in Fig 4.1.2j. After a number of tests, the boundary of the failure zone was clearly visible by still photography (Fig 3.1.1.). This was made possible by the mixing action of successive penetrations within the mobilised material. Rollers were carried down in the wedge attached to the base of the footing. (Figs 4.1.3.). The base wedge angle varied between $57^o$ and $60^o$ beneath a rough footing. However, it is not possible to lay too much stress on these figures because there was a tendency for the rollers to be arranged in the ideal packing formation by displacing the larger rollers (Fig 4.1.4.). This results in a base wedge angle of $60^o$ which does not necessarily reflect on the actual value of $\emptyset$ or the correct stress field when both sizes of rollers are present.

A comparison between the experimental and theoretical failure geometry is shown in Fig 4.1.6. for three penetration ratios. Considering the experimental variation between tests, the relationships are very satisfactory. At the largest penetration ratio, the photograph of the roller movement (Fig 4.1.2i.) clearly shows two roller streams, one moving in a direction similar to that predicted, and the other moving outwards and upwards following the line of least resistance for uniformly packed rollers. The movement of both streams is largely dissipated before they reach the surface.

## 4.2  Failure under Rough Strip Foundations and Footings in Dry Sand

Preparatory tests with the penetration device were conducted in a large mass of dry sand to determine the effect of density on the base resistance and on the appearance of rupture planes at the sand surface. The influence is demonstrated by the two pressure penetration records for Ohio Sand (Fig 4.2.1.). In soil at the minimum density the trace is a smooth curve which is the result of localised compaction failure within the soil mass. Almost no surface upheaval occurred at the larger penetration ratios. When the compressibility effect is eliminated, the experimental penetration resistance is much less uniform with each successive peak relating to the development of a clearly defined failure boundary. The pressure troughs

36

represent the continued failure along an existing failure plane. Thus any predicted curve should pass through the pressure peaks. The theoretical penetration resistance in Fig 4.2.1. is based on a measured coefficient of earth pressure on the shaft of 1.23 and $\delta$ was assumed to be equal to $\emptyset$ at the minimum density of the sand.

The base penetration resistance for a long strip footing (aspect ratio of 6:1) in compact Leighton Buzzard sand was used as a control test to determine the effect of the glass interface. As the shaft parameters for a footing are indeterminate, the penetration resistance is predicted in accordance with the assumptions given in Section 2.8. The experimental and theoretical curves shown in Fig 4.2.2. exhibit a close similarity. The comparison between these results and those shown in Fig 4.3.2. indicates that two dimensional failure may be simulated in a glass sided soil tank.

## 4.3    Failure under Rough Footings in Dry Sand

A series of photographs record the soil movement which was caused by a 2 in wide sand coated footing driven progressively into dry sand from the surface to a penetration ratio of 3 (Figs 4.3.1a. to 4.3.1f.). The location of each of the succession of photographs, together with the theoretical base resistance is shown on the XY plotter record for this particular experiment (Fig 4.3.2.). Photographs (a) and (b) show the initial development of a long sharp wedge and sand particle movement extending very widely on both sides of the footing. Photographs (c) and (d) are taken just after the first soil failure and show a much blunter wedge and smaller zone of moving sand. Photograph (e) again shows a sharper wedge and a wider zone. Notice that this coincides with the second pressure peak on the XY plotter record. This cycle is repeated throughout the test and is accompanied by a general widening of the failure zone with increasing depth as shown in photograph (f). The existence and the variation in the size of the wedge is shown more clearly in photographs taken with the camera attached to the footing (Figs 4.3.3a. and 4.3.3b.). The maximum pressure tends to occur when the wedge is at its sharpest and the peak values correspond well with the theory.

The variation in wedge shape and the smaller failure boundaries are attributed to the variation in $\emptyset$ with changes in density. The dilation of the sand due to the first footing failure was measured with a planimeter from photographs 4.3.1b. amd 4.3.1d. In both cases the volume of sand has increased and corresponds to an 8% expansion of the sand lying above the soil failure boundary. Photograph 4.3.1d. also shows two edges to the surface heave. The inner edge corresponds with the intersection between the main failure boundary and the surface of the sand. The outer edge is much further out and represents the much large volume of sand mobilised in photographs 4.3.1a. and 4.3.1b.

As the footing begins to sink, the sand deforms. Since it is originally at its maximum density, it dilates and the value of $\emptyset$ diminishes. This process tends to spread from the edges of the footing, and before the complete failure zone develops, the footing is operating in a sand with $\emptyset$ = 32° instead of 40°. For such a material, the failure surface is only half as large. A secondary failure therefore occurs entirely within the soil loosened by the initial penetration of the footing. It is shown in Fig 4.3.4. that the measured failure surfaces correspond very closely to the theoretical one for $\emptyset$ = 32°. This comparison is based not on the same penetration ratio for theory and experiment, but on the same position of the wedge tip. As the original wedge tip constitutes a pattern of weakness, it tends to remain in its initial position. The wedge angle is reduced within the loosened material by the sinkage of the footing which is required to produce the first failure.

37

With further penetration, the footing nears the original wedge tip and forms a new sharp wedge. From this wedge, the soil is mobilised outwards and upwards to start a new cycle of soil loosening, weakening and failing.

The magnitude of the recorded penetration resistance confirms this explanation. It is only the peak values of the pressure that equal the theory. In between, the pressure falls towards the value appropriate to the lower value of $\phi$. There is a tendency for only the first peak to reach the predicted value and all the subsequent peaks to be lower. This is because the subsequent failures have previously loosened sand above the newly generated boundary.

### 4.4    Failure under Smooth Footings in Dry Sand

Photographs 4.4.1a. to 4.4.1d. are of a lubricated glass footing taken with a camera rigidly mounted to the footing and show the fixed wedge and, less clearly, the failure zone boundary. The experimental penetration resistance is shown in Fig 4.4.2. The photographs (and others which were taken) show that the failure zones are of the same magnitude as those for the rough footing and have a wedge behaving in the same cyclic manner. The only difference is that the wedge can disappear altogether and, on occasion, a double wedge can be formed. This latter phenomenom together with the maximum size of the wedge at the surface are illustrated in Fig 4.4.3.

The cycle variation of the wedge beneath a rough and smooth footing is shown diagrammatically in Figs 4.4.4a. and 4.4.4b. Note that the tip of the original wedge, resting on the compact soil, remains constant throughout one cycle. The minimum size of the wedge depends on the mobilisation of shear stresses on the base of the footing. Beneath a rough footing, the wedge never completely disappears (2nd stage of Fig 4.4.4a.). A larger wedge then forms to start a new cycle but it never reaches the maximum size of the wedge present during the initial process because the upper half of the new wedge is developing in previously loosened material.

Beneath a smooth footing, no shear stresses can be developed and the complete cycle includes two further stages. In some cases, a mere vestige of the wedge is retained (3rd stage of Fig 4.4.4b.). Finally, the footing may penetrate until it reaches the original curved boundaries emanating from the tip to form two planes of weakness at an angle of $\pi/2 + \phi/2$ to each other joining at the centre of the base. Thus, they form the inner boundaries of two wedges such that the soil flows horizontally outwards from the centre of the footing (4th stage of Fig 4.4.4b.). Thereafter, the cycle is repeated. The new wedge is almost as large as the original because it is being developed in almost totally undisturbed material. This explains why all the peaks in the pressure penetration record are of the same amplitude as the first peak and why they occur less frequently than in the record for the rough footing.

There is no theoretical explanation for the cyclic variation of wedge shape based on the assumption of a rigid footing penetrating a homogeneous material. The observed tendency for assymmetrical failure after the initial mobilisation of the soil imposes considerable lateral thrust on the wedge and can cause its partial destruction (Fig 4.4.5.). The mode and extent of the destruction is then determined by the interface properties along the base of the footing. In the presence of interface friction, the lateral thrust is imparted to the footing, causing it to 'weave' during penetration. Slices of the wedge are removed by a shearing action until the base angle reaches the value of $\phi$. At this point, the lateral thrust is eliminated because the resultant forces, acting at an angle of $\phi$ to the normal on the sides of the wedge, are vertical

and maximum shear stresses can be developed along the base to prevent a further reduction in the wedge size. The footing must now displace the dense sand beneath the blunt wedge. Applying the principle of conservation of energy, the sharp wedge is formed when the penetration pressure for the development of a new failure boundary through the undisturbed soil is less than that for the blunt wedge. The process is similar for a smooth footing except that the absence of shear stresses permits the complete disappearance of the wedge without imposing any lateral thrust on the footing itself.

## 4.5    Penetration Failure in Damp Sand

Preliminary experiments were carried out to assess the difference between a rough and smooth footings. No difference in either the failure patterns or the pressures could be detected. This may well be attributed to the difficulty of eliminating soil to structure adhesion. The wedge beneath a lubricated glass footing (Fig 4.5.1.) may be compared with the wedges for a sand coated base (Fig 4.5.7a.).

The main experiments were with buried footings at initial penetration ratios of 0, 1, 2 and 3. The footing was driven until complete failure was observed in each case. The failure patterns are shown in Fig 4.5.2. to 4.5.5.

Failure always occurred on one side of the footing first, with a relatively sharp wedge (Figs 4.5.2., 4.5.4a. and 4.5.5a.). Further sinkage was necessary to produce failure on the other side, and by this time the wedge was smaller (Figs 4.5.3., 4.5.4b. and 4.5.5b.). The photographs show the same general patterns as in dry sand. The failure surfaces are of the correct form but are much smaller than the theory predicts. The predicted and experimental failure patterns are compared for penetration ratios of 0 and 2 in Fig 4.5.6.

The development of the wedge beneath a rough footing is illustrated in Fig 4.5.7. Initially, the theoretical sharply pointed wedge develops but later there is a tendency to form a double wedge on which appear the half sized Hill type failure surfaces.

The soil failure seemed to be different to that occurring in dry sand where there was a general disturbance throughout the soil progressing from the corner of the footing. In damp sand, it appeared as if large masses moved bodily. It is clear that large cracks could open up to separate the various parts of the mobilised sand at failure. Furthermore, the first signs of failure occurred in the deepest layer, but before they were fully developed, much smaller failure surfaces were generated at the mid point of the original wedge and broke to the surface first.

The successive development of the failure surfaces for a driven footing are shown in Fig. 4.5.8. In this case, there is an obvious tendency for the successive failures to rise sharply upwards and coalesce with previous failures, thus producing a very small rupture distance.

The force measurements for both buried and driven footings are shown in Fig 4.5.9. together with the predicted values. Once again, there is good agreement considering that the interface effects were higher in this material. (The adhesion and interface friction were not reduced by the lubricant to the same degree as in dry sand.)

Once again, the measured value of $\emptyset$ for the sand in its dense state gives the correct theoretical value for the base resistance but the failure surface is much smaller and

corresponds to the lower value of $\emptyset$. The explanation used for the dry sand does not seem applicable here. The photographs do not exhibit much evidence of general dilation throughout the soil mass. It seems more likely that the frictional resistance was reduced and the cohesion almost eliminated only along the actual lines of rupture. The problem of soil compressibility was only overcome at the expense of over-consolidation and the resultant material exhibited some recovery after deformation. This, combined with the evidence that parts of the soil were in tension, could yield the observed failure geometry and the rapid reduction in the penetration resistance after the critical point of failure.

A further noteworthy observation was the marked tendency to unilateral soil failure. Perhaps this situation should be investigated theoretically. It seems possible that an alternating succession of one sided failures is kinematically feasible and might lead to a reduced size of failure pattern.

## 4.6    Penetration Failure in Clay

Entirely different trends were noted in clay. The pressure penetration traces for buried footings driven from penetration ratios of 0, 1, 2 and 3 were all smooth curves (Fig 4.6.1.). In each case, the gradient of the curves rapidly reduced to a small constant value after the footing displacement exceeded a distance equal to the width of the footing. An example of the total deformation of the soil during this footing displacement is illustrated in the superposed photograph (Fig 4.6.2.). The magnitude and direction of the actual soil deformations were obtained from the two images of each grid intersection and presented in a displacement diagram (Fig 4.6.3.). Note the vertical displacement of the soil together with the complete absence of any bulging of the unsupported walls of the excavation. It was also found that the extent of failure increased in proportion to the depth of penetration.

This type of failure was rather unexpected. It was anticipated that the soil, which was displaced by the passage of the footing, would flow into the excavation and rapidly yield some constant maximum value for the base resistance independent of depth in accordance with Jaky's theory[8]. Although Jaky's theory is for $c/\gamma B = \infty$, it does compare well with the experimental base resistance for $c/\gamma B = 15$, but not with the failure geometry. The observed failure patterns are attributed to two factors, the effect of adhesion and the effect of weight. First, the failure boundaries shown in Fig 4.6.3. can be reproduced theoretically in the absence of weight only when full passive earth pressure is acting along the walls of the excavation. Although no side thrust was used in the experiments, a small calculation suffices to show that the adhesion of the glass interfaces is more than adequate to create the necessary side thrust for this type of failure. The introduction of gravitational stresses also tends to increase the size of the zone of mobilised soil. Although some tentative conclusions have be been drawn, confirmation of failure mechanism in clay depends on the complete elimination of the adhesion by a suitable interface film which controls the adhesion without also affecting the cohesion.

## 4.7    Comparison with Other Experimental Research

The current theory tends to underestimate the surface bearing capacity in sand but to a lesser extent compared with other theories with the exception of Balla's theory. For example, Selig and McKee[41] measured an average base resistance of 22.2 lb in$^{-2}$ using 3 in wide rectangular footings with an aspect ratio varying from 5:1 to 7:1. The density of sand was 0.065 lb in$^{-3}$ and $\emptyset$ was 'around' $41^{\circ}$ - to quote the author - and yield a theoretical base resistance of 19.5 lb in$^{-2}$.

Comparisons between driven or buried footing tests results and the theoretical values is difficult because the sand falling into the cavity left by the footing present indeterminate shaft conditions. An indication of comparative trends may be obtained by assuming the values of $k_\gamma s$ and $\delta$ to be 1 and 0 respectively in accordance with the reasoning stated in section 2.8.

Lebeque[39] conducted driven footing tests in a poorly graded, round grained sand at three different densities ranging from 1.425 gm cm$^{-3}$ to 1.57 gm cm$^{-3}$ (0.0515 lb in$^{-3}$ and 0.0566 lb in$^{-3}$ ) for which $\emptyset$ varied from 32° to 38°. As the properties of the sand show a marked similarity to the Leighton Buzzard sand used in the current series of tests, it is suspected that maximum density was not achieved. Thus, compressibility and dilation effects may be present, and only the results for the dense sand are considered (Fig. 4.7.1.). The discrepancy between theory and practice is greater near the surface. This may well be due to compressibility, which would yield a higher experimental bearing capacity because compaction under the footing increases the density of the sand prior to failure. The improved correlation with depth may be attributed to the fact that the footing penetration required to cause failure becomes less significant in terms of the total penetration depth for the larger penetration ratios.

The correlation between the theoretical penetration resistance and the experimental data obtained by Wills in very compact Ohio sand show an entirely opposite effect (Fig 4.7.2.). There is close agreement up to a penetration ratio of 2 and thereafter the experimental values increase more rapidly than the predicted values. Inaccuracies in the measurement of $\emptyset$ may well explain this divergence. Although the penetration test was conducted in sand at a density of 0.067 lb in$^{-3}$, the initial density of the triaxial shear test samples was 0.059 lb in$^{-3}$. Using confining pressures of up to 150 psi, Wills obtained $\emptyset = 40°$ whereas the author obtained $\emptyset = 40.5$ in the same sand at a density of 0.065 lb in$^{-3}$ (c.f. section 3.2.). The values of $N_\gamma$ are extremely sensitive to changes in $\emptyset$ when $\emptyset$ is large. For example, a 1° change in $\emptyset$ from 40° to 41° increased the value of $N_\gamma$ by approximately 20%. This increase would be sufficient to yield a predicted curve almost identical with the mean experimental curve throughout its length.

With this general tendency towards theoretical underestimation, it is rather surprising to find that the theory overestimates the test data obtained by Biarez[37] in the roller model. At a penetration ratio of 2 the theoretical value is 29.6 kg cm$^{-1}$ as opposed to an average experimental value of 22.5 kg cm$^{-1}$. This tends to indicate that the model is suspect.

Biarez found that the value of the coefficient of earth pressure $k_\gamma s$ on the rough sides of the foundation was 2.6 for $\emptyset = 26°$. This is also surprisingly high. From an analysis of skin friction measurements on piles, Meyerhof found that $k_\gamma s$ varied from 0.5 for loose sand to 1 for dense sand. Similar results to those of Meyerhof are quoted by Vesic for long rectangular foundations.

# 5. FURTHER THEORETICAL INVESTIGATIONS

During the development of the theory of penetration resistance, ancillary investigations yielded some interesting results.

## 5.1 The Minimising Fallacy

The bearing capacity of a foundation is frequently derived by taking moments of all the soil forces about some convenient point. When the curved boundary of the zone of shearing flow is described by the equation to the logarithmic spiral, the calculation is simplified by taking moments about the pole of the spiral because the frictional forces acting on the spiral boundary pass through the pole of the spiral and may be neglected in the moment equation. In order to overcome the problem that the stress field composed of radii and logarithmic spirals is true only in the case of a weightless soil, a smaller failure zone with a modified shape is achieved for a soil with weight by relaxing the constraints on the position of the pole. The pole does not necessarily lie at the corner of the footing, but at some point close to it such that the resultant bearing capacity factor, $N_\gamma$, is a minimum. As has been described previously, this view is rejected because the resulting inconsistencies in the calculation appear to be greater than the original problem. Nevertheless a considerable amount of work was expended in investigating the effect of the wandering pole.

If the pole is restrained to move along the boundary between the plane and radial shear zones or that line extended (line OBD, Fig 1.4.1a.), the variation in the value of the resultant frictional force on the contact face, BC, is dependent on the distance, OB, defined as $\lambda$, which defines the distance of the pole from the corner of the footing and is taken as positive when the pole lies outside the failure zone. Lotkin[53] published the general shape of the curve satisfying the equation:-

$$N_\gamma = f(\lambda) \qquad \dots\dots 5.1.1.$$

The particular curve for $\beta = 30°$ is shown in Fig 5.1.1.

It is observed that the resultant factor can become infinite when the pole is located at quite small distances from the position of $\lambda_{min}$ at which $N_\gamma$ is a minimum. This is simply explained by the fact that when the pole is located on the line of action of the resultant force, the moment arm becomes zero. Hence, the resultant force and $N_\gamma$ tend to infinity. Similarly, if the pole is located immediately beyond this limiting value of $\lambda$, the value of $N_\gamma$ tends to a negative value of infinity, even though the failure geometry is entirely reasonable and the change in shape is almost imperceptible.

Although the increasing values of $N_\gamma$ for negative values of $\lambda$ are related to increasing size of the failure zone, the minimum value of $N_\gamma$ is usually located at a positive value of $\lambda$. Hence, the minimum value of $N_\gamma$ is governed, to a large extent, by:-

(a) The point of application of the resultant force for soil weight on the contact face or wedge boundary and its direction.

(b) The variation in the extent of failure.

(c) The angle of inclination of the contact face with respect to the horizontal

(d) The degree of constraint placed on the location of the pole.

42

As the point of application of the force is normally governed by hydrostatics and the force is assumed to act at an angle $\emptyset$ to the normal, the effect of these parameters can be considered constant. The location of the pole does affect the extent of failure, but the variation is not systematic - the changes in extent of failure and in values of $N_\gamma$ are considered in more detail for a fixed pole (cf section 5.2.). The most significant effect on the bearing capacity is achieved by increasing the backward rake of the contact face (wedge boundary) or by decreasing the angle of inclination of the line along which the pole is restrained. Separately or jointly, these changes serve to create greater constraint on the possible positions of the pole and, hence, increase the minimum value of $N_\gamma$.

In perspective, then, Ohde originally devised the minimising procedure for retaining walls for which the calculation was an acceptable way of optimising for the interface properties along the contact face. Terzaghi increased the constraints on the pole by considering a backward raked contact face. Meyerhof relaxed the constraints again by adopting the unrestrained pole no longer confined to a line, but free to take any position in two dimensional space. Fortuitously, however, this freedom of movement was largely inhibited and governed by the same limits determined for the restrained pole i.e. the line of action of the resultant force effectively halving two dimensional space and an excessively large failure geometry. The location of the unrestrained pole is thus never far removed from the location of the restrained pole. Wills, modifying Meyerhof's theory, again restrained the pole to the boundary BD or to that line extended (Fig 1.5.1.); here the angle of inclination of the boundary to the horizontal decreases with sinkage. Hence the constraint is more severe and the final answer is nearer to that achieved in the absence of any minimising procedure.

The effect of the minimising techniques on the value of the surface bearing capacity factor $N_\gamma$ may be summarised, for $\emptyset = 40^\circ$ and $\psi = 45 + \emptyset/2$, as follows;-

| | |
|---|---|
| No minimising (corner pole) | 163 |
| Line restraint | 129 |
| Unrestrained | 119 |

At a penetration ratio of 2.5 the approximate values of the $N_\gamma$ factor for the pole restrained to a line (Wills) and the unrestrained pole (Meyerhof) are 640 and 500 respectively. The trend indicated by these figures is similar to that for the surface case.

It has been demonstrated that different pole locations can provide a large number of solutions for the resultant forces generated on the contact face by the soil mass during failure. This is plainly impossible. This absurdity results from using a method which does not relate the frictional forces on the spiral boundary to both the soil properties and the dimensions of the failure surface.

The apparently cunning method, whereby knowledge of the frictional force on the spiral boundary is not required, is fallacious. The resultant force on the wedge boundary can be calculated only if all the forces are known, are shown to be in equilibrium and are compatible with the soil properties. Such knowledge can only be gained by a process of rigorous analysis but owing to the complexity of the problem has not been fully achieved. A reasonable alternative for immediate applications is to accept a plausible failure surface with some rigorous foundation and eliminate the dangers inherent in the minimising procedures.

## 5.2    The Effect of the Wedge Angle

The comparative effect of the wedge angle, $\psi$, on the surface bearing capacity is more apparent when minimising techniques are eliminated. For the pole of the spiral located at the corner of the footing, the factors $N_c$, $N_q$ and $N_\gamma$ are given by the following equations:-

$$N_c = \tan \psi + \frac{\cos (\psi - \emptyset)}{\sin \emptyset \cos \psi} \left[ a_\theta^2 (1 + \sin \emptyset) - 1 \right] \qquad \ldots\ldots 5.2.1.$$

$$N_q = \frac{\cos (\psi - \emptyset)}{\cos \psi} \; a_\theta^2 \; \tan (\pi/4 + \emptyset/2) \qquad \ldots\ldots 5.2.2.$$

$$N_\gamma = \frac{\cos (\psi - \emptyset)}{2 \cos^2 \psi} \left\{ a_\theta^3 \left[ \cos \epsilon + \frac{3 \sin \emptyset \cos (\psi - \emptyset) - \cos \emptyset \sin (\psi - \emptyset)}{1 + 8 \sin^2 \emptyset} \right] \right.$$

$$\left. + a_\theta^2 \; \frac{3 (\cos \psi - \sin \epsilon)}{4} + \frac{3 \sin \emptyset \sin \epsilon + \cos \emptyset \cos \epsilon}{1 + 8 \sin^2 \emptyset} \right\} - \tan \psi$$

$$\ldots\ldots 5.2.3.$$

where $a_\theta = e^{(\pi - \psi - \epsilon) \tan \emptyset}$ and the range of values for the wedge angle is $\emptyset \leqslant \psi \leqslant \pi/4 + \emptyset/2$. In order to complete the comparison, the rupture distance, f, measured horizontally from the corner of the footing to the point at which the failure boundary joins the soil surface, can be used in dimensionless form, f/B, to give the extent of failure:-

$$f/B = a_\theta \cos \epsilon / \cos \psi \qquad \ldots . 5.2.4.$$

The rupture distance and the bearing capacity factors are calculated for the two limiting values of the wedge angle over the complete range of $\emptyset$ (Figs 5.2.1a. and 5.2.1b.). The variation in the same functions with respect ot $\psi$ is also given for a constant value of $\emptyset$ (Figs 5.2.1d. and 5.2.1e.). Although the rupture distances increase exponentially with respect to $\psi$, the curves for the $N_c$ and $N_q$ factors always exhibit a negative gradient. The curve for the $N_\gamma$ factor resembles a parabola reaching some minimum value with respect to $\psi$ between almost identical values of the $N_\gamma$ factor at $\psi = \emptyset$ and $\psi = \pi/4 + \emptyset/2$. Thus, the value of the bearing capacity factor is not related to the extent of failure.

This is completely unrealistic and is determined by the mathematical constraints imposed on the free body of mobilised soil rather than to the mechanism of failure. Any system of forces can be resolved into the resultant horizontal and vertical forces acting at any point in the plane plus a couple. However, the force required to balance the couple depends on the length of the moment arm which in turn depends on the line of action of the resultant force relative to the corner of the footing. The resultant frictional forces act vertically when the wedge angle assumes the minimum value of $\emptyset$, whereas they require resolution to obtain the vertical component of the frictional force for any value of the wedge angle which is greater than the minimum. In addition, the moment arm for the small wedge is less than that for the large wedge. These combined characteristics more than counteract for the greater extent of the failure zone in the determination for the larger values of $N_c$ and $N_q$. The parabolic form of the equation for $N_\gamma$ is probably due to the cubic exponential function of the term $a_\theta$, resulting

from the moment product of area and distance. It is purely incidental that this term offsets the influence of the wedge angle on the length of the moment arm and on the direction of the resultant forces.

In view of these facts, the adoption of the correct values for the base angle of the wedge forms an essential part of the bearing capacity calculation and must be determined from the boundary stress conditions. Consequently, the determination of the bearing capacity by minimising with respect to the wedge angle[20] is of doubtful validity. It is also interesting to note that Terzaghi adopts a wedge angle which contravenes the stress boundary conditions to yield a high value for the $N_c$ and $N_q$ factors and yet went to tremendous lengths of minimising the $N_\gamma$ factor.

# 6. CONCLUSIONS

6.1      A general theory of penetration failure has been developed for strip footings or foundations both lying on the surface and buried up to depths of not greater than ten times their width. This is an inprovement on previous theories in the following ways:-

(a)      The stress field has fewer inconsistencies.

(b)      Only one set of simple assumptions are consistently employed to describe the distribution of stresses along a failure boundary.

(c)      New, and quite different conclusions are made on the effect of roughness of the base. It is shown that rough and smooth foundations must have exactly the same penetration resistance under ideal conditions.      __

(d)      The theory treats all the weight of the soil within the figure of rupture as a complete entity and not partly as a surcharge.

(e)      The theory goes some way towards a more realistic combination of cohesion and weight, utilising one figure of rupture.

(f)      The dimensionless factors are functions not only of $\emptyset$ and the $c/\gamma B$ and penetration ratios, but also of the shaft parameters

(g)      The computed results may be applied more easily to practical problems

6.2      The theory still has certain differences:-

(a)      Consideration of the effects of dilation had to be sacrificed for the sake of simplicity and generality over a wide range of parameters.

(b)      Computations of the dimensionless factors proved impossible at the higher penetration ratios with low values of $\emptyset$ because of the excessive tendency for the failure boundary to close into the shaft without achieving equilibrium.

6.3.      The experimental penetration resistance data support the quantitative theoretical values.

6.4      The measured failure patterns are shown to be in agreement with the predicted shapes only when the effect changing soil properties and constraints are carefully evaluated throughout the duration of the test.

# 7. RECOMMENDATIONS

The new theory of penetration failure is given in a form which is amenable to further extension in the development of a theory of slip-sinkage.

# BIBLIOGRAPHY

1. Sokolovski, V.V., 'Statics of Soil Media', Butterworth Scientific Publications, London (1960).

2. Coulomb, C.A., 'Application des règles de maximis et minimis à quelques problèmes de statique relatifs à l'architecture, Mem. Math. et Phys., 7, 343 (1773).

3. Prager, W., 'A Geometrical Discussion of the Slip Line Field in Plane Plastic Flow', Kungl. Tekn. Högsk. Hardlinger, Stockholm, No. 65 (1953).

4. Josselin de Jong, G., 'Statics and Kinematics in the Failure Zone of a Granular Material', Uitgeverij Waltman, Delft (1959).

5. Prandtl, L., 'Uber die Härte plasticher Körper', Gottinger Nachr., Maths-Phys., K1 1920, 74-85 (1920).

6. Hill, R., 'The Plastic Yielding of Notched Bars under Tension', Q.J. Mech. Appl. Math., 2, 40-52 (1949).

7. Shield, R.T., 'Mixed Boundary Value Problems in Soil Mechanics', Quart. Appl. Math., 11, 61-75 (1953).

8. Jaky, J., 'On the Bearing Capacity of Piles', Proc. 2nd Int. Conf. Soil Mech. and Found. Eng., 1, 100 (1948).

9. Drucker, D.C., and W. Prager, 'Soil Mechanics and Plastic Analysis or Limit Design', Quart Appl. Math., 10, 157-165 (1952).

10. Drucker, D.C., 'On Stress-Strain Relations for Soils and Load Carrying Capacity', Proc. 1st Int. Conf. Mechanics of Soil Vehicle Systems, 15-23 (1961).

11. Haythornthwaite, R.M., 'Methods of Plasticity in Land Locomotion Studies', Proc. 1st Int. Conf. Mechanics of Soil Vehicle Systems, 28-43 (1961).

12. Shield, R.T., 'On Coulomb's Law of Failure in Soils'. J. Mech. Phys. Solids, 4, 10-16 (1955).

13. Drucker, D.C., 'Some Implications of Work Hardening and Ideal Plasticity', Quart. Appl. Math., 7, 411-418 (1950).

14. Drucker, D.C., and R.T. Providence, 'Coulomb Friction, Plasticity and Limit Loads', J. Appl. Mech., 21, 71-74 (1954).

15. Terzaghi, K., 'Theoretical Soil Mechanics', John Wiley & Sons, New York (1943).

16. Meyerhof, G.G., 'The Ultimate Bearing Capacity of Foundations', Geotechnique, 2, 301-332 (1951).

17.   Ohde, J., 'Zur Theorie des Erddruckes unter besonderer Berucksichtingung der
          Erddruck Verteilung', Die Bautechnick, Vol 16 (1938).

18.   Lundgren, H., and K. Mortensen, 'Determination by the Theory of Plasticity of the
          Bearing Capacity of Continuous Footings on Sand', Proc. 3rd Int. Conf.
          Soil Mech. and Found. Eng., 1, 409-412 (1953).

19.   Gorbunov-Possadov, M.I., 'Calculations for the Stability of a Sand Bed by a Solution
          Combining the theories of Elasticity and Plasticity', Proc. 6th Int.
          Conf. Soil Mech. and Found. Eng., 1, 51-55 (1965).

20.   Hu. G.C.Y., 'Variable Factor Theory of Bearing Capacity', J. Soil Mech. and Found.
          Div., A.S.C.E., 90, 85-93 (1964).

21.   Rowe, P.W., 'Stress Dilatancy, Earth Pressures and Slopes', J. Soil Mech. and Found.
          Div., A.S.C.E., 89, 30-61 (1963).

22.   Bishop, A.W., 'The Use of the Slip Circle in Stability Analysis of Slopes',
          Geotechnique, 5, 1 (1957).

23.   Janbu, N., 'Earth Pressures and Bearing Capacity Calculations by Generalised
          Procedure of Slices', Proc. 4th Int. Conf. Soil Mech. and Found. Eng.,
          2, 207-212 (1957).

24.   Meyerhof, G.G., 'An Investigation into the Bearing Capacity of Shallow Foundations
          on Dry Sand', Proc. 2nd Int. Conf. Soil Mech. and Found. Eng.,
          1, 237-243 (1948).

25.   Balla, A., 'Bearing Capacity of Foundations', J. Soil Mech. and Found. Div.,
          A.S.C.E. 88, 13-34 (1962).

26.   Brinch Hansen, J., 'A General Formula for Bearing Capacity', Bulletin 11, Geoteknisk
          Institute, Copenhagen (1961).

27.   Skempton, A.W., 'The Bearing Capacity of Clays', Proc. Build. Res. Congr.,
          London (1951).

28.   Bernstein, R., 'Probleme sur experimentellen Motorflugmechanik', Der Motorwagen
          16 (1913).

29.   Letoshnev, M.N., 'Wheeled Carts and their Performance on Country Roads', Teoria i
          proisvod-stvo Sielskohozoynik Mashin, Moscow (1938).

30.   Bekker, M.G., 'Off the Road Locomotion'. Univ. of Michigan Press, Ann Arbor (1960).

31.   Reece, A.R., 'Problems of Soil Vehicle Mechanics'., U.S.A.T.A.C., Land Locomotion
          Division, Warren, Mich., Report No. 97 (1964).

32.   Wills, B.M.D., 'The Load Sinkage Equation in Theory and Practice', Proc. 2nd Int.
          Conf. Soil Vehicle Systems (1965).

33. Haley, P.W., and E. Hegedus, 'Pressure Sinkage Relationships in Soil - Part 1: Speed and Geometry Effects on Plate Penetrometer Tests in Saturated Sand'. U.S.A.T.A.C, Land Locomotion Division, Warren, Mich., Report No. 82 (1963).

34. Emori, R.I. and D. Schuring, 'Model Study in Earthmoving Equipment', ASAE (1961).

35. Osman, M.S., 'The Measurement of Soil Shear Strength', J. Terramechanics, 1, 3, 54-60 (1964).

36. Jumikis, A.R., 'Rupture Surfaces in Sand under Oblique Loads', J. Soil Mech. and Found. Div., A.S.C.E., 82, 1-25 (1956).

37. Biarez, J., M. Burel and B. Wack, 'Contribution à l'etude de la force portante des foundations' Proc. 5th Int. Conf. Soil Mech. and Found. Eng., 1, 603-609 (1961).

38. Meyerhof, G.G., 'The Bearing Capacity of Sand', Ph.D. (Eng) Thesis, Univ. of London (1950).

39. Lebègue, Y., 'Experimental Analysis on Shallow Footings', Ann. Inst. Tech. Bat. Traveaux Publics, 18, 855-862 (1965).

40. Witney, B.D., 'The Determination of Soil Particle Movement in Two Dimensional Failure'. J. Terramechanics, 5, 1 (1968).

41. Selig, E.T., and K.E. McKee, 'The Static and Dynamic Behaviour of Small Footings', J. Soil Mech. a  Found. Div., A.S.C.E., 87, 29-47 (1961).

42. Muhs, E., 'Uber die zulässige Belastung nicht bindigen Böden', Mitteilagen der Degebo, Berlin Heft 16 (1963).

43. Vesic, A.S., D.C. Banks and J.M. Woodward, 'An Experimental Study of Dynamic Bearing Capacity of Footings on Sand', Proc. 6th Int. Conf. Soil Mech, and Found. Eng., 2, 209-213 (1965).

44. Goodman, L.J., 'Small Scale Footing Studies on Clay Soils', Paper prepared for U.S.A.T.A.C., Land Locomotion Division, Warren, Mich. (1961).

45. Witney, B.D., D.R.P. Hettiaratchi and A.R. Reece,' The Basis of Soil Failure', Proc. 2nd Int. Conf. Mechanics of Soil Vehicle Systems, 353-366 (1966).

46. Witney, B.D., 'Pressure Sinkage Relationships in Compact Soil', Ph.D. Thesis, University of Newcastle upon Tyne (1966).

47. Reece, A.R., 'The Fundamental Equation of Earthmoving Mechanics', Symposium on Earth Moving Machinery, Inst. of Mech. Engrs. (1965).

48. Hettiaratchi, D.R.P., B.D. Witney and A.R. Reece, 'The Calculation of Passive Earth Pressure in Two Dimensional Soil Failure', J. Agric. Engng. Res., 11, 2, 89-107 (1966).

49. Mintskovsky, M.Sh., 'On the Stability of Strip Foundation Footings'. 6th Int. Conf. Soil Mech. and Found. Eng., 2, 145-148 (1965).

50. Vesic, A.S., 'Investigations of Bearing Capacity of Piles in Sand', Proc. North American Conference on Deep Foundations (1964).

51. Vesic, A.S., 'Ultimate Loads and Settlements of Deep Foundations in Sand Proc. Sym. Bearing Capacity and Settlements of Founda ns, Duke University Durham, N. Carolina. (1965).

52. Nelder, J.A., and R. Mead, 'Simpler Method for Function Minimisation', Computer Journal, 7, 4, 308-313 (1965).

53. Lotkin, M., 'Trafficability Functions in Soil Mechanics', Ballistics Research Laboratories Report No. 696 (forming part of Introduction to Research on Vehicle Mobility, Part 1 - Stability Problem by M.G. Bekker, Land Locomotion Laboratory, U.S.A.T.A.C., Report No. 22, 1957).

54. Mizuno, T., 'On the Bearing Power of Soil in a Two Dimensional Problem', Proc. 2nd Int. Conf. Soil Mech. and Found. Eng., 1, 44-48 (1948).

55. Caquot, A and J. Kerisel, 'Traité de Mechanique des Sols', Gauthier Villars, Paris (1956).

## APPENDIX A - THEORETICAL ANALYSIS

The complete theoretical analysis for the determination of bearing capacity is described. The failure geometry is derived by considering the equilibrium of the plane shear zone and the boundary conditions. The magnitude and directions of all the forces and the moment arms are determined. By taking moments about the pole of the spiral, the bearing capacity is evaluated.

A.1.                    THE WEIGHT AND WEIGHT-FRICTIONAL FORCES
                          IN THE PLANE SHEAR ZONE

The plane shear zone, BDEG, is bounded by the foundation shaft, BG, the horizontal soil surface, GE, and the two failure planes, BD and DE, along which the shear stresses are fully mobilised (Fig. A.1.1.). Using co-ordinate geometry, the weight of the zone, BDEG, is given by the equation:

$$W_1 = \tfrac{1}{2} \gamma \; [ \, p_1 \, (z_2 - z_1) + p_2 \, (z_3 - z_1) \, ] \quad \ldots \ldots \qquad \text{A.1.1.}$$

When the failure boundary breaks into the horizontal free surface, the following relationships apply :

$$z_1 = 0 \qquad\qquad \text{A.1.2a.}$$

$$z_2 = z - r_1 \sin \zeta \qquad\qquad \text{A.1.2b.}$$

$$z_3 = z \qquad\qquad \text{A.1.2c.}$$

$$p_1 = \frac{r_1 \cos \varphi + z \sin (\varphi - \zeta)}{\cos (\varphi - \zeta)} \qquad\qquad \text{A.1.2d.}$$

$$p_2 = r_1 \cos \zeta \qquad\qquad \text{A.1.2e.}$$

Substituting for the co-ordinates in equation A.1.1. :

$$W_1 = \frac{\gamma \, A}{2 \cos (\varphi - \zeta)} \qquad\qquad \text{A.1.3.}$$

where

$$A_1 = z^2 \sin (\varphi - \zeta) + 2 z r_1 \cos \varphi - r_1^2 \sin \zeta \cos \varphi \qquad\qquad \text{A.1.4.}$$

The weight-frictional forces on the two failure planes are a function of the depth from the nearest horizontal free surface :

$$F_{\gamma 1} = \int_{z_1}^{z_2} \gamma \, k_{\varphi \gamma} \left( \frac{z_c}{B} \right)^{z_c} \frac{z_c}{\cos (\varphi - \zeta)} \, d z_c$$

Integrating :

$$F_{\gamma 1} = \frac{\gamma \, k_{\varphi \gamma} \, V_s}{2 \, (n+1) \, B^{z_b} \, \cos (\varphi - \zeta)} \qquad\qquad \text{A.1.5.}$$

where:

$$V_5 = z_2^{2(n+1)} - z_1^{2(n+1)}$$ A.1.6.

Similarly:

$$F_{\gamma 2} = \int_{z_2}^{z_3} \gamma \, k_{\varphi \gamma} \left(\frac{z_0}{B}\right)^{2t} \frac{z_0}{\sin \zeta} \, dz_0$$

and after integration:

$$F_{\gamma_2} = \frac{\gamma \, k_{\varphi \gamma} \, V_6}{2(n+1) \, B^{2t} \sin \zeta}$$ A.1.7.

where:

$$V_6 = z_3^{2(n+1)} - z_2^{2(n+1)}$$ A.1.8.

The weight-frictional side thrust is:

$$F_{\gamma_s} = \frac{\gamma \, k_{\gamma_s}}{\cos \zeta} \int_{z_1}^{z_3} z_0 \, dz_0$$

and after integration:

$$F_{\gamma_s} = \frac{\gamma \, k_{\gamma_s} \, z^2}{2 \cos \zeta}$$ A.1.9.

A.2. THE MOMENT ARMS FOR THE WEIGHT AND WEIGHT-FRICTIONAL FORCES IN THE PLANE SHEAR ZONE

The moment arm for the force due to the weight of the soil in the plane shear zone may be obtained by co-ordinate geometry:

$$d_1 = \cos(\varphi - \zeta) \, [\, p_1^2 \, (z_2 - z_1) + p_1 p_2 \, (z_3 - z_1) + p_2^2 \, (z_3 - z_1) \,]$$

and substituting for the co-ordinates from equation A.1.2. :

$$d_1 = \frac{A_2}{3 A_1 \cos(\varphi - \zeta)}$$ A.2.1.

where:

$$A_2 = z^3 \sin^2(\varphi - \zeta) + 3 z^2 r_1 \sin(\varphi - \zeta) + 3 z \, r_1^2 \cos^2 \varphi$$

$$- r_1^3 \cos \varphi \sin \zeta \, [\cos \varphi \cos(\varphi - \zeta) + \cos \varphi]$$ A.2.2.

53

The moment arms, $d_3$ and $d_4$, for the weight-frictional forces, $F_{\gamma_1}$ and $F_{\gamma_2}$, may be found by integration:

$$d_3 = \left\{ \frac{z_2}{\cos(\varphi - \zeta)} - \frac{\displaystyle\int_{z_1}^{z_2} \frac{\gamma k_{\varphi\gamma}}{\cos^2(\varphi - \zeta)} \left(\frac{z_0}{B}\right)^{z_n} z_0^{2} \, dz_0}{\displaystyle\int_{z_1}^{z_2} \frac{\gamma k_{\varphi\gamma}}{\cos(\varphi - \zeta)} \left(\frac{z_0}{B}\right)^{2n} z_c \, dz_c} \right\} \cos \varphi$$

$$= \left\{ z_2 - \frac{2(n+1) \, V_7}{(2n+3) \, V_5} \right\} \frac{\cos \varphi}{\cos(\varphi - \zeta)} \qquad \text{A.2.3.}$$

where $V_5$ is given by equation A.1.6. and:

$$V_7 = z_2^{(2n+3)} - z_1^{(2n+3)} \qquad \text{A.2.4.}$$

Similarly:

$$d_4 = \left\{ z_3 - \frac{2(n+1) \, V_8}{(2n+3) \, V_6} \right\} \frac{\cos \varphi}{\sin \zeta} \qquad \text{A.2.5.}$$

where $V_6$ is given by equation A.1.8. and:

$$V_8 = z_3^{(2n+3)} - z_2^{(2n+3)} \qquad \text{A.2.6.}$$

Finally, the moment arm for the side thrust may be found by hydrostatics:

$$d_5 = \frac{z \cos \delta}{3} \qquad \text{A.2.7.}$$

## A.3. THE COHESIVE, COHESIVE-FRICTIONAL AND ADHESIVE FORCES IN THE PLANE SHEAR ZONE

The cohesive forces are proportional to the relative lengths of the failure boundaries:

$$C_1 = c \, \overline{DE} = \frac{c(z - r_1 \sin \zeta)}{\cos(\varphi - \zeta)} \qquad \text{A.3.1.}$$

$$C_2 = c \, \overline{BD} = c \, r_1 \qquad \text{A.3.2.}$$

The cohesive-frictional force, $F_{c1}$, is given by the equation:

54

$$F_{c1} = \int_{z_1}^{z_2} \frac{c\,k_{\varphi c}}{\cos(\varphi - \zeta)} \left(\frac{z_0}{B}\right)^{n} dz_0$$

$$= \frac{c\,k_{\varphi c}\,V_1}{(n+1)\,B^n\,\cos(\varphi - \zeta)} \qquad \text{A.3.3.}$$

where:

$$V_1 = z_2^{(n+1)} - z_1^{(n+1)} \qquad \text{A.3.4.}$$

Similarly:

$$F_{c2} = \frac{c\,k_{\varphi c}\,V_2}{(n+1)\,B^n\,\sin\zeta} \qquad \text{A.3.5.}$$

where:

$$V_2 = z_3^{(n+1)} - z_2^{(n+1)} \qquad \text{A.3.6.}$$

The cohesive-frictional side force depends on the cohesive component of the coefficient of earth pressure:

$$F_{c3} = \frac{c\,k_{c3}\,z}{\cos\zeta} \qquad \text{A.3.7.}$$

The adhesive force on the shaft is:

$$C_4 = c_a\,z \qquad \text{A.3.8.}$$


## A.4. THE MOMENT ARMS FOR THE COHESIVE AND COHESIVE-FRICTIONAL FORCES IN THE PLANE SHEAR ZONE

The moment arm, $d_7$, of the cohesive force, $C_1$, is:

$$d_7 = r_1 \cos\varphi \qquad \text{A.4.1.}$$

The moment arms of the cohesive force, $C_3$, and of the adhesive force, $C_4$, are zero as the lines of action pass through the corner of the footing.

The moment arms for the cohesive-frictional forces are found in a similar manner to their weight-frictional counterparts:

$$d_8 = \left\{ z_2 - \frac{(n+1)\,V_3}{(n+2)\,V_1} \right\} \frac{\cos\varphi}{\cos(\varphi - \zeta)} \qquad \text{A.4.2.}$$

where $V_1$ is given by equation A.3.4. and:

$$V_3 = z_2^{(n+2)} - z_1^{(n+2)}$$ A.4.3.

Similarly, the moment arm for $F_{c2}$ is:

$$d_9 = \left| z_3 - \frac{(n+1) V_4}{(n+2) V_2} \right| \frac{\cos \psi}{\sin \zeta}$$ A.4.4.

where $V_2$ is given by equation A.3.6. and:

$$V_4 = z_3^{(n+2)} - z_2^{(n+2)}$$ A.4.5.

The side thrust is assumed to be uniformly distributed and thus:

$$d_{10} = \frac{z \cos \delta}{2}$$ A.4.6.

## A.5.  SPECIAL RELATIONSHIP FOR $\zeta = 0$

When $\zeta = 0$, the failure plane, BD, is horizontal. Thus, $z_2 = z_3$ and the forces $F_{\gamma_2}$ and $F_{c2}$ are indeterminate. In this case, the forces are given by the following equations:

$$F_{\gamma_2} = \frac{\gamma \, k_{\varphi\gamma} \, r_1 \, z^{(2n+1)}}{B^{2n}}$$ A.5.1.

$$F_{c2} = c \, k_{\varphi c} \, r_1 \left( \frac{z}{B} \right)^n$$ A.5.2.

Both forces are uniformly distributed. Hence:

$$d_4 = d_9 = \tfrac{1}{2} r_1 \cos \psi$$ A.5.3.

## A.6.  THE EQUATIONS OF EQUILIBRIUM FOR THE PLANE SHEAR ZONE

The general equations of equilibrium are presented in section 2.3. By expanding and rearranging the terms, equations 2.3.4. and 2.3.5. may be derived in a form which is more amenable for solution. The equation for horizontal equilibrium is:

$$F_{\gamma_1} \cos \zeta - F_{\gamma_2} \sin(\varphi - \zeta) + F_{c1} \cos \zeta - F_{c2} \sin(\varphi - \zeta)$$

$$= F_{\gamma_s} \cos \delta + F_{c_s} \cos \delta + C_2 \cos \zeta - C_1 \sin(\varphi - \zeta)$$

Multiply each term by $B/\gamma B$. Thus:

$$k_{\varphi\gamma} \left[ V_5 \sin \zeta \cos \zeta - V_6 \sin(\varphi-\zeta) \cos(\varphi-\zeta) \right]$$

$$+ 2 k_{\varphi c} S_1 B^{(n+1)} \left[ V_1 \sin \zeta \cos \zeta - V_2 \sin(\varphi-\zeta) \cos(\varphi-\zeta) \right]$$

$$= \left[ A_3 + S_1 A_4 \right] 2(n+1) B^{2n} \sin \zeta \cos(\varphi-\zeta) \qquad \text{A.6.1.}$$

where:

$$A_3 = \tfrac{1}{2} k_{\gamma_r} z^2 \qquad \text{A.6.2.}$$

$$A_4 = B \left[ r_1 \cos \zeta + k_s z - (z - r_1 \sin \zeta) \tan(\varphi - \zeta) \right] \qquad \text{A.6.3.}$$

$$S_1 = c/\gamma B \qquad \text{A.6.4.}$$

Equation A.6.1. may be written in the form:

$$k_{\varphi\gamma} R_1 + k_{\varphi c} R_2 - R_3 = 0 \qquad \text{A.6.5.}$$

where:

$$R_1 = V_5 \sin \zeta \cos \zeta - V_6 \sin(\varphi-\zeta) \cos(\varphi - \zeta) \qquad \text{A.6.6.}$$

$$R_2 = 2 S_1 B^{(n+1)} \left[ V_1 \sin \zeta \cos \zeta - V_2 \sin(\varphi-\zeta) \cos(\varphi-\zeta) \right] \qquad \text{A.6.7.}$$

$$R_3 = \left[ A_3 + S_1 A_4 \right] 2(n+1) B^{2n} \sin \zeta \cos(\varphi - \zeta) \qquad \text{A.6.8.}$$

When $\zeta = 0$, special forms of equations A.6.1., A.6.6., A.6.7. and A.6.8. are required:

$$k_{\varphi\gamma} \left[ V_5 - 2(n+1) r_1 z^{(2n+1)} \sin \varphi \cos \varphi \right]$$

$$+ 2 k_{\varphi c} S_1 B^{(n+1)} \left[ V_1 - (n+1) r_1 z^n \sin \varphi \cos \varphi \right]$$

$$= \left[ A_3 + S_1 A_4 \right] 2(n+1) B^{2n} \cos \varphi \qquad \text{A.6.1a.}$$

but when $\zeta = 0$:

$$V_1 = z^{(n+1)}$$

$$V_5 = z^{(2n+2)}$$

Thus:

$$R_1 = z^{(2n+1)} \left[ z - 2(n+1) r_1 \sin \varphi \cos \varphi \right] \qquad \text{A.6.6a.}$$

$$R_2 = 2 S_1 B^{(n+1)} z^n \left[ z - (n+1) r_1 \sin \varphi \cos \varphi \right] \qquad \text{A.6.7a.}$$

$$R_3 = \left[ A_3 + S_1 A_4 \right] 2(n+1) B^{2n} \cos \varphi \qquad \text{A.6.8a.}$$

57

The equation for the vertical equilibrium of the plane shear zone may be similarly re-arranged:

$$F_{V_c} \cos(\varphi - \zeta) - F_{Y_1} \sin \zeta + F_{c2} \cos(\varphi - \zeta) - F_{c1} \sin \zeta$$

$$= W_1 + F_{Y_s} \sin \zeta + F_{c3} \sin \zeta + C_1 \cos(\varphi - \zeta) - C_2 \sin \zeta + C_4$$

Multiply each term by $B/\gamma B$:

$$k_{\varphi \gamma} \left[ V_6 \cos^2(\varphi - \zeta) - V_5 \sin^2 \zeta \right]$$

$$+ 2 k_{\varphi c} S_1 B^{(n+1)} \left[ V_2 \cos^2(\varphi - \zeta) - V_1 \sin^2 \zeta \right]$$

$$= \left[ A_5 + S_1 A_6 + S_2 A_7 \right] 2 (n+1) B^{2n} \sin \zeta \cos(\varphi - \zeta) \qquad \text{A.6.9.}$$

where:

$$A_5 = \frac{A_1}{2 \cos(\varphi - \zeta)} + \frac{k_{Y_s} z^2 \tan \zeta}{2} \qquad \text{A.6.10.}$$

$$A_6 = B \left[ z (1 + k_{c_1} \tan \zeta) - 2 r_1 \sin \zeta \right] \qquad \text{A.6.11.}$$

$$A_7 = Bz \qquad \text{A.6.12.}$$

$$S_2 = c_a / \gamma B \qquad \text{A.6.13.}$$

Expressing equation A.6.9. in the form:

$$k_{\varphi \gamma} R_4 + k_{\varphi c} R_5 - R_6 = 0 \qquad \text{A.6.14.}$$

the equations for the constants are:

$$R_4 = \left[ V_6 \cos^2(\varphi - \zeta) - V_5 \sin^2 \zeta \right] \qquad \text{A.6.15.}$$

$$R_5 = 2 S_1 B^{(n+1)} \left[ V_2 \cos^2(\varphi - \zeta) - V_1 \sin^2 \zeta \right] \qquad \text{A.6.16.}$$

$$R_6 = \left[ A_5 + S_1 A_6 + S_2 A_7 \right] 2 (n+1) B^{2n} \sin \zeta \cos(\varphi - \zeta) \qquad \text{A.6.17.}$$

When $\zeta = 0$, a special form of equation A.6.9. is again required:

$$k_{\varphi \gamma} r_1 z^{(2n+1)} \cos \varphi + k_{\varphi c} S_1 B^{(n+1)} r_1 z^n \cos \varphi$$

$$= \left[ A_5 + S_1 A_6 + S_2 A_7 \right] B^{2n} \qquad \text{A.6.9a.}$$

For this special case, the equations for the constants are:

58

$$R_4 = r_1 \, z^{(2b+1)} \cos \varphi \qquad\qquad \text{A.6.15a.}$$

$$R_5 = S_1 \, B^{(b+1)} \, r_1 \, z^b \, \cos \varphi \qquad\qquad \text{A.6.16a.}$$

$$R_6 = [A_2 + S_1 \, A_6 + S_2 \, A_7] \, B^{2b} \qquad\qquad \text{A.6.17a.}$$

## A.7. THE SOLUTION FOR $k_{\varphi \gamma}$, n AND $\zeta$ IN A FRICTIONAL MATERIAL WITH WEIGHT

In a non-cohesive soil, the values of $k_{\varphi \gamma}$ and n may be obtained in terms of $\zeta$ from the equations of horizontal and vertical equilibrium. Selecting the relevant terms due to weight in equations A.6.1. and A.6.9. respectively:

$$k_{\varphi \gamma} = \frac{2 \, A_3 \, (n+1) \, B^{2b} \, \sin \zeta \, (\varphi - \zeta)}{V_5 \sin \zeta \cos \zeta - V_6 \sin (\varphi - \zeta) \cos (\varphi - \zeta)} \qquad\qquad \text{A.7.1.}$$

and:

$$k_{\varphi \gamma} = \frac{2 \, A_5 \, (n+1) \, B^{2b} \, \sin \zeta \, \cos (\varphi - \zeta)}{V_6 \cos^2 (\varphi - \zeta) - V_5 \sin^2 \zeta} \qquad\qquad \text{A.7.2.}$$

Combining equations A.7.1. and A.7.2., and expanding the terms $V_5$ and $V_6$ according to equations A.1.6. and A.1.8. :

$$z_3^{2(b+1)} \, A_8 = z_2^{2(b+1)} \, (A_8 + A_9) \qquad\qquad \text{A.7.3.}$$

where:

$$A_8 = \cos (\varphi - \zeta) \, [A_3 \cos (\varphi - \zeta) + A_5 \sin (\varphi - \zeta)] \qquad\qquad \text{A.7.4.}$$

$$A_9 = \sin \zeta \, [A_3 \sin \zeta + A_6 \cos \zeta] \qquad\qquad \text{A.7.5.}$$

Thus:

$$n = \frac{\log (A_8 + A_9) - \log A_8}{2(\log z_3 - \log z_2)} - 1 \qquad\qquad \text{A.7.6.}$$

Similarly the expressions for $k_{\varphi \gamma}$ and n may be determined from equations A.6.1a. and A.6.9a. when $\zeta = 0$:

$$k_{\varphi \gamma} = \frac{2 \, A_3 \, (n+1) \, B^{2b} \, \cos \varphi}{V_5 - 2 \, (n+1) \, r_1 \, z^{(2b+1)} \sin \varphi \, \cos \varphi} \qquad\qquad \text{A.7.1a.}$$

and:

$$k_{\varphi \gamma} = \frac{2 \, A_5 \, (n+1) \, B^{2b} \, \cos \varphi}{2 \, (n+1) \, r_1 \, z^{(2b+1)} \, \cos^2 \varphi} \qquad\qquad \text{A.7.2a.}$$

Thus:

$$n = \frac{z \, A_5}{2 \, r_1 \, A_3} - 1 \qquad\qquad \text{A.7.6a.}$$

The values of $n$ and $k_{\varphi c}$ may be determined for any value of $\zeta$ and the input parameters. The value of $\zeta$ satisfying all three equations may be found by substitution in the equation of rotational equilibrium (equation 2.3.5.).

## A.8. THE SOLUTION FOR $k_{\varphi c}$, $n$ AND $\zeta$ IN A FRICTIONAL-COHESIVE MATERIAL WITHOUT WEIGHT

In a frictional-cohesive material without weight, the foundation shaft is assumed to be unsupported. Using the same analytical method as in section A.7., equations A.6.1. and A.6.9., respectively, may be presented in the form:

$$k_{\varphi c} = \frac{[r_1 \cos \zeta - (z - r_1 \sin \zeta) \tan (\varphi - \zeta)](n+1) \; B^n \; \sin \zeta \; \cos (\varphi - \zeta)}{V_1 \sin \zeta \cos \zeta - V_2 \sin (\varphi - \zeta) \cos (\varphi - \zeta)} \qquad \text{A.8.1.}$$

and

$$k_{\varphi c} = \frac{[z - 2 r_1 \sin \zeta] (n+1) \; B^n \; \sin \zeta \; \cos (\varphi - \zeta)}{V_2 \cos^2 (\varphi - \zeta) - V_1 \sin^2 \zeta} \qquad \text{A.8.2.}$$

Thus:

$$n = \frac{\log [z_2 \sin \zeta + r_1 \cos^2 (\varphi - \zeta)] - \log [r_1 \cos^2 (\varphi - \zeta)]}{\log z_3 - \log z_2} - 1 \qquad \text{A.8.3.}$$

It may be shown that rotational equilibrium is achieved only when the two failure boundaries, BD and DE, are of equal length which gives the relationship:

$$z = r_1 \sin \zeta + r_1 \cos (\varphi - \zeta)$$

Using this equilibrium condition in equation A.8.1. and A.8.3., $k_{\varphi c} = 1$ and $n = 0$ for any value of $\zeta$.

## A.9. THE SOLUTION FOR $k_{\varphi c}$, $n$ AND $\zeta$ IN A FRICTIONAL-COHESIVE MATERIAL WITH WEIGHT

When both weight and cohesion are present, the coefficient $k_{\varphi c}$ may be determined from the quadratic equation A.6.9. in terms of $n$ and $\zeta$:

$$k_{\varphi c} = \frac{- R_5 \pm (R_5^2 + 4R_4 \; R_6)^{\frac{1}{2}}}{2 R_4} \qquad \text{A.9.1.}$$

One root, derived by subtracting the discriminator, is valid when $\zeta < 0$ and the other root is valid when $\zeta \geq 0$.

The values of $n$ and $\zeta$ may be found by substitution in the equations for the horizontal and rotational equilibrium of the plane shear zone.

60

THE FORCES IN THE RADIAL SHEAR ZONE

The area of the spiral sector, BCD, is determined first:

$$\Delta_c = \int_c^u \tfrac{1}{2} r^2 \, d\psi$$

$$= \frac{1}{4 \tan \varphi} (r_1^2 - r_c^2) \qquad\qquad \text{A.10.}$$

Thus, the weight of the zone is:

$$W = \gamma \Delta_c \qquad\qquad \text{A.10.}$$

In order to calculate the moment of cohesion about the pole of the spiral, consider a small element of length $\delta l$ (Fig. A.10.1.). Taking moments about B:

$$dM_c = c \, dl \, r \, \cos \varphi$$

But:

$$dl = \frac{r \, d\psi}{\cos \varphi}$$

$$\therefore \qquad dM_c = c \, r^2 \, d\psi$$

Integrating:

$$M_c = \int_c^u c \, r^2 \, d\psi$$

$$= \frac{c}{2 \tan \varphi} (r_1^2 - r_c^2) \qquad\qquad \text{A.10.3.}$$

For the special case when $\varphi = 0$, the spiral reduces to a circle:

$$\Delta_0 = \tfrac{1}{2} r_0^2 \, \psi \qquad\qquad \text{A.10.1a.}$$

$$M_c = c \, r_0^2 \, \psi \qquad\qquad \text{A.10.3a.}$$

## A.11. THE MOMENT ARM FOR THE WEIGHT FORCE IN THE RADIAL SHEAR ZONE

The determination of the moment arm, $d_2$, for the weight force, W, of the spiral sector, BCD, is not possible directly. The moment of area for the spiral sector with respect to the pole of the spiral is determined instead (Fig. A.11.1.). In the limit, as $\psi \to 0$, the area of the spiral sector approximates to that of a triangle and the centroid is then approximately that of a triangle. Taking one axis, $\eta$, along $r_0$ and the other axis, $\zeta$, normal to it and passing through the pole of the spiral, the cartesian co-ordinates of the centroid are $(\eta_0, \zeta_0)$ where:

61

$$\eta_0 = \int_0^u \tfrac{2}{3}\, r \cos\omega\, d\omega$$

and:

$$\zeta_0 = \int_0^u \tfrac{2}{3}\, r \cos\omega\, d\omega$$

The moment of area, $\Delta_0\, \zeta_0$, is given by the equation:

$$M_\zeta = \tfrac{1}{2} \int_0^u r^2\, d\omega \cdot \tfrac{2}{3} \int_0^u r \sin\omega\, d\omega$$

$$= \tfrac{1}{3}\, r_c^3 \int_0^u e^{3\omega\tan\varphi} \sin\omega\, d\omega$$

Integrating by parts, the final expression is in the form:

$$M_\zeta = v\, [\, r_1^3\, (u \sin\omega - \cos\omega) + r_0^3\,]\qquad\qquad \text{A.11.1.}$$

where:

$$u = 3 \tan\varphi \qquad\qquad \text{A.11.2.}$$

$$v = \frac{1}{3\,(1 + u^2)} \qquad\qquad \text{A.11.3.}$$

The moment of area, $\Delta_c\, \eta_0$, may be derived in a similar way:

$$M_\eta = \tfrac{1}{3}\, r_c^3 \int_0^u e^{3\omega\tan\varphi} \cos\omega\, d\omega$$

After integration:

$$M_\eta = v\, [\, r_1^3\, (\sin\omega + u \cos\omega) - u r_c^3\,]\qquad\qquad \text{A.11.4.}$$

Transforming the $\eta$, $\zeta$ axes at the pole of the spiral to x, y axes, the following relationships are derived (Fig. A.11.2.):

$$x_0 \cos\omega = -(r_0 + y_0 \sin\omega) \qquad\qquad \text{A.11.5.}$$

$$x_0 \sin\omega = \zeta_0 + y_0 \cos\omega \qquad\qquad \text{A.11.6.}$$

The moments of area, $\Delta_0\, x_0$, about the pole of the spiral can be written in the form:

$$\Delta_0 x_0 = \Delta_0 x_0 (\cos^2\omega + \sin^2\omega)$$

$$= \Delta_c \cos\omega\, (x_0 \cos\omega) + \Delta_0 \sin\omega\, (x_c \sin\omega)$$

Substituting for $x_0 \cos\omega$ and $x_0 \sin\omega$ from equations A.11.5. and A.11.6., the following expression for the moment of area is obtained:

$$\Delta_0 x_0 = M_\zeta \sin\omega - M_\eta \cos\omega \qquad\qquad \text{A.11.7.}$$

$$\therefore \quad d_2 = x_0 = \frac{M_\zeta \sin \psi - M_\eta \cos \psi}{A_2}$$

The moment arm, $d_2$, is derived in this general form to be applicable to bearing capacity analyses in which the pole of the spiral is not necessarily located at the corner of the footing.

## A.12.    THE MOMENT ARMS FOR THE RESULTANT FORCES

It is assumed that the resultant weight-frictional component of pressure is distributed hydrostatically. Considering an inclined plane surface of unit width immersed in a homogeneous material, the centre of pressure may be determined by hydrostatics (Fig. A.12.1.).

$$L = k^2 d$$

where K is the radius of gyration and is given by the equation:

$$k^2 = \frac{1^2}{12} + d^2$$

But, it can be shown that:

$$d = \frac{z_1 + z_2}{2 \sin \zeta}$$

and

$$1 = \frac{z_2 - z_1}{\sin \zeta}$$

Combining these relationships, the distance, L, of the centre of pressure from the surface along an inclined plane is:

$$L = \frac{2(z_1^2 + z_2^2 + z_1 z_2)}{3(z_1 + z_2) \sin \zeta} \qquad \text{A.12.1.}$$

The moment arm for the resultant weight-frictional force on the wedge boundary may be found by substituting the values:

$$z_1 = z$$

$$z_2 = z + \tfrac{1}{2} B \tan \psi$$

in equation A.12.1. This yields the equation:

$$d_c = \frac{B(3z \cos \psi + B \sin \psi) \cos \omega}{3(4z \cos \psi + B \sin \psi) \cos \psi} \qquad \text{A.12.2.}$$

As the resultant cohesive-frictional force is assumed to act at the midpoint of the wedge

boundary, the moment is:

$$d_{11} = \frac{B \cos \varphi}{4 \cos(45 + \varphi/2)}$$

A.12.3.

## A.13. THE DETERMINATION OF THE RESULTANT BEARING CAPACITY

The complete system of forces and moment arms is shown in Fig. A.13.1. By taking moments about the pole of the spiral, the resultant forces, $F_\gamma$ and $F_c$, are determined for the general case when a side thrust is applied to the wall of the excavation:

$$F_\gamma = \frac{W_1 \ d_1 + W \ d_2 - F_{\gamma_1} \ d_3 + F_{\gamma_2} \ d_4}{d_5}$$

A.13.1.

$$F_c = \frac{C_1 \ d_7 - F_{c1} \ d_8 + F_{c2} \ d_{10} + M_c}{d_{11}}$$

A.13.2.

The total force on the base of the footing due to the weight of the soil mass at failure is obtained from the vertical component of the force, $F_\gamma$, on both boundaries of the wedge, less the weight of the soil wedge; the total force due to cohesion is obtained from the vertical components of the forces $F_c$ and $C_3$ acting on the wedge boundaries (Fig. A.13.2.):

$$F \ lb/in = 2F_\gamma \cos(\zeta - \omega) - \frac{\gamma B^2 \tan \psi}{4} + 2F_c \cos(\psi - \varphi) + 2 \ C_3 \sin \tau$$

This expression for the base resistance may be written in the form of a two part additive equation:

$$F \ lb/in = \tfrac{1}{2} \gamma B^2 N_\gamma + cBN_c$$

A.13.3.

where:

$$N_\gamma = \frac{4 F_\gamma \cos(\gamma - \varphi)}{\gamma B^2} \cdot \tan \gamma$$

A.13.4.

$$N_c = \frac{2 [F_c \cos(\psi - \varphi) + C_3 \sin \psi]}{c B}$$

A.13.5.

The dimensionless bearing capacity factors, $N_\gamma$ and $N_c$, are a function of $\varphi$, $\delta$, $c/\gamma B$, $z/B$, $k_{\gamma_s}$ and $k_{c_s}$.
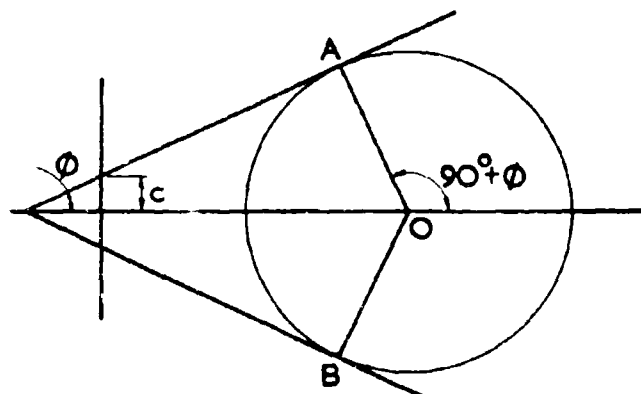
FIG. I. 2.I. MOHR CIRCLE ILLUSTRATING THE
TWO PLANES OF INCIPIENT FAILURE.
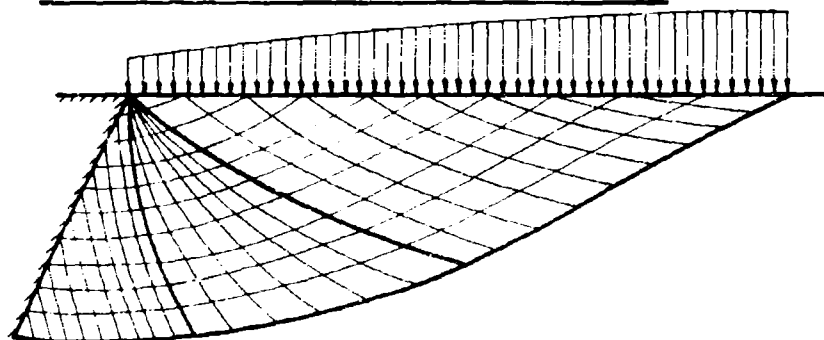
FIG. I. 2.2. THE GENERAL FORM OF A CURVED
SLIP LINE FIELD WITH ONE SINGULAR POINT.
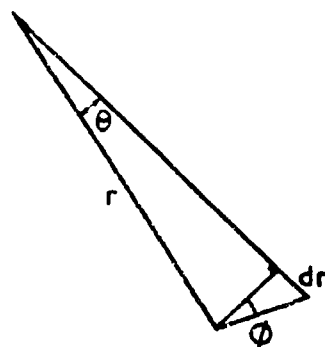
FIG. I. 2.3. THE DEVELOPMENT OF THE EQUATION
FOR THE CURVED SLIP LINES IN A RADIAL FAN.

65
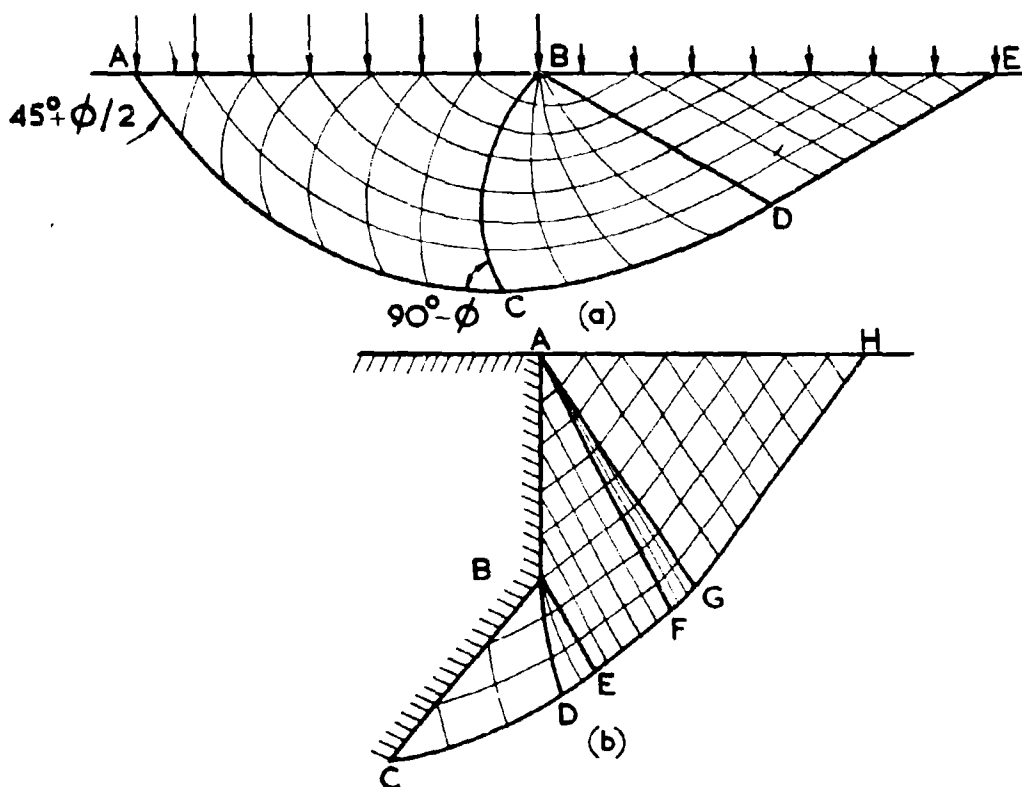
FIG.I.2.4. TYPICAL SLIP LINE FIELDS DETERMINED BY SOKOLOVSKI.

(a) THE ASYMMETRICAL FAILURE FOR A SURFACE FOUNDATION.

(b) FAILURE FOR A BROKEN BACK RETAINING WALL.
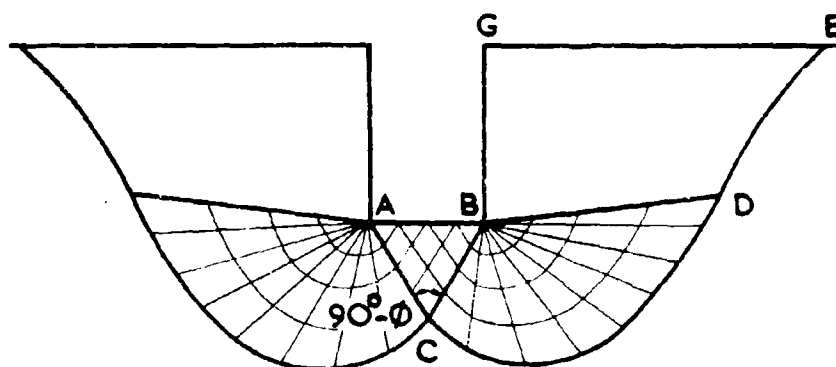


FIG. I. 2.5. THE INCOMPLETE SLIP LINE FIELD FOR SYMMETRICAL
SOIL FAILURE BENEATH A BURIED FOUNDATION.
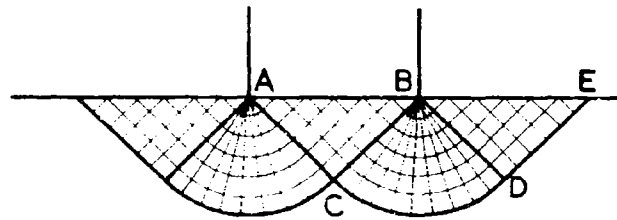
(a) PRANDTL
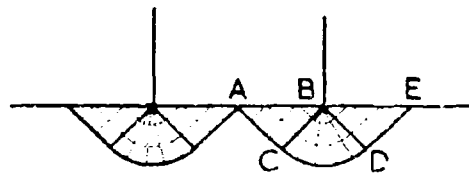


(b) HILL

FIG. 1.3.1. SOLUTIONS FOR THE STRESS FIELDS IN AN
IDEALLY PLASTIC METAL DEFORMED BY A FLAT PUNCH.
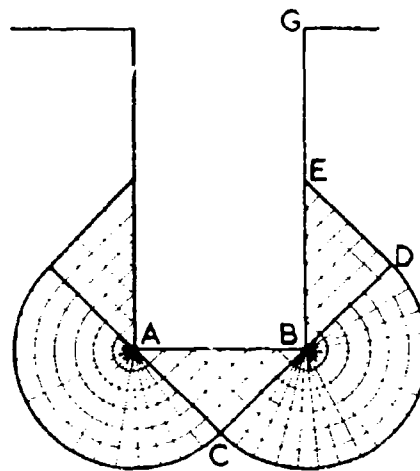


FIG. 1.3.2. JAKY'S SOLUTION OF THE STRESS FIELD
FOR THE MAXIMUM BASE RESISTANCE OF A
DEEP PILE IN AN IDEALLY PLASTIC CLAY.
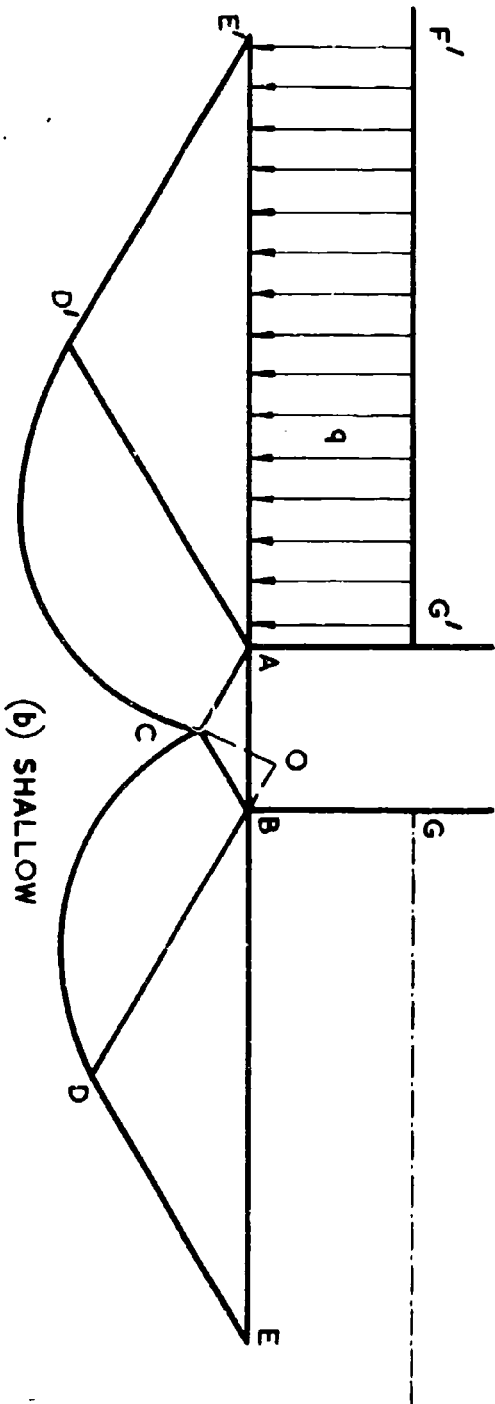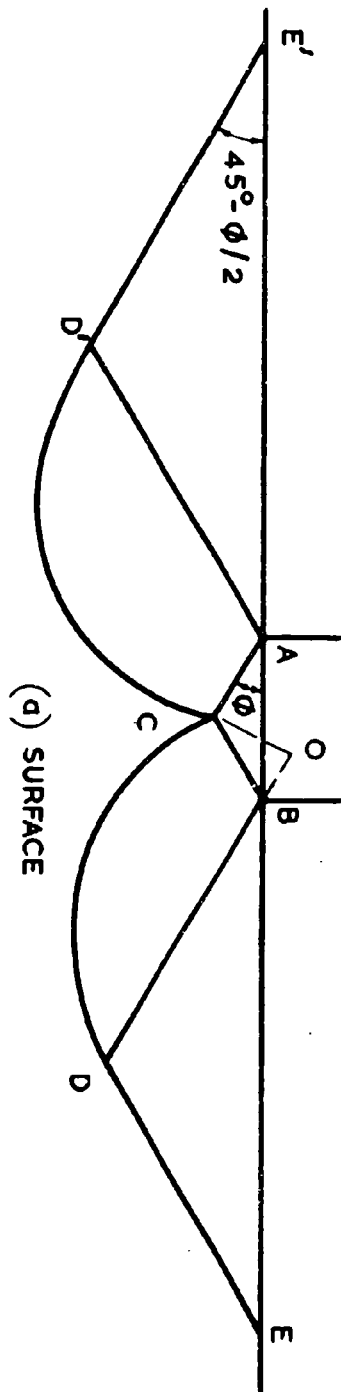
FIG. 1.4.1. FOUNDATION FAILURE AFTER TERZAGHI, FOR COHESION AND SURCHARGE (LHS), AND WEIGHT (RHS)

(a) SURFACE

(b) SHALLOW

SMOOTH BASE ⊢— B —⊣ ROUGH BASE q

(a) $q/\gamma B = \infty$

(b) $0 < q/\gamma B < \infty$

(c) $q/\gamma B = 0$
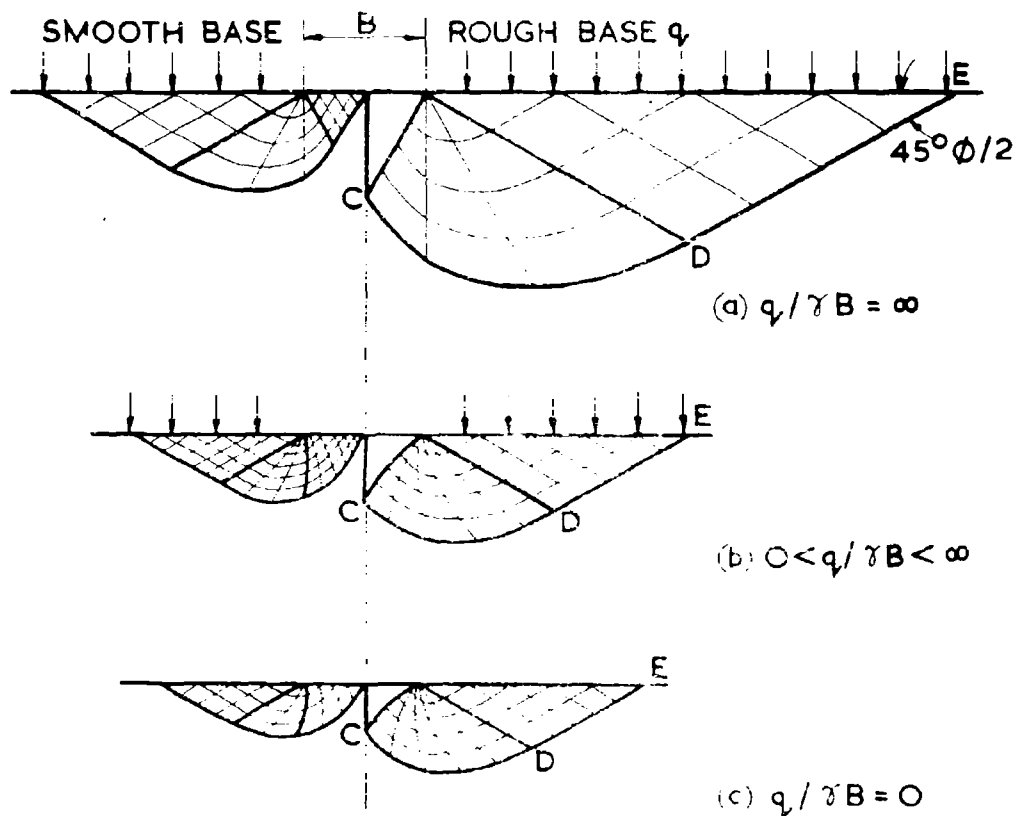
FIG. I.4.2. FAILURE PATTERNS UNDER A SHALLOW FOUNDATION
FOR c = O AND Ø = 30° (AFTER LUNDGREN AND MORTENSEN)
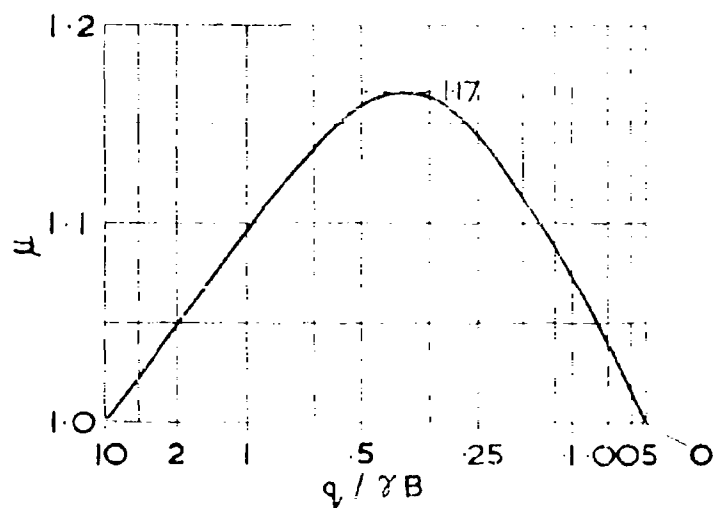
FIG 1.4.3. CORRECTION FACTOR FOR THE BEARING CAPACITY
OF A SHALLOW FOUNDATION
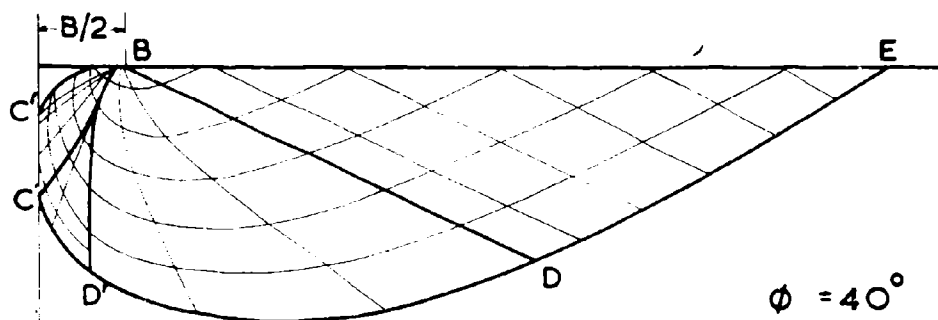
FIG. I.4.4. THE FAILURE PATTERN BY THE THEORIES OF PLASTICITY AND ELASTICITY (AFTER GORBUNOV − POSSADOV)

BC'− BOUNDARY OF THE ELASTIC PART OF THE COMPACTED CORE.

BC − BOUNDARY OF COMPLETE CORE.
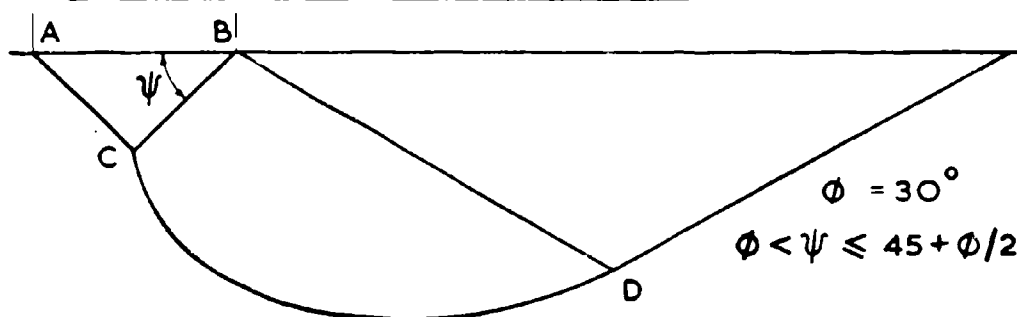


FIG. I.4.5. THE FAILURE PATTERN BY THE VARIABLE FACTORS THEORY (AFTER HU)
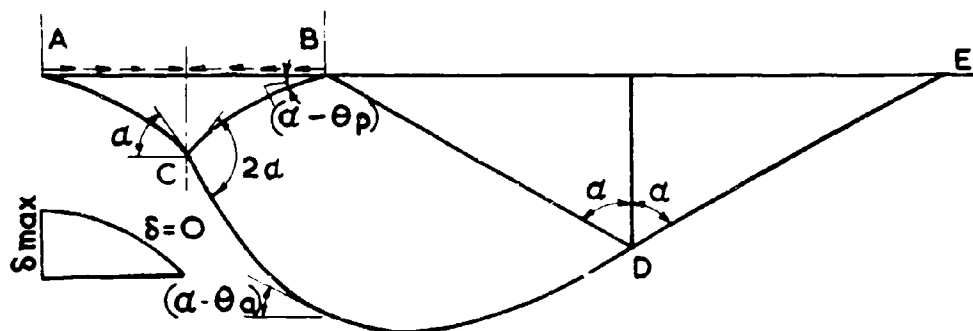


FIG. I.4.6. THE FAILURE PATTERN BY THE STRESS − DILATANCY THEORY (AFTER ROWE)

70

FIG.1.5.1.   FOUNDATION FAILURE AFTER MEYERHOF, FOR
COHESION, SURCHARGE AND SKIN FRICTION (LHS),
AND WEIGHT (RHS).



FIG.1.5.2.   FAILURE BENEATH A BURIED FOUNDATION
AT  z/B $\lessgtr$ 1.5 AFTER BALLA
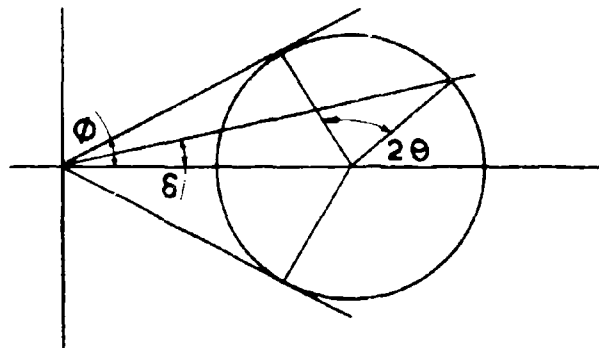
FIG.2.1.1. THE ORIENTATION OF SLIP PLANES AT THE
STRUCTURE FOR KNOWN INTERFACE FRICTION.
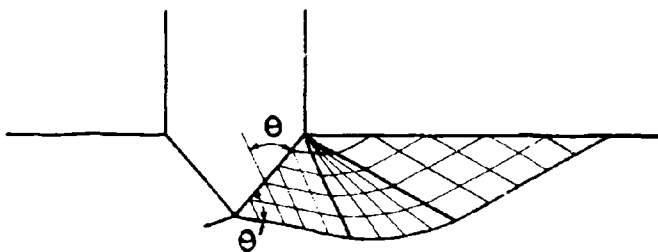


FIG.2.1.2. THE STRESS FIELD FOR A WEDGE-SHAPED
FOUNDATION AFTER MINTSKOVSKY.
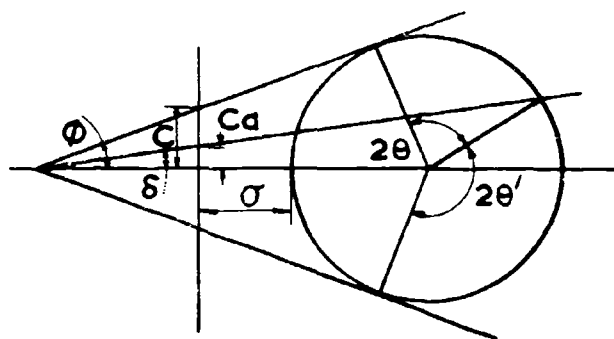


FIG.2.1.3. THE ORIENTATION OF THE SLIP PLANES AT THE
STRUCTURE FOR KNOWN INTERFACE FRICTION AND
ADHESION.

72
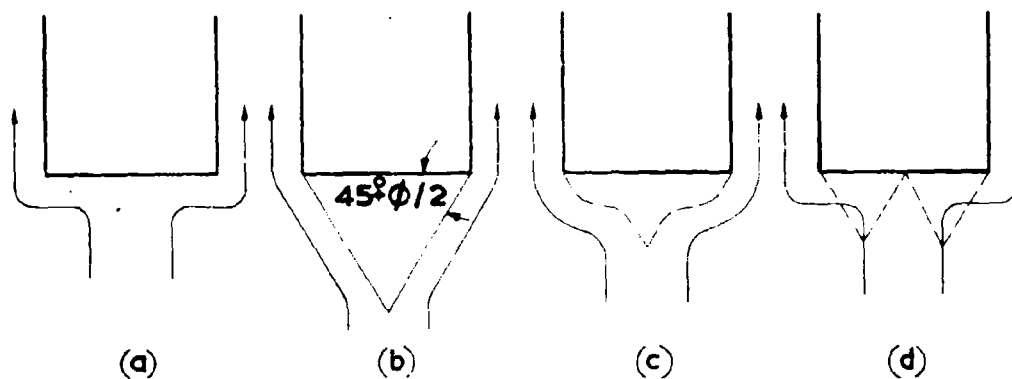
FIG. 2.2.1. THE SOIL FLOW PATH BENEATH A PERFECTLY SMOOTH FOOTING MODIFIED BY POSSIBLE CONFIGURATION OF THE FIXED SOIL BODY.
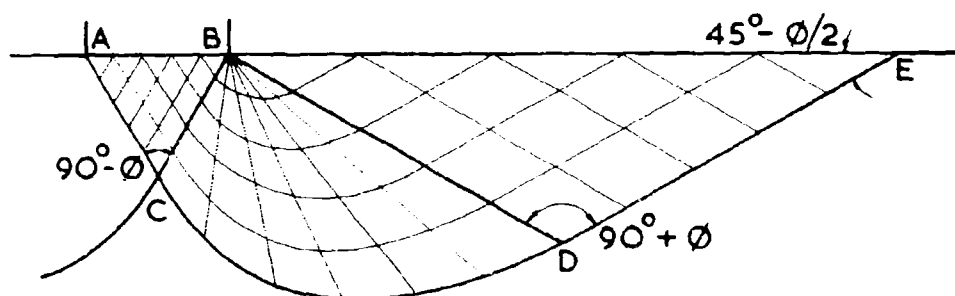


FIG. 2.2.2. THE COMPLETE STRESS FIELD FOR A SURFACE FOUNDATION.
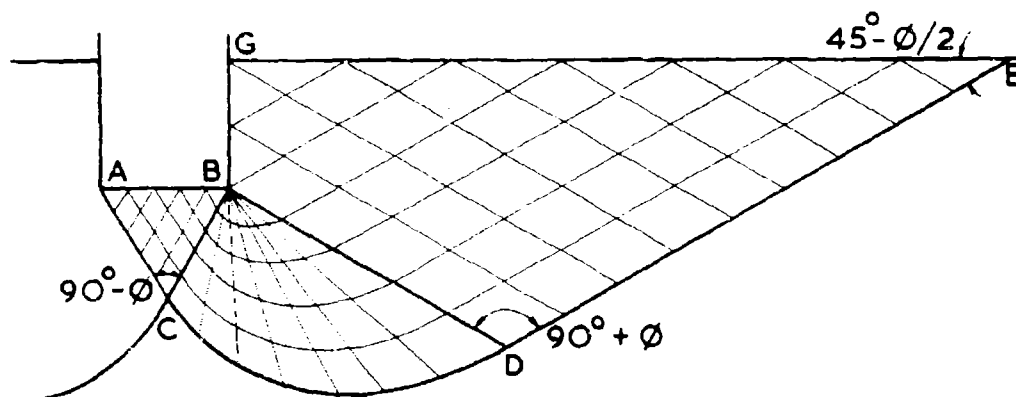


FIG. 2.2.3. THE COMPLETE STRESS FIELD FOR A DEEP FOUNDATION WHEN PASSIVE PRESSURE ACTS ALONG WALL BG.
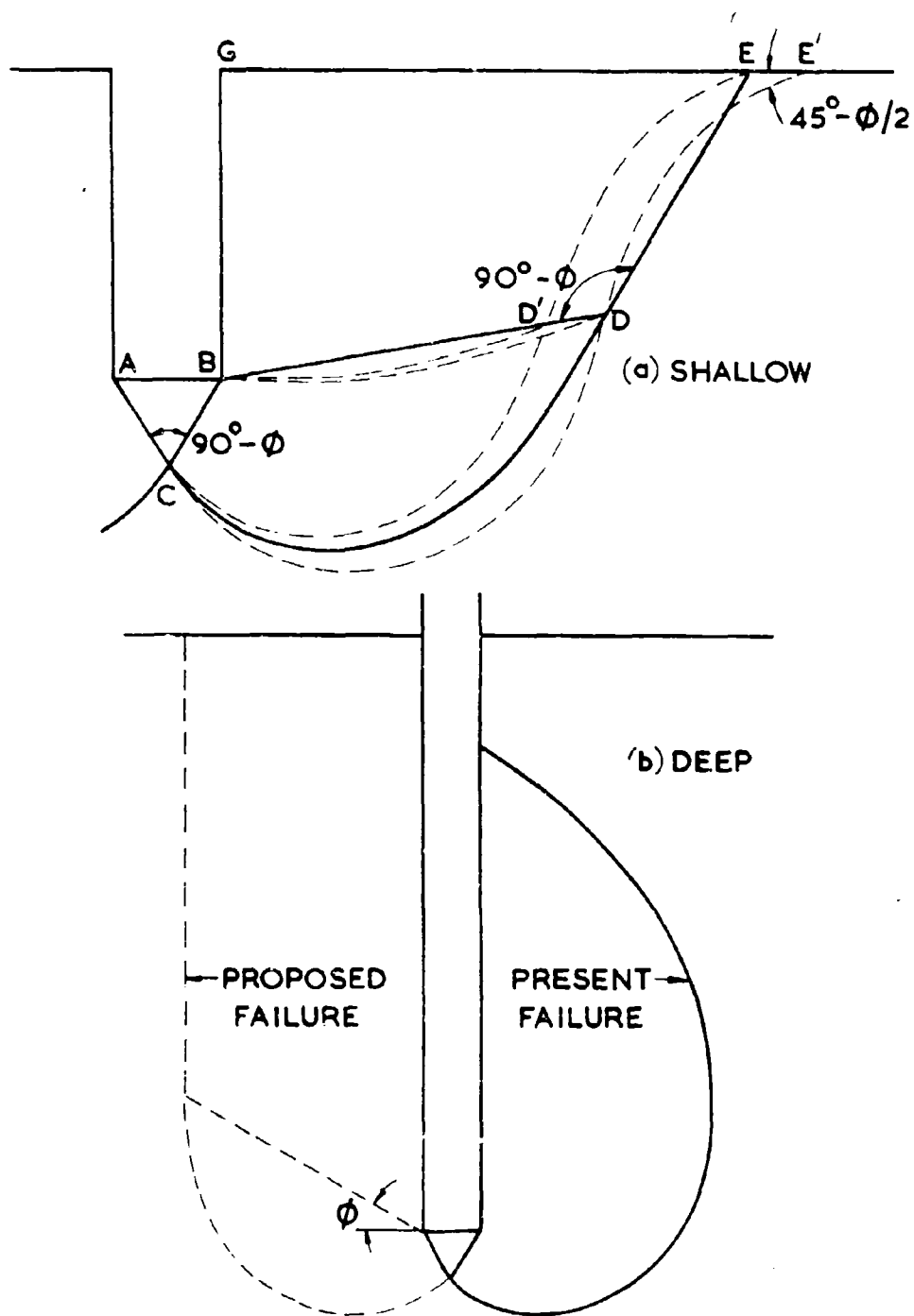
FIG. 2.2.4. THE POSSIBLE CONFIGURATIONS OF THE
FAILURE GEOMETRY FOR A BURIED FOUNDATION

74
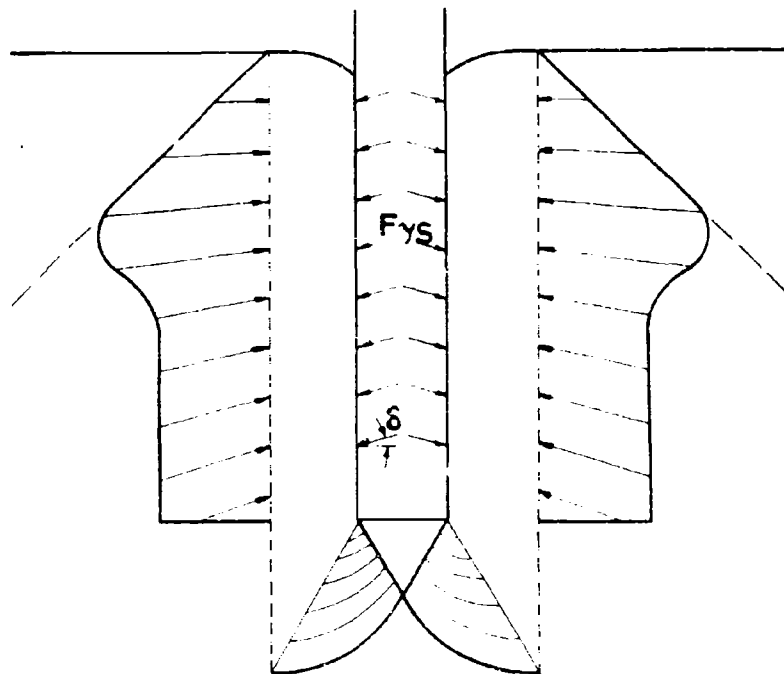
FIG. 2.2.5. THE FAILURE PATTERN AND VARIATION IN SKIN RESISTANCE
FOR A DEEP FOUNDATION IN DENSE SAND (AFTER VESIĆ)
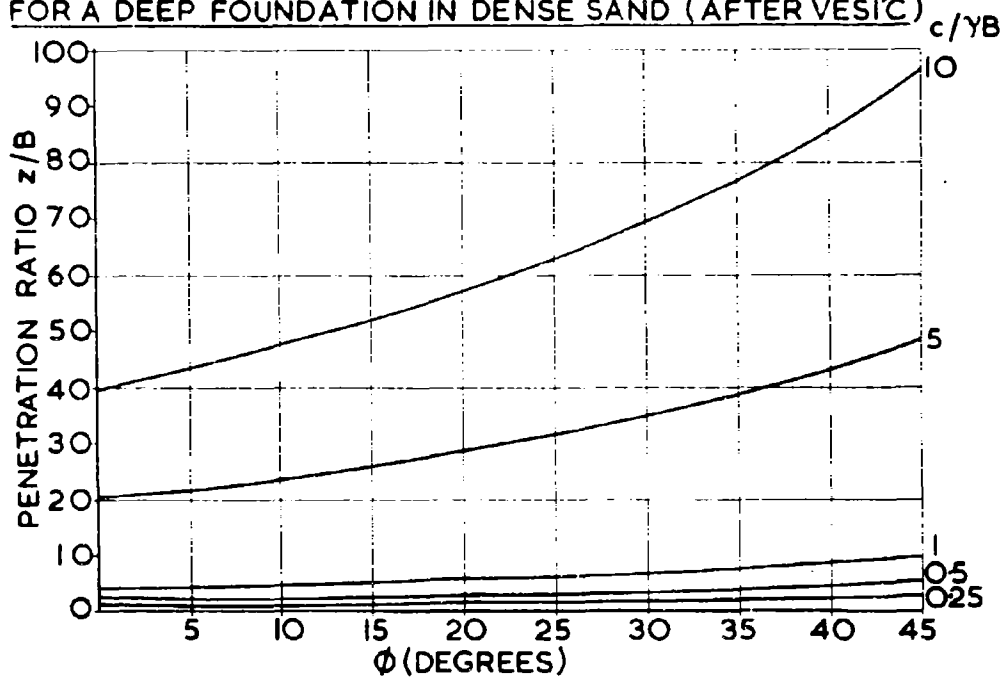


FIG. 2.2.6. THE CRITICAL HEIGHT OF A VERTICAL BANK.

FIG. 2.3.1. THE GENERAL SHAPE OF THE FIGURE OF RUPTURE IN A FRICTIONAL SOIL WITH WEIGHT SHOWING THE FORCES IN THE PLANE SHEAR ZONE, THE NORMAL STRESS DISTRIBUTION ALONG THE BOUNDARIES & THE MOMENT ARMS.

START

**INPUT DATA**

| | | | |
|---|---|---|---|
| $\emptyset$ | ANGLE OF INTERNAL SHEARING RESISTANCE | c | COHESION |
| $\delta$ | ANGLE OF INTERFACE FRICTION | $c_a$ | ADHESION. |
| $k_{\delta s}$ | SHAFT COEFFICIENT OF EARTH PRESSURE DUE TO SOIL WEIGHT | $\gamma$ | DENSITY |
| $k_{cs}$ | SHAFT COEFFICIENT OF EARTH PRESSURE DUE TO COHESION | z | SINKAGE |
| B | WIDTH OF FOOTING | | |

YES — $z/B = 0$ — NO — $c/\gamma B = \infty$ — YES

$\delta = -(45 - \emptyset/2)$
$n = 0$
$k_{\emptyset s} = TAN^2(45 + \emptyset/2)$

SELECT VALUE OF ZETA IN RANGE : $-(45 - \emptyset/2) < \delta < 90$

$n = 0$
$k_{\emptyset c} = 1$

DETERMINE SINKAGE FOR COMPLETE SHEAR BULB
$z_{LIM} = B \cdot e^{n\,TAN\emptyset} TAN(45 + \emptyset/2)$

SELECT NEW VALUE OF $\delta$

DETERMINE $n$ EQN 1 2 3

$\delta > \emptyset$ — YES

$z \geq z_{LIM}$ — YES

DETERMINE SINKAGE FOR COMPLETE SHEAR BULB
$z_{LIM} = \dfrac{r \cos\emptyset}{SIN(\emptyset - \delta)}$

NO

$\delta = 45 + \emptyset/2$

SOLVE FOR $\delta$ BY SUBSTITUTION
$z/B = e^{\omega\,TAN\emptyset}[COS(\emptyset - \delta) + SIN \delta]/2 \, TAN(45 + \emptyset/2)$

$z_{LIM} > z$ — NO

NO SOLN

YES

$c/\gamma B = 0$ — YES

DETERMINE $n$
EQN A.7.6 OR A.7.6a

DETERMINE $k_{\emptyset s}$
EQN A.7.1 OR A.7.1a

SELECT VALUE OF $n$ IN RANGE : $-0.99 < n < 3$

SELECT NEW VALUE OF $n$

DETERMINE $k_{\emptyset c}$
EQN A.9.1

$\omega = 3\pi/4 - \emptyset/2 + \delta$

DETERMINE $\Sigma F_H$
EQN 2.3.4

DETERMINE $N_c$ :
$N_c = [1 - 1/SIN\emptyset + e^{\omega\,TAN\emptyset}(1 + 1/SIN\emptyset)] TAN(45 + \emptyset/2)$

$\Sigma F_H = 0$ — NO

DETERMINE $\Sigma M_o$
EQN 2.3.6

$\Sigma M_o = 0$ — NO

DETERMINE $N_\delta$, $N_c$
EQNS 5.2.1, 5.2.3

DETERMINE $N_\delta$, $N_c$
EQNS A.13.4, A.13.5

DETERMINE $N_\gamma$
EQN A.13.4

DETERMINE $f$
$f = [r \, COS\emptyset - z \, SIN(\emptyset - \delta)] \, COS(\emptyset - \delta)$

**PRINT OUT**

| | |
|---|---|
| $\delta$ | ANGLE OF INCLINATION OF PLANE BOUNDARY |
| $k_{\emptyset c}, k_{\emptyset s}$ | BOUNDARY COEFFICIENTS OF EARTH PRESSURE |
| $n$ | BOUNDARY EXPONENT |
| $N_\gamma$, $N_c$ | BEARING CAPACITY FACTORS |
| $f$ | RUPTURE DISTANCE |

END

## FIG. 2.4.1. THE BLOCK DIAGRAM.

FIG. 2.5.1. VALUES OF THE $N_\gamma$ FACTOR FOR $c/\gamma B = 0$ AND $k_{\gamma s} = 1$.

FIG. 2.5.2. VALUES OF THE $N_\gamma$ FACTOR

FOR $c/\gamma B = 0$ AND $k_{\gamma s} = k_a$.
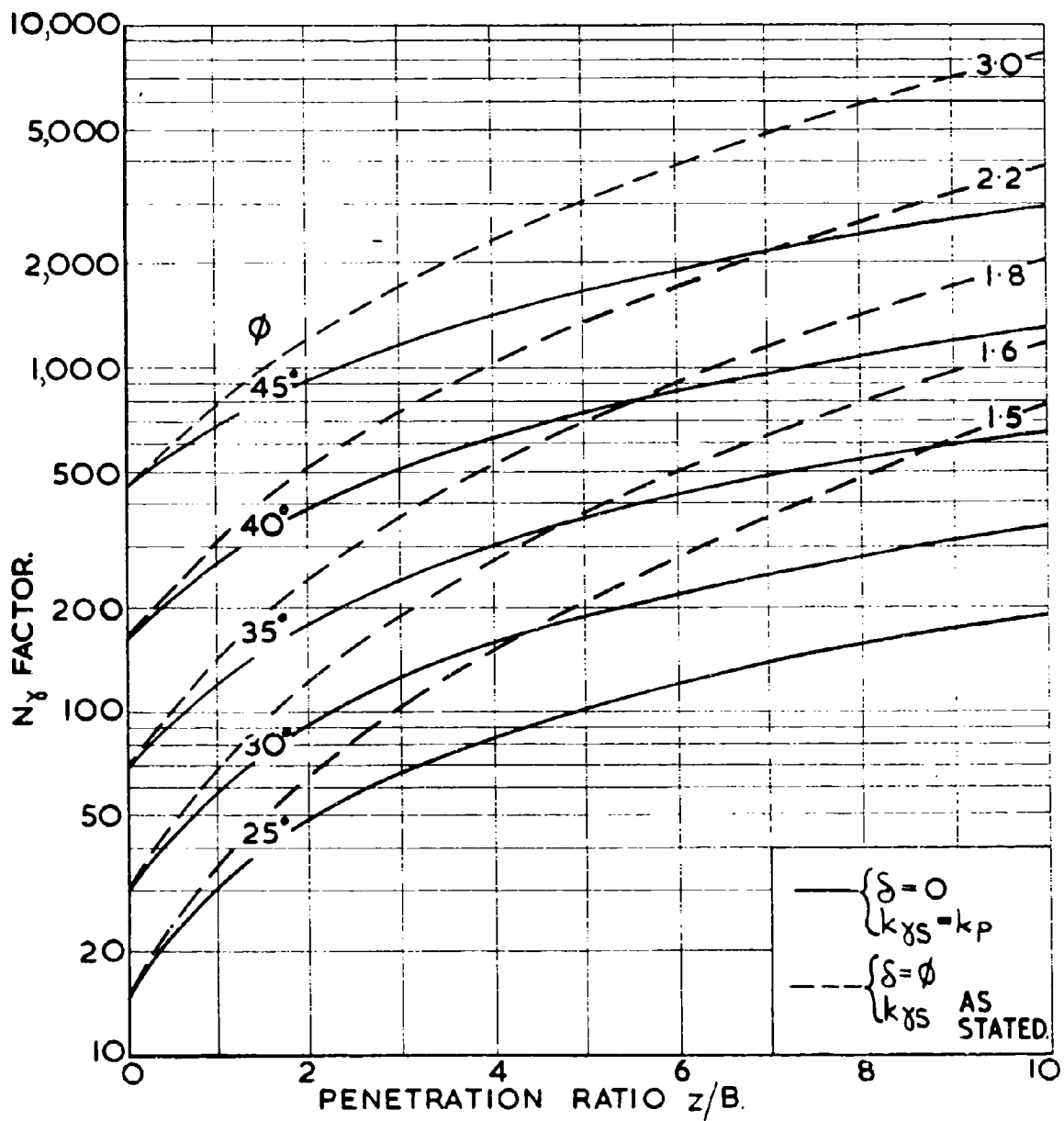
FIG. 2.5.3. VALUES OF THE $N_\gamma$ FACTOR FOR $c/\gamma B = 0$ AND $k_{\gamma S} > 1$.
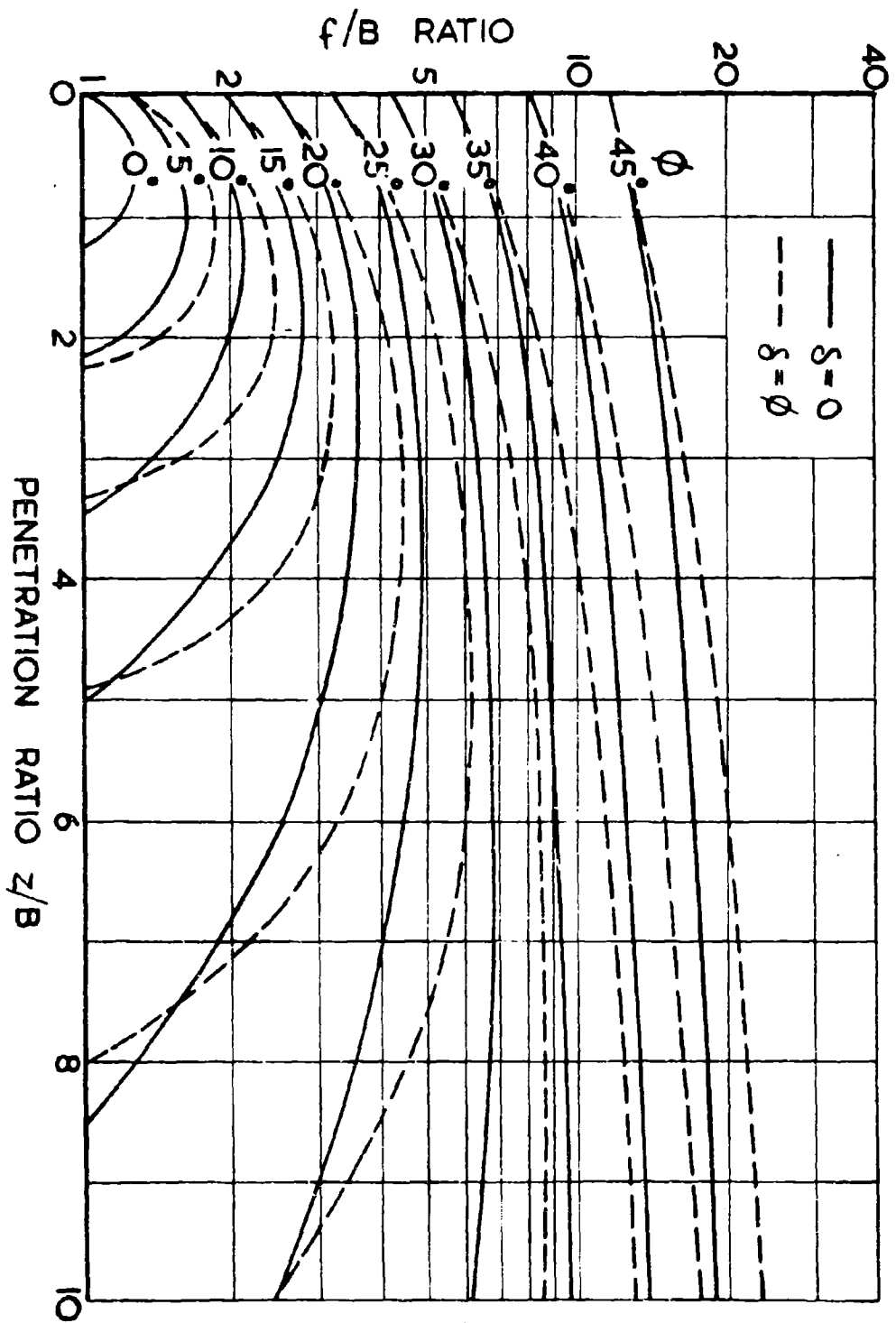
FIG. 2.5.4. THE RUPTURE DISTANCE FOR $c/\gamma B = 0$ AND $k_{\gamma s} = 1$.
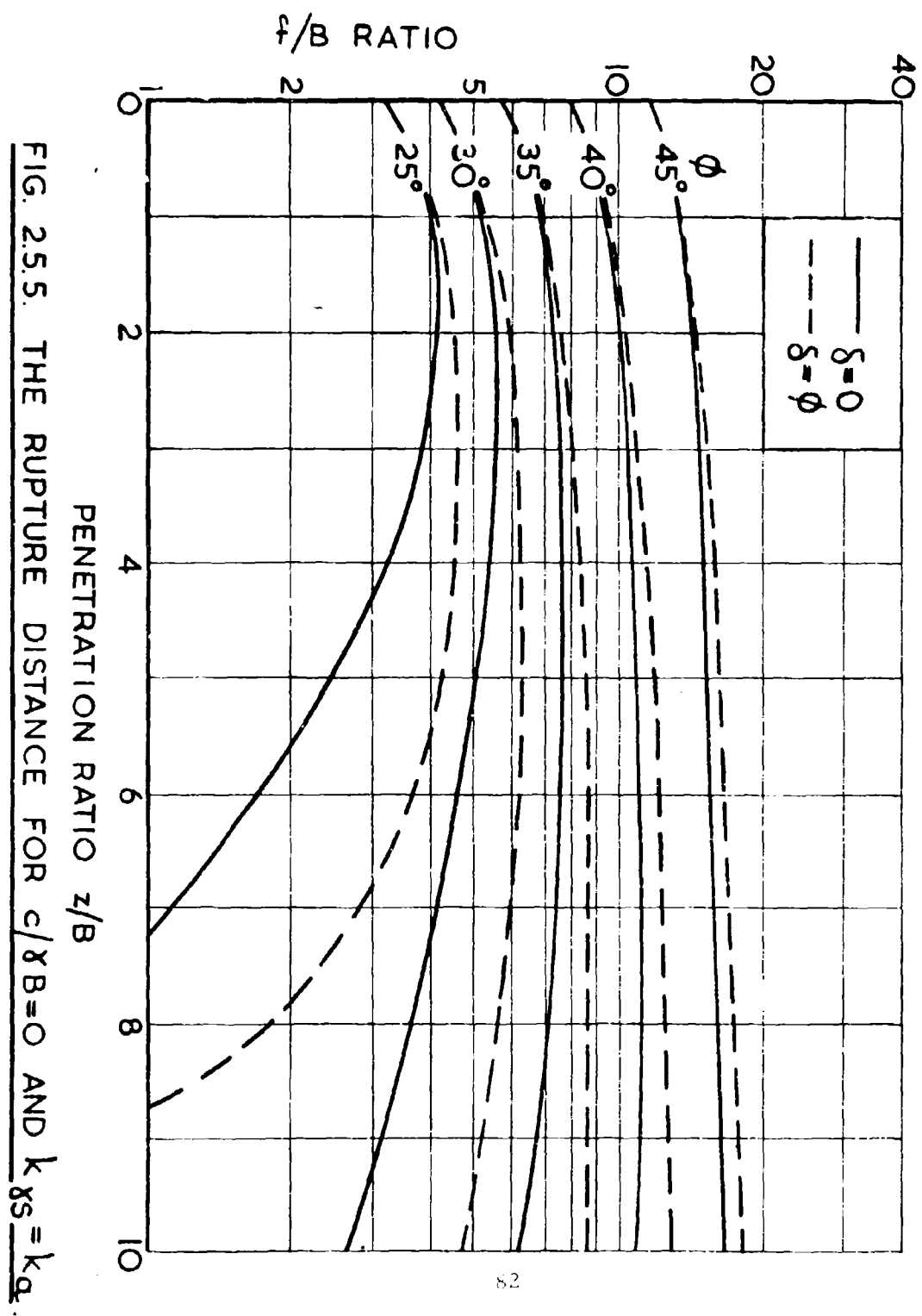
FIG. 2.5.5. THE RUPTURE DISTANCE FOR $c/\gamma B=0$ AND $k_{\gamma s}=k_a$.

82
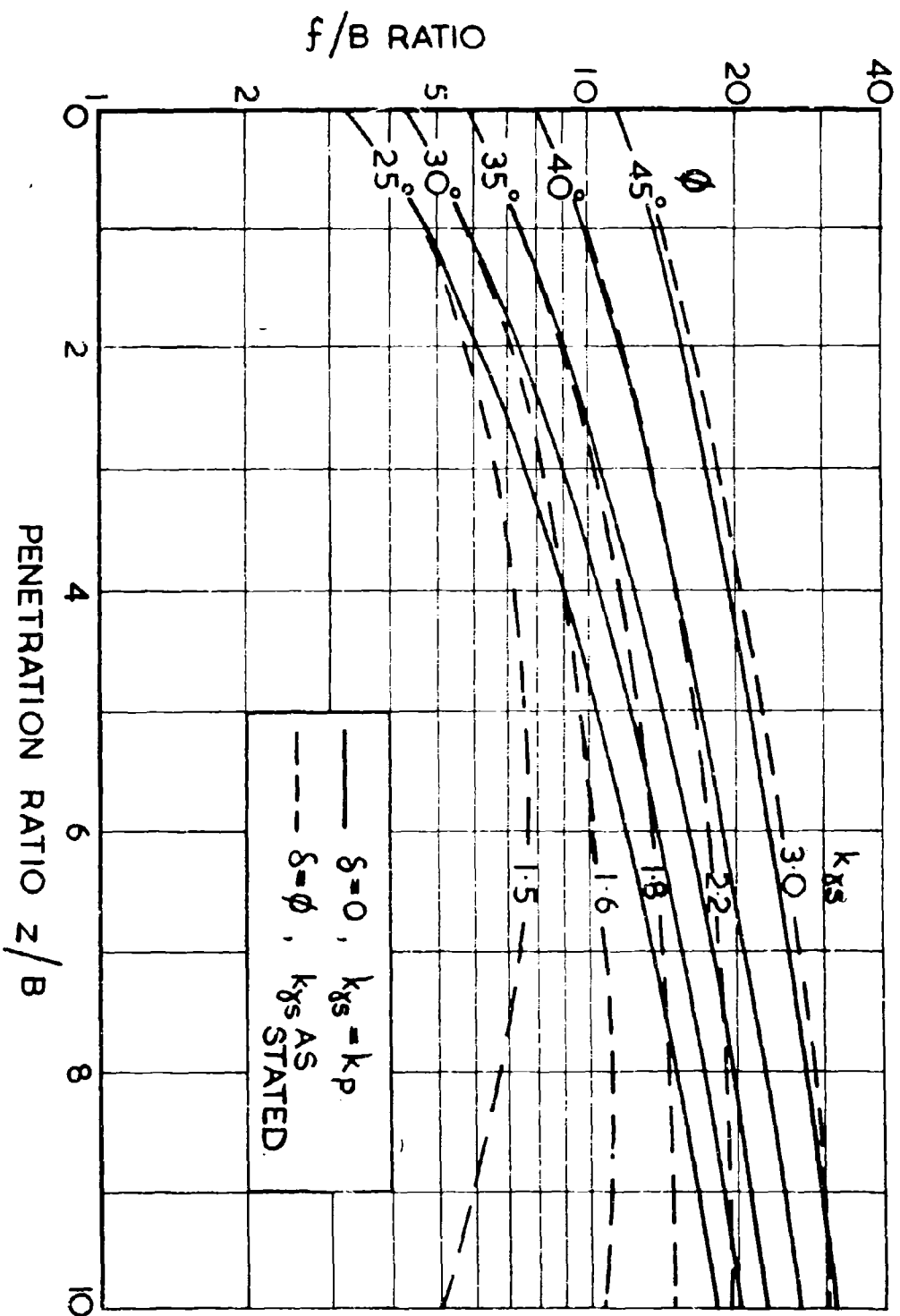
FIG. 2.5.6. THE RUPTURE DISTANCE FOR $c/\gamma B=0$ AND $k_{\gamma s}>1$.
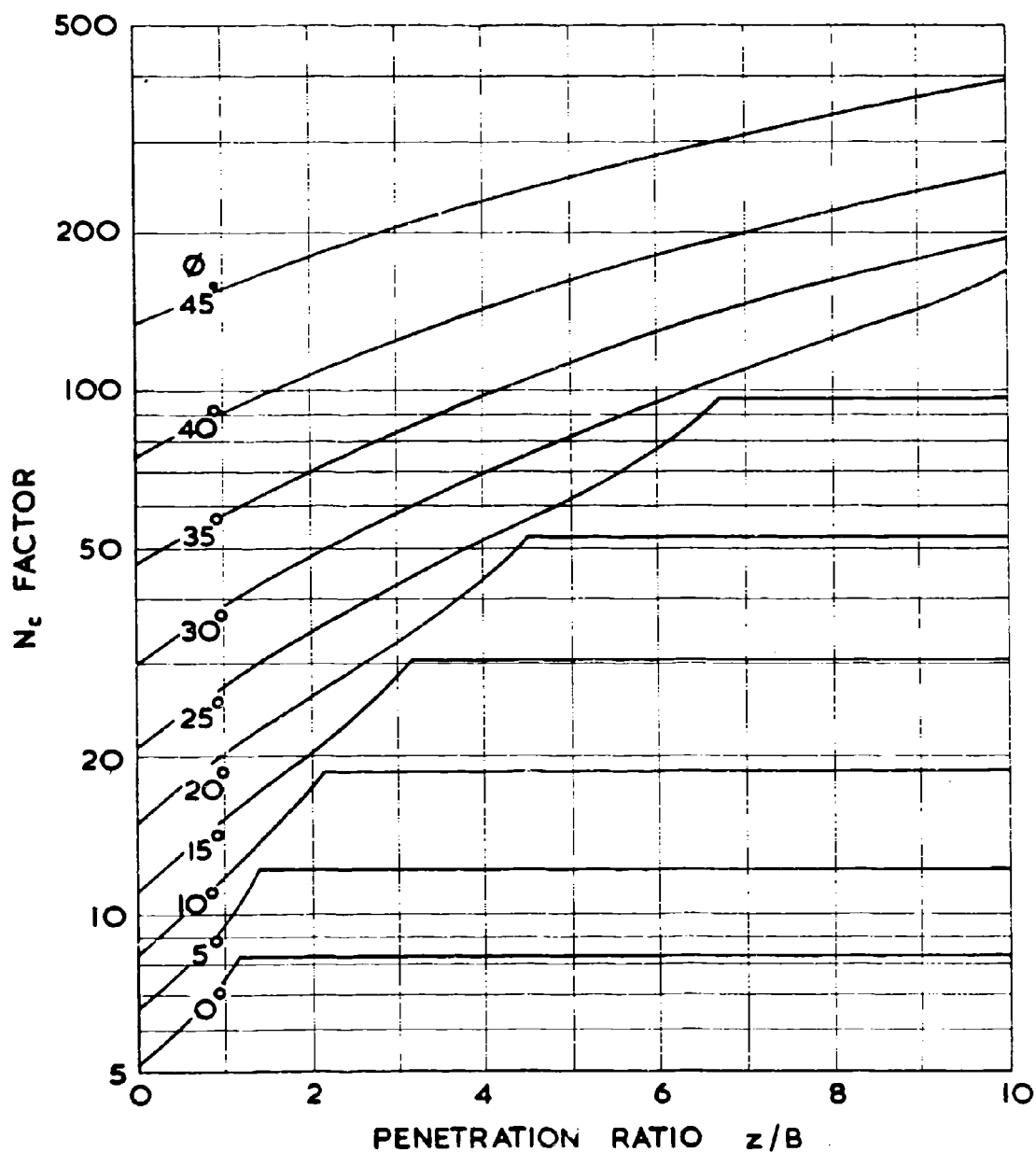
FIG. 2.6.1. VALUES OF THE $N_c$ FACTOR FOR
FOR $c/\gamma B = \infty$ WHEN THE SHAFT IS UNSUPPORTED

84
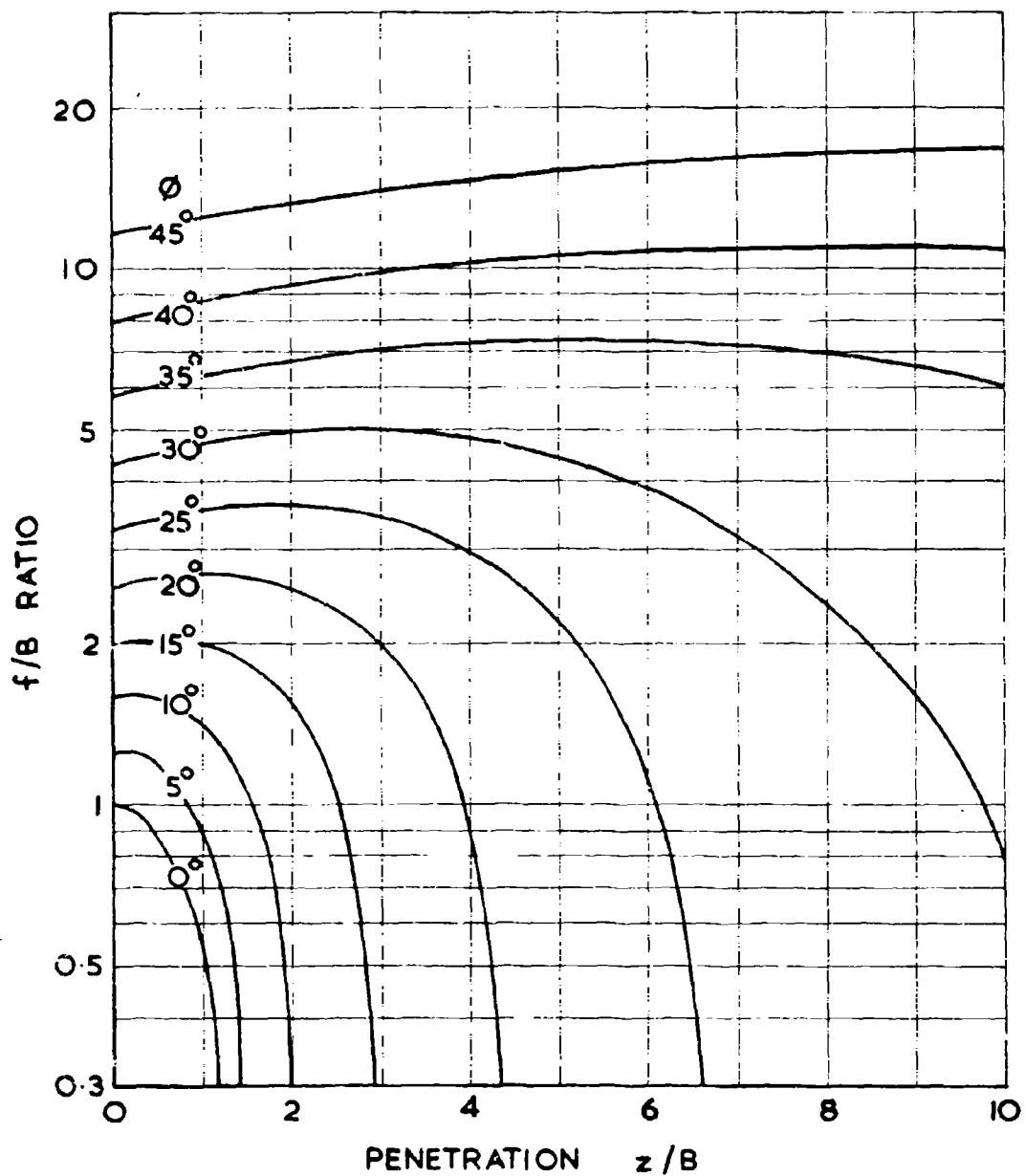
FIG. 2.6.2. THE RUPTURE DISTANCE FOR c/γB ≃ ∞
WHEN THE SHAFT IS UNSUPPORTED
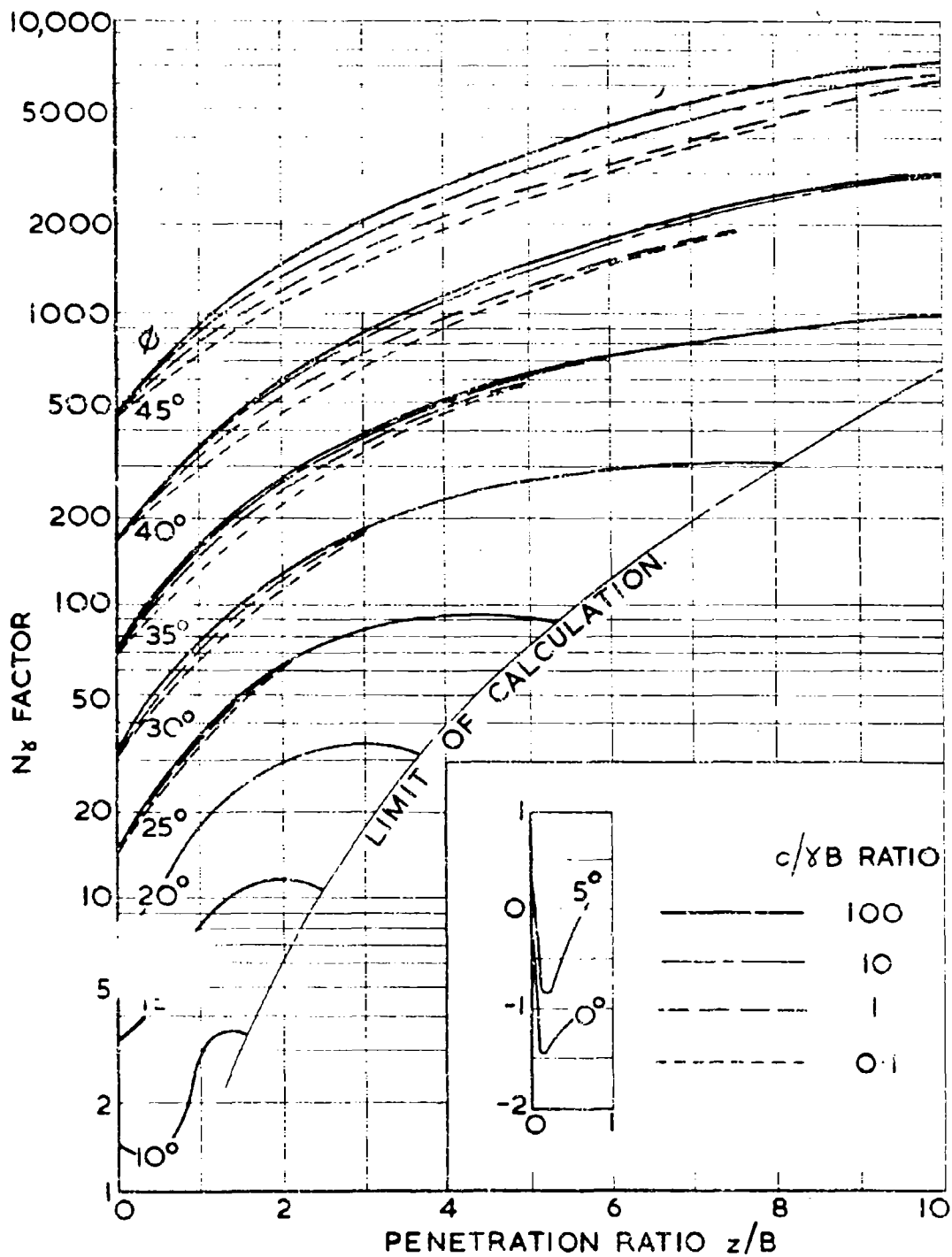
FIG. 2.7.1. VALUES OF THE $N_\gamma$ FACTOR FOR INTERMEDIATE $c/\gamma B$ RATIOS WHEN THE SHAFT IS UNSUPPORTED.
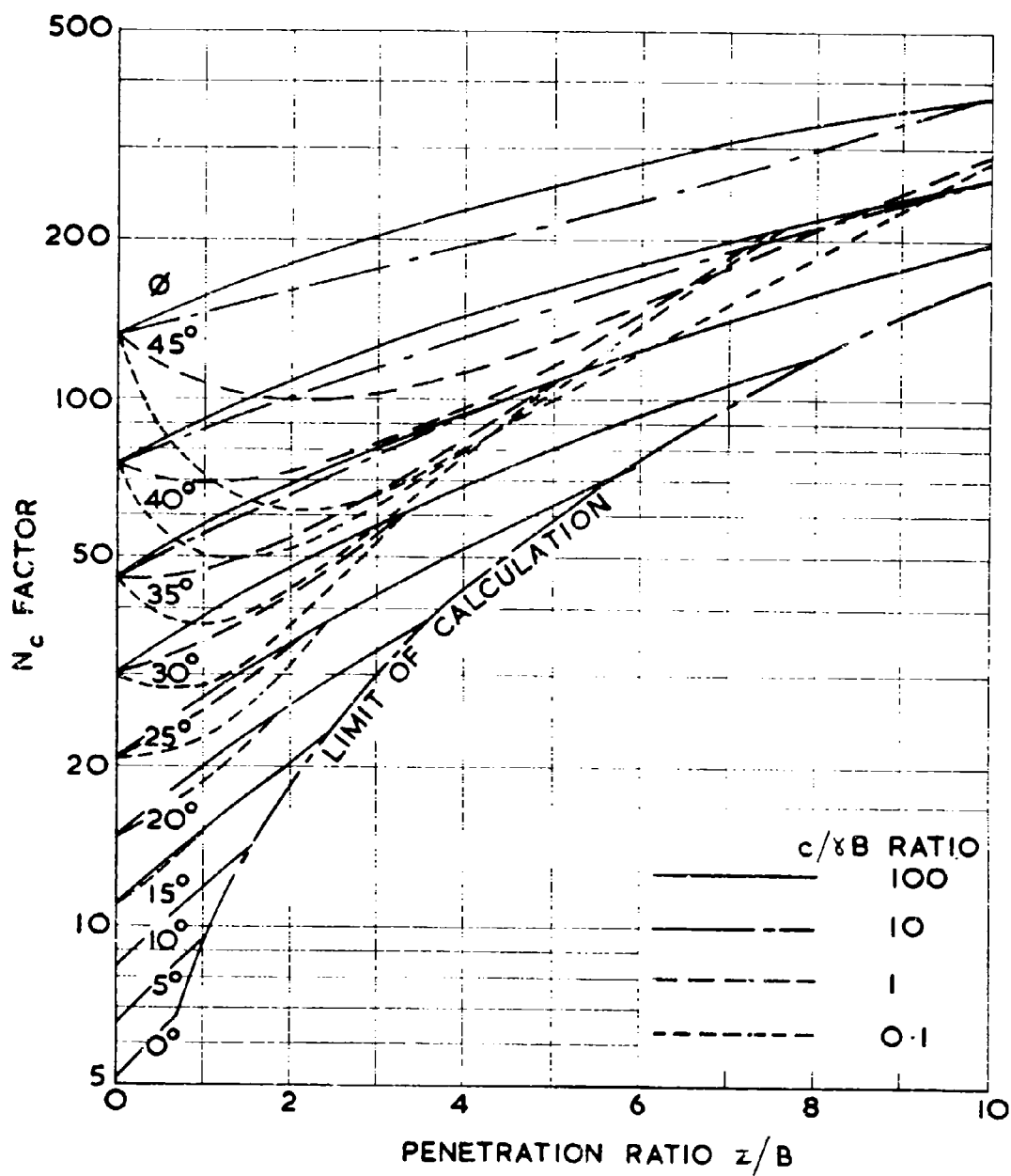
FIG. 2.7. 2.   VALUES  OF  THE  $N_c$  FACTOR  FOR
INTERMEDIATE  $c/\gamma B$  RATIOS  WHEN  THE  SHAFT  IS
UNSUPPORTED
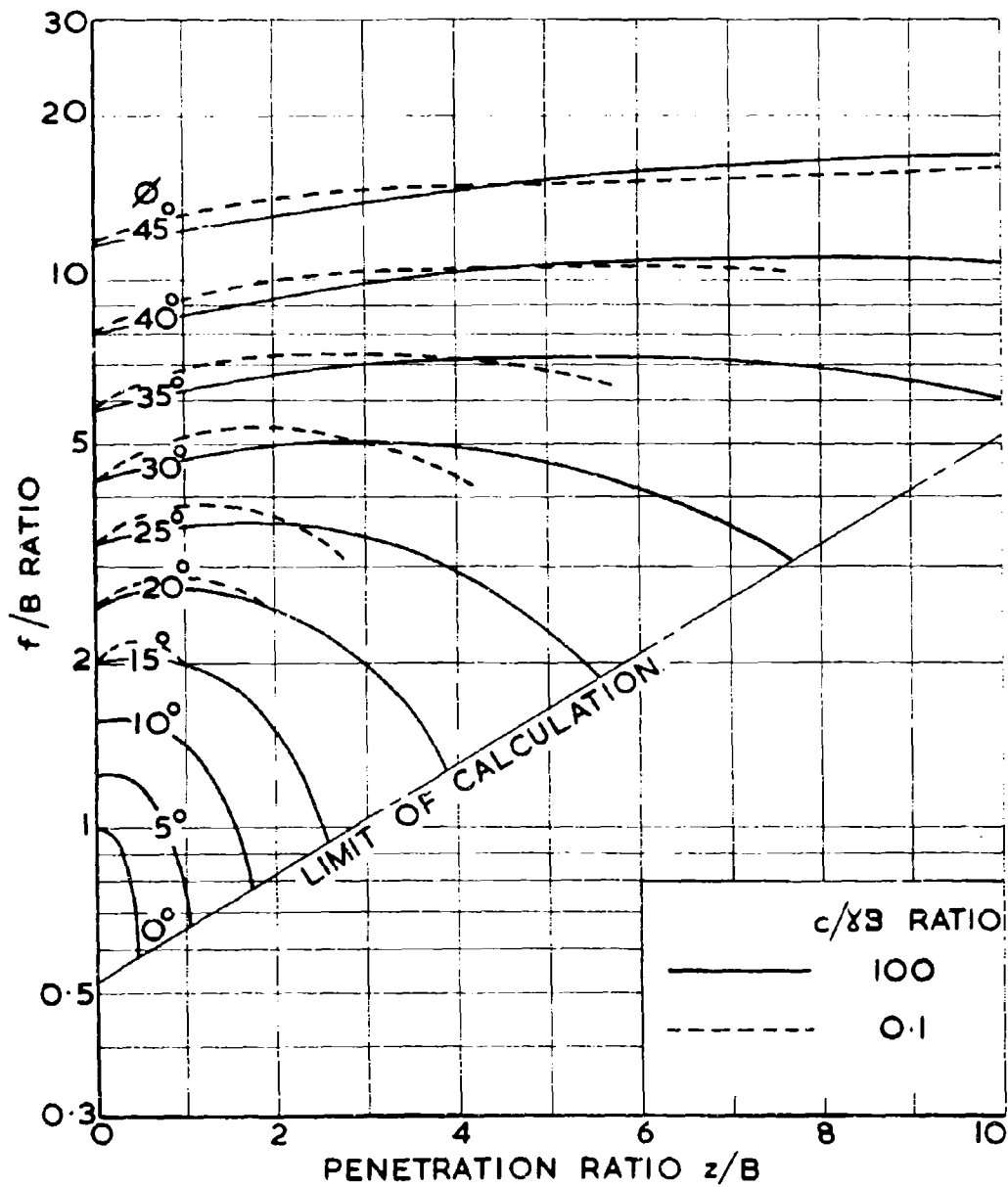
FIG. 2.7.3. THE RUPTURE DISTANCE FOR INTERMEDIATE $c/\gamma B$ RATIOS WHEN THE SHAFT IS UNSUPPORTED.

88
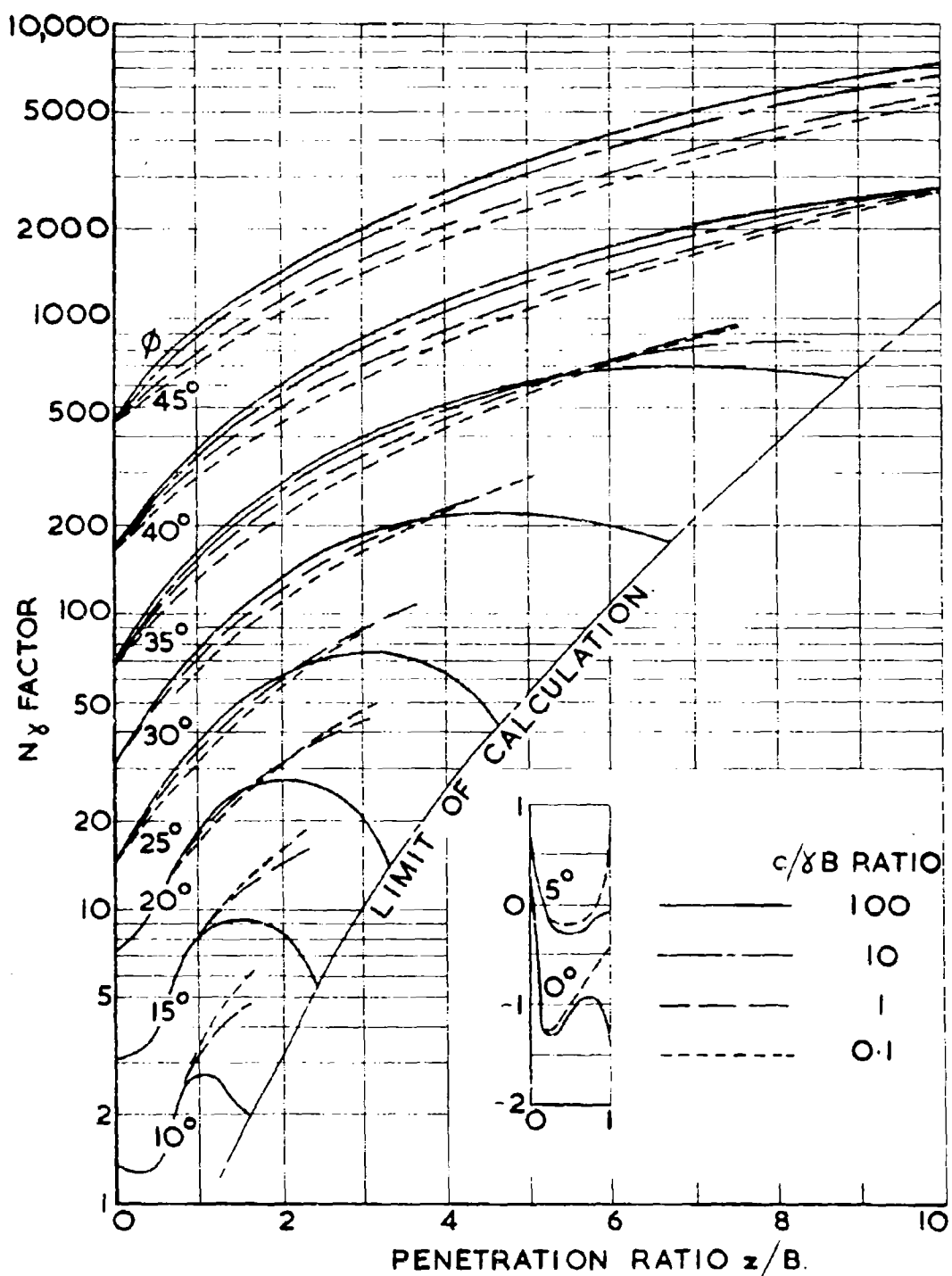
FIG. 2.7.4. VALUES OF THE $N_\gamma$ FACTOR FOR INTERMEDIATE $c/\gamma B$ RATIOS WHEN THE SHAFT IS PERFECTLY SMOOTH.
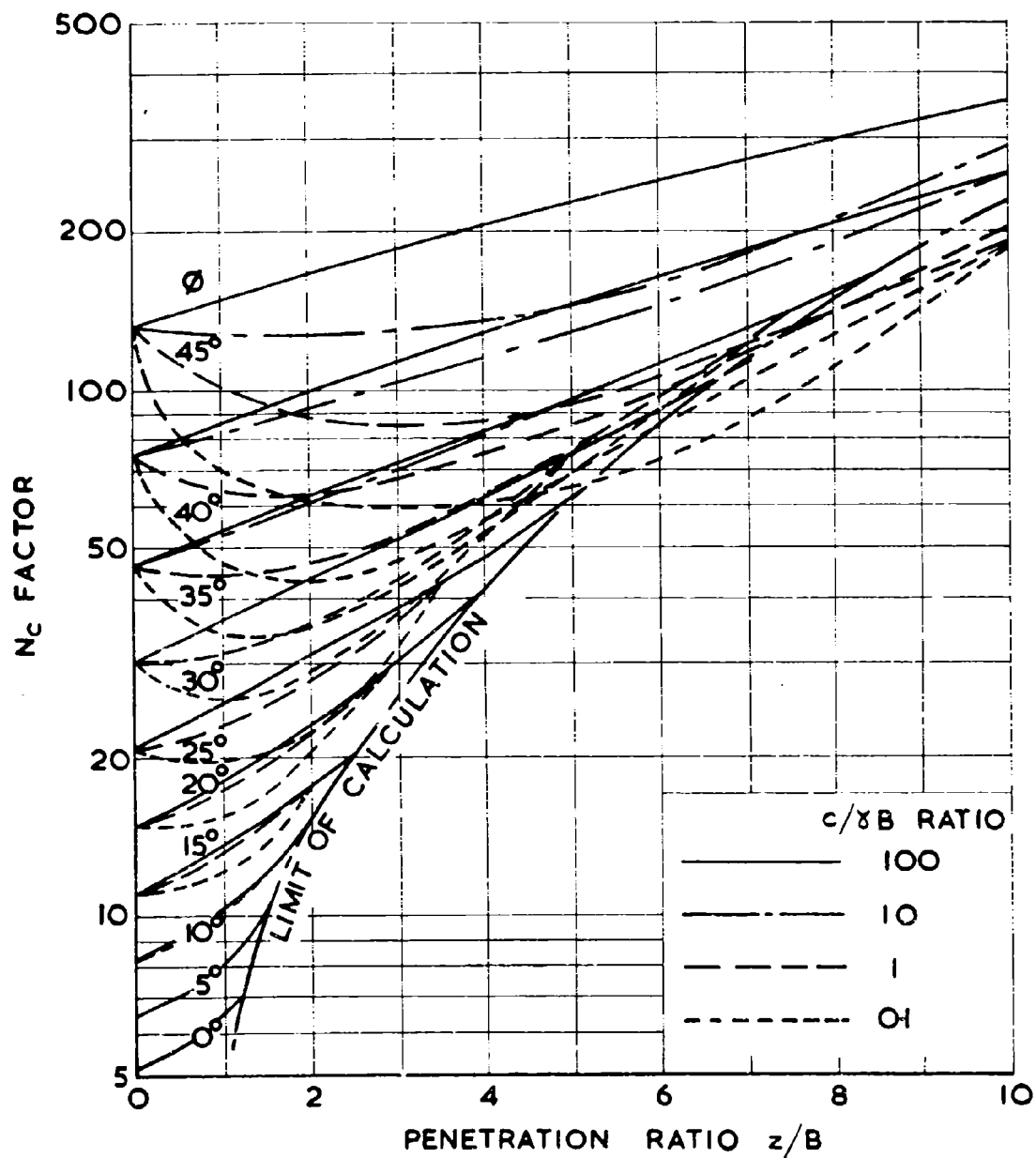
FIG. 2.7.5. VALUES OF THE $N_c$ FACTOR FOR INTERMEDIATE $c/\gamma B$ RATIOS WHEN THE SHAFT IS PERFECTLY SMOOTH
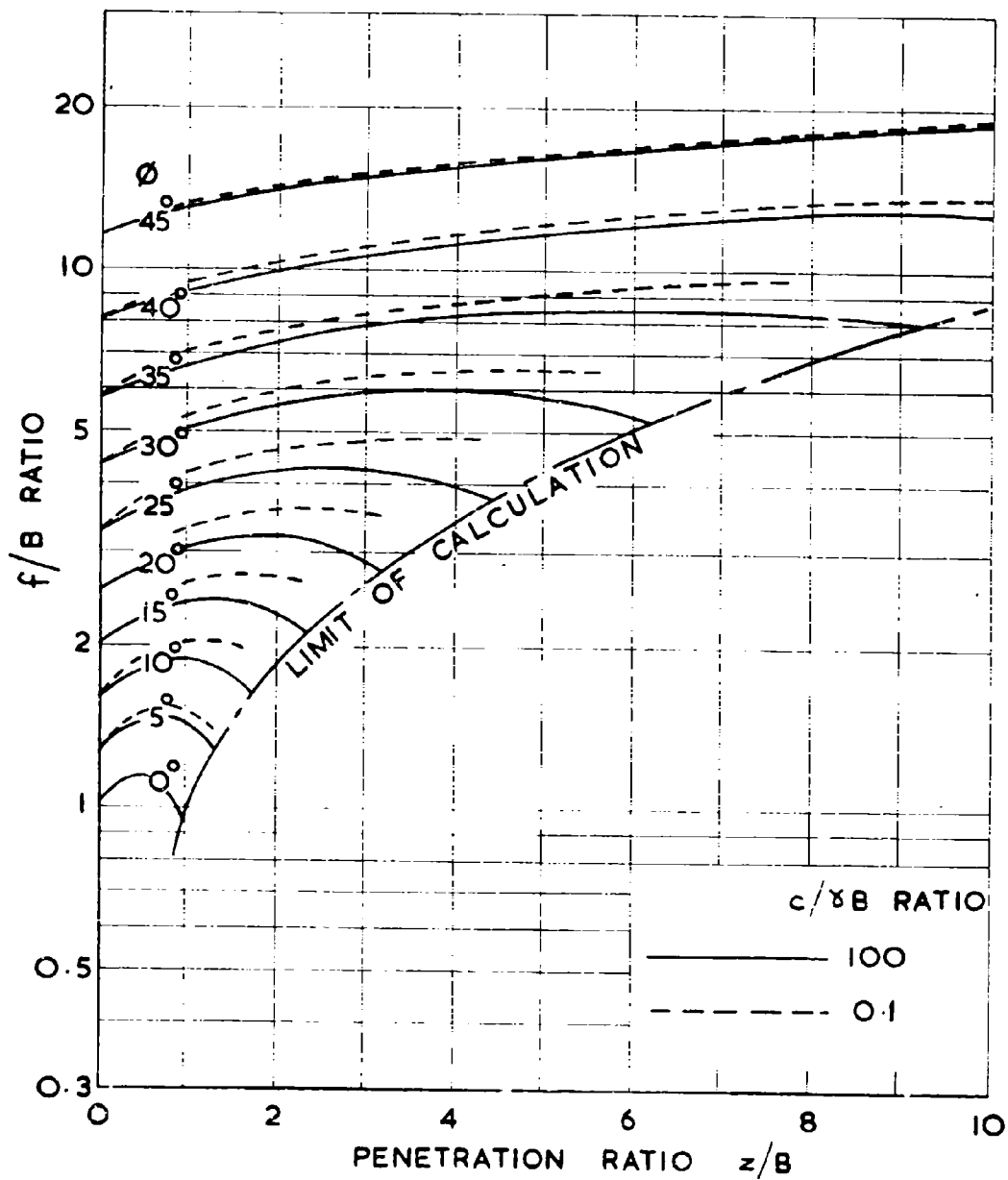
FIG. 2.7.6. THE RUPTURE DISTANCE FOR
INTERMEDIATE $c/\gamma B$ RATIOS WHEN THE
SHAFT IS PERFECTLY SMOOTH
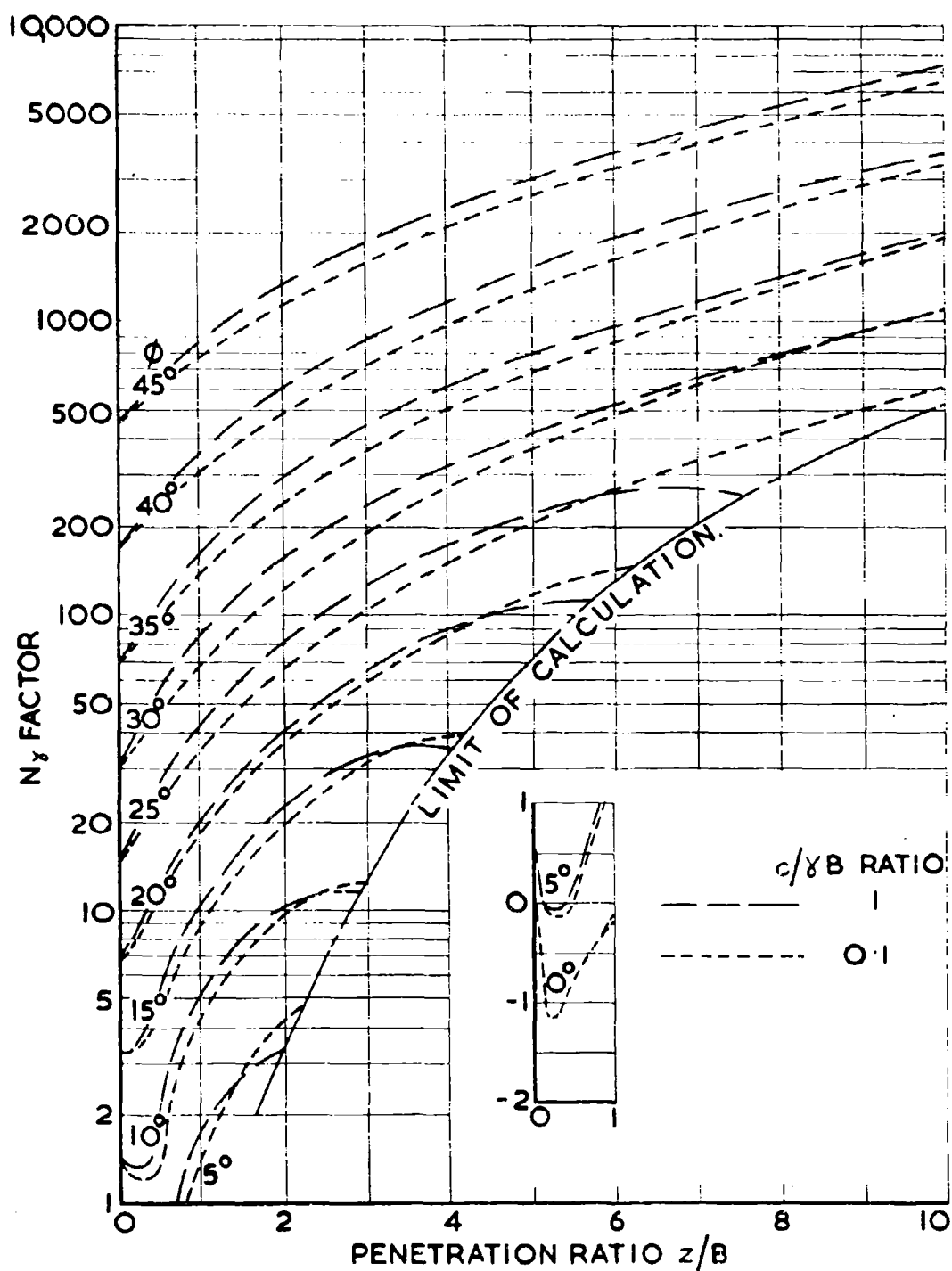
FIG. 2.7.7. VALUES OF THE $N_\gamma$ FACTOR FOR INTERMEDIATE $c/\gamma B$ RATIOS WHEN THE SHAFT IS PERFECTLY ROUGH.
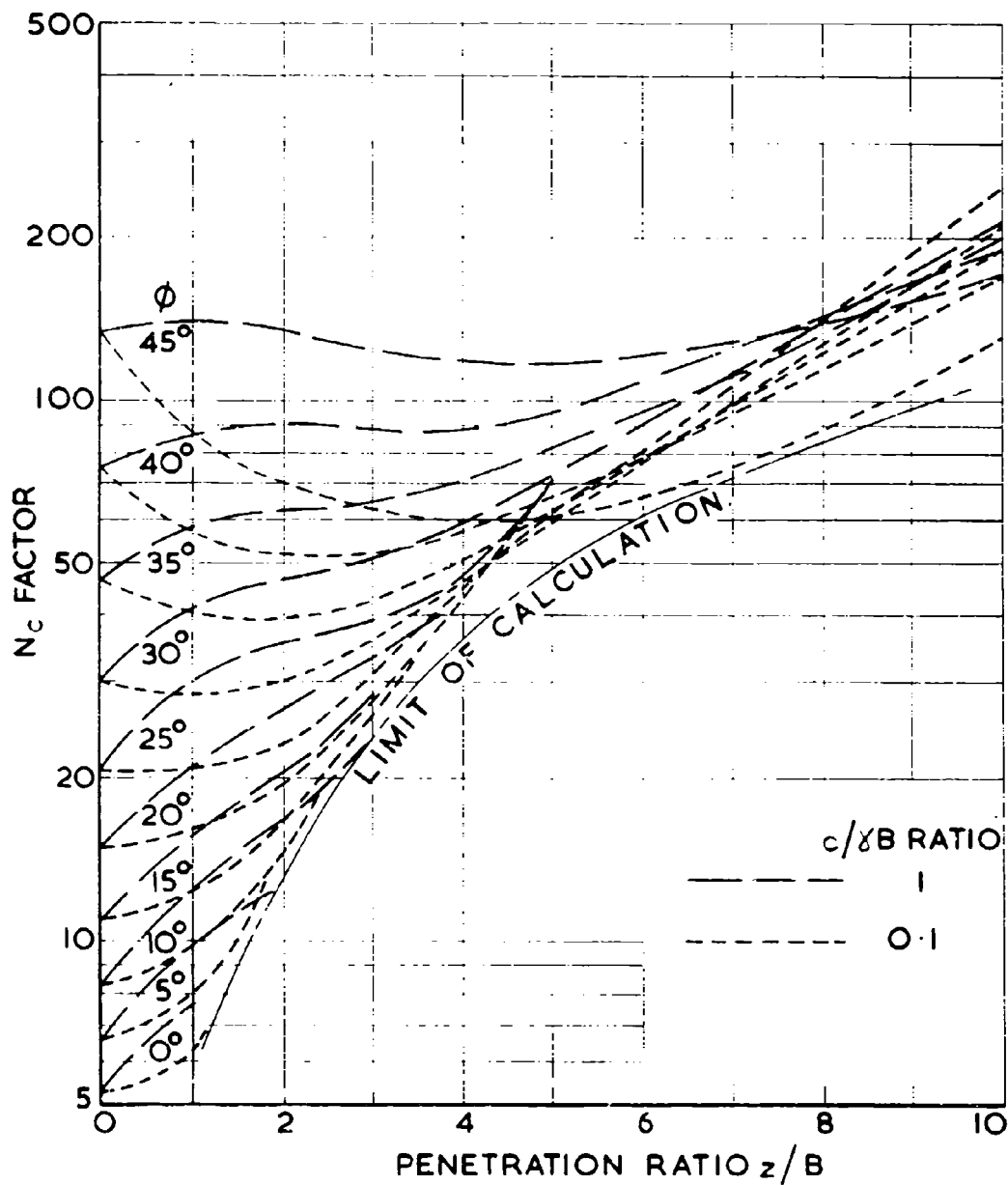
FIG. 2.7. 8.   VALUES   OF   THE   $N_c$   FACTOR   FOR
INTERMEDIATE  c/$\gamma$B  RATIOS   WHEN THE
SHAFT   IS   PERFECTLY   ROUGH.
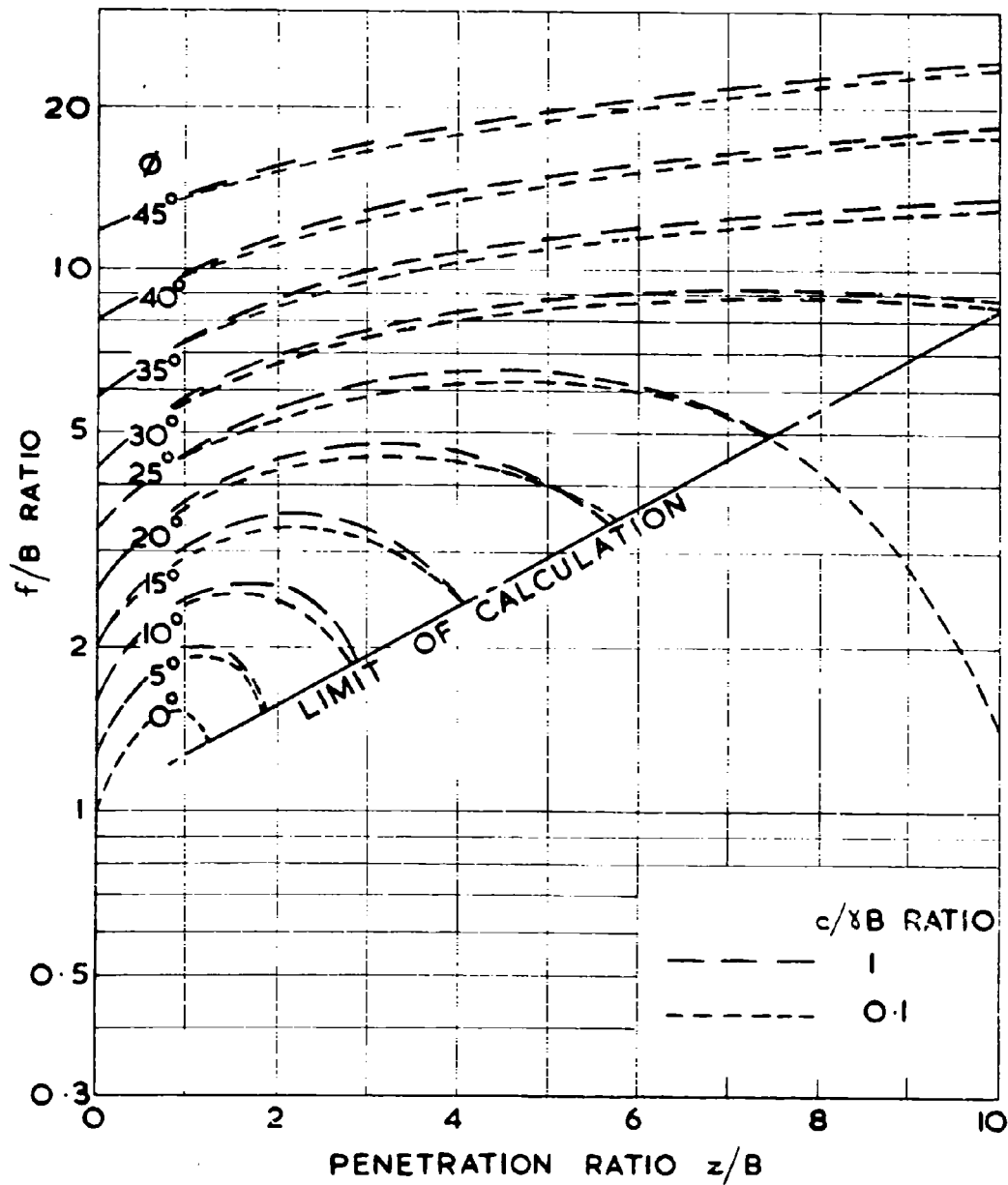
FIG. 2.7.9. THE RUPTURE DISTANCE FOR INTERMEDIATE $c/\gamma B$ RATIOS WHEN THE SHAFT IS PERFECTLY ROUGH
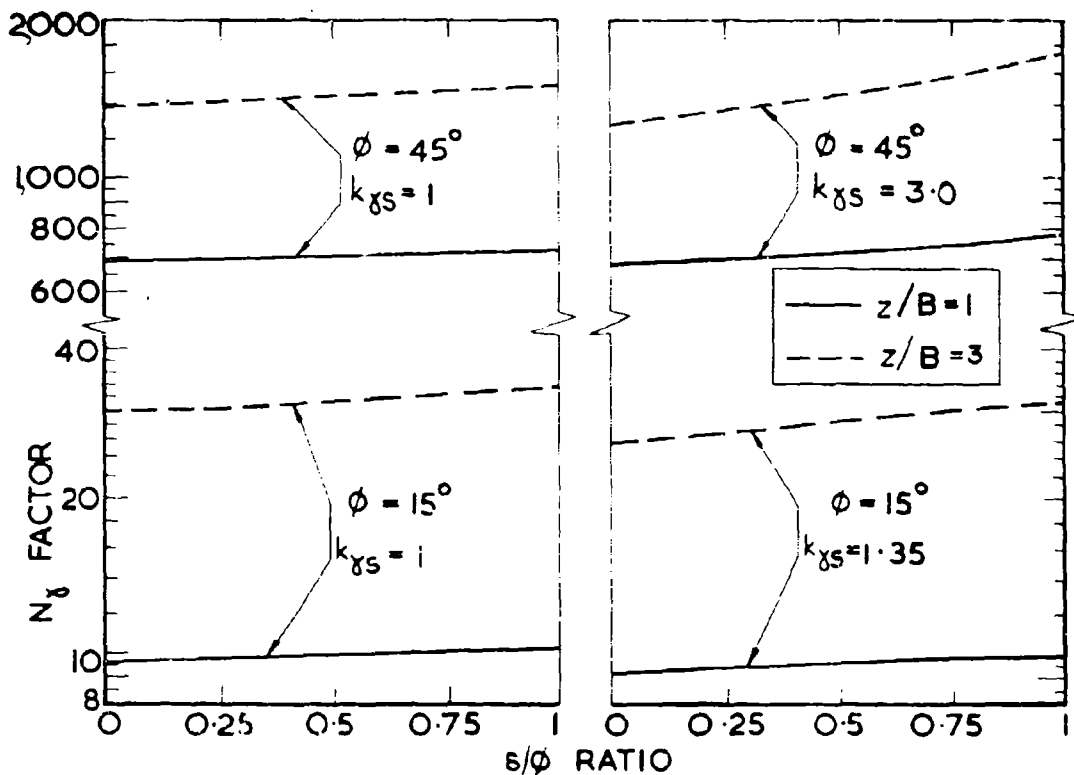
FIG. 2.8.1. THE VARIATION OF THE $N_\gamma$ FACTOR WITH THE $\delta/\phi$ RATIO FOR $c/\gamma B = 0$
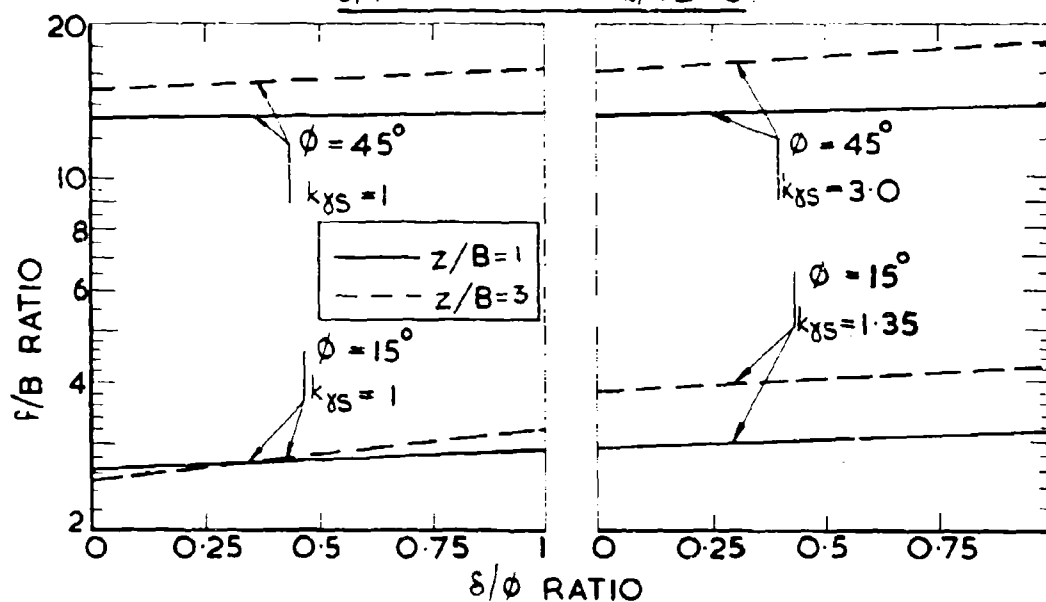


FIG. 2.8.2. THE VARIATION OF THE RUPTURE DISTANCE WITH THE $\delta/\phi$ RATIO FOR $c/\gamma B = 0$.
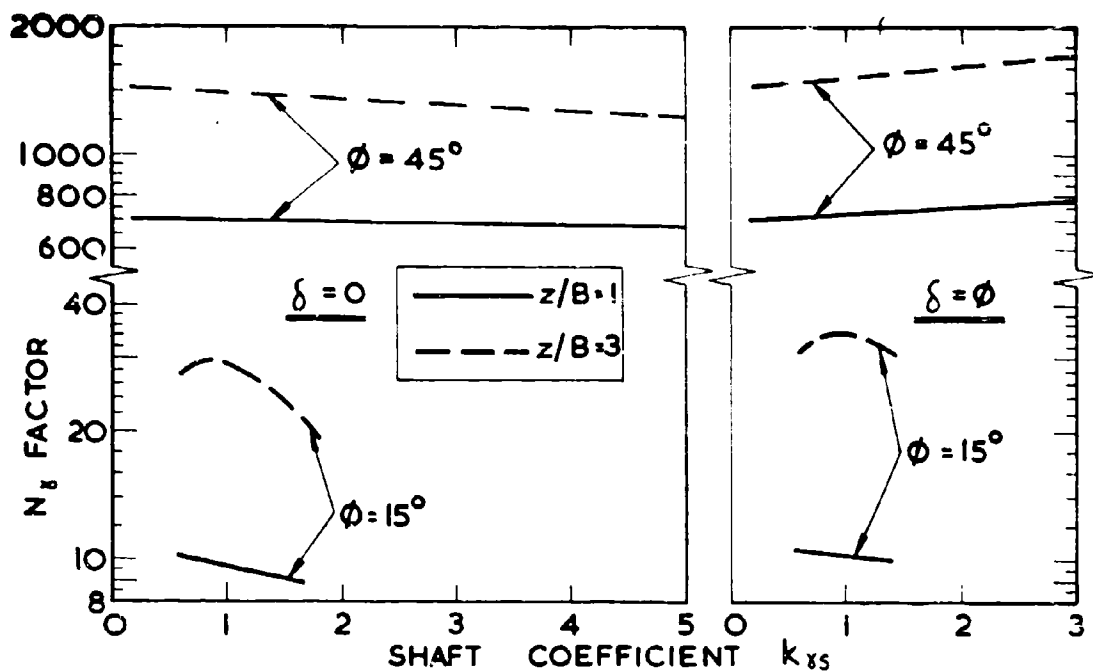
FIG. 2.8.3. THE VARIATION OF THE $N_\gamma$ FACTOR WITH THE SHAFT COEFFICIENT FOR $c/\gamma B = 0$
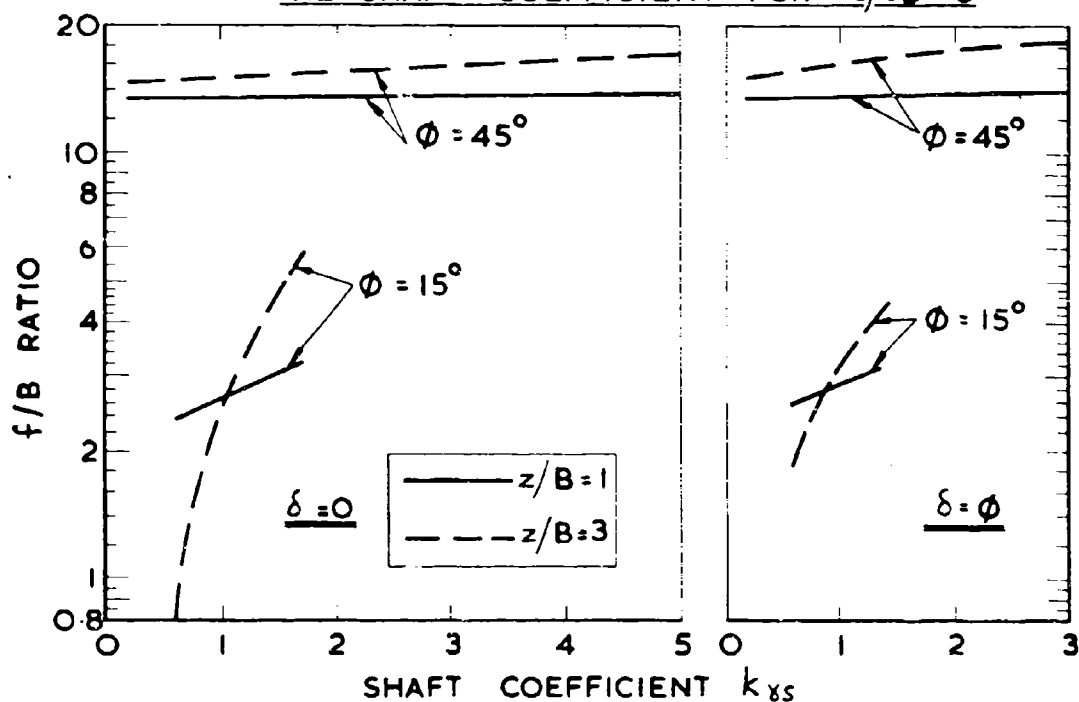


FIG. 2.8.4. THE VARIATION OF THE RUPTURE DISTANCE WITH THE SHAFT COEFFICIENT FOR $c/\gamma B = 0$
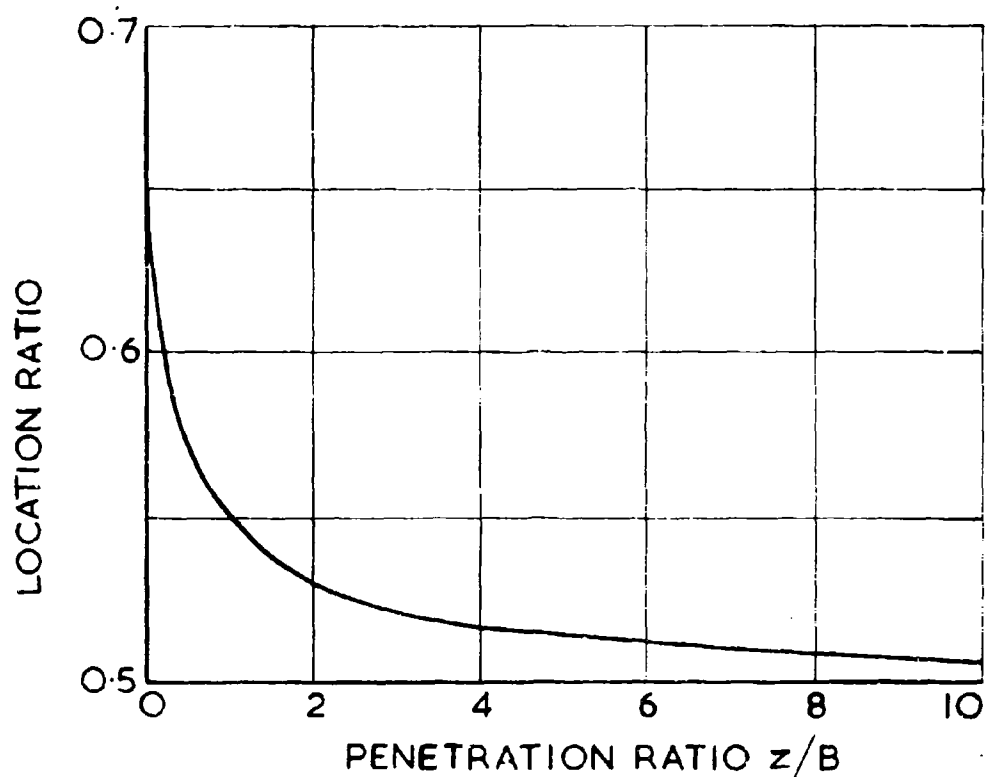
FIG. 2.9.1.   THE MOVEMENT OF THE CENTRE OF
PRESSURE  ALONG THE WEDGE BOUNDARY
EXPRESSED AS THE RATIO OF THE DISTANCE
BETWEEN  THE CORNER OF THE FOOTING AND
THE CENTRE  OF PRESSURE TO THE  TOTAL
LENGTH  OF THE WEDGE BOUNDARY.

97
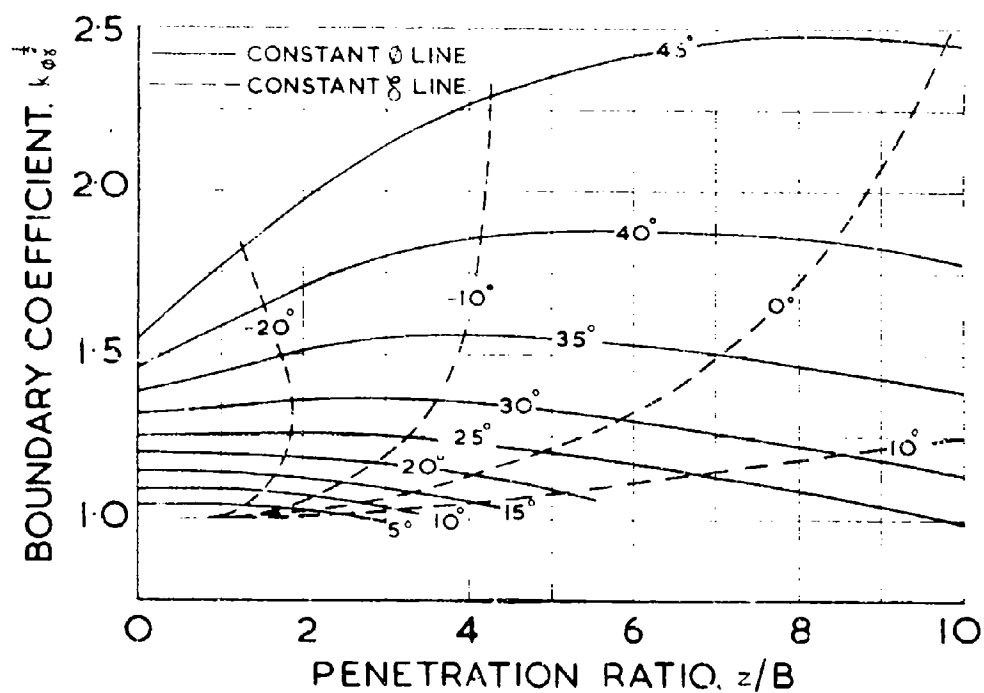
FIG. 2.9.2. VALUES OF THE BOUNDARY COEFFICIENT $k_{\phi\delta}^{\frac{1}{2}}$ FOR $c/\gamma B = O$, $k_{\gamma S} = 1$ AND $\delta = O$.
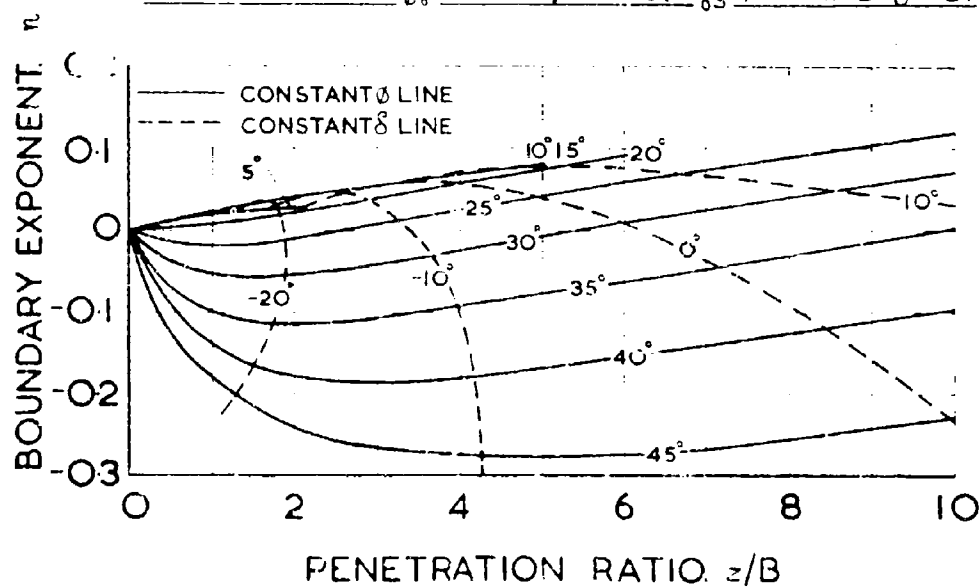


FIG. 2.9.3. VALUES OF THE BOUNDARY EXPONENT $n$ FOR $c/\gamma B = O$, $k_{\gamma S} 1$ & $\delta = O$.
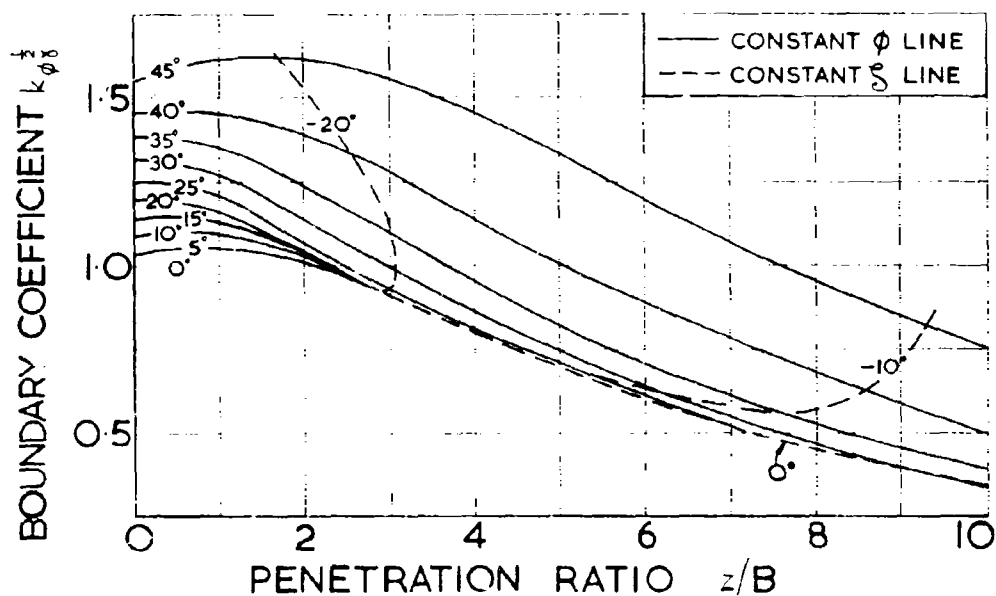
FIG. 2.9.4. VALUES OF THE BOUNDARY COEFFICIENT,
$k_{\phi\delta}^{\frac{1}{2}}$ FOR $c/\gamma B = 0$ $k_{\gamma s} = 1$ AND $\delta = \phi$.
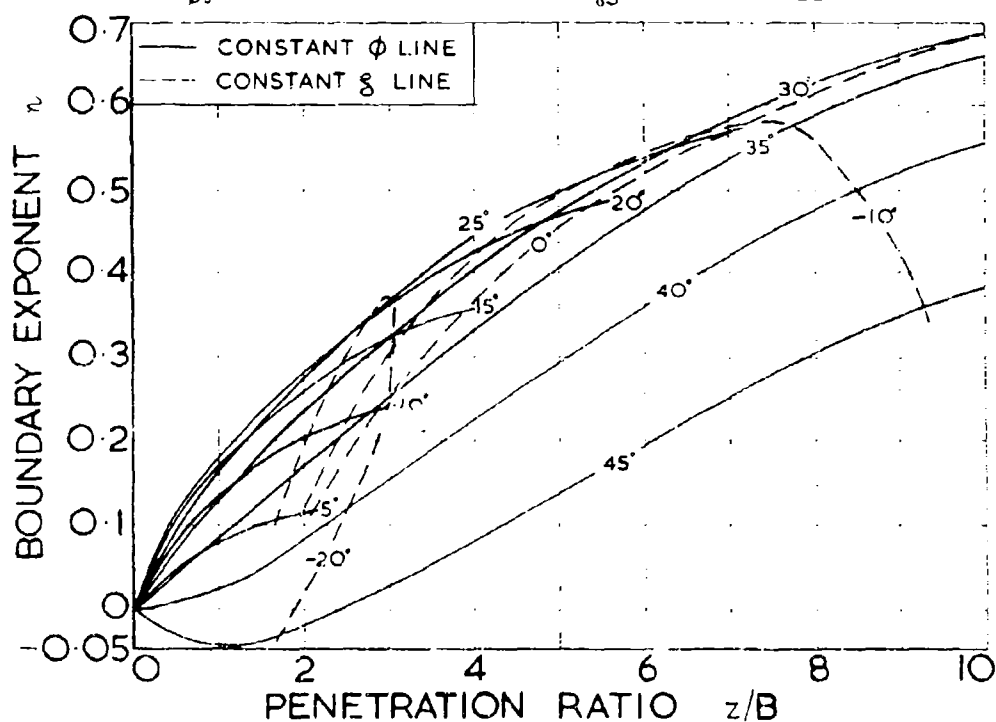


FIG. 2.9.5. VALUES OF THE BOUNDARY EXPONENT,
$n$ FOR $c/\gamma B = 0$ $k_{\gamma s} = 1$ AND $\delta = \phi$.
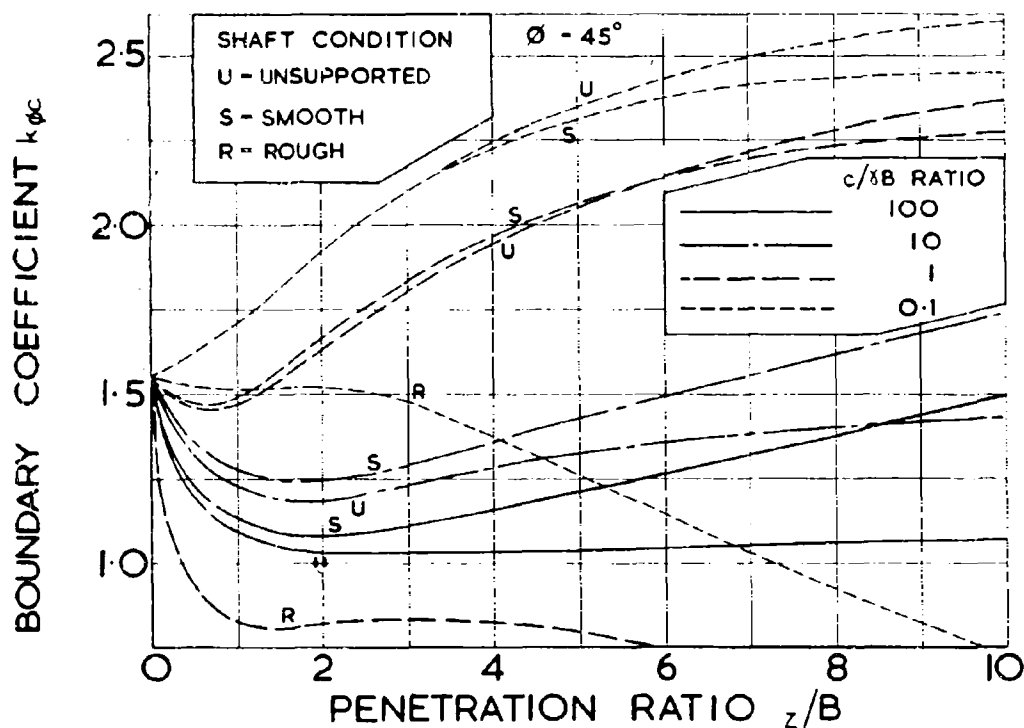
FIG. 2. 9. 6. VALUES OF THE BOUNDARY COEFFICIENT $k_{\phi c}$ FOR $c/\gamma B > 0$
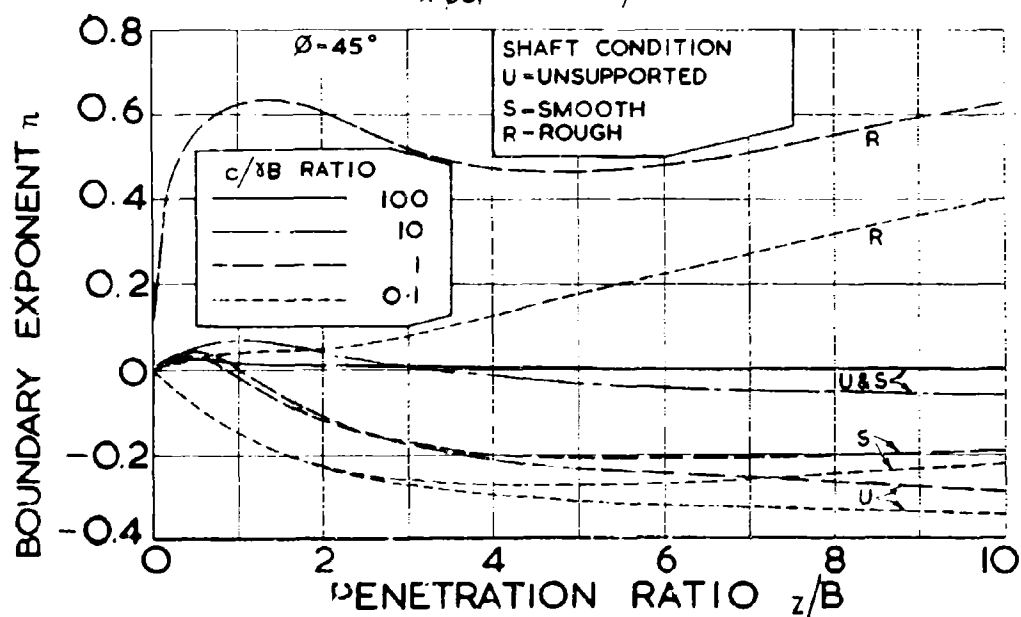


FIG. 2. 9. 7. VALUES OF THE BOUNDARY EXPONENT, $n$, FOR $c/\gamma B > 0$.

Legend:
- ──+── TERZAGHI
- ────── MEYERHOF
- ·········· LUNDGREN & MORTENSEN
- ──o── CAQUOT & KERISEL
- ──·── MIZUNO
- ──·── BALLA
- ────── WITNEY
- GORBUNOV-POSSADOV

| $\phi$ | LUNDGREN MORTENSEN | BALLA |
|---|---|---|
| 20° | — | 7·1 |
| 30° | 14·8 | 37·2 |
| 40° | 93·5 | 216 |

| $\phi$ | TERZAGHI | MEYERHOF | CAQUOT KERISEL | MIZUNO | WITNEY |
|---|---|---|---|---|---|
| 5° | 0·14 | 0·39 | — | 0·4 | 0·50 |
| 10° | 0·56 | 1·12 | 1·60 | 1·0 | 1·45 |
| 15° | 1·53 | 2·54 | — | 2·3 | 3·28 |
| 20° | 3·64 | 5·31 | 5·69 | 4·6 | 6·91 |
| 25° | 8·34 | 10·7 | — | 9·4 | 14·3 |
| 30° | 19·1 | 22·9 | 22·7 | 18 | 30·4 |
| 35° | 45·4 | 50·5 | — | 37 | 67·7 |
| 40° | 115·2 | 119·4 | 114 | 80 | 163·5 |
| 45° | 325·4 | 314·7 | — | — | 4428 |
| 50° | — | 969·4 | 916 | — | — |
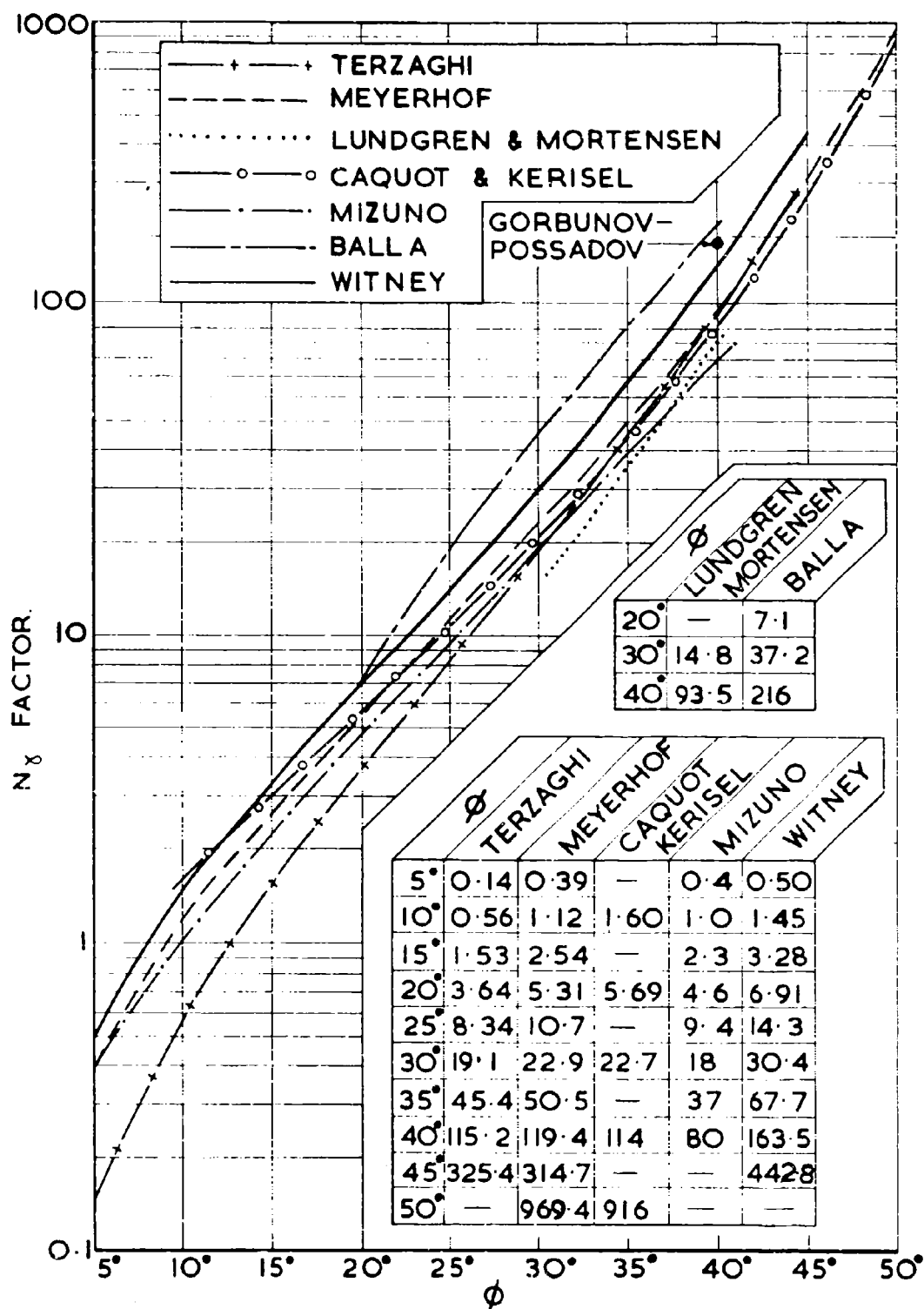
FIG. 2.10.1. COMPARISON OF SURFACE BEARING CAPACITY THEORIES
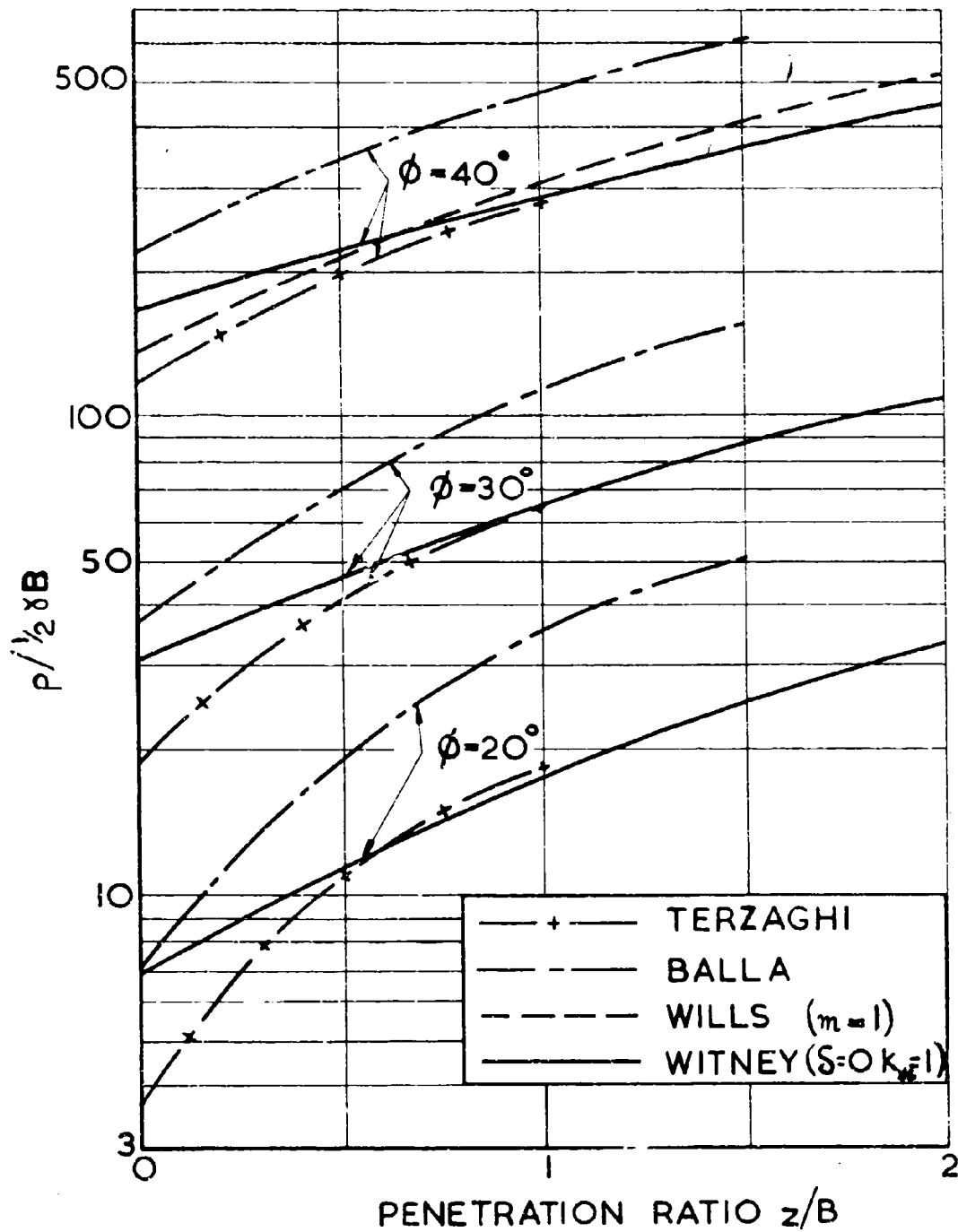
FIG. 2. 10. 2. COMPARISON OF THEORIES
AT SHALLOW SINKAGE FOR c/$\gamma$B=O
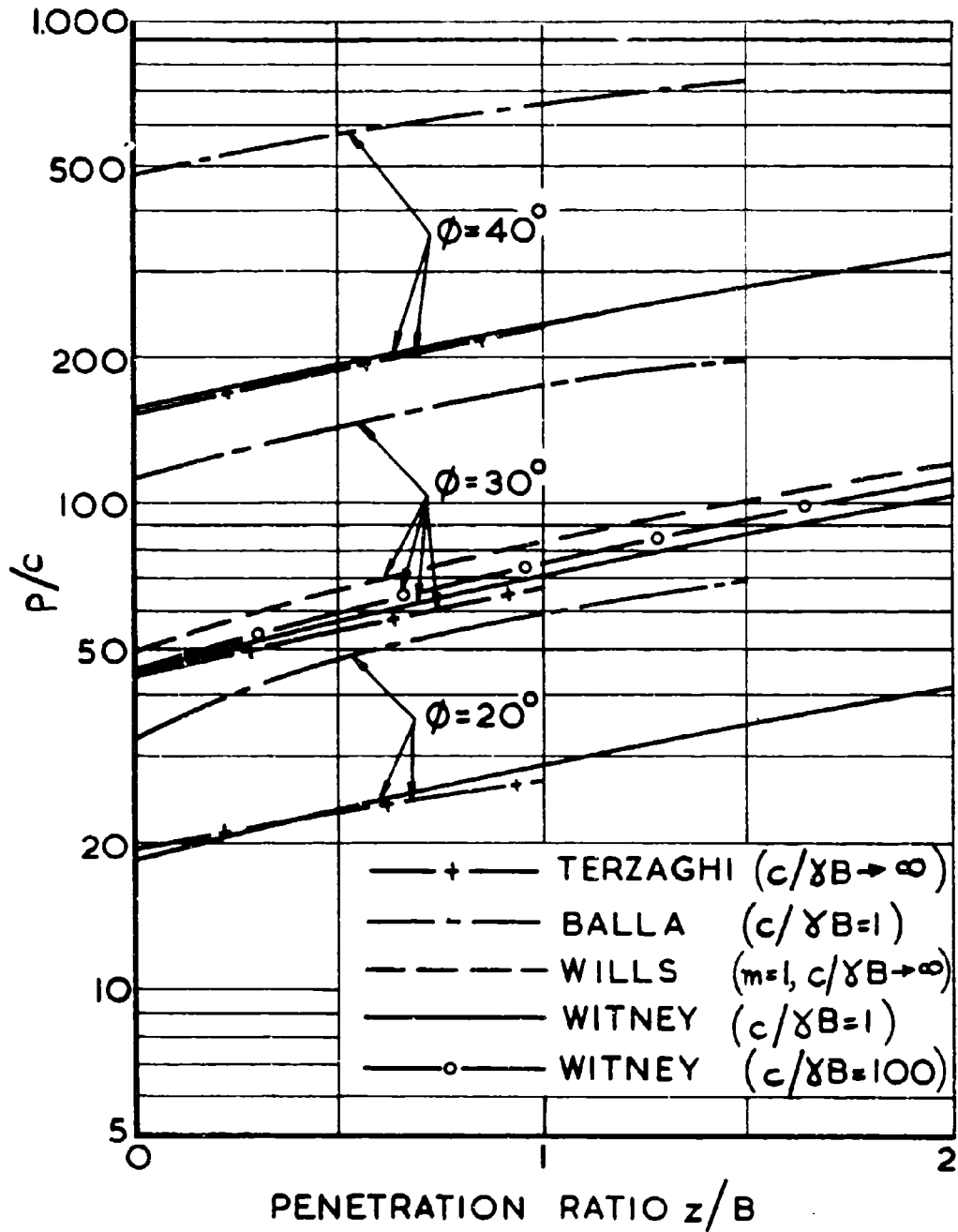
FIG. 2.10.3. COMPARISON OF THEORIES AT
SHALLOW SINKAGE FOR $c/\gamma B > 0$ WHEN THE
SHAFT IS UNSUPPORTED.

103
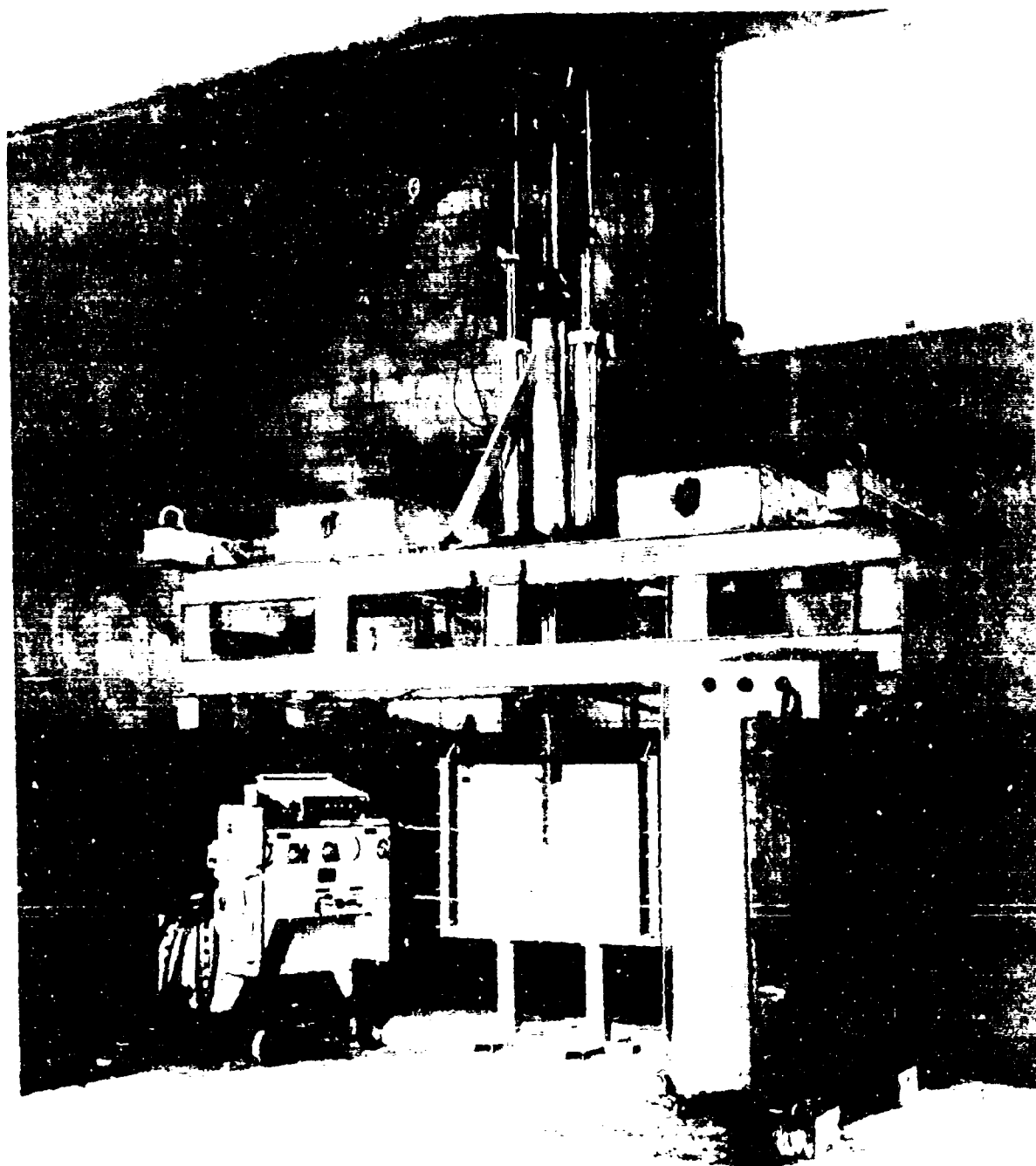
FIG 3.1.1    U.S.A.T.A.C. PENETROMETER
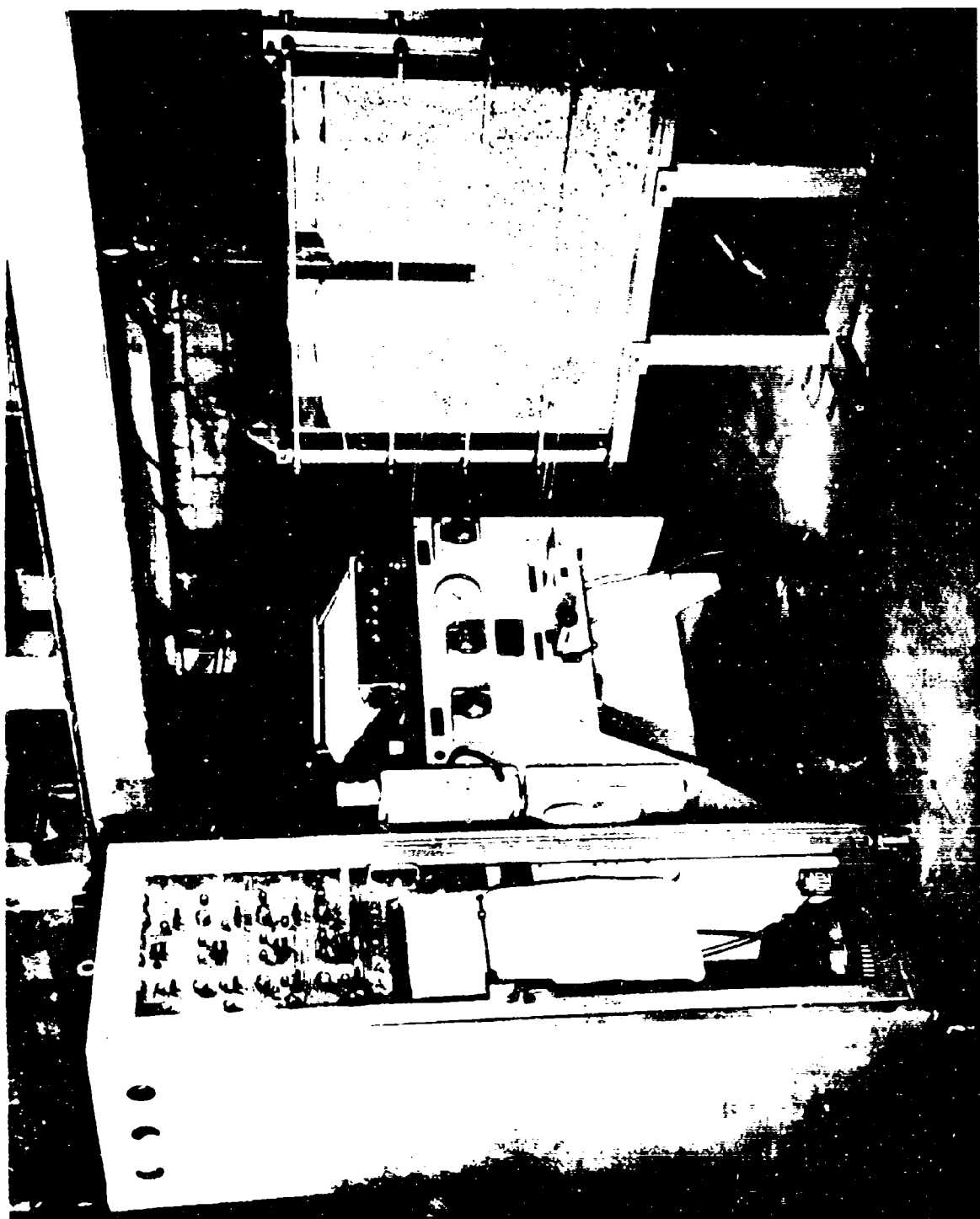
FIG 3.1.2    VIEW OF THE TEST EQUIPMENT AND SOIL TANK

MOUNTING PLATE

CHAIN CONNECTING
LINKS

SIDE PLATE
RIBS

OUTER
SHELL

SIDE
PLATE

CANTILEVERS

SPHERICAL
ROD END
BEARINGS

REMOVABLE
FOUNDATION
EXTENSION

INTEGRAL RING
DYNAMOMETER

BASE PLATE

LOADING SHAFT
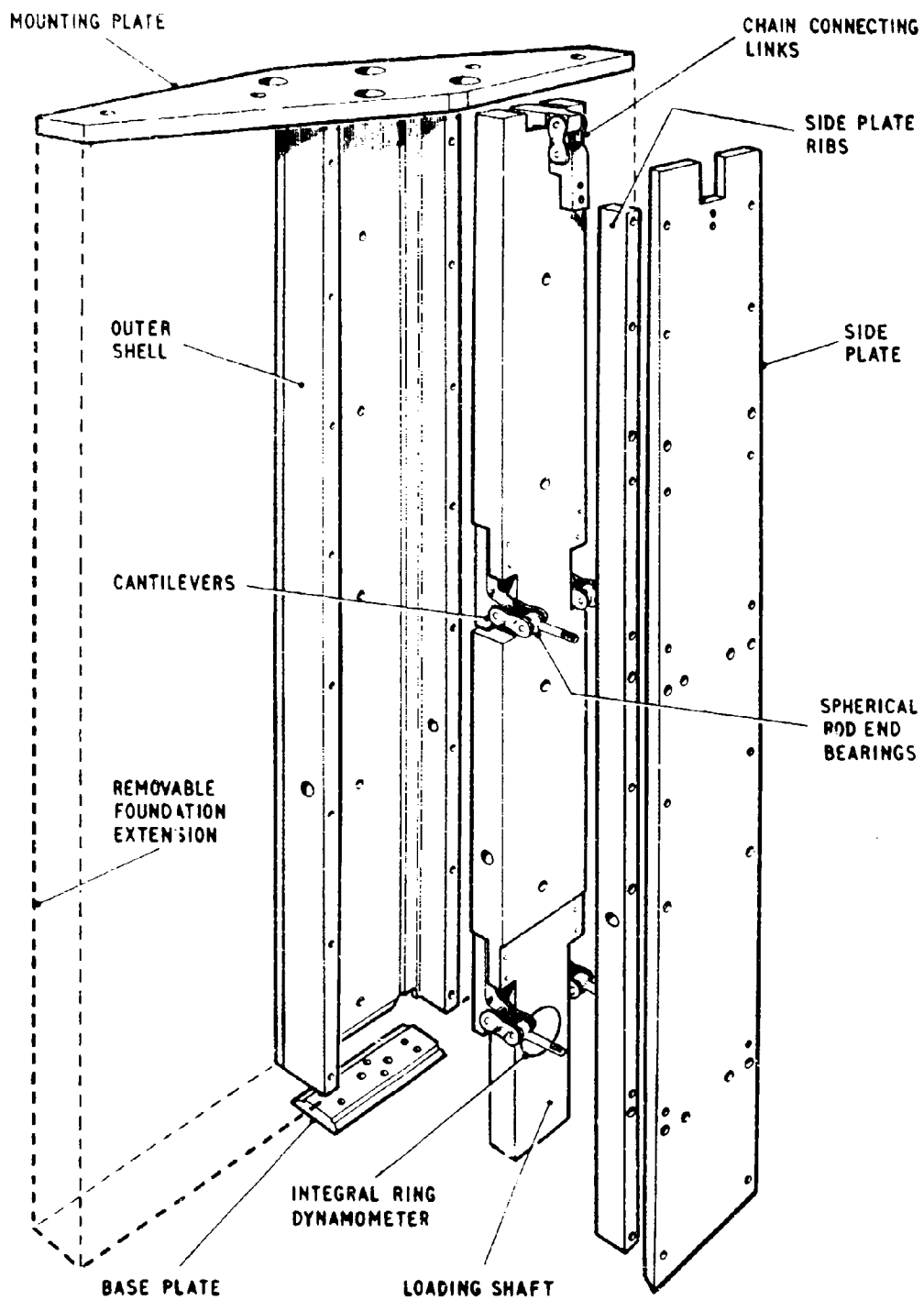
## FIG 3.1.3  THE DESIGN OF THE PENETRATION DEVICE
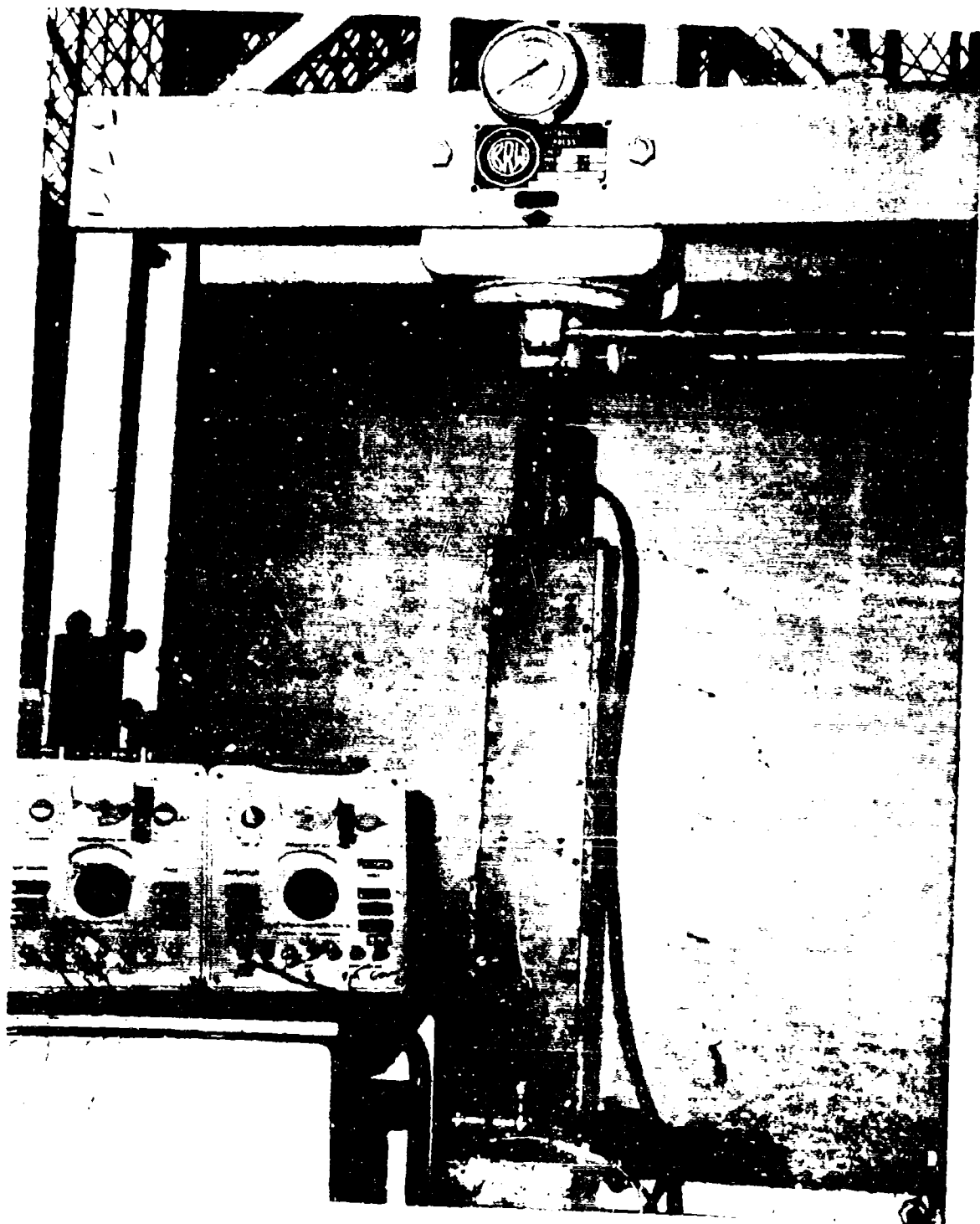
FIG 3.1.4    CALIBRATION OF THE BASE RESISTANCE DYNAMOMETER
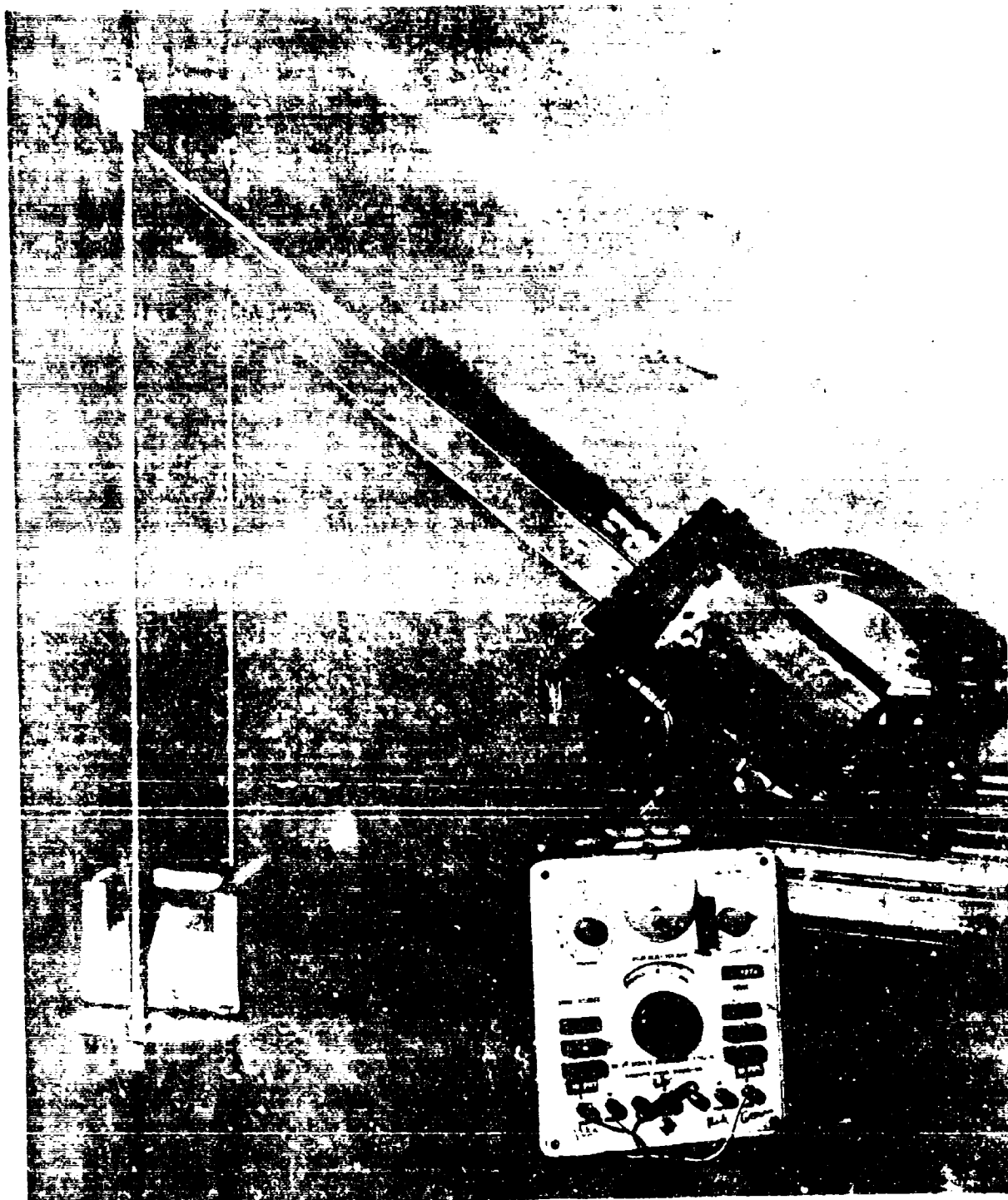
CALIBRATION OF THE SIDE PLATE CANTILEVERS
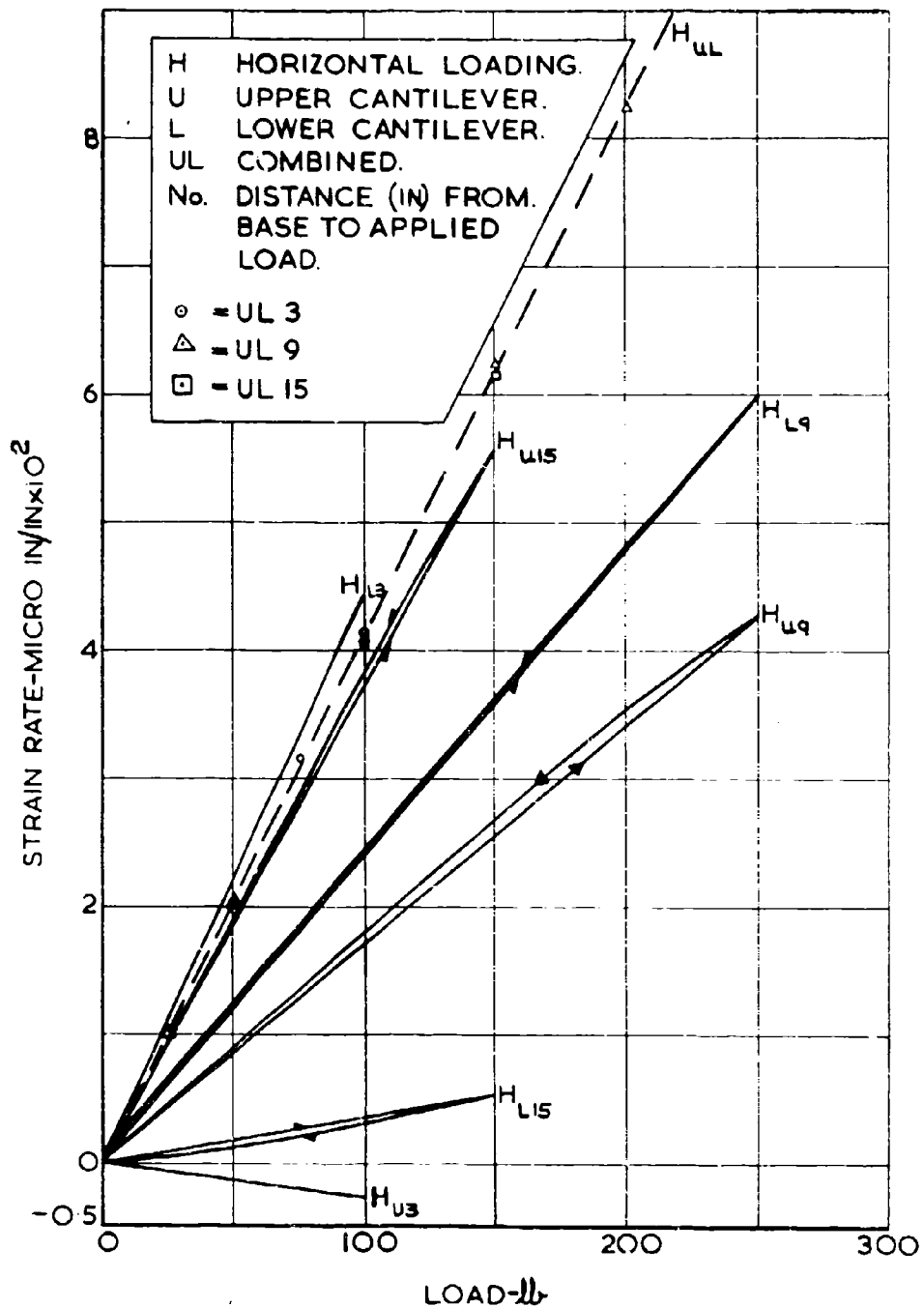
FIG. 3. 1. 6.   SIDE  PLATE  CALIBRATION  CURVE
FOR  NORMAL  LOADING.

109
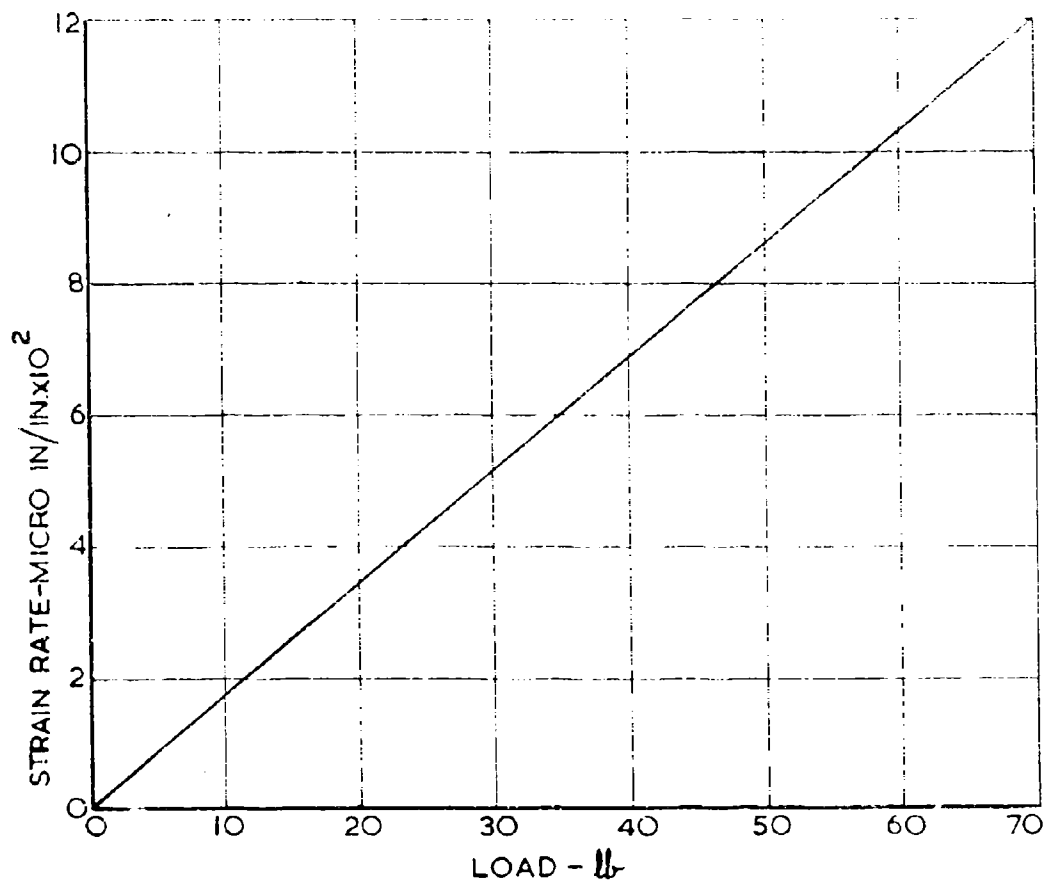
FIG. 3. 1. 7.   SIDE  PLATE  CALIBRATION  CURVE
FOR  SURFACE  TRACTION
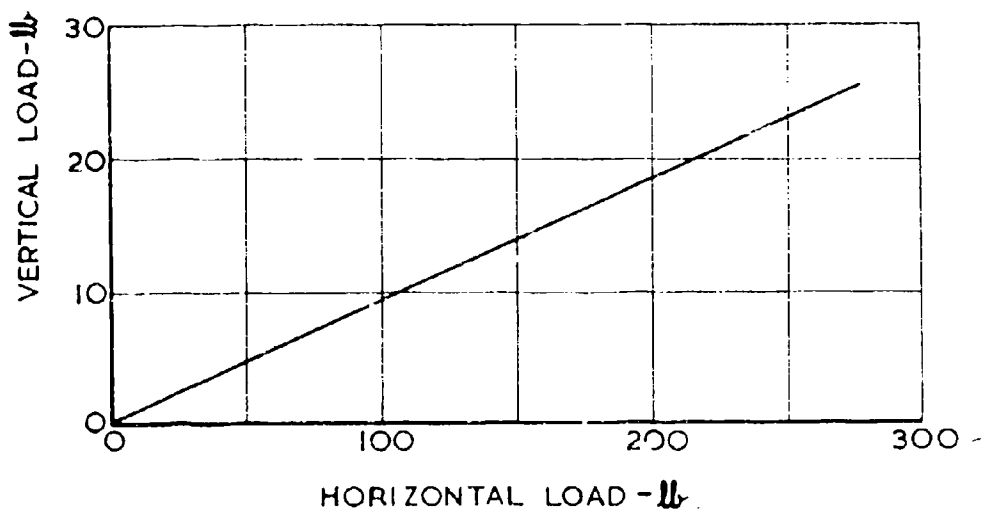


FIG.  3. 1. 8.   INTERACTION.
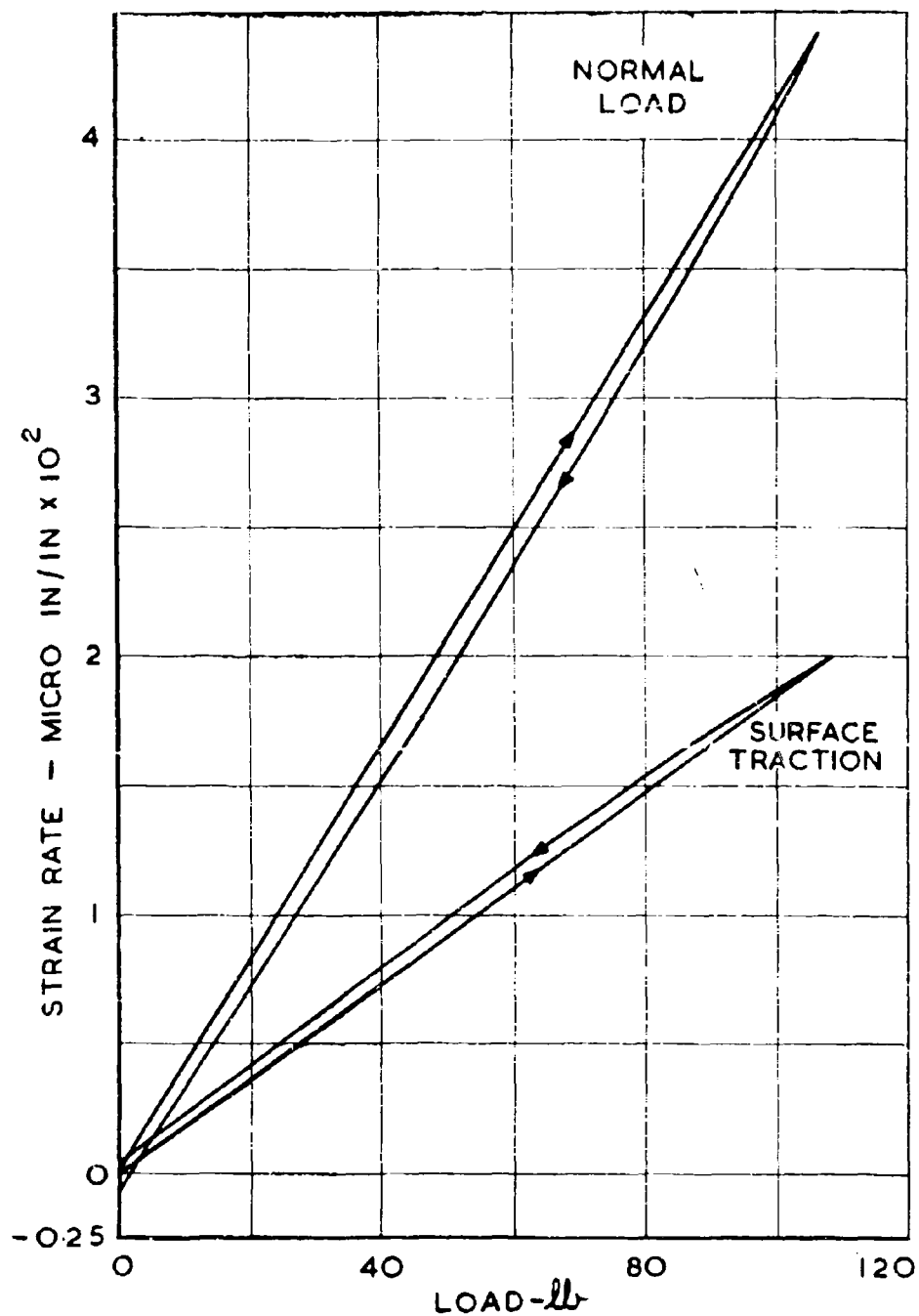
FIG. 3.1.9. SIDE PLATE CALIBRATION
CURVE FOR 45° LOADING.

111

FIG 3.1.10   TESTING A STRIP FOUNDATION

112
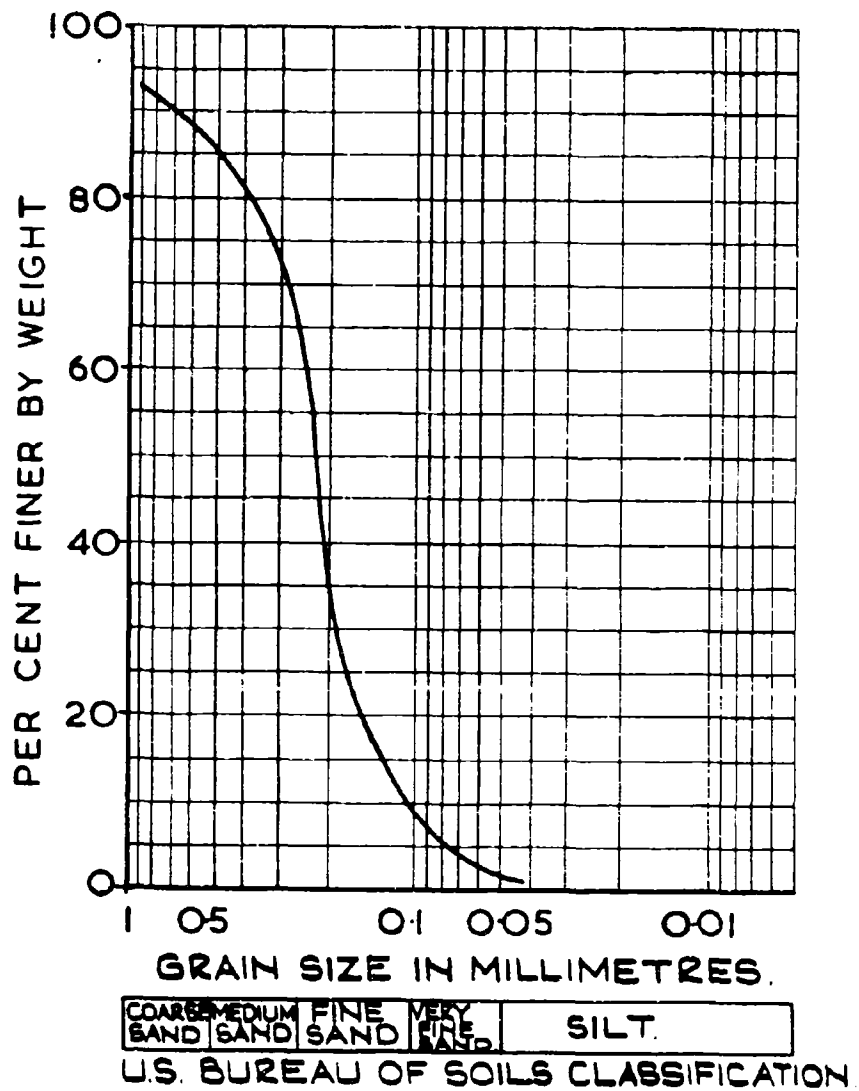
FIG. 3.2.1    GRAIN SIZE DISTRIBUTION
DIAGRAM FOR OHIO SAND.

113
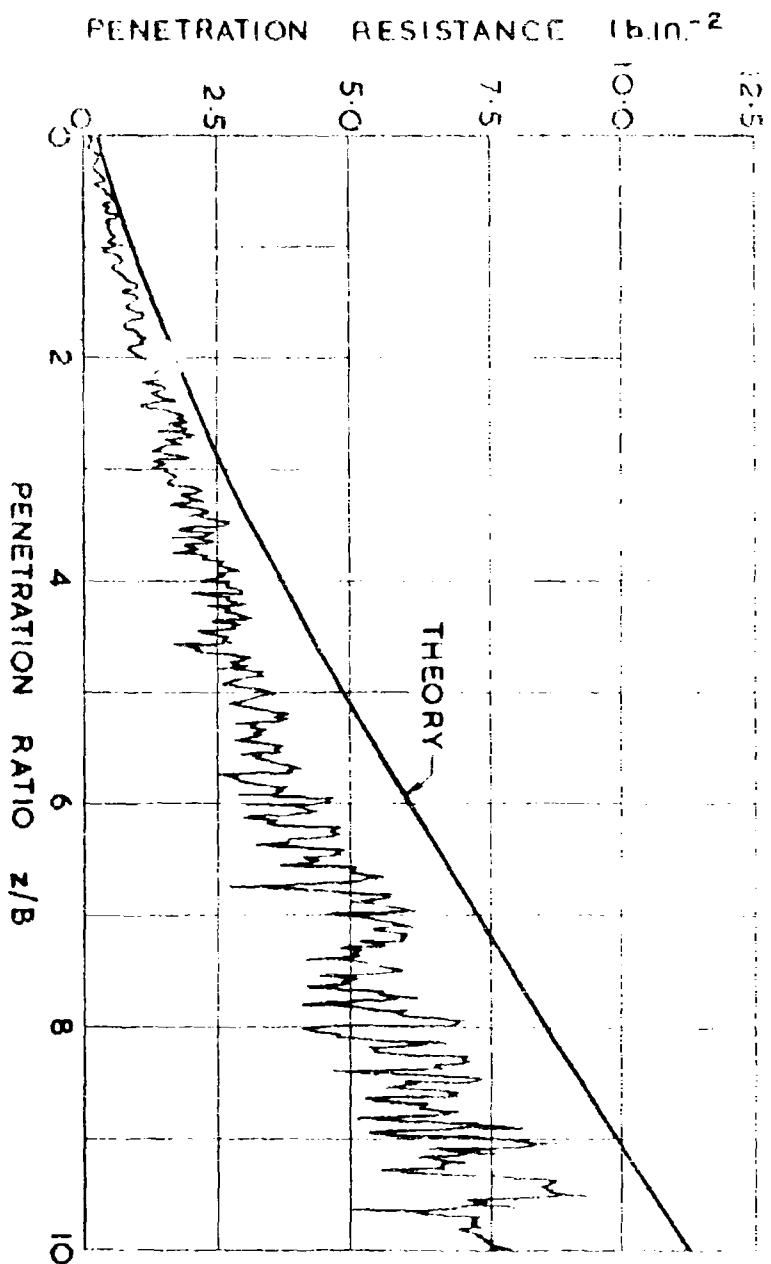
FIG. 4.1.1. COMPARISON BETWEEN THE THEORETICAL AND
EXPERIMENTAL BASE PENETRATION RESISTANCE OF A ROUGH
FOUNDATION DRIVEN PROGRESSIVELY INTO THE ROLLER MODEL

114
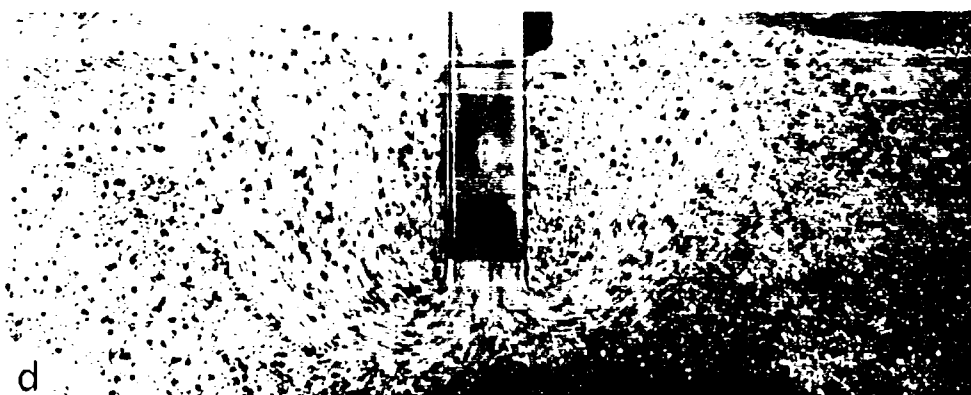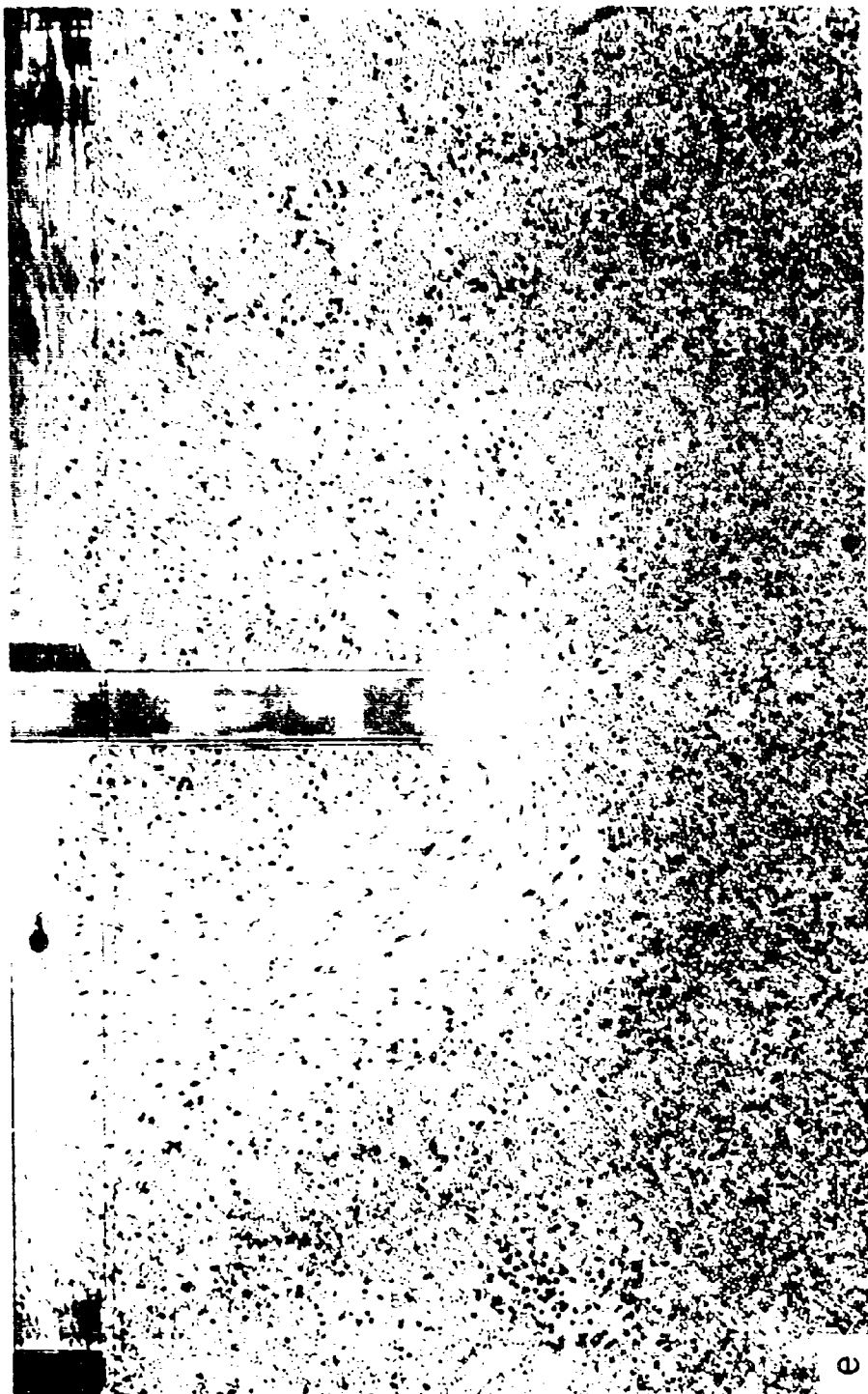
FIG 4.1.2

FIG 4.1.2

FIG 4.1.2

117

FIG 4.1.2

FIG 4.1.2

11
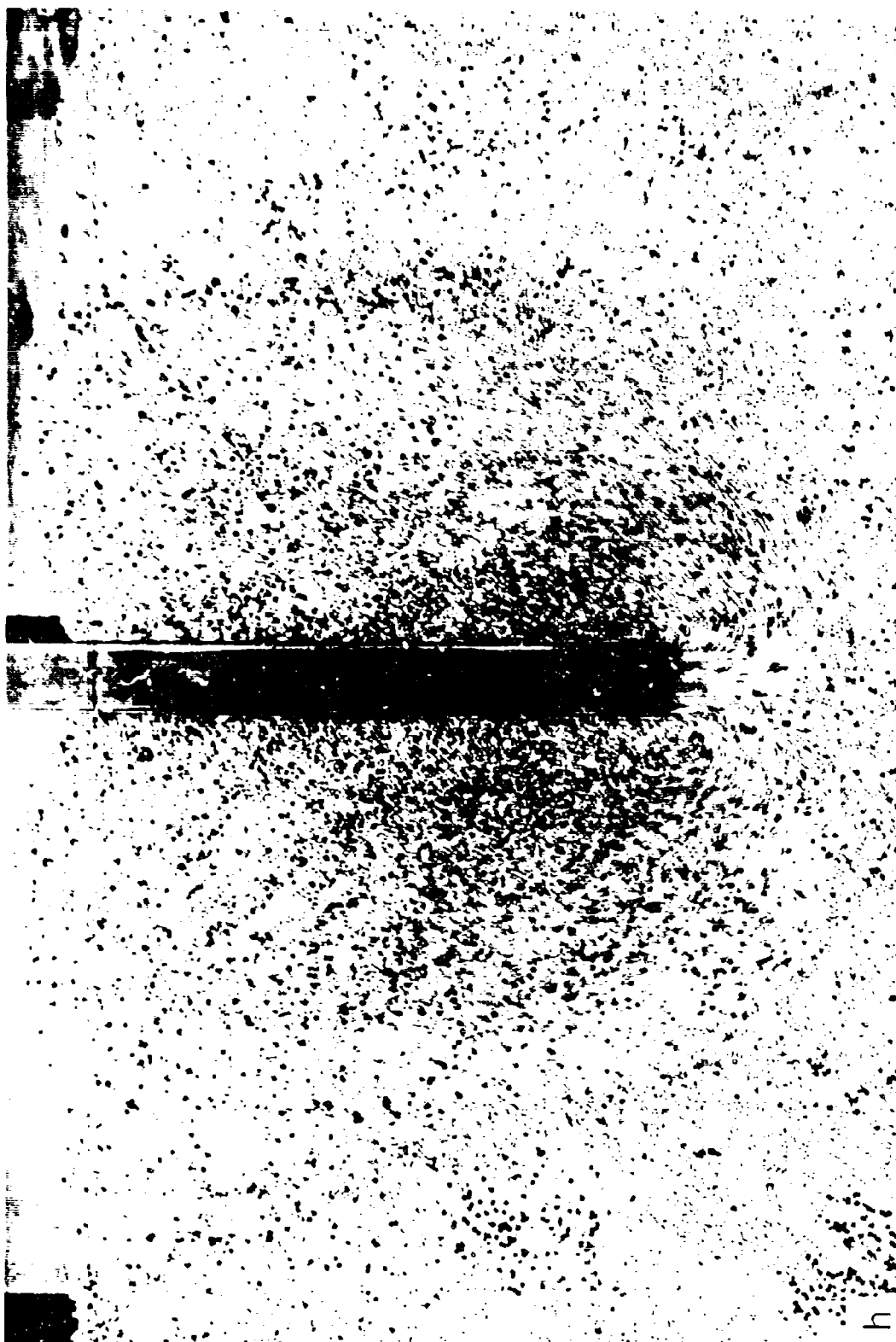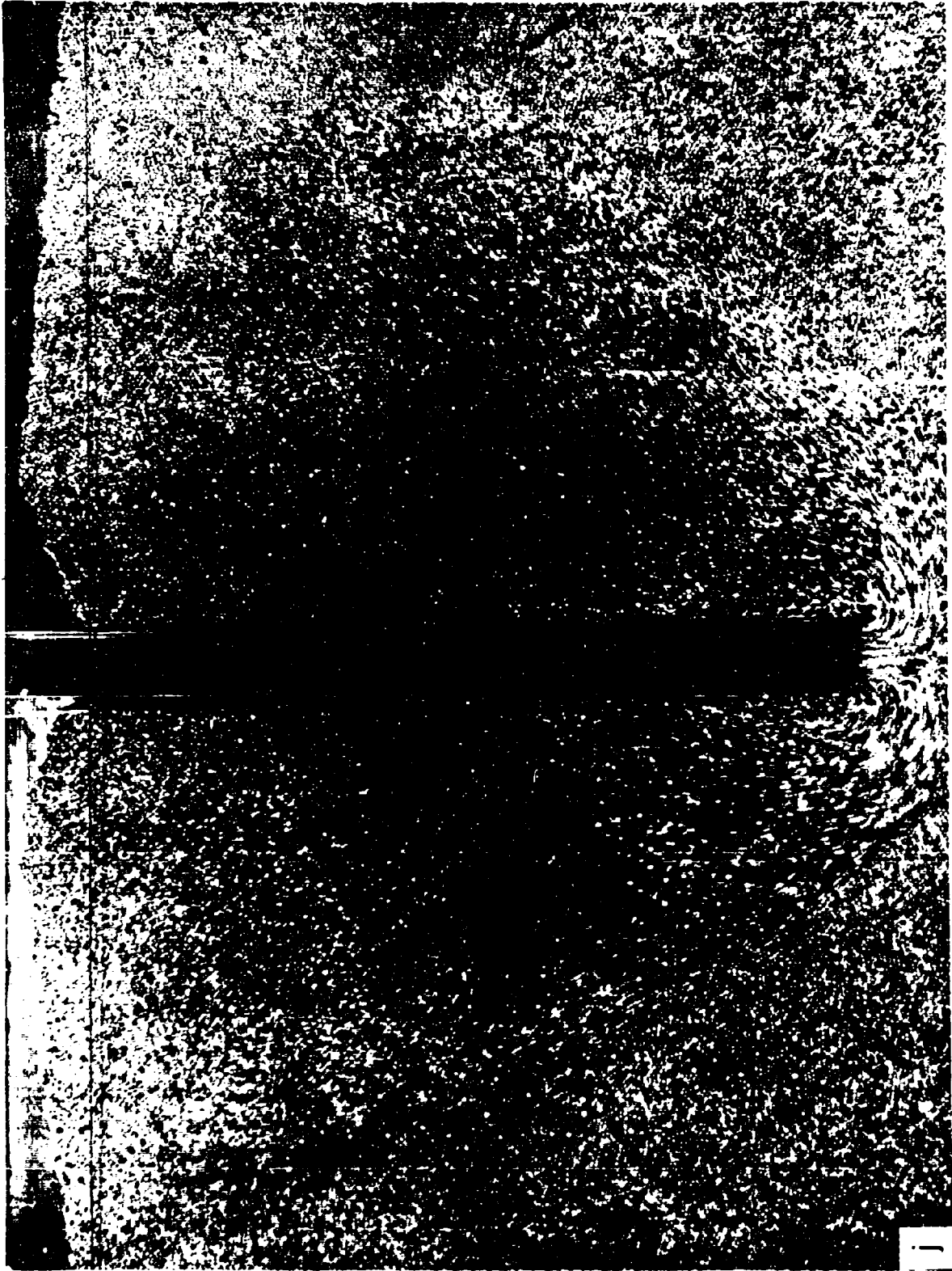
FIG 4.1.2

FIG 4.1.2a to 4.1.2j    The failure patterns for a 2 in. wide rough foundation
driven progressively into the roller model
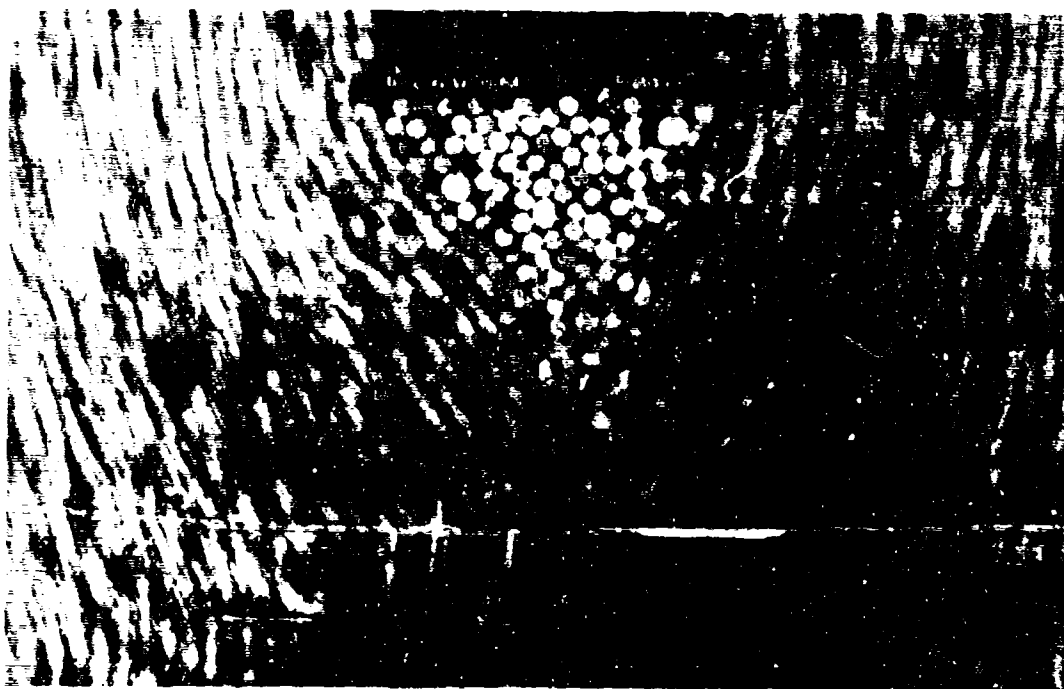
FIG 4.1.3     The formation of the wedge beneath a rough base in
              the roller model
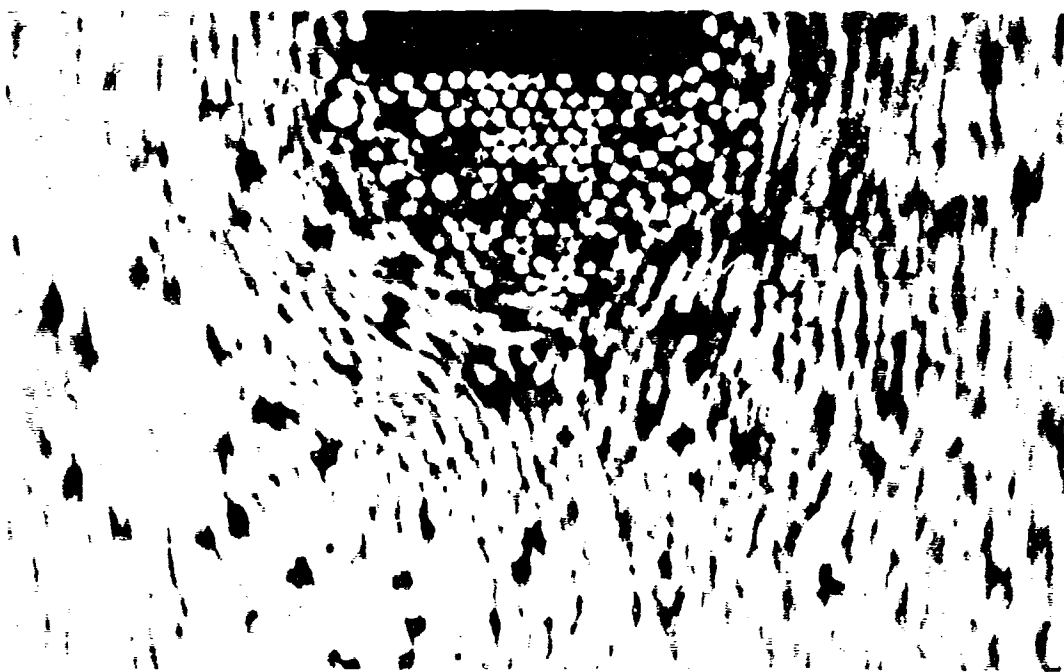


FIG 4.1.4     The shape of the wedge beneath a rough base with
              ideal packing of the rollers

z/B = 1.5

z/B = 4.75

z/B = 9.5
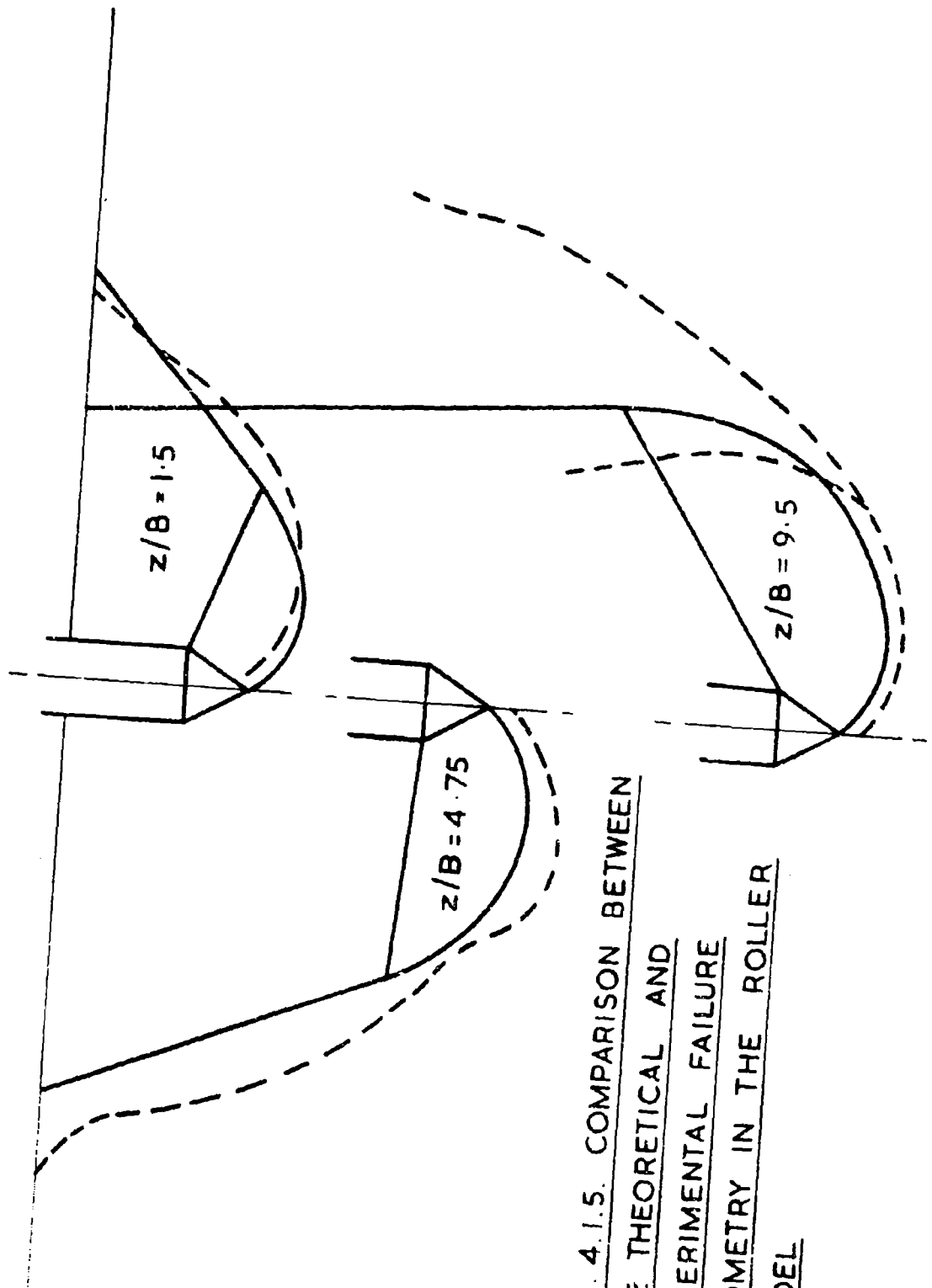
FIG. 4.1.5. COMPARISON BETWEEN
THE THEORETICAL AND
EXPERIMENTAL FAILURE
GEOMETRY IN THE ROLLER
MODEL

123
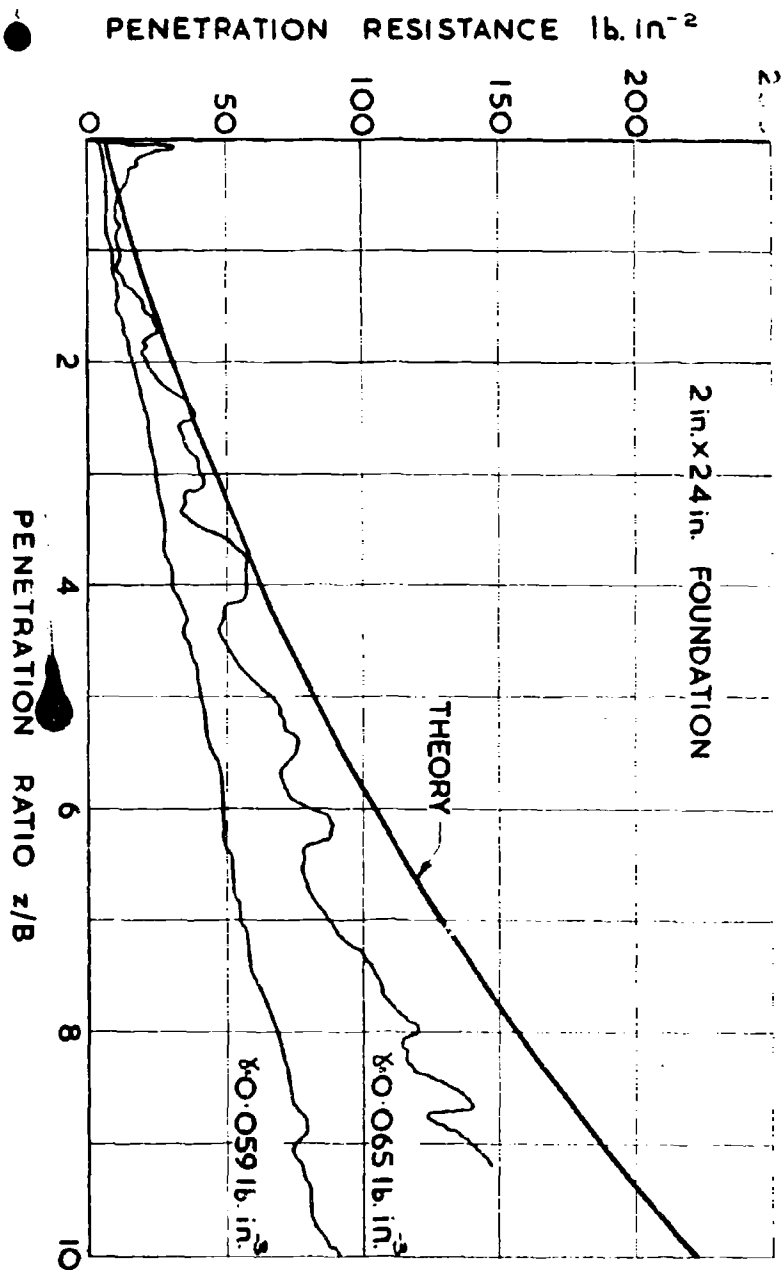
FIG. 4.2.1. COMPARISON BETWEEN THE THEORETICAL AND EXPERIMENTAL BASE PENETRATION RESISTANCE OF A STRIP FOUNDATION DRIVEN PROGRESSIVELY INTO OHIO SAND AT TWO DIFFERENT DENSITIES

124

PENETRATION RESISTANCE
lb. in.⁻²
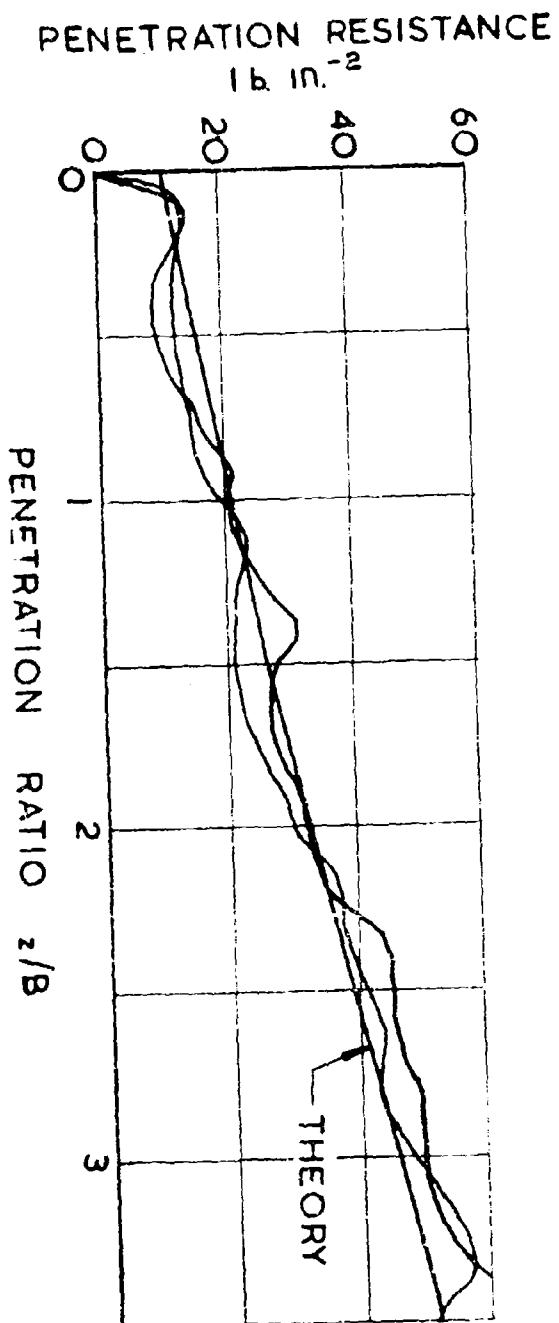
FIG. 4. 2. 2. COMPARISON BETWEEN THE THEORETICAL AND
EXPERIMENTAL BASE PENETRATION RESISTANCE OF A STRIP
FOOTING IN LEIGHTON BUZZARD SAND.

FIG 4.3.1

FIG 4.3.1
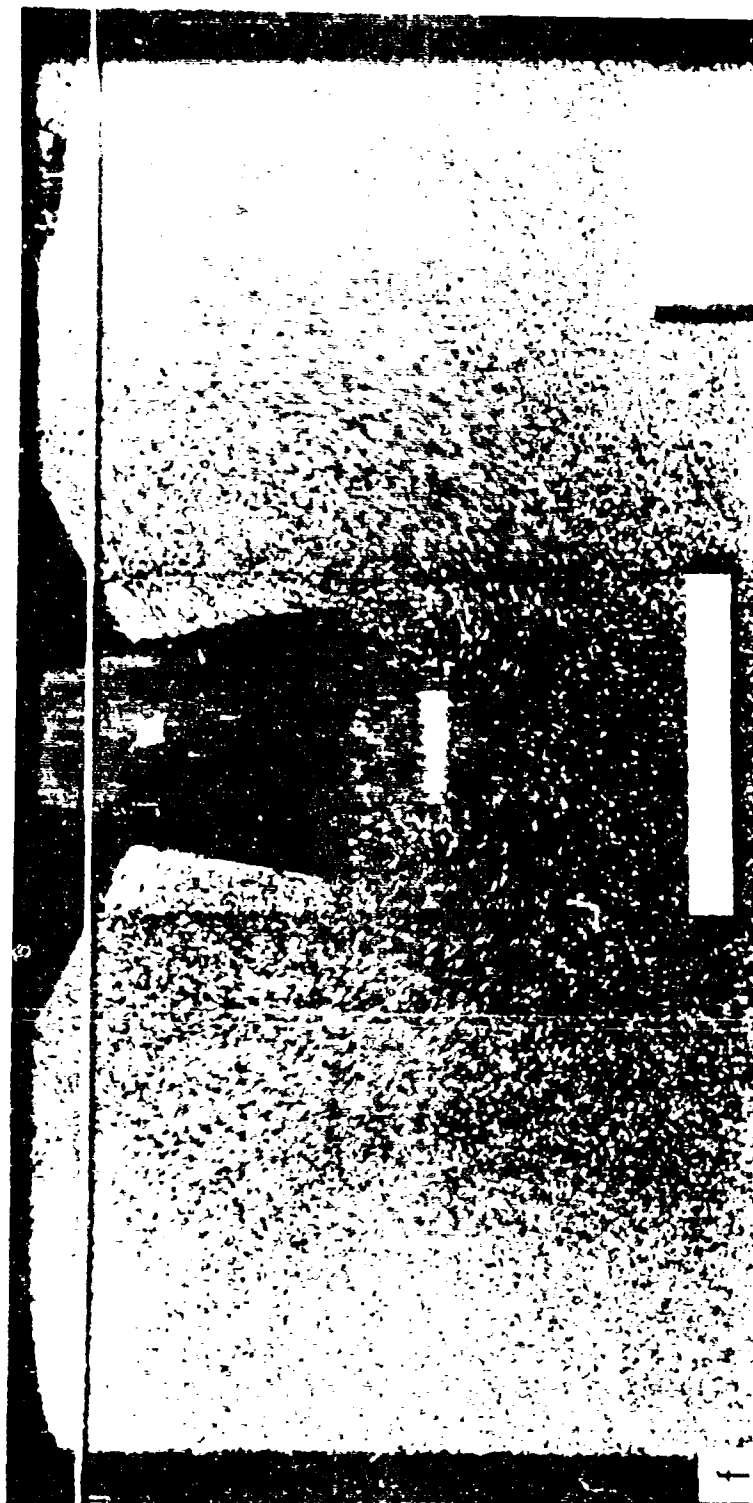
FIG 4.3.1a to 4.3.1f    The failure patterns for a 2 in. wide rough
footing driven progressively into dry sand

# PENETRATION RESISTANCE
## lb. in.$^{-2}$



**PENETRATION RATIO z/B**
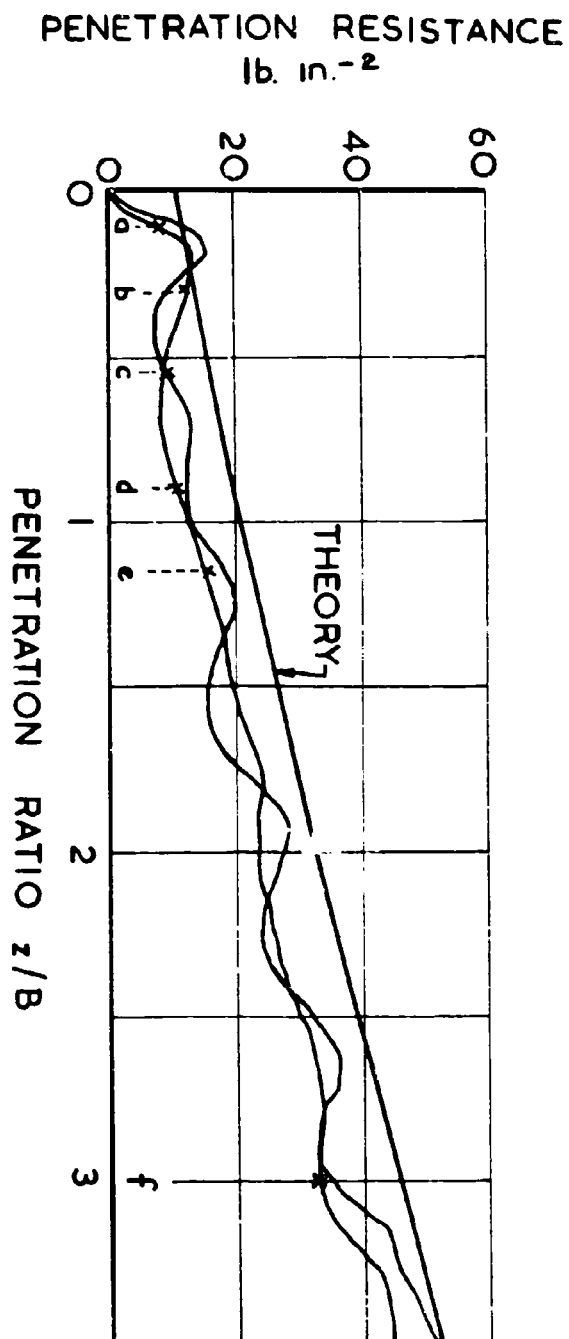
FIG. 4.3.2. COMPARISON BETWEEN THE THEORETICAL AND EXPERIMENTAL BASE PENETRATION RESISTANCE OF A 2 IN. WIDE ROUGH FOOTING IN DRY SAND TOGETHER WITH THE LOCATION OF THE SERIES OF PHOTOGRAPHS 4.3.1.a. TO 4.3.1.f.
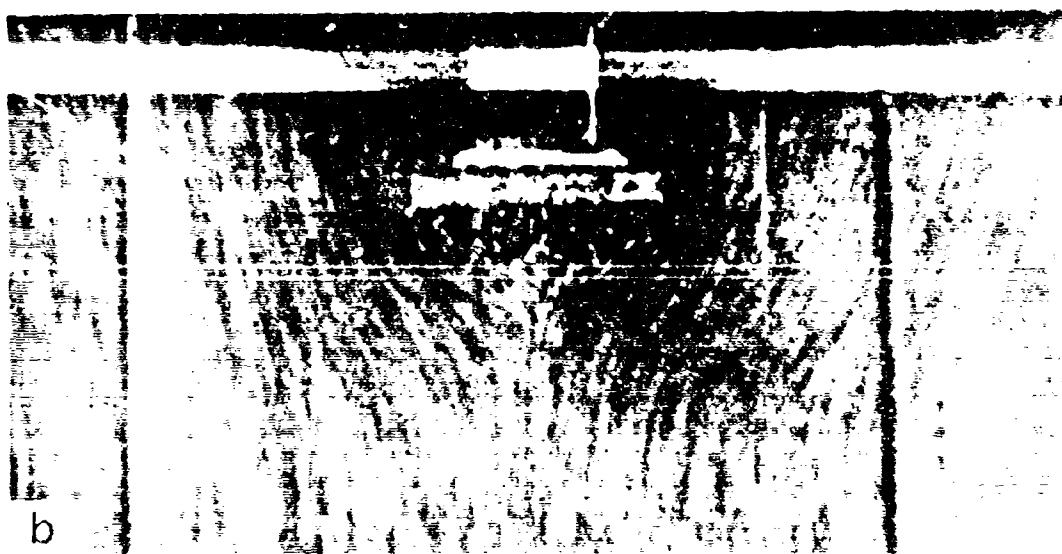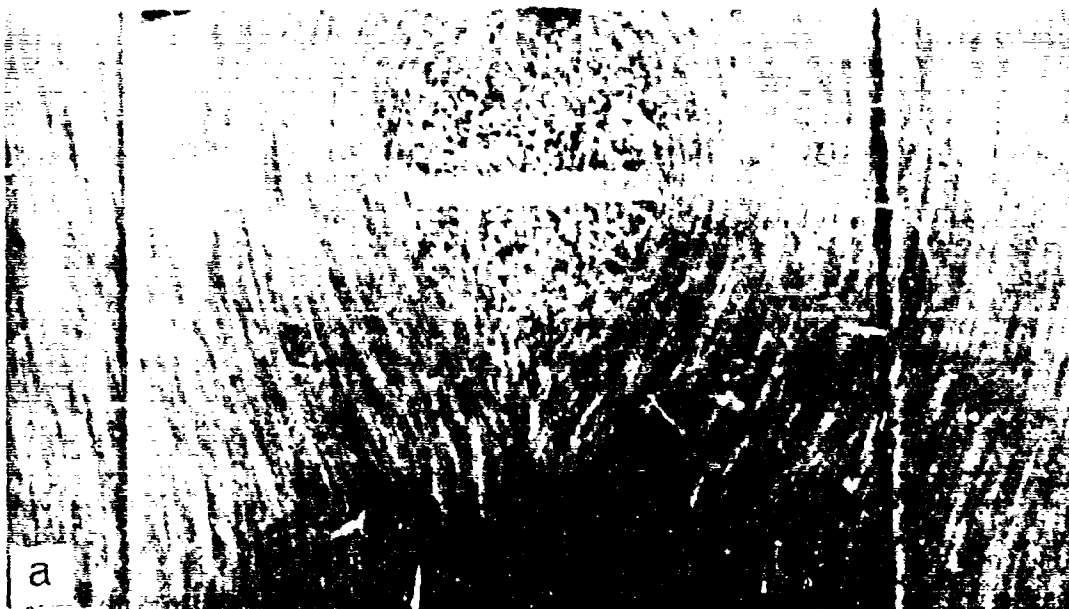
FIG 4.3.3    The shape of the wedge beneath a 2 in. wide rough
             footing in dry sand showing  (a) the maximum size
             and  (b) the minimum size

$\phi = 32°$

$\phi = 40.5°$

z/B=0

z/B=3

——— THEORY

----- EXPERIMENT
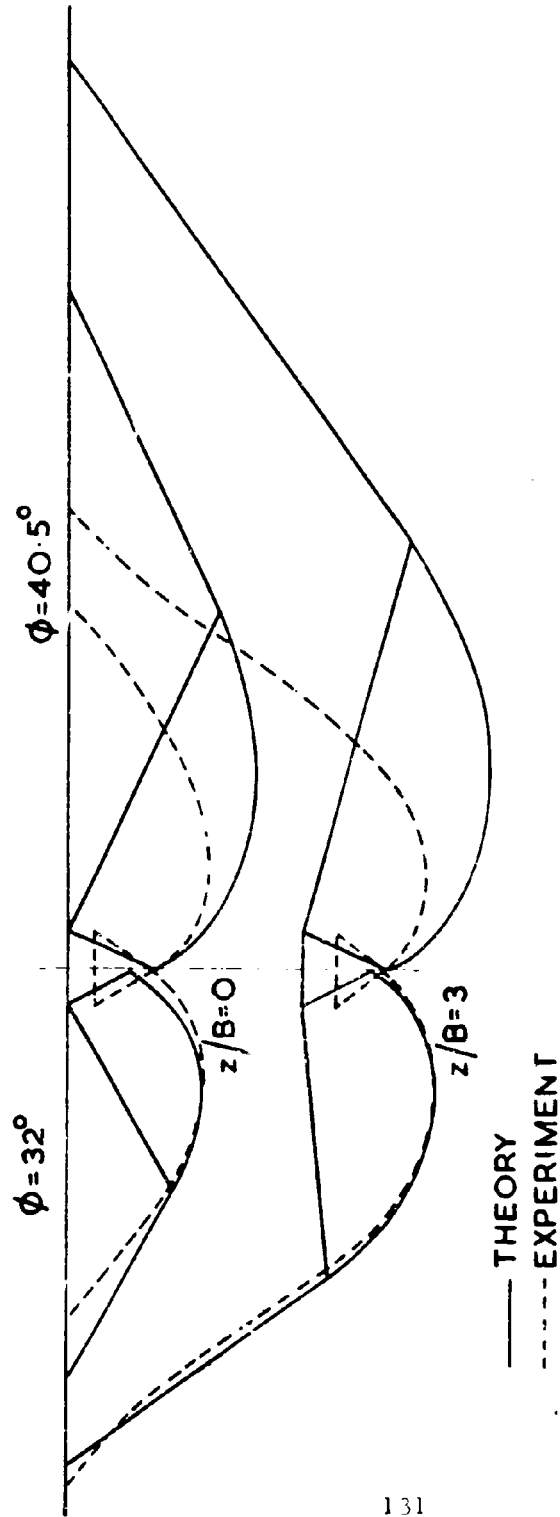
FIG. 4.3.4. THE COMPARISON BETWEEN THE ACTUAL FAILURE PATTERNS IN DRY SAND AT TWO PENETRATION RATIOS AND THE PREDICTED SHAPES FOR THE MAXIMUM AND MINIMUM VALUES OF $\phi$.

131
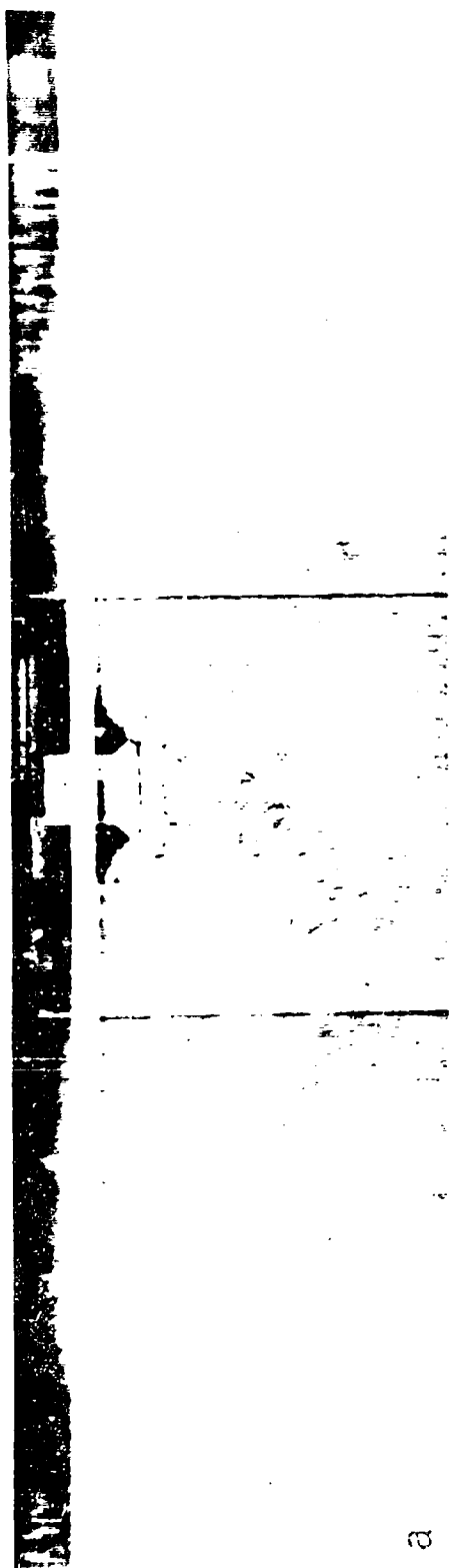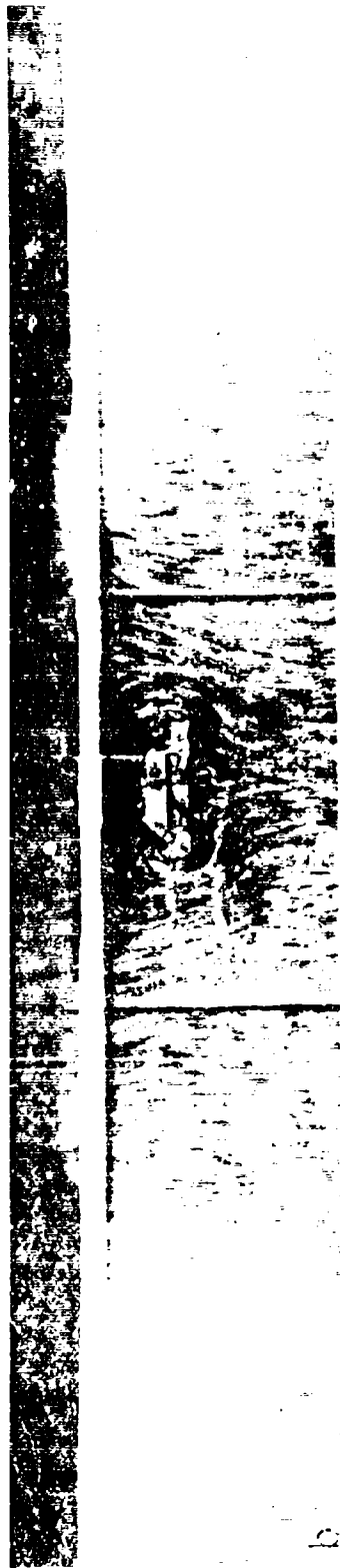
FIG 4.4.1

FIG 4.4.1a to 4.4.1d    The progressive variation in the shape of the wedge beneath
a 2 in. wide smooth footing driven into dry sand
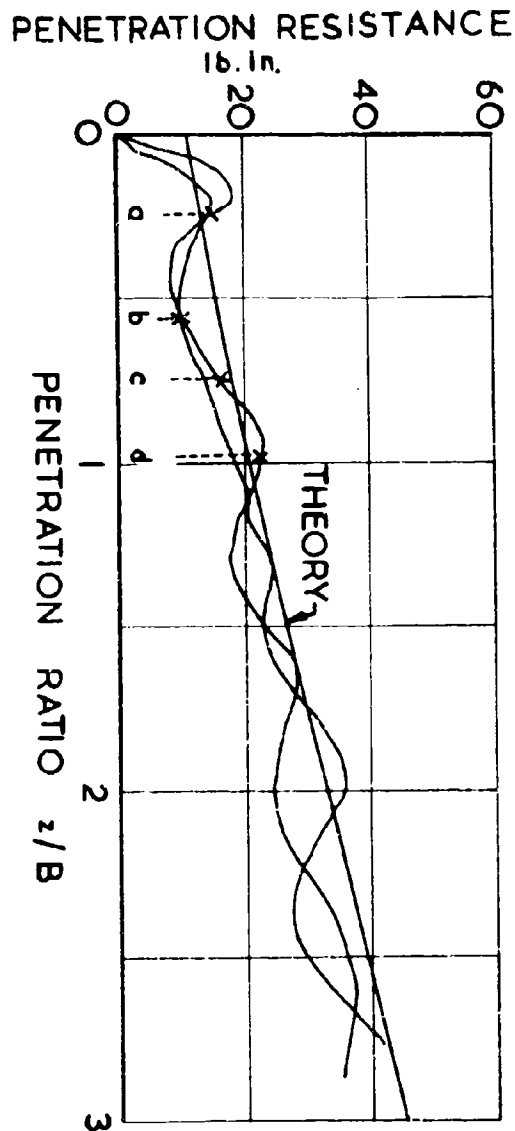
FIG. 4.4.2. COMPARISON BETWEEN THE THEORETICAL AND EXPERIMENTAL BASE PENETRATION RESISTANCE OF A 2 IN. WIDE LUBRICATED GLASS FOOTING IN DRY SAND TOGETHER WITH THE LOCATION OF THE SERIES OF PHOTOGRAPHS 4.4.1a. TO 4.4.1d.
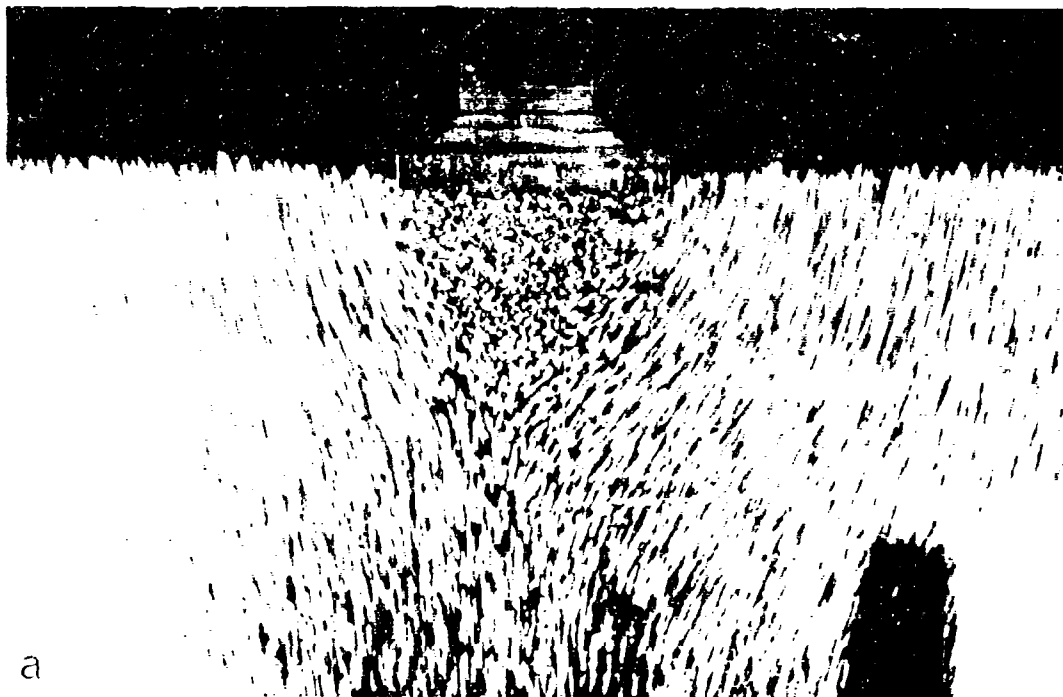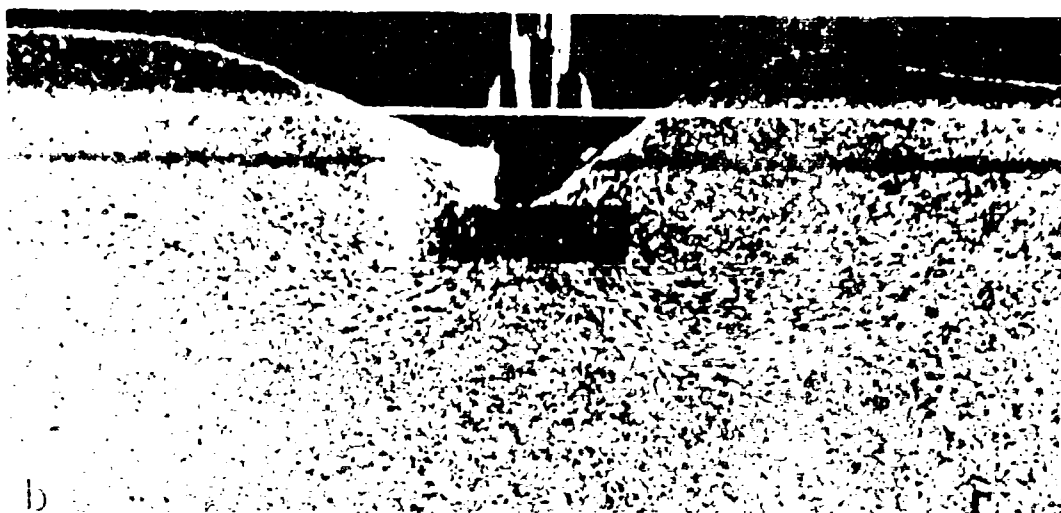
FIG 4.4.3    The formation of the wedge beneath a 2 in. wide smooth
             footing driven into dry sand.

             (a) The maximum size during the initial mobilisation process
             (b) The complete development of the double wedge.
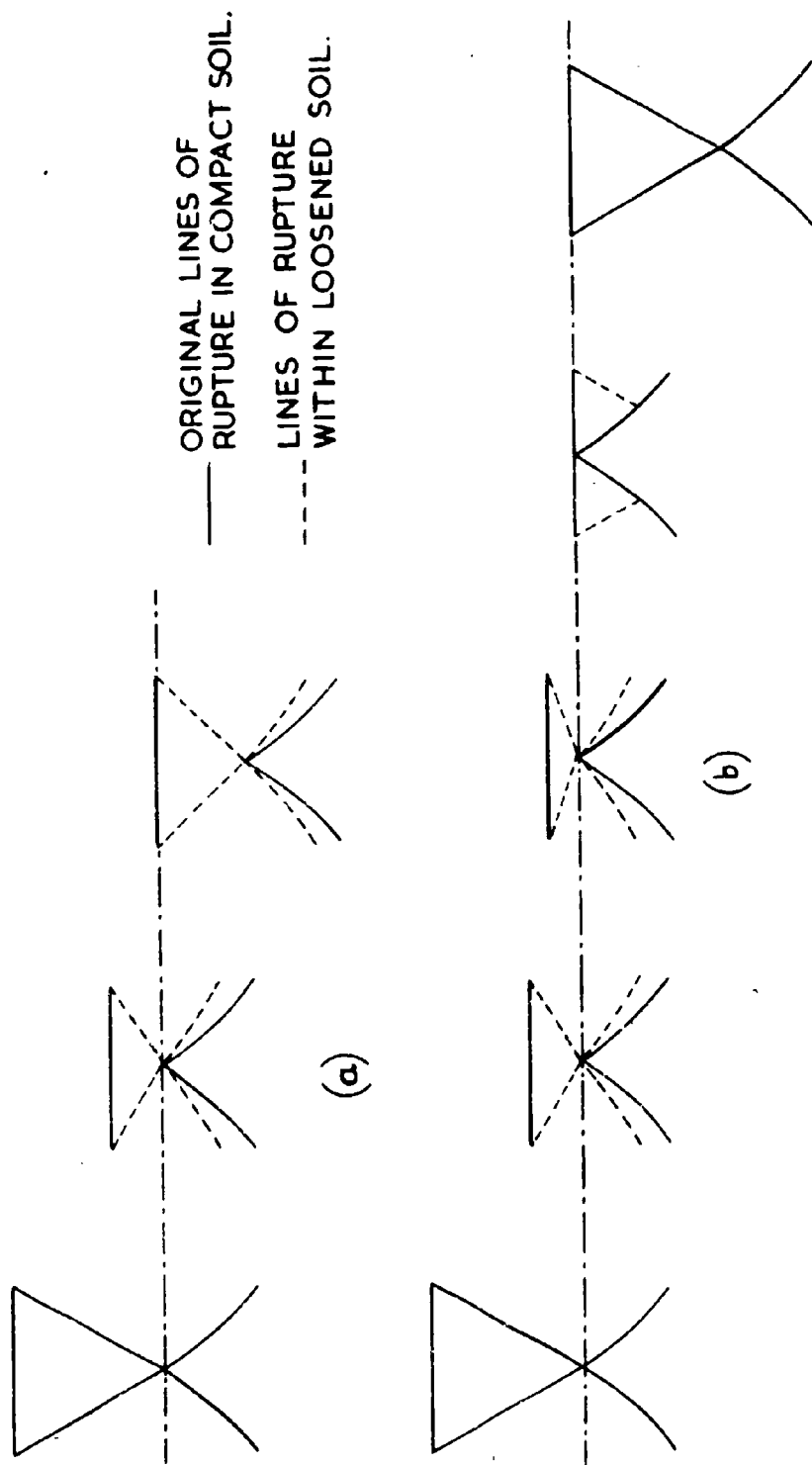
FIG. 4.4.4. THE CYCLIC VARIATION IN WEDGE SHAPE BENEATH (a) A ROUGH BASE AND (b) A SMOOTH BASE AS THE FOOTING IS DRIVEN INTO THE SOIL.

ORIGINAL LINES OF RUPTURE IN COMPACT SOIL.

LINES OF RUPTURE WITHIN LOOSENED SOIL.

(a)

(b)

DIRECTION OF PENETRATION



(a) ROUGH BASE

(b) SMOOTH BASE
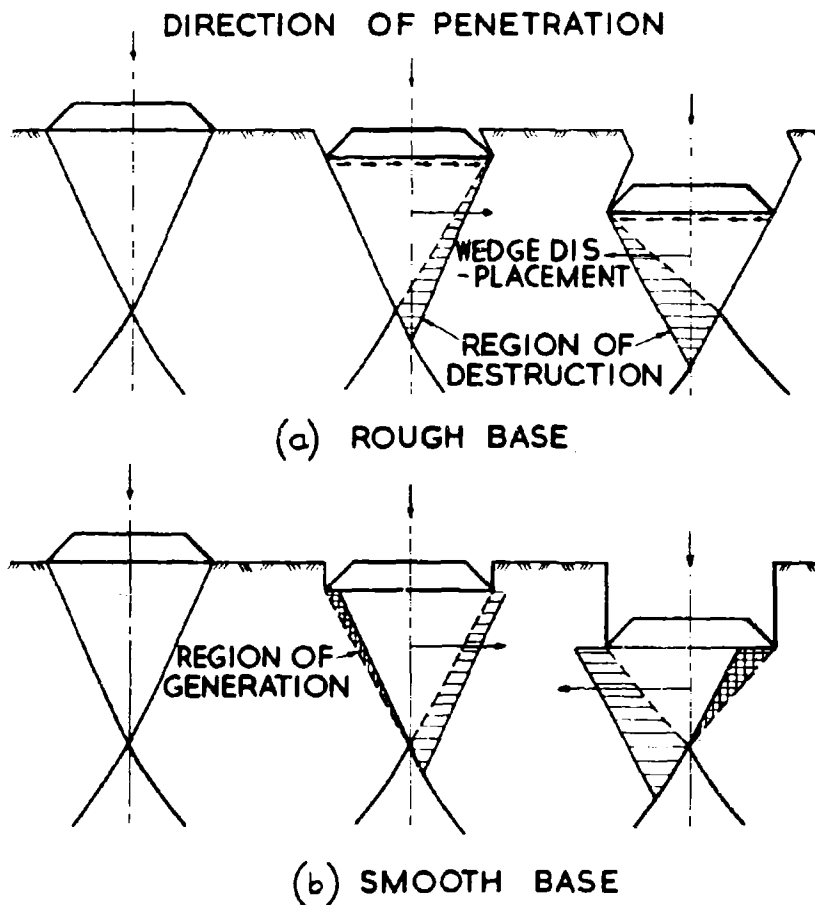
—————— ORIGINAL BOUNDARIES

------ GENERATED BOUNDARIES

FIG. 4.4.5. THE PARTIAL DESTRUCTION OF THE WEDGE BY ASYMMETRICAL FAILURE.

(a) BENEATH A ROUGH FOOTING WHERE LATERAL THRUST IS IMPARTED TO THE FOOTING.

(b) BENEATH A SMOOTH FOOTING WHERE THE LATERAL THRUST IS CONFINED TO THE WEDGE IN THE ABSENCE OF SHEAR STRESSES ALONG THE SOIL FOOTING INTERFACE.

137
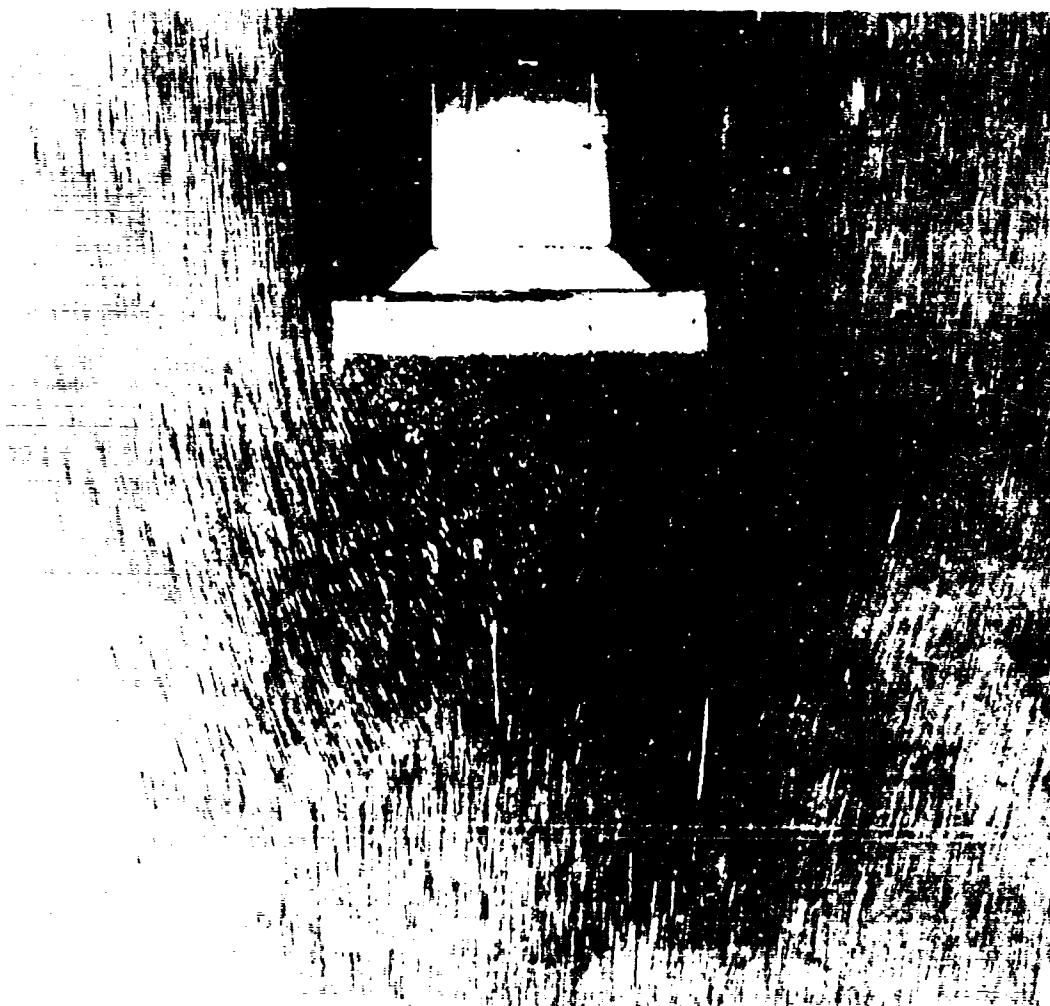
FIG 4.5.1    The shape of the wedge beneath a 2 in. wide smooth
             footing buried in damp sand
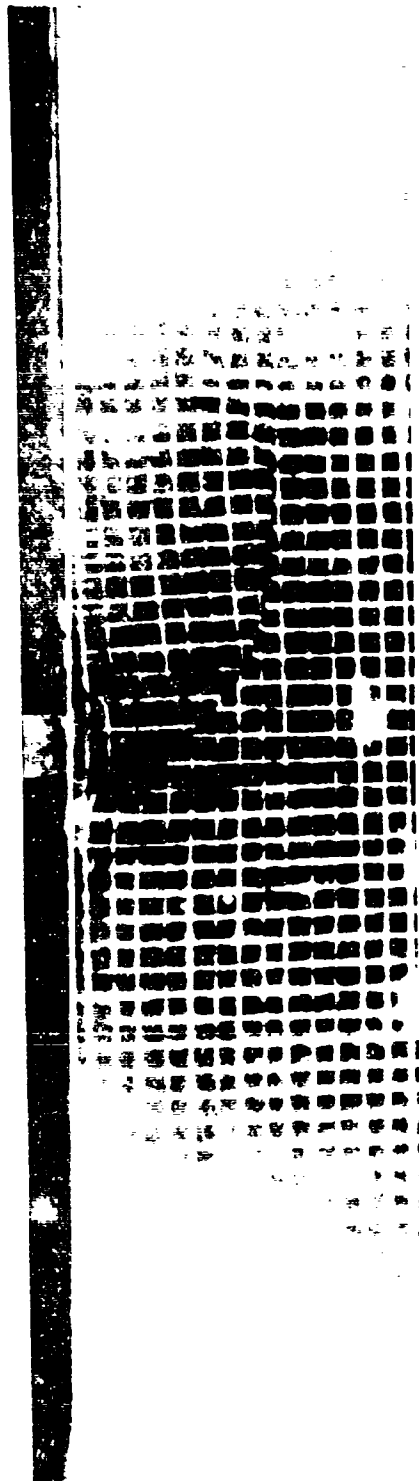
FIG 4.5.2   Asymmetrical failure in damp sand for a 1·5 in. wide steel footing driven from the surface
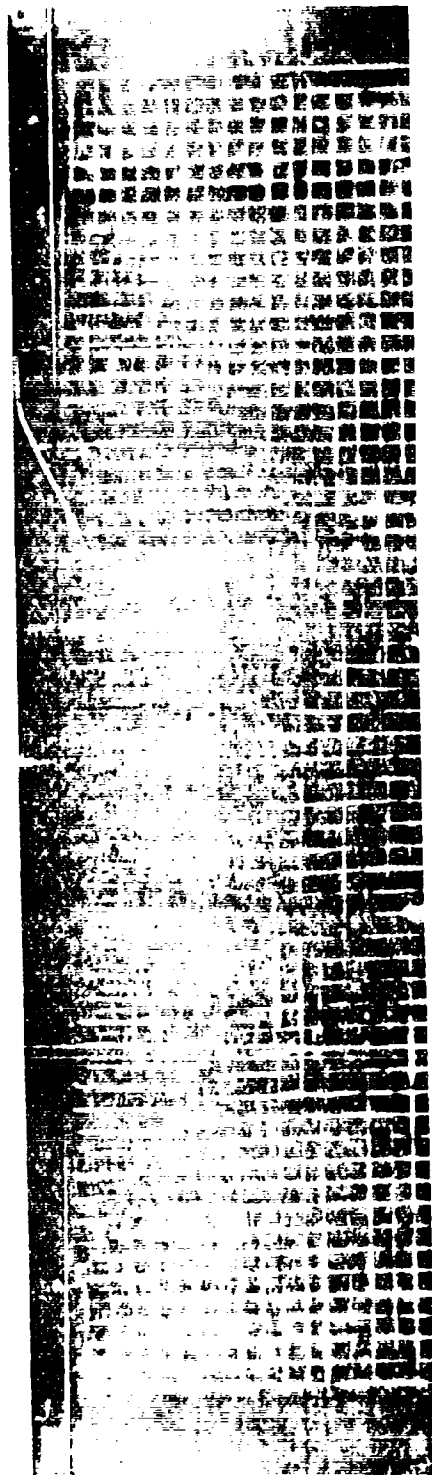


FIG 4.5.3   Failure in damp sand for a 1·5 in. wide steel footing driven from a penetration ratio of 1

FIG 4.5.4 Failure in damp sand for a 1·5 in. wide steel footing driven from a penetration ratio of 2

(a) Asymmetrical failure
(b) Complete failure with further footing displacement
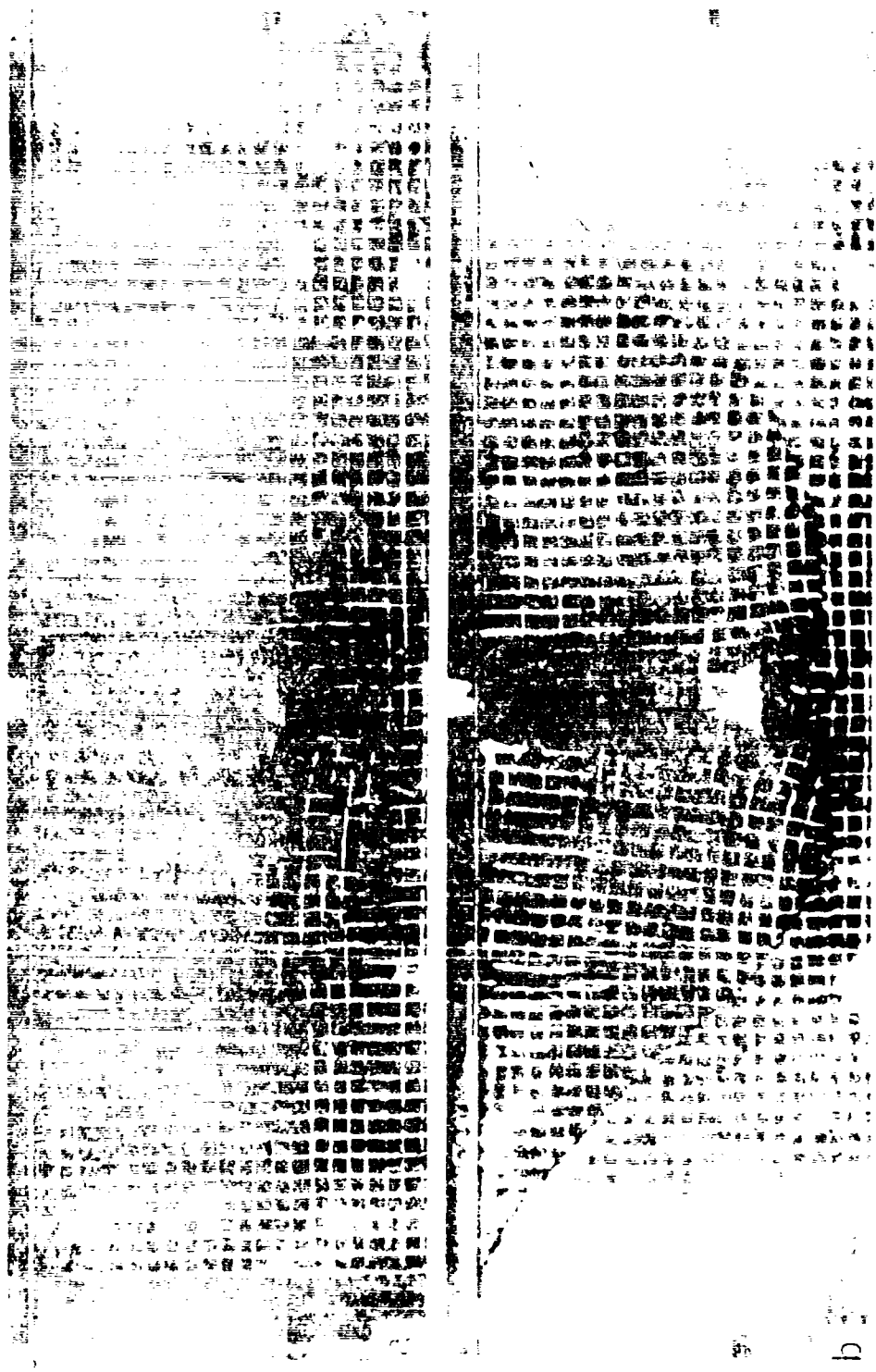
FIG 4.5.5    Failure in damp sand for a 1·5 in. wide steel footing driven from a
penetration ratio of 3

(a)  Asymmetrical failure
(b)  Complete failure with further footing displacement

z/B=0

z/B=3

—— THEORY
– – – EXPERIMENTAL
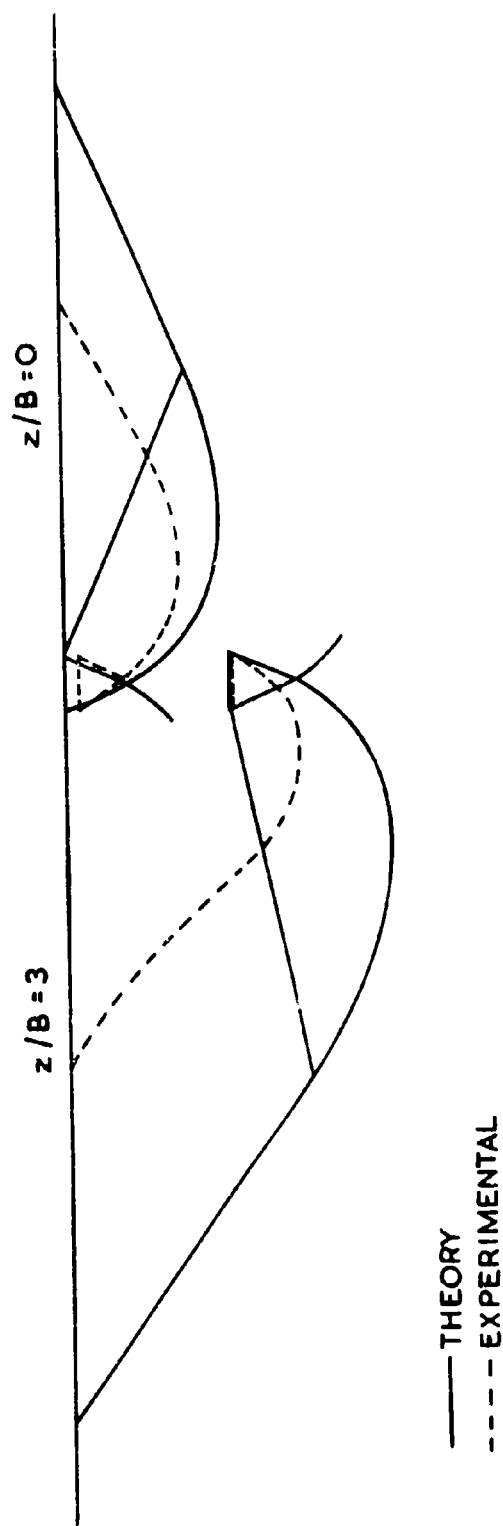
FIG. 4. 5. 6. THE COMPARISON BETWEEN THE ACTUAL ASYMETRICAL FAILURE PATTERNS IN DAMP SAND AT TWO PENETRATION RATIOS & THE PREDICTED SYMMETRICAL SHAPES.

142

FIG 4.5.7    The development of the zone ......    in. wide rough
             footing driven progressively, ...    and from a
             penetration ratio of ...

             (a) The initial stage when ...       ...ilure boundaries
             (b) Progressive ... to from the ...
             (c) The appearance of a ...           ... boundary from
                 the ...
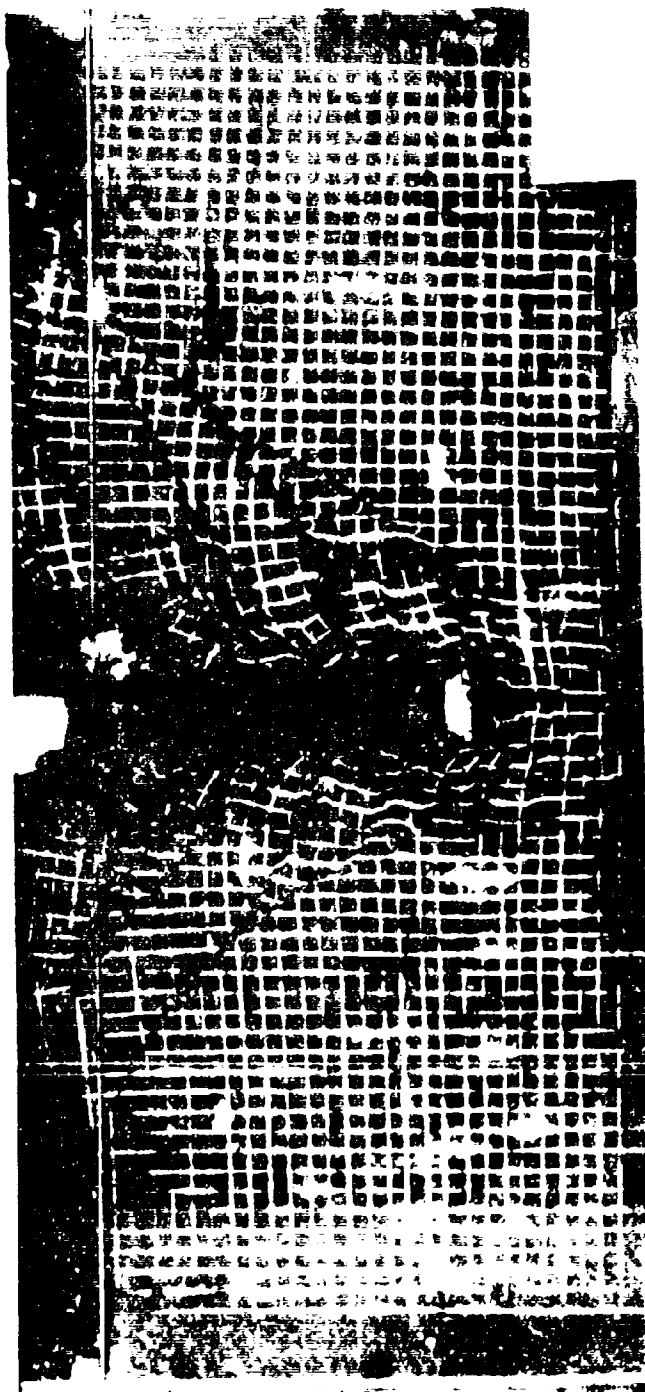
FIG 4.5.8   Progressive failure in damp sand for a 1·5 in. wide steel footing driven from the surface
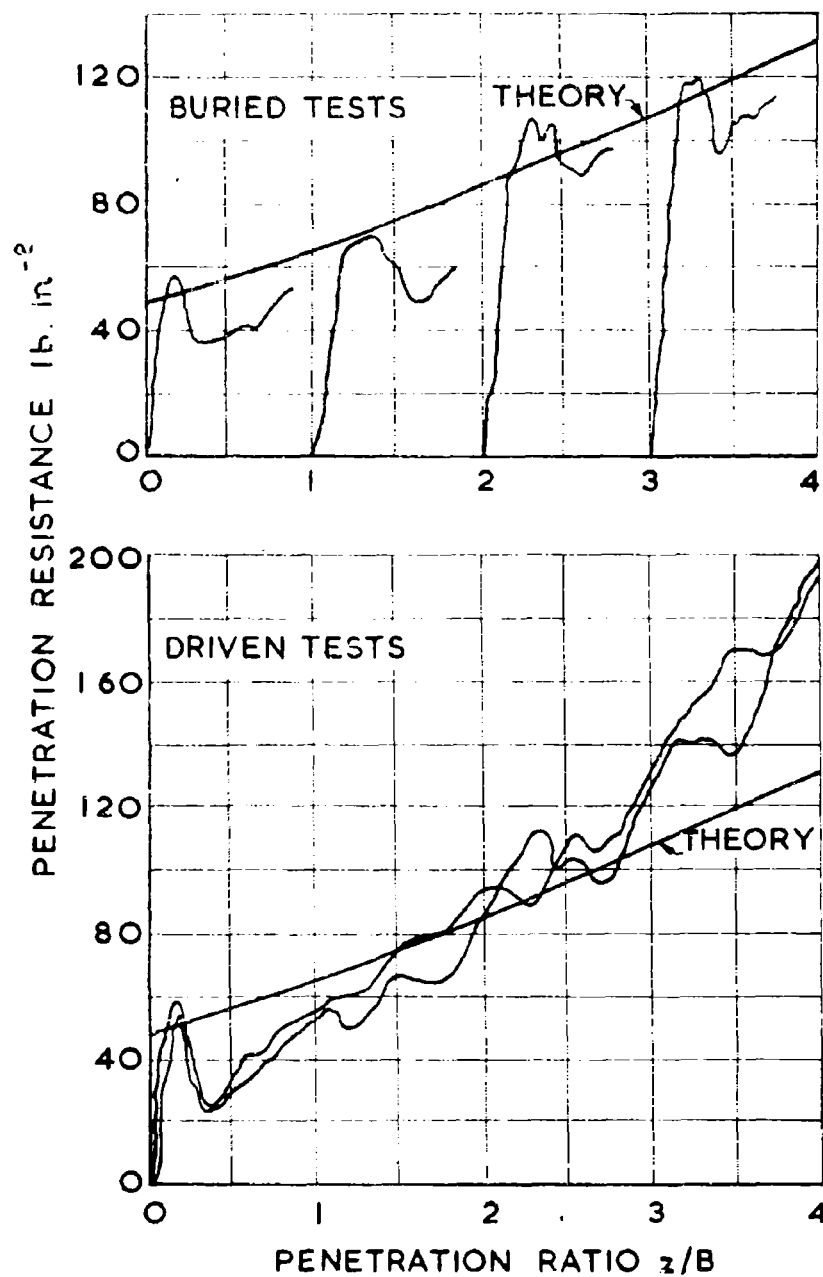
FIG. 4.5.9. COMPARISON BETWEEN THE THEORETICAL
AND EXPERIMENTAL BASE PENETRATION RESISTANCE
IN DAMP SAND FOR BOTH BURIED AND DRIVEN FOOTINGS.

PENETRATION RESISTANCE
lb. in.⁻²
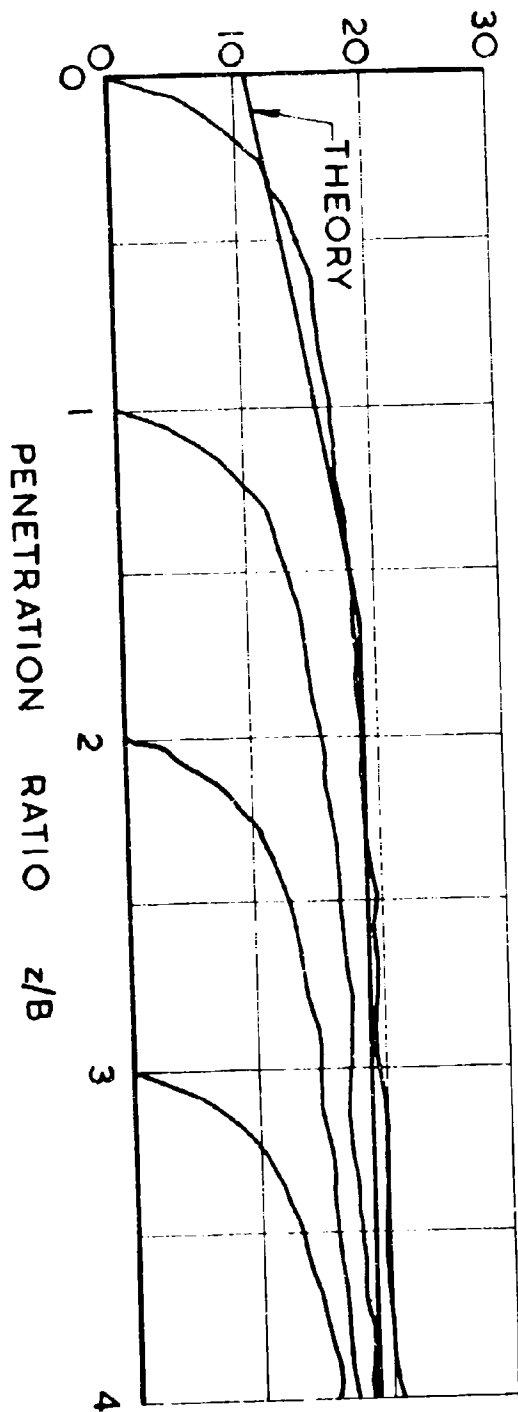
FIG 4.6.1. COMPARISON BETWEEN THE THEORETICAL AND
EXPERIMENTAL BASE PENETRATION RESISTANCE IN CLAY

146
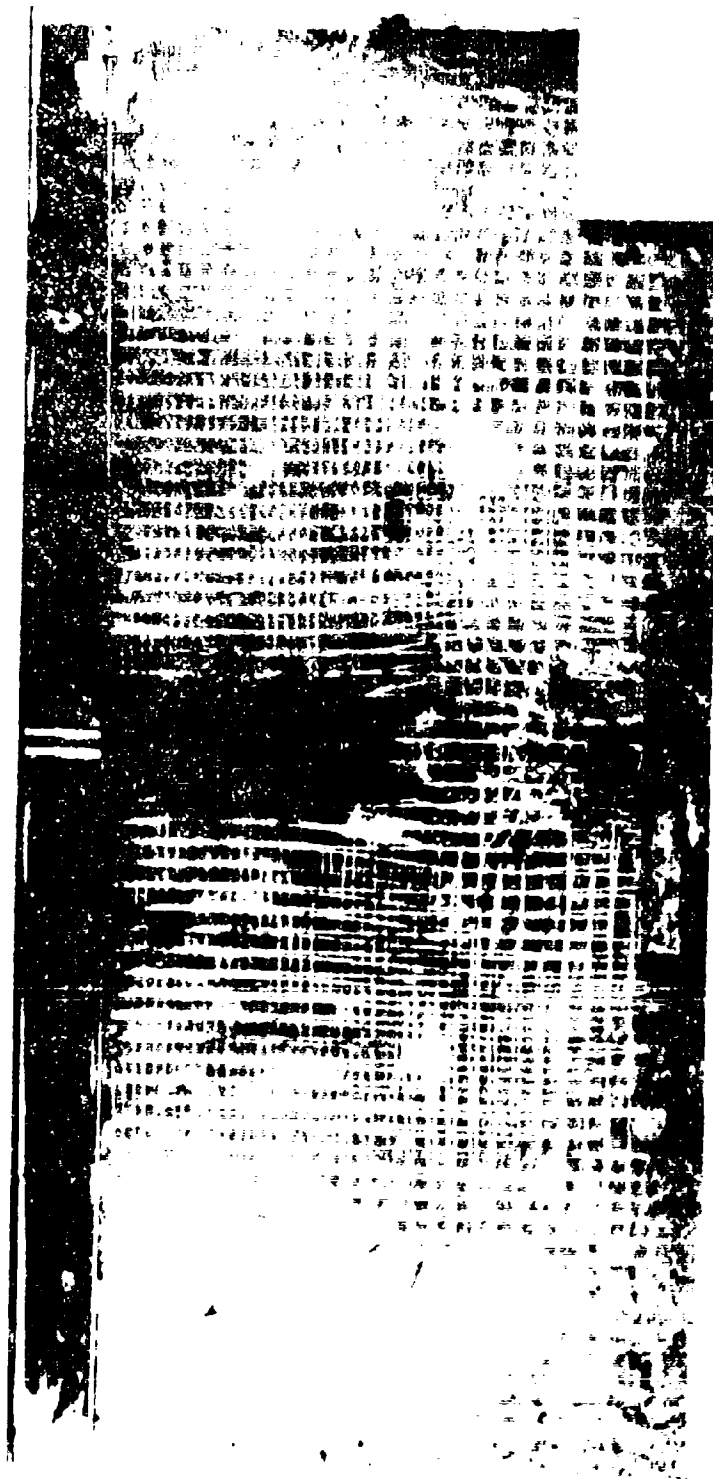
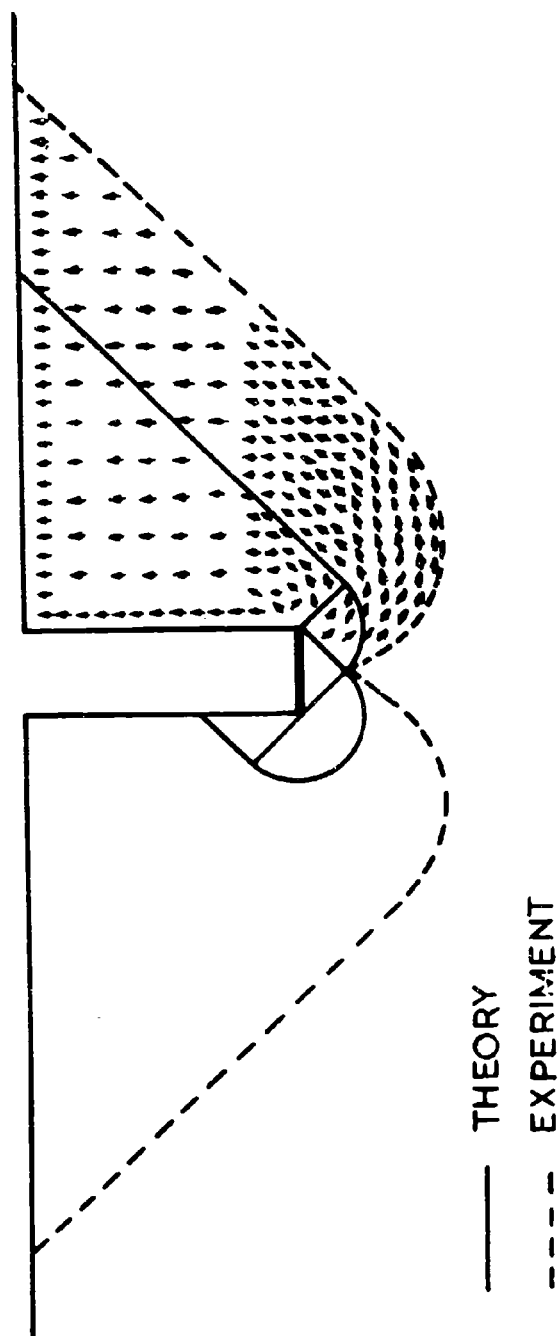FIG 4.6.2    Superposed grid displacements for a 2 in. wide rough buried footing driven from a penetration ratio of 2 to 3

——— THEORY

– – – EXPERIMENT

FIG. 4. 6. 3.  THE DISPLACEMENT DIAGRAM SHOWING THE MAGNITUDE AND DIRECTION OF THE DISPLACEMENTS IN CLAY FOR A BURIED FOOTING DRIVEN FROM A PENETRATION RATIO OF 2 TO 3 TOGETHER WITH THE PREDICTED FAILURE PATTERNS FOR AN UNSUPPORTED (LHS) AND A SUPPORTED SHAFT (RHS).

148
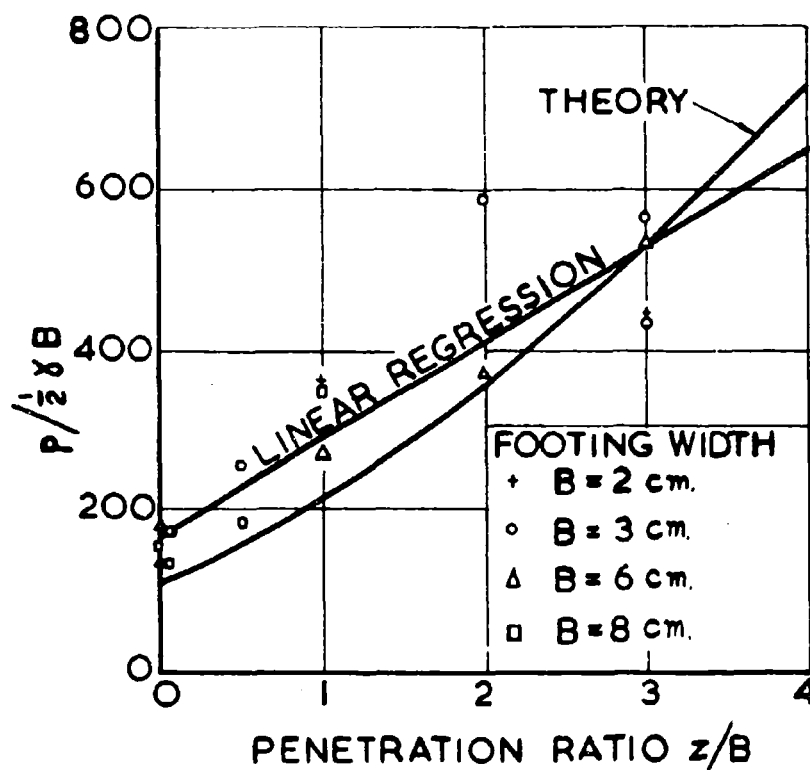
FIG. 4.7.1. COMPARISON BETWEEN THE TEST RESULTS OBTAINED BY LEBEQUE AND THE PREDICTED BASE PENETRATION RESISTANCE.
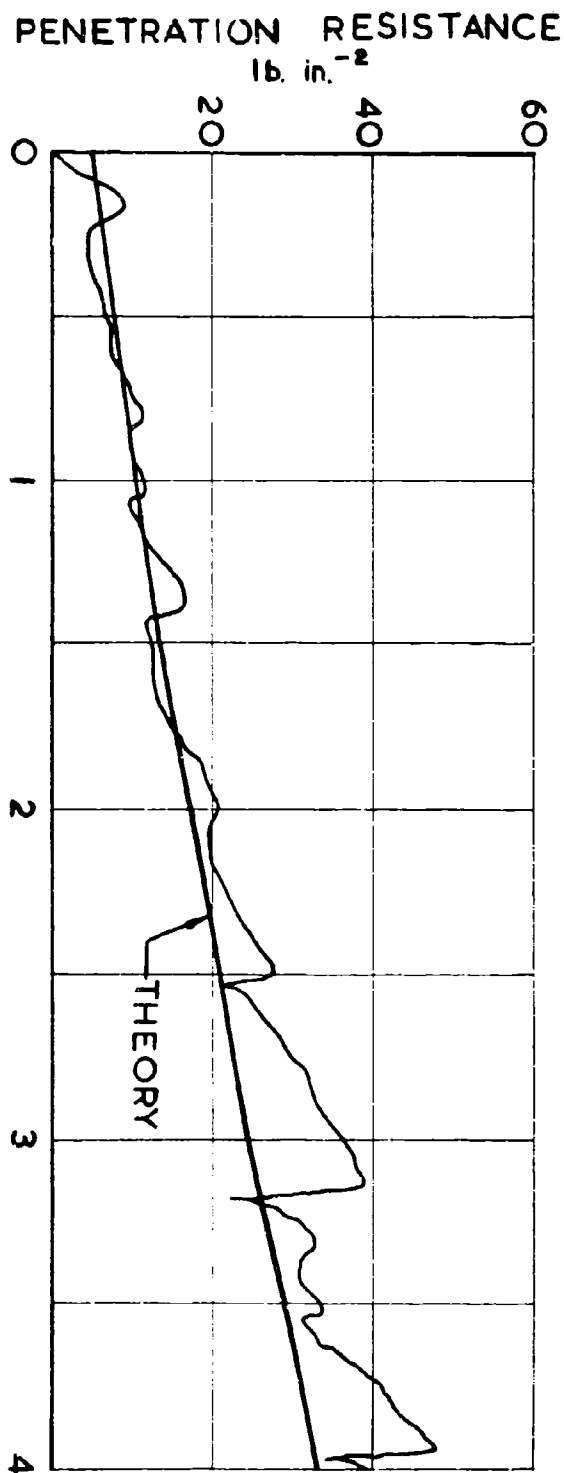
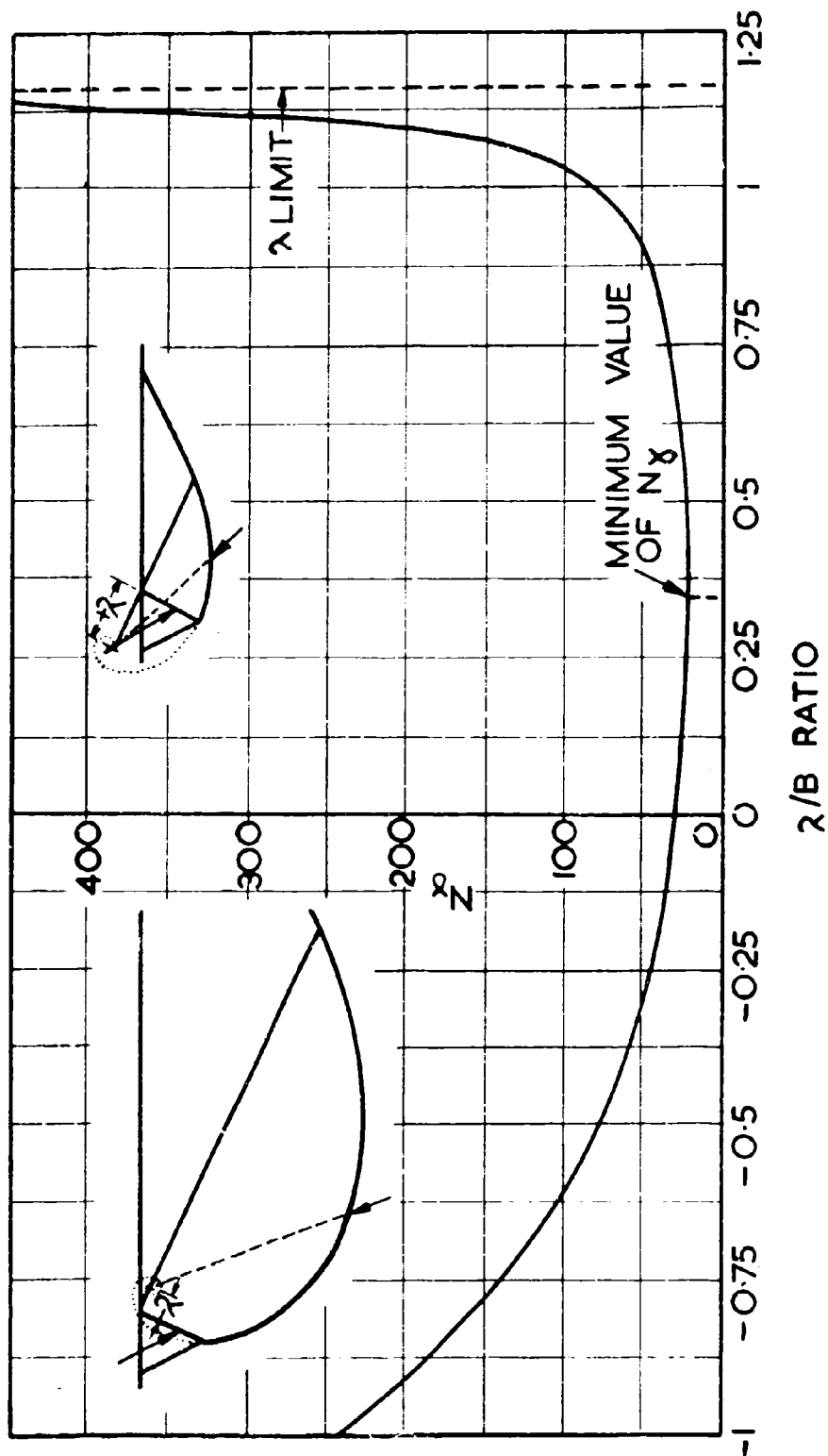FIG. 4.7.2. COMPARISON BETWEEN THE TEST RESULT OBTAINED BY WILLS AND THE PREDICTED BASE PENETRATION RESISTANCE

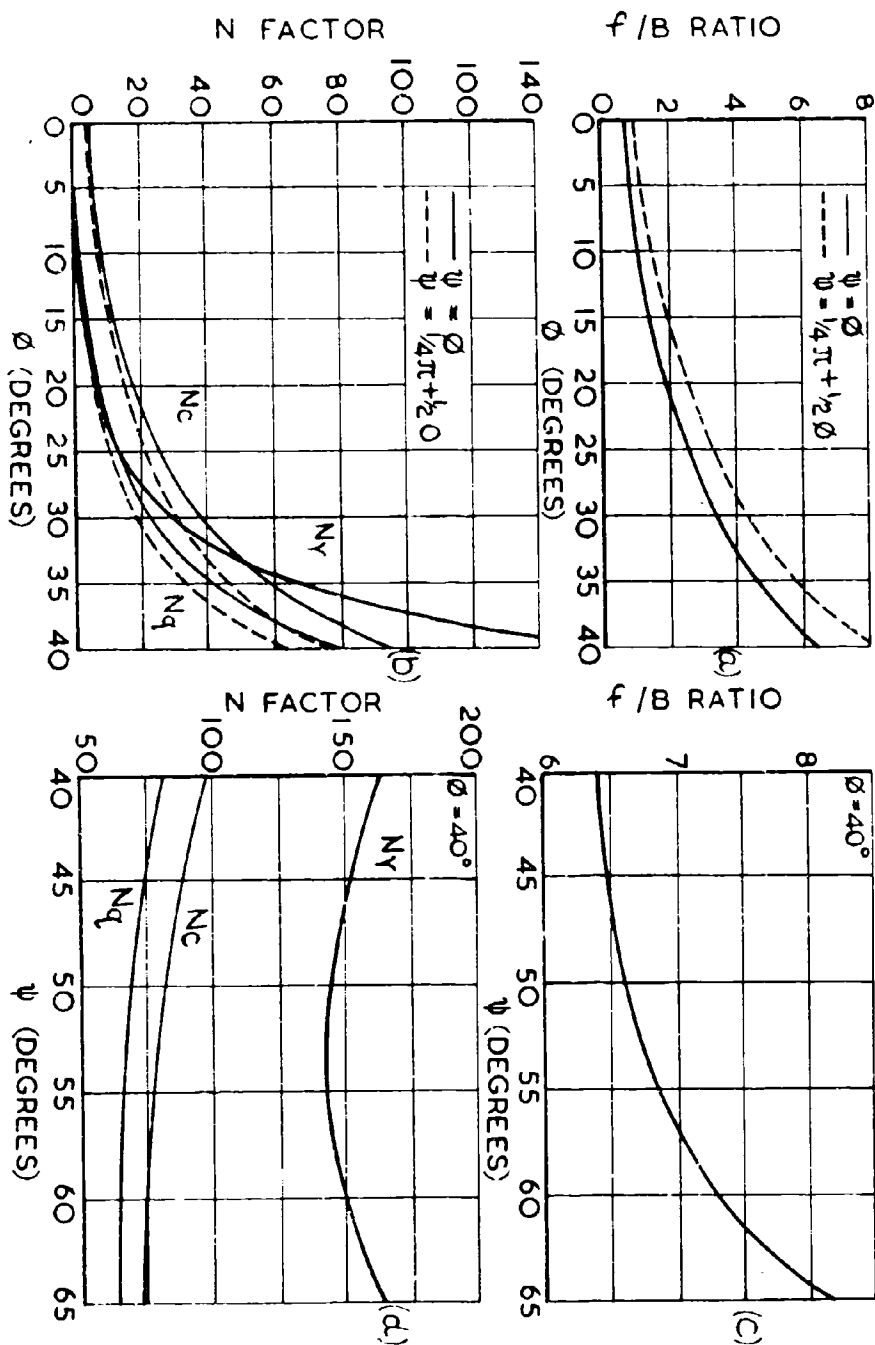FIG. 5.1.1. $N_\gamma$ AS A FUNCTION OF THE $\lambda/B$ RATIO FOR THE RESTRAINED POLE AND $\emptyset = 30°$

FIG 5.21. THE EFFECT OF WEDGE ANGLE ON THE RUPTURE DISTANCE AND THE N FACTORS.
a AND b  LIMITING VALUES OF THE FUNCTIONS OVER A RANGE OF ∅.
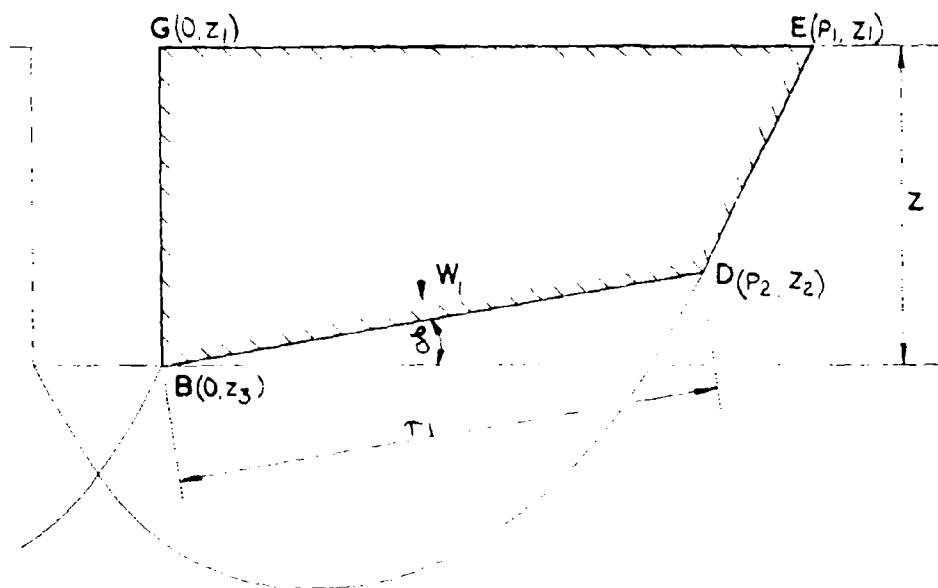c AND d  VARIATION OF THE FUNCTIONS WITH RESPECT TO ψ FOR ∅ CONSTANT.

152

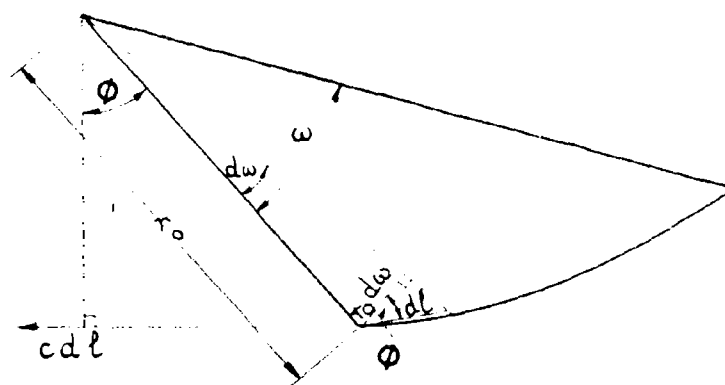FIG. A.1.1. THE DETERMINATION OF THE WEIGHT OF
THE PLANE SHEAR ZONE.



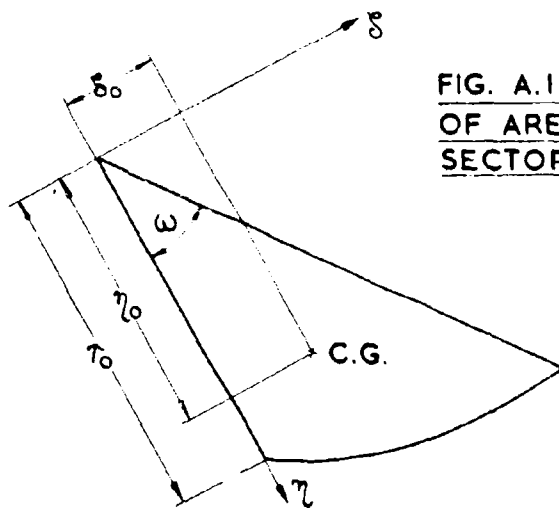FIG. A.10.1. THE DETERMINATION OF THE MOMENT OF
COHESION.

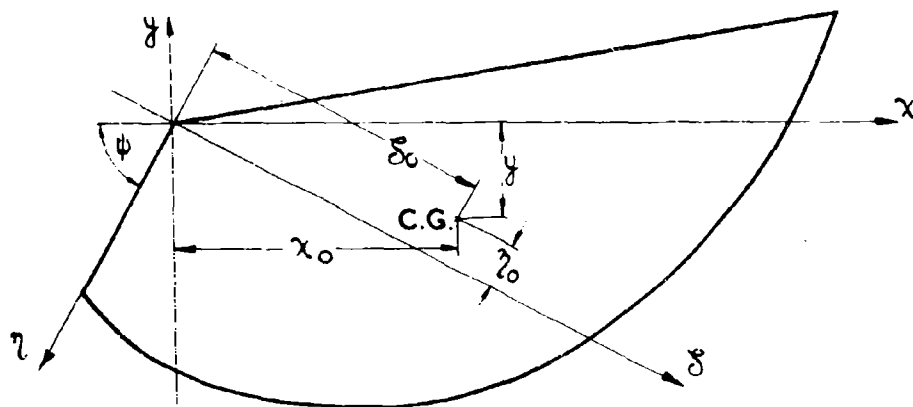FIG. A.11.1. THE MOMENTS OF AREA FOR THE SPIRAL SECTOR.



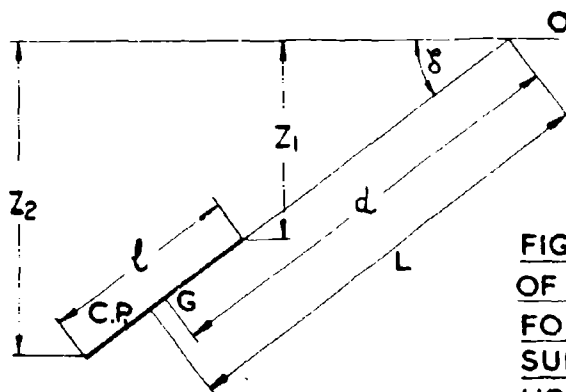FIG. A.11.2. THE TRANSFORMATION OF AXES



FIG. A.12.1. THE DETERMINATION OF THE CENTRE OF PRESSURE FOR AN INCLINED PLANE SURFACE IMMERSED IN A HOMOGENEOUS MATERIAL
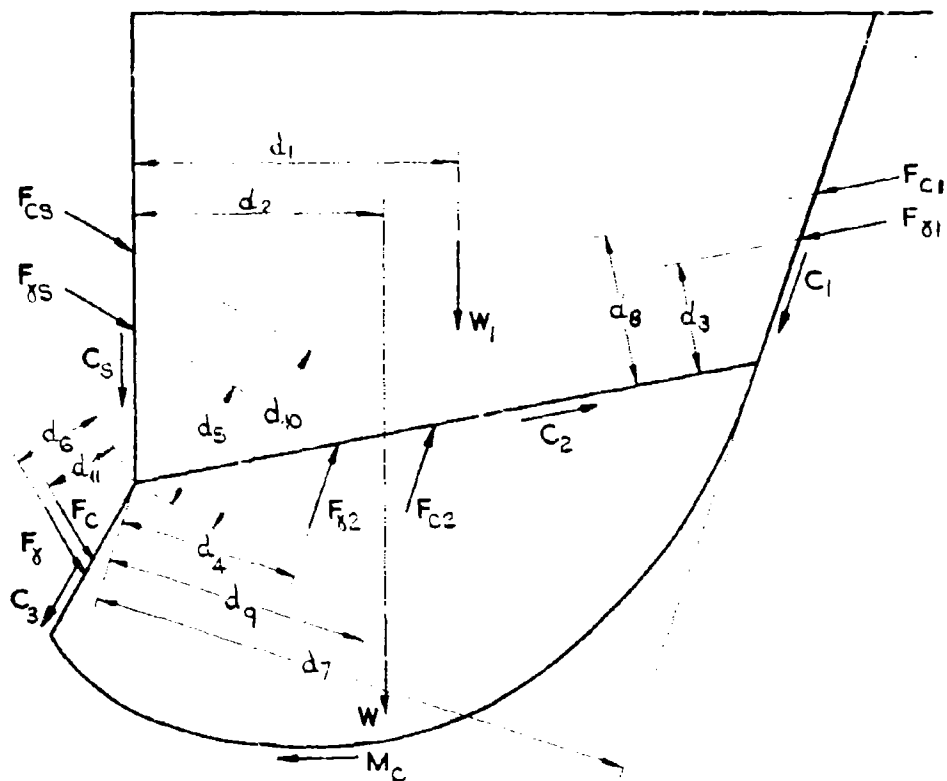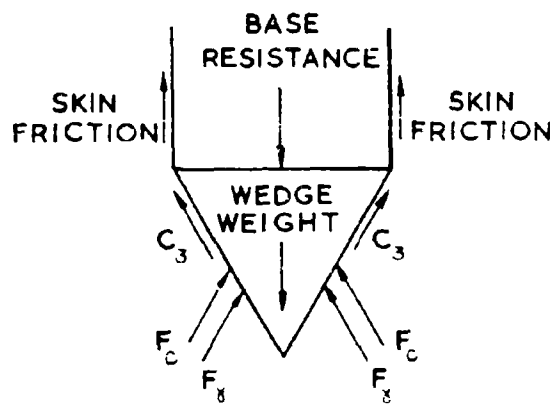
154

FIG. A. 13. 1.　THE COMPLETE SYSTEM OF FORCES



FIG. A. 13. 2.　BEARING CAPACITY

## DOCUMENT CONTROL DATA - R&D

*(Security classification of title, body of abstract and indexing annotation must be entered when the overall report is classified)*

| 1 ORIGINATING ACTIVITY (Corporate author) | 2a. REPORT SECURITY CLASSIFICATION |
|---|---|
| Land Locomotion Division AMSTA-UL | Unclassified |
| | 2b GROUP |

**3 REPORT TITLE**

The Theory of Penetration Failure in Compact Soils

**4 DESCRIPTIVE NOTES** *(Type of report and inclusive dates)*

**5 AUTHOR(S)** *(Last name, first name, initial)*

Brian D. Witney

| 6. REPORT DATE | 7a. TOTAL NO. OF PAGES | 7b. NO. OF REFS |
|---|---|---|
| November 1969 | 180 | 55 |

| 8a CONTRACT OR GRANT NO. | 9a. ORIGINATOR'S REPORT NUMBER(S) |
|---|---|
| AMCMS 5011.11.861 | 10733 (LL 136) |
| b PROJECT NO. | |
| c. | 9b. OTHER REPORT NO(S) (Any other numbers that may be assigned this report) |
| d | |

**10 AVAILABILITY/LIMITATION NOTICES**

Each transmittal of this document outside the agencies of the U.S. Government must have prior approval of U.S. Army Tank-Automotive Command ATTN: AMSTA-BSL

| 11. SUPPLEMENTARY NOTES | 12. SPONSORING MILITARY ACTIVITY |
|---|---|
| | Land Locomotion Division Mobility Systems Laboratory U.S. Army Tank-Automotive Command Warren, Michigan 48090 |

**13. ABSTRACT**

A unified procedure is employed in the determination of the penetration resistance of continuous strip footings and foundations buried up to ten times their width in compact soil. The quasi-static analysis is based on the soil failure theory of classical soil mechanics.

The theoretical data is presented by means of a two part additive equation, two dimensionless factors describing the effect of weight and cohesion. These factors are functions not only of the angle of internal friction and the penetration ratio but also of the shaft parameters and the dimensionless group dependent on the density, the cohesion and the breadth of the footing. The factors are calculated for the same figure of rupture and the practice of treating a portion of weight within the failure boundary as a surcharge has been eliminated. The inherent approximations and resultant errors in the computation are fully stated.

Experimental verification is given both of the penetration resistance and of the failure geometry by model testing in a glass sided soil tank. The penetration resistance data in compact soil support the quantitative theoretical values. The measured failure patterns are shown to be in agreement with the predicted shapes only when the effect of changing soil properties and constraints are carefully evaluated throughout the duration of the test.

| 14. KEY WORDS | LINK A | | LINK B | | LINK C | |
|---|---|---|---|---|---|---|
| | ROLE | WT | ROLE | WT | ROLE | WT |
| Soil mechanics | | | | | | |
| Strip footings | | | | | | |
| Penetration resistance | | | | | | |
| Failure theory | | | | | | |

## INSTRUCTIONS

1. ORIGINATING ACTIVITY: Enter the name and address of the contractor, subcontractor, grantee, Department of Defense activity or other organization (*corporate author*) issuing the report.

2a. REPORT SECURITY CLASSIFICATION: Enter the overall security classification of the report. Indicate whether "Restricted Data" is included. Marking is to be in accordance with appropriate security regulations.

2b. GROUP: Automatic downgrading is specified in DoD Directive 5200.10 and Armed Forces Industrial Manual. Enter the group number. Also, when applicable, show that optional markings have been used for Group 3 and Group 4 as authorized.

3. REPORT TITLE: Enter the complete report title in all capital letters. Titles in all cases should be unclassified. If a meaningful title cannot be selected without classification, show title classification in all capitals in parenthesis immediately following the title.

4. DESCRIPTIVE NOTES: If appropriate, enter the type of report, e.g., interim, progress, summary, annual, or final. Give the inclusive dates when a specific reporting period is covered.

5. AUTHOR(S): Enter the name(s) of author(s) as shown on or in the report. Enter last name, first name, middle initial. If military, show rank and branch of service. The name of the principal author is an absolute minimum requirement.

6. REPORT DATE: Enter the date of the report as day, month, year; or month, year. If more than one date appears on the report, use date of publication.

7a. TOTAL NUMBER OF PAGES: The total page count should follow normal pagination procedures, i.e., enter the number of pages containing information.

7b. NUMBER OF REFERENCES: Enter the total number of references cited in the report.

8a. CONTRACT OR GRANT NUMBER: If appropriate, enter the applicable number of the contract or grant under which the report was written.

8b, 8c, & 8d. PROJECT NUMBER: Enter the appropriate military department identification, such as project number, subproject number, system numbers, task number, etc.

9a. ORIGINATOR'S REPORT NUMBER(S): Enter the official report number by which the document will be identified and controlled by the originating activity. This number must be unique to this report.

9b. OTHER REPORT NUMBER(S): If the report has been assigned any other report numbers (*either by the originator or by the sponsor*), also enter this number(s).

10. AVAILABILITY/LIMITATION NOTICES: Enter any limitations on further dissemination of the report, other than those imposed by security classification, using standard statements such as:

(1) "Qualified requesters may obtain copies of this report from DDC."

(2) "Foreign announcement and dissemination of this report by DDC is not authorized."

(3) "U. S. Government agencies may obtain copies of this report directly from DDC. Other qualified DDC users shall request through

_____."

(4) "U. S. military agencies may obtain copies of this report directly from DDC. Other qualified users shall request through

_____."

(5) "All distribution of this report is controlled. Qualified DDC users shall request through

_____."

If the report has been furnished to the Office of Technical Services, Department of Commerce, for sale to the public, indicate this fact and enter the price, if known.

11. SUPPLEMENTARY NOTES: Use for additional explanatory notes.

12. SPONSORING MILITARY ACTIVITY: Enter the name of the departmental project office or laboratory sponsoring (*paying for*) the research and development. Include address.

13. ABSTRACT: Enter an abstract giving a brief and factual summary of the document indicative of the report, even though it may also appear elsewhere in the body of the technical report. If additional space is required, a continuation sheet shall be attached.

It is highly desirable that the abstract of classified reports be unclassified. Each paragraph of the abstract shall end with an indication of the military security classification of the information in the paragraph, represented as (TS), (S), (C), or (U).

There is no limitation on the length of the abstract. However, the suggested length is from 150 to 225 words.

14. KEY WORDS: Key words are technically meaningful terms or short phrases that characterize a report and may be used as index entries for cataloging the report. Key words must be selected so that no security classification is required. Identifiers, such as equipment model designation, trade name, military project code name, geographic location, may be used as key words but will be followed by an indication of technical context. The assignment of links, rules, and weights is optional.

164